Modelling the Spatiotemporal Change of Urban Heat Islands and Influencing Parameters

A thesis submitted by

Jasim Mohammed Ali

For the degree of

Doctor of Philosophy

Department of Civil Engineering

Faculty of Engineering

University of Nottingham

2017

Abstract

This study identifies the spatial and temporal change of three types of Urban Heat Island (UHI). The Surface Urban Heat Island (SUHI) and Canopy Urban Heat Island (CUHI) are common UHI phenomena; however, the Radiant Urban Heat Island (RUHI) is proposed as a new type of UHI. Surface temperature, air temperature, and mean radiant temperature are used as indicators to measure the SUHI, CUHI, and RUHI respectively. Visual, statistical and microclimate approaches are carried out to increase the spatial and temporal resolution of the UHI modelling. The modelling approaches employ the integration of remote sensing, GIS, and ground measurements to improve the 2D and 3D representation of the UHI. Furthermore, the influencing parameters on the formation of the three types of UHI are investigated. The research aim is to produce an integrated approach that improves the low spatial or temporal coverage of UHI models in the literature. Moreover, it quantifies the causative parameters on the formation of UHI, and proposes mitigation strategies accordingly.

London, Baghdad and Birmingham are the study areas of the SUHI, to test the variability of the size, population, Land Use/Cover (LULC), geometry, microclimate, geography, and level of development. Birmingham is chosen to study the CUHI and RUHI, because of the availability of the required data to model these UHIs. The SUHI is carried out between (2000- 2015) by the Land Surface Temperature (LST) of the thermal bands of Landsat, ASTER, MODIS and other auxiliary data. The CUHI, on the hand, is undertaken for two years (June 2012- June 2014) using high density air temperature measurements (HiTemp data), and the RUHI is simulated based on the mean radiant temperature (T_{mrt}) for four seasonal days that are part of the HiTemp. The integrated approach of the research employs three indictors (LST, air temperature, and T_{mrt}) to model the UHI which is unprecedented in the literature. Furthermore, within the use of each indicator there is a novel approach. The LST is acquired for three different cities using thermal bands from 1 m to 1000 m spatial resolution by employing diverse satellite and airborne images for about 15 years. The air temperature is hourly measured for two years by over 100 ground stations to produce high spatial and temporal thermal maps, and some of the ground stations are used to simulate the T_{mrt}. The T_{mrt} is used for the first time to model the UHI as a new indictor, which upgrades the 2D UHI using LST and air temperature to 3D UHI simulation. The influencing parameters on the formation of three types of UHI derived from the three indicators are identified, and they include many potential factors not investigated together in the literature.

The findings of such topic might be useful for decision-makers when building new cities or modifying the existing ones, even the public can know more about their environment. The results show that, London and Birmingham core area usually work as SUHI during the day and night-time. However, Baghdad city exhibits low LST in the daytime except for high density residential area as well as indusial and commercial units. Similarly, Baghdad city becomes a SUHI in the night-time, and the water bodies have high LST during the cold nights for the three cities. Despite

the higher diurnal, daytime and night-time LST of Baghdad compared to London and Birmingham, the London SUHI intensities were higher than those of Baghdad.

The temporal change of the average LST and SUHI for Birmingham did not show significant change over the study period just like London; however, they both gave high spatial variability. The diurnal averages of SUHI are 9.41, 11.29, and 7.63 ºC for Baghdad, London, and Birmingham (during 2003-2015) respectively. The CUHI appear daytime and night-time in Birmingham urban and suburban areas throughout the different seasons for 56% of the total hours of two years, to reach 13.53 ºC. The simulation of T_{mrt} show the presence of daytime Radiant Urban Cool Island (RUCI) in the City Centre of Birmingham, while, the night-time induced the development of RUHI. Various influencing parameters contribute to the different types of UHI. The land cover types and anthropogenic heat are the main contributors to the SUHI. Fourteen controllable and uncontrollable predictors control the CUHI development. On the other hand, the radiation fluxes and shadow patterns direct the RUHI formation. Overall, the spatial and temporal behaviour of UHI varies for the different types of UHI. Each type of UHI is controlled by a set of causative parameters, and these might differ based on the type of UHI as well as where and when it occurs.

Dedication

To my Family

Acknowledgment

It has been a very long journey. The dream comes true, it started a long time ago, when I was doing undergraduate studies. One day I was standing in front of the door of professional’s room, and noticed that his name is initiated with Doctor Engineer. From that time, this title has drawn my dreams.

I would like to express my very great appreciation to my supervisors Professor Stuart Marsh and Associate Professor Martin Smith for providing me sufficient guidance, useful critiques and support to complete this research. Also, I would like to thank Professor Darren Robinson for his supervision during the first six months of the study. Great thanks to Professor Heiko Balzter and Assistant Professor Stephen Grebby for their interesting comments in the viva.

The study was funded by the Iraqi government through its cultural attaché in London. Much gratitude goes to The Iraqi Ministry of Water Resources/ Anbar Directorate of Water Resources Management for giving me the permission to undertake this research. I would like to thank the U.S. Department of the Interior, United States Geological Survey for providing the Landsat data free of charge. Another special thanks to the USGS Earth Resources Observation and Science (EROS) Data Centre, who provided the ASTER data on the same basis. Furthermore, this work was supported by The Natural Environment Research Council (NERC) through providing HiTemp project's data. Likewise, I would like to thank The Birmingham Urban Climate Laboratory (BUCL) team as they were responsible for capturing the HiTemp data and provided useful explanations about some details. Furthermore, valuable data were obtained from the Ordnance Survey and Met office, so their free of charge data were important to achieve this research. Also, GF-1 satellite images of Baghdad were provided by Professors LiTao and Guanzhou, Wuhan University. A special thanks to Dr. Fredrik Lindberg, Department of Earth Sciences, University of Gothenburg for his support to run the SOLWEIG model.

I appreciate the technical support and resources from the University of Nottingham through providing the training courses, and making all the facilities available for comfort and study. Thanks to Mr. Jareer Mohammed for his support and other Nottingham Geospatial Institute (NGI) staff.

I am much thankful to my family members who always support me in difficult times. I am grateful to my Father and Mother, who assisted with valuable support. A special gratitude goes to my wife engineer Zainab Ahmed for her patience and support throughout the duration of my research. Finally, I do apologize to my Kids Taim and Yamaan for not spending enough time with them in their childhood.

Publications and Conferences

Publications

- ALI, JASIM M., MARSH, STUART H. and SMITH, MARTIN J., 2017. A comparison between London and Baghdad surface urban heat islands and possible engineering mitigation solutions. Sustainable Cities and Society. 29, 159-168.

- ALI, JASIM M., MARSH, STUART H. and SMITH, MARTIN J., 2016. Modelling the spatiotemporal change of canopy urban heat islands . Building and Environment. 107, 64-78.

Conferences

Conference Name/ sponsor	Date	Place	Participation
Geoforum/ EDINA	June 2014	Edinburgh, UK	Attendance
Silver Anniversary/ GRSG	December 2014	London, UK	Poster presentation
Wavelength/ RSPSoc	April 2015	Newcastle, UK	Oral presentation
RSPSoc, NCEO and CEOI-ST Joint Annual Conference	September 2015	Southampton, UK	Accepted abstract
Erath observations/ RSPSoc	September 2016	Nottingham, UK	Oral presentation

Table of Contents

List of Tables

List of Figures

List of Acronyms and Abbreviations

°C: Degree Celsius

3D: Three Dimensional

3DUI: Three-dimensional urbanization index

AH: Anthropogenic Heat

ASM: Aginova Sentinel Micro

AST_05: ASTER On-Demand L2 Surface Emissivity

AST_08: ASTER surface kinetic temperature

ASTER: Advanced Spaceborne Thermal Emission and Reflection Radiometer

AUHI: Atmospheric Urban Heat Island

AVHRR: Advanced Very High-Resolution Radiometer

AWS: Automatic Weather Stations

BUCL: Birmingham Urban Climate Lab

BUHI: Boundary Urban Heat Island

CEDA: Centre for Environmental Data Archival

CEH: Centre for Ecology and Hydrology

CHEOS: China High-resolution Earth Observation System

cm: centimetres

CUHI: Canopy Urban Heat Island

DSM: Digital surface model

DTM: Digital terrain model

ENM: Emissivity Normalisation Method

EOSDIS: Earth Observing System Data and Information System

EROS: Earth Resources Observation and Science

ESOC: Empirical Studies of Conflict Project

ESPA: Centre Science Processing Architecture

ETM+: Enhanced Thematic Mapper Plus

EVI: Enhanced Vegetation Index

HI: Heat Index

HiTemp: High density Temperature measurements

hPa: hectoPascals

IDW: Inverse Distance Weighting

K: Kelvin

K: Shortwave

L: Longwave

LaSRC: Landsat Surface Reflectance Code

LC: Land classes

LDCM: Landsat Data Continuity Mission

LEDAPS: Landsat Ecosystem Disturbance Adaptive Processing System

LIDAR: Light Detection and Ranging

LP DAAC: Land Processes Distributed Active Archive Centre
LSE: Land Surface Emissivity
LST: Land Surface Temperature
LULC: Land Use/Cover
m: metres
MCR: MATLAB Compiler Runtime
MIDAS: Met office Integrated Data Archive System
MLC: Maximum Likelihood Classifier
MODIS: Moderate resolution imaging Spectroradiometer
MRM: Multiple Regression Model
MRT: MODIS Reprojection Tool
MSAVI: Modified Soil Adjusted Vegetation Index
MSS: Multispectral Scanner System)
NASA: National Aeronautics and Space Administration
NBR: Normalized Burn Ratio
NBR2: Normalized Burn Ratio 2
NDMI: Normalized Difference Moisture Index
NDVI: Normalized Difference Vegetation Index
NERC: The Natural Environment Research Council
NLST: Normalised Land Surface Temperature
NO_x: Nitrogen Oxides
OS: Ordnance Survey
PCA: Principle Component Analysis
PET: Physiological Equivalent Temperature
PO: Population
PR: Atmospheric pressure
QE: Latent heat
QG: Ground heat flux
QH: Sensible heat
RADAR: Radio Detection And Ranging
RH: Relative humidity
RMSE: Root Mean Square Error
RR: Retro-Reflective
RS: Remote Sensing
RUCI: Radiant Urban Cool Island
RUHI: Radiant Urban Heat Island
SAVI: Soil Adjusted Vegetation Index
SD: Standard Deviation
SEBAL: Surface Energy Balance Algorithm for Land
SO_2: Sulfur Dioxide

SOLWEIG: SOlar and Long Wave Environmental Irradiation Geometry
SPSS: Statistical Package for the Social Sciences
SR: Solar radiation
SUCI: Surface Urban Cool Island
SUHI: Surface Urban Heat Island
SVF: Sky View Factor
T_a: Air temperature
TABI: Thermal Airborne Imagery
TES: Temperature-Emissivity Separation
TG: Topographic groups
TIR: Thermal Infrared
TM: Thematic Mapper
T_{mrt} : Mean Radiant Temperature
TT: Topographic themes
TVF: Terrain View Factor
UA: Urban Atlas
UCZs: Urban Climate Zones
UHA: Urban Heat Advection
UHI: Urban Heat Island
UMEP: Urban Multi-Scale Environmental Predictor
USA: United State of America
USE: Urban Surface Energy
USGS: U.S. Geological Survey
VS: Visible Sky
WPS: Web Processing Service
WRF: Weather Research and Forecasting
WS: Wind speed
WUHI: Water Urban Heat Island

Chapter 1: Introduction

1.1. Research background

The accelerating growth of global populations has led to more crowded cities being a driving force of human development. Besides, cities face major challenges such as air pollution, heat waves, and flooding. Consequently, urban planners need to take long term actions to build truly resilient cities to reduce their vulnerability and promote sustainable development (WHO, 2008). Some of these serious challenges to sustainable cities is the excessive heat they generate, reduced vegetation, increased urban impervious materials, increased energy consumption and reduced air quality (Environmental Protection Agency, 2008, Gartland, 2008). Voogt (2004) defines an Urban Heat Island (UHI) as the unintentional climate modification when both atmosphere and surfaces in urbanised areas have warmth characteristic compared to their non-urbanised surroundings. UHI was first documented in 1818 when Luke Howard found an artificial excess of heat in the city compared with the country (Gartland, 2008). The term UHI was first used in the literature by Manley (1958). Gartland (2008) clarifies that urban and suburban areas can have higher air and surface temperature than rural areas, due to several reasons such as replacing the natural areas by impervious surfaces. Urban expansion is becoming a common concern worldwide as people accumulate in the major cities leaving the rural areas. The percentage of the humans living in cities increased from one third of the 2.5 billion world's population in 1950 to more than half of the 6.9 billion the global population in 2010 (Yang, 2011). The increase of urban population has economic and environmental consequences; however, the environmental changes have got much attention due to the climate change and global warming which have direct impacts on human's life. Lenzholzer (2015) explains that the urban climate is very different from the countryside, and even the intra-urban microclimate varies among places in the same city. Morice et al. (2012) suggested two baselines of the global near-surface air temperature and sea-surface temperature. The first baseline is the pre-industrial period (1850-1900), and the second baseline is the long term or post-industrial period (1961-1990). Recently, the National Aeronautics and Space Administration (NASA) has reported that most of the global warming occurred in the past 35 years, with 16 of the 17 warmest years on record for the two baselines occurring since 2001 (NASA, 2017). The Met Office has marked that the planet's temperature series shows that 2016 was 0.77±0.1 °C above the long-term (1961-1990) average, and it is 1.1 °C above the pre-industrial (1850 – 1900) (MetOffice, 2017). Accordingly, the temperatures continue a long-term warming trend, and it is essential to monitor and mitigate this heat increase generated by man's activities.

There is a lack of awareness of the urban climate not only by the public, however, even some designers and policy makers do not take into account phenomena such as UHI when planning new cities or rebuilding existing cities (Lenzholzer, 2015). There is more than one type of UHI, and in this study the term UHI is used to describe the different types of UHI, which represents the difference in temperature between places where the place of the higher temperature forms the heat island. The definition and history of UHI will be discussed later more details. Studies in the literature have focused on the impacts and mitigation strategies of UHI.

However the spatial and temporal change of UHI have not been fully understood as well as the causes of UHI (Sung, 2013, Doick et al., 2014, Agency, 2013, Al-musaed, 2007, Gorsevski, 1998). Akbari and Muscio (2015) highlighted some of the negative impacts of UHI on urban inhabitants such as higher outdoor summertime temperature, higher urban air pollution, higher demand for air conditioning, and higher heat stress-related mortalities. They emphasised that urbanisation is driven by macro and global economic needs and little can be done in the short term to reverse the migration back to rural areas. Therefore, identifying the causative factors that induce the spatial and temporal development of UHI is crucial to countermeasure this phenomenon. However, prior to the analysis of influencing parameters, the spatiotemporal trends of the UHI need to be evaluated.

Even though there have been a large number of UHI studies, they still fail to produce a high spatial and temporal evaluation of UHI trends (Zhou et al., 2015). The reason for that is the available technology is not sufficient to investigate the spatial and temporal change of UHI together, because air temperature measurements lack the high spatial resolution and remotely sensed or aerial images have poor temporal coverage (Gartland, 2008). Pairs of urban/rural weather stations or air temperature traverses have been the traditional ways of measuring near surface UHI. On the other hand, thermal remote sensing techniques are used to investigate the surface or skin UHI due to the heterogeneity of the urban surface (Hu and Brunsell, 2013, Tomlinson et al., 2012). Surface and air temperature have different behaviour. Guan (2011) examined the surface temperatures of impervious, pervious, and natural ground materials and their association to ambient air temperatures in the urban microclimate. The study found differences in surface temperatures of each material, but air temperatures showed no significant difference. Nevertheless, the study site was small and limited to the University of California, Berkeley (UCB) campus in Northern California. Schwarz et al. (2012) stated that different indicators quantify the different types of UHIs, as specific indicators are calculated with either air or surface temperatures. Accordingly, an integrated approach that adopts both surface and air temperatures is needed, because both approaches have advantages and disadvantages but are rarely combined. Moreover, the mean radiant temperature is adopted in this study as the third indictor that combines the causative parameters on air and surface temperature.

Gartland (2008) asserts that the ideal hypothesis of measuring the impacts of urban heat island on the climatic variables such as the temperature is to measure them with and without the city in place, which is impossible in the real world. The magnitude of UHI can be measured by various methods; these methods have been developing with the development of science and technology. However, measuring techniques cannot provide information about how the UHI works. Hence, models are used to tell us about UHI impacts, causes, and mitigation strategies under different conditions. This research adopts fixed stations and remote sensing as two measuring techniques, and a modelling application to fulfil the purpose of the study. The traditional methods in the literature (as will be discussed in detail in the literature review) mainly provide the ability to investigate the UHI change between urban and rural areas. Nevertheless, in this study the spatiotemporal change of various types of UHI will be investigated for intra-urban differences, due to the development of technology and meteorological infrastructure. The intra-urban differences provides a better understanding over the urban-rural difference to study the UHI, because it is impossible to remove or replace cities in the real world as Gartland (2008) stated. Furthermore, choosing a meteorological station in a rural area to be a reference to measure the UHI might give an inadequate value, as cities (compared to adjacent natural lands) fundamentally modify the aerodynamic, radiative, thermal, and moisture properties in the urban region (Roth, 2012). However, cities could be improved in terms of thermal comfort by mitigating the sources of anthropogenic heat in the cities themselves (Chrysoulakis and Grimmond, 2016).

A detailed explanation of UHIs' impacts, causes, types, and its measurement and modelling will be described later. Three study areas were chosen to highlight the effect of geographical location and different level of development on UHI formation. Accordingly, the broader aim of this study is to fill the gap in knowledge in the field of UHI studies which results due to the interaction between the urban climate and the biophysical parameters that form the underlying ground cover through the radiative fluxes. The specific aims and objectives that derived the research questions are detailed in the next section.

1.2. Research questions, aims, and objectives

The research questions have been determined to answer unsolved problems highlighted in the literature. Furthermore, the objectives and aims have been developed to be achievable and realistic based on the study timeline and available technology.

Question 1: What is the spatial change of UHI?

Question 2: What is the temporal change of UHI?

Question 3: What is the potential of quantifying the parameters that influence the development of UHI using remote sensing, GIS and ground measurements techniques?

Question 4: To what extent do RS, GIS, and ground measurements improve the visual and statistical models of UHI?

The research's aims and objectives have been derived based on the research questions as follow:

Aims: The first aim is to employ the ground measurements with remotely sensed and GIS data to produce an integrated approach that adopts high spatial and temporal resolution data, to cover the gap in knowledge resulting from only using one approach and so lacking either spatial or temporal coverage. The second aim is to investigate the influencing parameters on the formation of UHI, and discuss the potential causes of UHI. Achieving the first and second aims will enable the evaluation of the applicability of RS, GIS and ground measurements techniques to study the UHI. Furthermore, the air and surface temperature will be tested whether they provide enough prediction of the UHI formation. Consequently, the objectives are summarised to be:

Objective 1: Investigate the spatial change of UHI using air, surface and mean radiant temperatures. **(Question 1)**
Objective 2: Investigate the temporal change of UHI using air, surface and mean radiant temperatures. **(Question 2)**

Objective 3: Identify the relationship between the dependant variables (temperature layers) and independent variables (influencing parameters) by the statistical or visual analysis. **(Question 3)**
Objective 4: Use the best available free remotely sensed, GIS and ground based data to enhance the spatial and temporal resolution of UHI visual and statistical models. **(Question 4)**

The influencing parameters in objective 3 can be grouped into:

1- Land use/cover and population: remotely sensed, GIS, or ground data from already available sources, or classification of the raw data where there is no already classified ones.
2- Geometry and topography: these involve the preparation of digital elevation models Digital Surface Model (DSM) and Digital Terrain Model (DTM) about the study site, and their use to derive the geometrical and topographical variables such as sky view vector, shadow patterns or elevations.
3- Radiation fluxes: a microclimate model and GIS techniques are used to deriving the shortwave and longwave radiations that impact people's outdoor thermal comfort. Radiation fluxes are modelled based on the above two groups as well as the meteorological data. These fluxes already combine the surface and air temperature measurements, so they include many independent variables joined to represent additional influencing parameters.

1.3. Research's novelty, importance and motivation

The integrated approach of the research employs three indictors (LST, air temperature, and T_{mrt}) to model the UHI which is unprecedented in the literature. Furthermore, within the use of each indicator there is a novel approach. The LST is acquired for three different cities using thermal bands from 1 m to 1000 m spatial resolution by employing diverse satellite and airborne images for about 15 years. The air temperature is hourly measured for two years by over 100 ground stations to produce high spatial and temporal thermal maps, and some of the ground stations are used to simulate the mean radiant temperature (T_{mrt}). The T_{mrt} is used for the first time to model the UHI as a new indictor, which upgrades the 2D UHI using LST and air temperature to 3D UHI simulation. The influencing parameters on the formation of three types of UHI derived from the three indicators are identified, and they include many potential factors not investigated together in the literature.

Planning for a sustainable city is a challenging task for decision makers, and evaluation of the long-term consequences should be taken on. The massive growth of urban areas makes them the biggest contributors to global greenhouse gas emissions by around 80% (Martos et al., 2016).

Martos et al. (2016) claims that UHI is one of the greatest environmental problems due to urbanisations and industrialisation. This makes the urban climate very different from the countryside, and even the intra-urban microclimate varies among places in the same city. For mega and medium and even small size cities the urban variation of climatic variables can be large, and the problem with larger cities is that the core is far away from the boundaries (Ng and Ren, 2015). Ng and Ren (2015) points out that the city must find its own solution as it is difficult to bring in help from rural areas, for instance cooling effects of rural vegetation cannot reach the City Centre. Studies in the literature have focused on the impacts and mitigation strategies of UHI with not much investigation on the causes and spatiotemporal change of UHI. To understand the influences of UHI and how to relieve it, that requires identifying the causes and the spatial as well as the temporal variation of UHI. The outcomes of such study might be beneficial to urban planners, architects, policy makers, civil engineers and even educated public. That will have a direct contribution to the efforts of meeting the sustainability criteria as the researcher's project is in sustainable energy technology.

The interaction between urban environment, morphology, land use/cover, geometry, and geography is a complicated issue. So, the research highlights some aspects of these relationships. That will help urban planners to make decisions for better cities in terms of surface cover and configurations as well as buildings' energy use. Furthermore, the causes of UHI formation are quantified in this study for the different types of UHI. Then, identifying the drivers that induce the UHI formation will give recommendations about mitigation strategies. Also, the study gives a civil engineering insight toward the interaction between urban surfaces and the environment. Specifically, the study explains the spatial and temporal change of UHI not only using the air and surface temperature; the other urban surface energy parameters are incorporated. In addition, the role of GIS and RS data in improving the urban modelling is highlighted by using free access data for academic purposes. On the other hand, the potential of classifying urban cover by training classes and indices using RS data is investigated. As the focus is on the microclimate and the ecosystem due to urbanisation, this highlights the impact of anthropogenic releases in urban environment compared to sun energy in rural areas as the major source of energy. Besides, the fourth dimension (time) as well as the three dimensions of the globe are incorporated to reflect the impact of time on the surface energy balance. Moreover, the study introduces the potential of combining different sources of data to be processed using RS and GIS techniques. This will help researchers in fields such as engineering, geography and urban planning to judge what the best data combination is better to represent the real world, which gives a robust approach for urbanisation challenges.

The engineering impacts of UHI can be societal, economic or environmental. For instance, the heat waves doesn't only lead to a bit of minor discomfort, nevertheless, extreme heat waves can cause various health problems as well as high energy consumption. Lenzholzer (2015) claims that a two days short heat wave might lead to 10-15% higher mortality rate in many countries. One of the headlines in the Guardian news the summer of 2015 says ''the death toll in India's heatwave has climbed towards 1500'' (Burke, 2015); another headline in Rudaw news says ''Iraqi's scorching heat kills 52 children in refugee camps'' (Rudaw, 2015), for examples. The presence of UHI increases the energy use particularly in the summer which leads to the rise of CO_2 equivalent annual emissions of up to 7% (Magli et al., 2015). Besides, some researchers relate the surface energy imbalance to high intensity UHI; also, higher surface temperature is responsible for impaired water quality due to thermal pollution (James, 2002). Santamouris (2013) emphasises that one of the most documented phenomena of climate change is the UHI for various places on the earth. Moreover, the United Nations have annual meeting to the level of world leaders to confront the climate change and cut the manmade negative emissions. One of the key elements agreed in these summits is to keep global temperatures "well below" 2.0 ºC above pre-industrial times (UN, 2015).

1.4. Thesis outline

The thesis contains eight chapters. The first three chapters are the introduction, literature review and methodology. The next three chapters include the results and their specific discussions. Finally, the last two chapters answer the research questions and highlight the research contributions, to sum up with brief conclusions and some suggestions for future work. The outline briefly describes the contents of the thesis to provide a simple guide to the reader.

Chapter one explains the research's background and gives a general overview of the research problem. Accordingly, the research questions, aims, and objectives were set. Then, the importance and motivation to undertake such topic are highlighted. Chapter two reviews the existing studies in the literature and state of the art related to the topic. So, it clarifies the characteristics of the different types of UHI with the behaviour of these types temporarily. After that a comparison is drawn between the surface and atmospheric UHI. The impacts and causes on the UHI development are discussed. Then, the role of the UHI in the surface urban energy and its contribution to radiation fluxes are interpreted. The used scale is justified as this research studies entire cities, and the different modelling scales are identified. The microclimate model adopted in this study is clarified, which combines the contributors to surface and atmospheric UHI. Based on the reviewed literature, the gaps in knowledge that derived the research questions are highlighted. Next, chapter three introduces the study areas and why they have been employed. Furthermore, a brief description of the various data and approaches in this study is provided, since each result chapter has its own data and method that are further clarified in the same chapter.

Chapters four, five and six are the body of the thesis where the results are presented and discussed. Each one of these three chapters tries to fulfil the four objectives that have been derived from the research's questions. Chapter four employs the surface temperature to study the spatial and temporal change of Surface UHI and addresses its relationship with some spectral indices. Chapter five uses the air temperature to model the spatiotemporal change of the Canopy UHI, and investigates many influencing parameters on the formation of Canopy UHI. Chapter six simulates the mean radiant temperature and radiation fluxes as well as shadow patterns. Furthermore, it investigates the impacts of radiation fluxes on the Radiant UHI. The latter was derived from the mean radiant temperature to introduce a new type of UHI.

The last two chapters summarise the research findings and give concluding remarks for the future work. Chapter seven analyses the results from the previous chapters to answer the research questions. Moreover, it demonstrates the study’s contributions to knowledge and its limitations. Then, chapter eight draws the conclusions, and suggests some recommendations for future studies. Finally, the references are attached at the end, just after the appendices.

Chapter 2: Literature Review

2.1. UHI types

The different types of UHIs have been classified based on different attributes. Cermak et al. (1995) classifies the urban climate into three layers. The first layer describes a street and its surrounding buildings, which is called the canyon layer. Second, the canopy layer extends upwards from the surface to approximately mean building height. Third, the boundary layer is a layer of air up to 2000 metres height above the canopy layer. Srivanit and Hokao (2012) explains that there are three types of UHI. First, the Surface Urban Heat Island (SUHI) refers to the difference in surface temperatures between urban and rural areas. Second, the Canopy Urban Heat Island (CUHI) indicates the difference in air temperature between urban and rural areas within the canopy layer. Third, the Boundary Urban Heat Island (BUHI) measures the difference in air temperature between the urban and rural areas within the boundary layer (see Figure 2.1). Yuan and Bauer (2007) mentions that the CUHI and BUHI are both Atmospheric Urban Heat Island (AUHI), since they measure the difference in air temperature, unlike the SUHI which adopts the surface temperature. This research investigates both SUHI and CUHI, as they have direct impact on people's life and incorporate the complex interaction between the surface and above climate.

As an example for the UHI, Roth et al. (1989) used NOAA AVHRR (Advanced Very High Resolution Radiometer) satellite data to display the LST of Vancouver, British Columbia, Seattle, Washington, and Los Angeles, California. They found that the SUHI is largest in the daytime, which is the reverse of the known characteristics of CUHI. On the other hand, when the core of the city has lower temperature than the surrounding rural areas, the city works as a cool island in opposite to the behaviour of the heat island (Frey et al., 2005). Rasul et al. (2017) explain that only few studies have investigated the formation of Surface Urban Cool Island (SUCI) in arid and semi-arid climates. For example, Frey et al. (2005) found a distinct daily cool island for Dubai and daily cooling areas of Abu Dhabi city and its surrounding mangrove areas using four ASTER (Advanced Spaceborne Thermal Emission and Reflection Radiometer) satellite scenes.

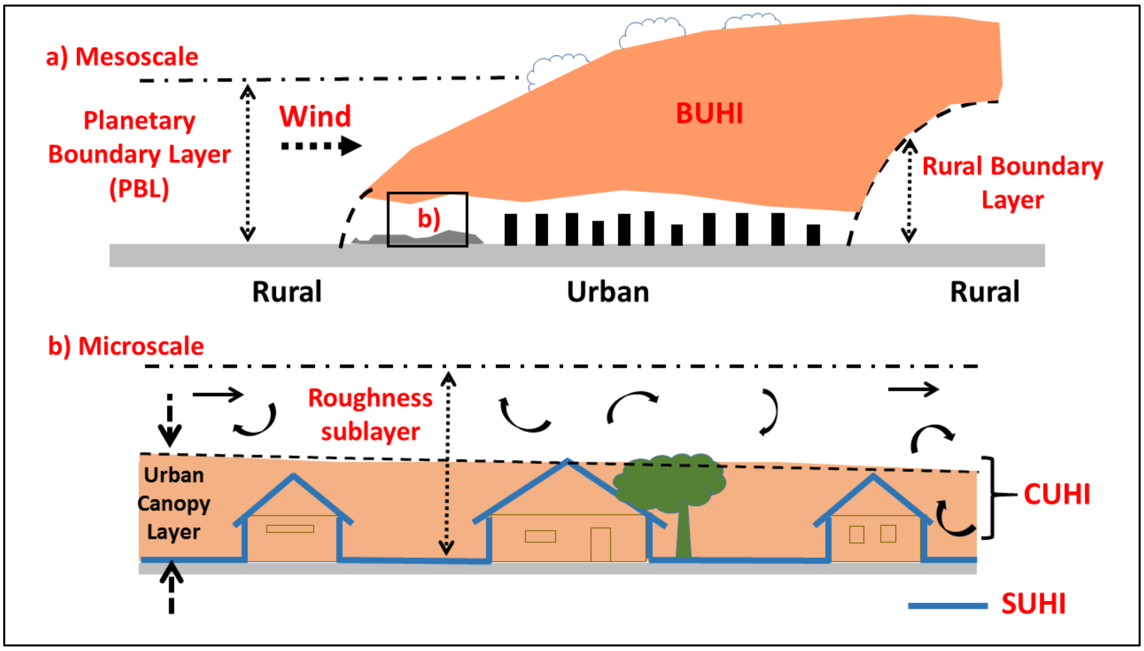

Figure 2.1 Types of urban heat islands and the main components of the urban atmosphere. Modified after Srivanit and Hokao (2012).

2.2. UHI development

The CUHI intensity varies throughout the day and night, and the synoptic weather has a large impact on its intensity for a specific location. Morris and Simmonds (2000) studied the intensity of CUHI in Melbourne, Australia between the central business district and the airport using meteorological stations. They found that temperatures are always warmer in the central business district than they are at the airport based on daily variations in air temperature as shown in Figure 2.2. The summer and winter CUHI were calculated by Morris and Simmonds (2000), then Gartland (2008) adapted the results as shown in Figure 2.2. It can been seen that the intensity peaks overnight and gradually declines during the day. Gartland (2008) indicates that this behaviour is common in most cities of moderate climate and latitude. However, Gartland (2008) modifies that by saying the CUHI intensity differs in magnitude and the peak time from city to city. Conversely, Watkins et al. (2002) studied London's UHI, and they pointed out that the heat island can happen during the day specifically in the winter or during the night particularly in the summer. The reason for that, in the summer the air temperature of a green space (such as a park) is often higher than a built up area during the daytime, because it is more exposed to the Sun's heat during the daytime (Watkins et al., 2002). Then, the cooling rate of the green space during the night is higher than the built-up area, and the green space acts as a cooling island towards the built-up area. While, in the winter the air temperature of the green space is roughly lower than the built up area, so the built up area works as heating island (Watkins et al., 2002). Morris and Simmonds (2000) did not differentiate between the summer and winter CUHI intensity, whereas, Watkins et al. (2002) notified different behaviours which supports the modification of Gartland (2008).

The SUHI is primarily measured using thermal RS, by capturing the radiances at the top of atmosphere, then retrieving the Land Surface Temperature (LST) (Hadjimitsis et al., 2013). A number of studies in the field have investigated the effect of SUHI using remote sensing techniques (Radhi et al., 2013, Agarwal et al., 2014, Shahmohamadi et al., 2011, Park and Suh, 2013, Tomlinson et al., 2012, Sobrino et al., 2013, Peng et al., 2011, Sung, 2013, Schwarz et al., 2011, Deng and Wu, 2013, Wu et al., 2013, Hu and Brunsell, 2013, Dousset and Gourmelon, 2003, Streutker, 2002, Kato and Yamaguchi, 2005, Lo and Quattrochi, 2003, Tran et al., 2006, Roth et al., 1989, Gallo et al., 1993). Early studies utilised AVHRR satellite data for SUHI assessment (Gallo et al., 1993, Roth et al., 1989). Later on, ASTER and Landsat ETM+ (Enhanced Thematic Mapper Plus) were employed to study the SUHI (Kato and Yamaguchi, 2005). However, recent studies have been trying to improve the spatial and temporal resolution of UHI by adopting multisource data as well as deriving new biophysical parameters for better representation and investigation of UHI.

For example, Wu et al. (2013) developed a three dimensional urbanization index (3DUI) using digital terrain models to assess the SUHI influences during heat waves in subtropical areas. The daytime SUHI reached 10.2 Degree Celsius (°C), and the correlation coefficient between 3DUI and surface temperature was greater than 0.6. Schwarz et al. (2011) explored indicators for quantifying the SUHI of European cities using MODIS (Moderate resolution imaging Spectroradiometer) satellite data, the indicators were almost land use/cover and deviation from the mean temperature. The research concluded that differences and instabilities of the indicators as well as several indicators in parallel should be taken for describing the SUHI of a city.

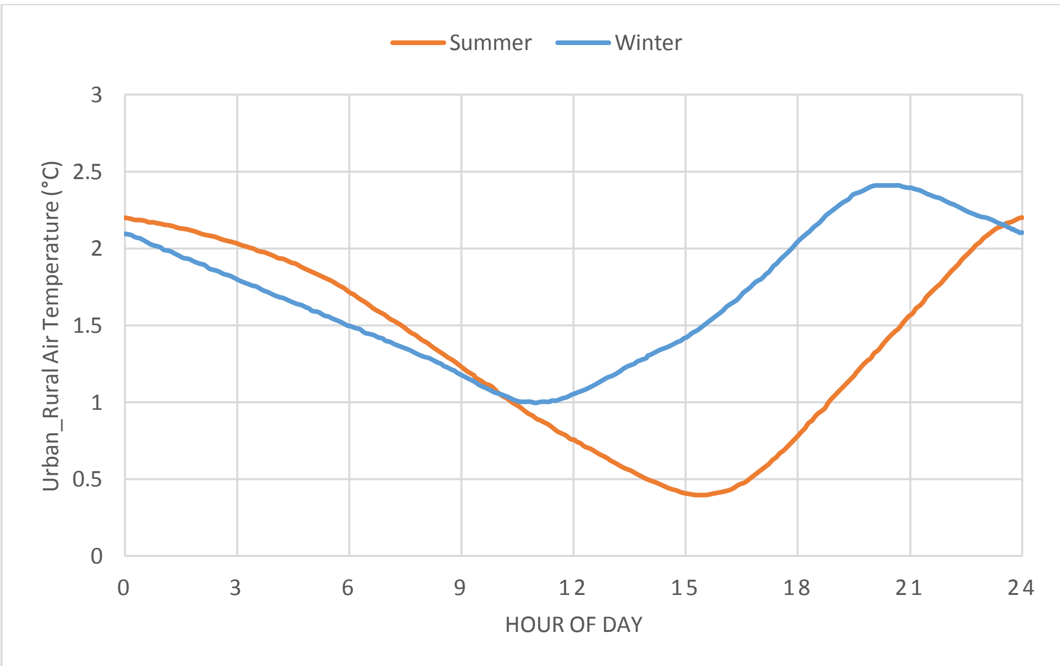

Figure 2.2: Summer and winter CUHI intensity between the central business district (urban) and airport (rural) of Melbourne, Australia. Modified after Gartland (2008).

2.3. A comparison between surface and atmospheric UHI

The relationship between surface and atmospheric UHI varies day and night over different land use areas. During the day surface temperatures vary more than air temperatures, however during the night they show fairly similar behaviour in spite of surface temperature showing more fluctuation (Environmental Protection Agency, 2008). The reason for that is during the day the main sources of energy are the Sun and anthropogenic activities, while, in the night the main source of energy is the anthropogenic activities. Surface temperature has significant indirect impact on air temperature, so green areas might cool the adjacent air in the night; whereas, the built-up areas emit the stored heat during the day to warm up the above air as illustrated in Figure 2.3. Nonetheless, the temperatures might fluctuate according to several parameters such as season, weather condition, sun energy intensity and land use/cover (Environmental Protection Agency, 2008). Therefore, Environmental Protection Agency (2008) distinguishes between the AUHI and SUHI as they show different behaviours. So, in a hot sunny summer day the urban surface can have a temperature of 27-50 °C higher than the air temperature. While, the surface temperature stays near to air temperatures for shaded or moist surfaces in most rural surroundings. Table 2.1 compares the characteristics of surface and atmospheric UHI in terms of temporal development, peak intensity, identification method and depiction.

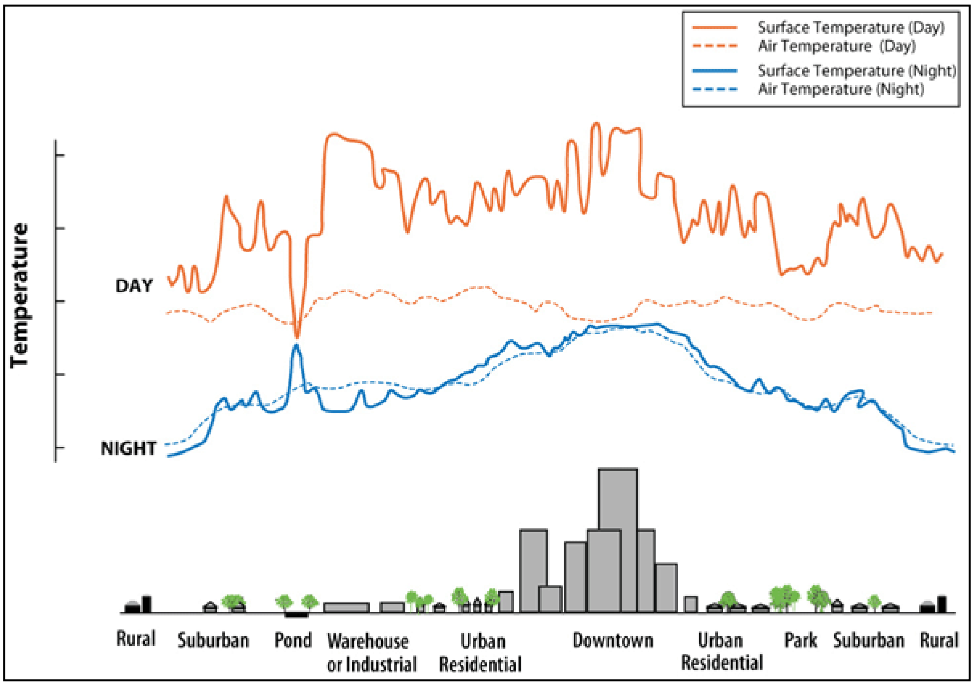

Figure 2.3: Differences of Surface and Atmospheric Temperatures. Surface and atmospheric temperatures vary over different land use areas (Environmental Protection Agency, 2008).

Table 2.1: Basic Characteristics of Surface and Atmospheric Urban Heat Islands and the differences between these two heat island types. Modified after Environmental Protection Agency (2008).

Feature	SUHI	AUHI
Temporal Development	❖ Present most of the day and night ❖ Most intense during the day and in the summer	❖ May be small or non-existent during the day ❖ Most intense at night or predawn and in the winter
Peak Intensity (Most intense UHI conditions)	❖ More spatial and temporal variation: • Day: 18 to 27°F (10 to 15 °C) • Night: 19 to 18°F (10 to 15 °C)	❖ Less variation: • Day: -1.8 to 5.4°F (-1 to 3 °C) • Night: 12.6 to 21.6°F (7 to 12 °C)
Typical Identification Method	❖ Indirect measurement: • Remote sensing	❖ Direct measurement: • Fixed weather stations • Mobile traverses
Typical Depiction	❖ Thermal image	• Isotherm map • Temperature graph

2.4. UHI impacts

Zhao et al. (2016) claim that the UHI generates profound effects on socioeconomics, human life, and the environment. The negative impacts of urban heat island can be increased energy consumption, air and water pollution, greenhouse gases, as well as reduced human health and comfort. In relation to increased energy consumption, the energy demand rises for cooling because of the increase in temperatures in cities. Akbari (2005) points out that the electricity demand for cooling increases by 1.5–2.0 % for every 0.6°C increase in air temperatures. Also, 5-10 % of the electricity production is used to substitute the steadily elevating temperature in cities. Consequently, the air pollution increases as the electricity production increases. For example, in the United State of America (USA) the electricity production mainly relies on fossil fuel. The contaminants from most power plants include Sulfur Dioxide (SO_2), Nitrogen Oxides (NO_x) and others, which contribute to greenhouse gases and therefore to global warming and climate change (Agency, 2013).

With respect to water quality, SUHI degrades water quality mainly by thermal pollution and lead to impaired aquatic ecosystems. James (2002) found that “pavements that are 100ºF (38°C) can elevate initial rainwater temperature from roughly 70 ºF (21 ºC) to over 95 ºF (35 ºC)”. Agency (2013) asserts that the change in water temperature in aquatic ecosystems resulting from the warm storm water runoff can be harmful or even fatal to aquatic life. Human health effects due to UHI might cause human mortality and disease. For example, the temperature of the land surfaces might increase up to 60 ºC in the hot summer in Iraq (Al-musaed, 2007). The differences of temperature between the surface and air cause a huge colonization of air, this can lead to nasal bleeding due to the lack of air zones and high pressure on earth surfaces. Another example from the USA, the Centres for Disease Control and Prevention claims that UHI contributed to more than 8,000 early deaths in the USA between 1979 and 2003 (Senate, 2009). This has induced the researchers to model the human heat balance.

Accordingly, empirical thermal indices were derived and have been developed considering the relevant meteorological and thermal physiological parameters (Höppe, 1999). As the real ambient air temperature only tells how warm or cold the air around us is, there was a need to develop indices that indicate how warm or cool our bodies are. In this sense, Steadman (1971) and Steadman (1979) calculated the apparent temperature "feels-like" using two indices, which takes into account the real air temperature and other weather conditions. The Heat Index (HI) combined the air temperature and relative humidity to determine how hot it actually feels in hot weather (Steadman, 1979). And the wind chill index combined effects of low temperature and wind in cold weather (Steadman, 1971). Then, Höppe (1999) introduced the Physiological Equivalent Temperature (PET) as a biometeorological index to assess the thermal environment. Since then much attention has been paid to evaluate the heat stress on the human body using thermal algorithms and indices (Rakib, 2013).

2.5. UHI causes

The formation of UHI in cities is a result of many factors. The main controllable motivators of the elevated temperatures in urban areas are reduced vegetation, increased urban impervious materials, urban geometry, and increased anthropogenic heat (Environmental Protection Agency, 2008, Gartland, 2008). In terms of vegetation cover, trees and vegetation are dominant in rural areas, in which, they provide shade and release water to the surrounding air through the evapotranspiration process. That reduces the air temperature compared to urban areas which have dry and impervious surfaces (such as buildings, streets, parking lots). Urban and rural materials differ in terms of heat capacity and thermal conductivity. Materials with high thermal conductivity and heat capacity tend to store more heat in their volume. The indicator to these two properties is thermal diffusivity, which reflects how the heat can easily penetrate a material. According to Figure 2.4 that shows the values of thermal diffusivity for different materials, the urban materials (such as insulation and pavements) have thermal diffusivity larger than natural materials (such as wood and soils). Hence, the urban materials considerably contribute to the increase of heat storage energy (Oke, 1981).

The urban geometry affects wind flow, energy absorption and emission as it represents the dimensions and spacing of buildings in a city (Environmental Protection Agency, 2008). The presence of built up areas reduces the wind speed by up to 60% because buildings act as wind breaks. The reduced wind speed minimises the convection of heat from surfaces to air and this increases the heat storage (Atkinson, 1982). Furthermore, the urban setting tends to collect the net radiation more than rural setting. The net radiation levels are affected by urban geometry because the heat radiates diffusely from surfaces to all directions evenly. For instance, building walls capture a lot of radiation instead of escaping it to the atmosphere, which increases the heat storage (Oke, 1981).

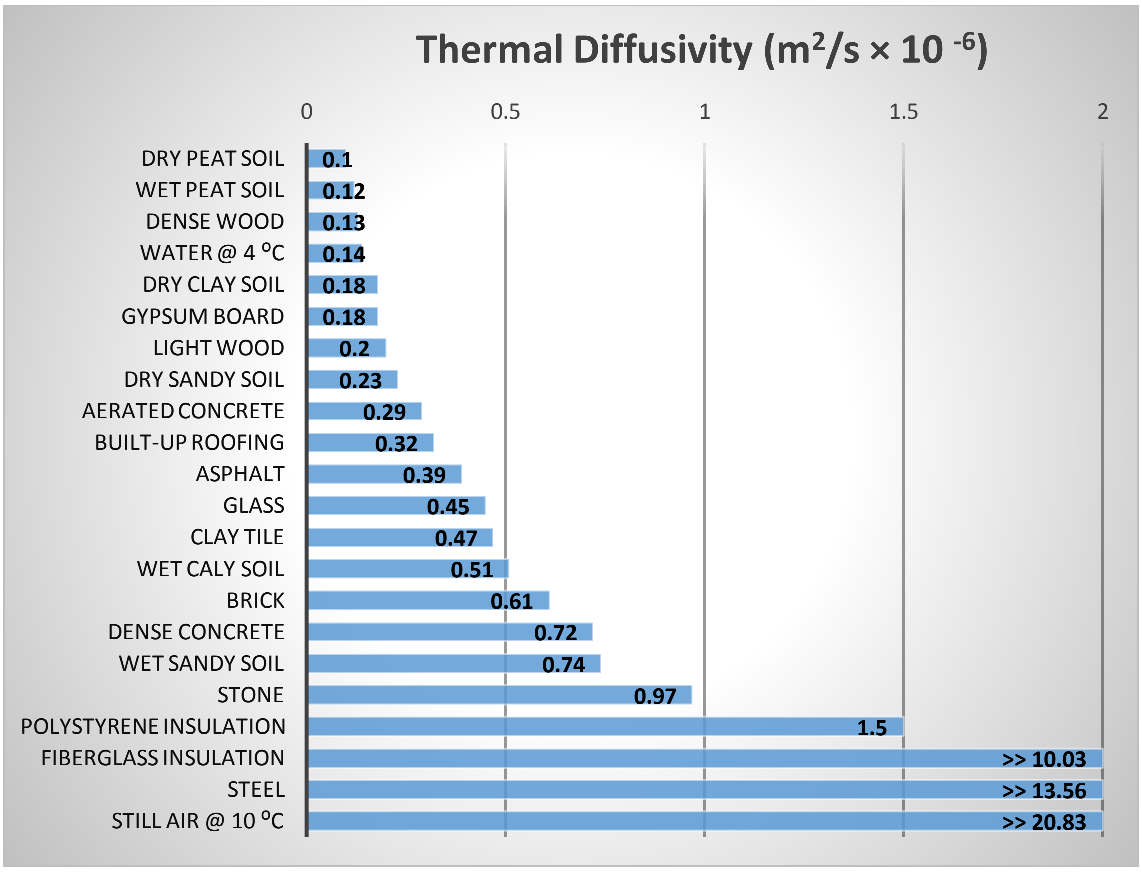

Figure 2.4: The values of thermal diffusivity for different urban materials. Urban materials considerably contribute to the increase of heat storage energy. Modified after Gartland (2008).

The anthropogenic heat is another source of UHI, generally produced by people activities and comes from several sources like industrial process, buildings, cars and people themselves. In order to determinate how much anthropogenic heat is produced by any region, all energy use for commercial, residential, industrial and transportation must be counted to find their sums, and divide these sums by the region`s area (Khan and Simpson, 2001). Figure 2.5 demonstrates that urban areas in Brisbane are the biggest producer of anthropogenic heat compared to suburban and rural areas.

Weather and location are additional factors that have strong impacts on the development of UHI, over which community has little control. Regarding the weather, clear sky and calm winds maximise the solar energy reaching the ground and minimise the heat convection. Moreover, climate and topography are governed by the geographical location. For instance, the presence of large water sheds reduces the above air temperature, and the mountains if present might block the winds (Environmental Protection Agency, 2008).

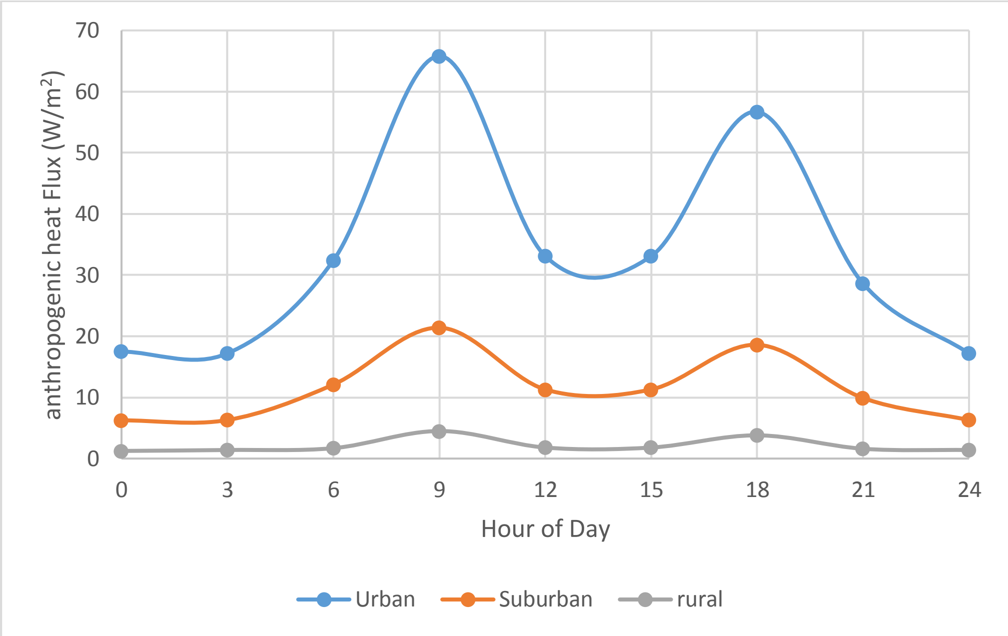

Figure 2.5: Daily anthropogenic energy generation rural, suburban, and urban areas of Brisbane, Australia in Dec. 1993. Modified after (Khan and Simpson, 2001) .

2.6. UHI mitigation

To counterbalance the influence of the UHI, there are two main mitigation strategies as described by Akbari and Kolokotsa (2016). The first strategy is increasing the solar reflectance of the surfaces, to reduce the amount of solar radiation absorbed by the urban fabric. It uses high reflectance and high thermal emittance materials, these materials decrease the LST by using them in the building's walls, roofs and pavements (Akbari and Kolokotsa, 2016). Morini et al. (2016) investigated the impact of albedo increase to countermeasure the UHI and its consequences in Terni (Italy) by using the Weather Research and Forecasting (WRF) model. Their findings after analysing three different scenarios of a summer heat wave in 2015 showed that albedo increase can mitigate the peak temperatures of the daytime by 1 ºC and night-time by up to 2 ºC. Furthermore, Rossi et al. (2015b) identified the beneficial effects of using Retro-Reflective (RR) materials in urban canyons to reduce the impact of UHI. They tested the application of a new RR material, which is a high reflective material that should reflect the incident radiation backward to the same direction of incidence. The results suggested that RR materials can improve the summer urban climate through providing cooling potential as coatings in urban canyons.

Furthermore, researchers in the field of UHI mitigation have demonstrated that the use of light-coloured surfaces (roofs and pavements) and urban vegetation (trees, grass, shrubs) can have considerable positive impacts on the development of UHI (Akbari et al., 1999, Melvin et al., 2000, Gartland, 2008). A study by Lawrence Berkeley National Laboratory pointed out that if rooftops were cooled using cool materials, the average surface temperature could be reduced by

5.5 °C (Akbari et al., 1999). This reduction is formed as soon as urban air is cooled by lessening the average of roof surface temperature. Also, Melvin et al. (2000) investigated the positive effects of cool paving on air temperatures, and their findings based on a model of Los Angeles predicted that the air temperature can be decreased by 0.5 °C when pavements are cooled. Also, a study that was done in Japan reported that the asphalt pavement with 10 % of solar reflectance reached up to 66 °C while a concrete pavement with 45% of solar reflectance reached up to 49°C (Gartland, 2008).

On the other hand, the second strategy to minimise the UHI effects is increasing the evapotranspiration by intensifying the urban greenery such as parks and green roofs (Akbari and Kolokotsa, 2016). The green vegetation cover such as trees provides shading and reduces solar radiation, which can minimise the UHI (Yu Joe et al., 1990). For example, a study by Jim (2015) assessed the use of green roofs on thermal comfort in Hong Kong by developing a full scale experiment in a high rise building. The study concluded that the green roof with high rate of evapotranspiration can mitigate the UHI impact by reducing the foliage surface temperature and surrounding air. The most effective green covers can be green roofs, street trees and parks. For example, rooftops in hot regions sometimes reach temperature at about 90 °C, while green roof temperature remains below 50°C (Gartland, 2008). Nevertheless, the implementation of green roofs heavily requires the involvement of the public. Besides, the green roof requires special considerations when constructing the buildings' roofs which increases the cost of construction materials. Therefore, other strategies have been implemented such as street trees and parks. Scott (2004) demonstrated that the temperature inside a car park can be declined by 25° C, when the cars are shaded by tress. However, Heiden et al. (2012) argues that even for large green areas within urban cities the small areas of buildings have larger impact.

The effects of UHI can lead to detrimental consequences of the indoor and outdoor public and private spaces (Ali et al., 2017). The outdoor thermal natural and built environment are important particularly in public spaces during outdoor events, and they contribute to improve the quality of life (Rossi et al., 2015a). Rossi et al. (2015a) proposed an integrated approach to improve the global comfort condition during outdoor entertainment events in the summer. Their system suggested the use of proper architectural solutions and materials to enhance the outdoor environment. Accordingly, understanding the causes of UHI and trying to mitigate them in the development phase of existing cites and when designing new cities will help minimising the severity of the UHI and reduces the efforts to compact it.

2.7. Urban Surface Energy

The urban ecosystem practise physical functioning called urban metabolism, which include a non-stop consumption of food, water, fuel, materials and power (Chrysoulakis et al., 2014). The intake of these resources results in waste products, some of them injected into the urban atmosphere such as waste heat, aerosols, and greenhouse gases (Chrysoulakis et al., 2014). Chrysoulakis et al. (2014) clarifies that the injected products into atmosphere convert to exchangeable fluxes between the land and atmosphere, which formulate the energy, water and carbon balance. The major sources of energy in urban areas are the Sun and anthropogenic activities, and these sources are the drivers of the Urban Surface Energy (USE) and UHI. The causes of UHI and USE are the same, and the variation between urban and rural areas is evident for both (Britter and Hanna, 2003). Piringer et al. (2002) clarified that the energy budget is the sum of incoming and outgoing energy fluxes (see Figure 2.6), and it provides a balanced equation as shown in equation 2.1. The left side of the equation is the net radiation (shortwave (K) and longwave (L)) plus the Anthropogenic Heat (AH). The K originates from the Sun, and the L mainly radiates from the surfaces and the sky. The AH is the manmade energy and comes from for instance cars, air conditioners and industrial facilities, which contribute to the USE particularly in urban areas (Piringer et al., 2002). The right side of the USE equation consists of the sensible heat (QH), latent heat (QE) and ground heat flux (QG). The heat that people feel as temperature is the sensible heat, and the latent heat is the heat that felt as humidity to evaporate water from the surfaces to the air (Environmental Protection Agency, 2008).

$$(K + L) + AH = QH + QE + QG \qquad (2.1)$$

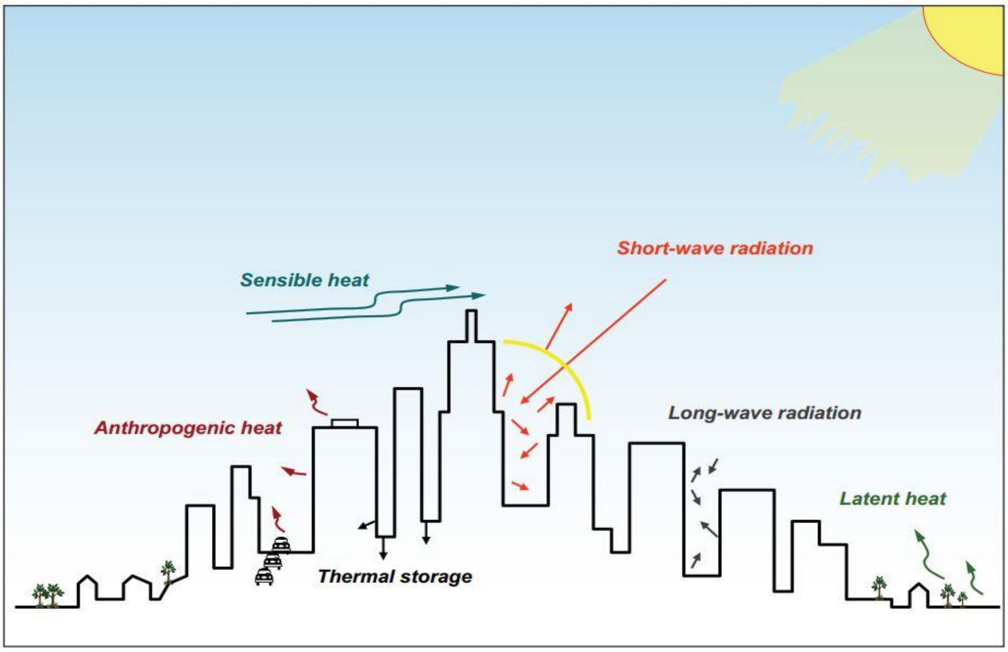

Figure 2.6: Urban surface energy budget. An energy budget provides the balance of incoming and outgoing energy fluxes (Environmental Protection Agency, 2008).

2.8. Microclimate Scales and modelling

Britter and Hanna (2003) explains that the urban surface is heterogeneous and its impact varies on a range of spatial scales. For example, to study the buildings geometry and morphology, the scale in this case should start from the individual building level. However, when the aim is investigating the diffusion of contaminants from a source within a building's collection, a street or a neighbourhood scale might be enough for full detail of the urban surface. While, studying UHI and Urban Energy Balance (UEB) needs approximately a city size to test the variation of different land use/cover types, which has impact on the local and regional climatology. Accordingly, within a spatial scale the physical process can be impacted by other process acting on a different spatial scale as described in Figure 2.7.

Gartland (2008) clarifies that there is no single cause of the UHI, and many factors combine to warm cities and suburbs. Net radiation, evaporation, heat storage, convection and anthropogenic heat are the leading urban characteristics contributing to UHI formation (Gartland, 2008). However, these characteristics do not have a specific measure, and they are investigated separately. Therefore, in this research a microclimate model is adopted that includes most of the urban characterising factors causing the formation of UHI. SOlar and Long Wave Environmental Irradiation Geometry (SOLWEIG) model simulates the spatial variation of three dimensional (3D) radiation fluxes and Mean Radiant Temperature (T_{mrt}) in complex urban settings (Lindberg and Thorsson, 2009). T_{mrt} is one of the important meteorological parameters governing human energy balance and thermal comfort outdoors, which sums up all the K and L radiation fluxes (both direct and reflected) (Lindberg et al., 2014). Nevertheless, such model needs many urban characteristics data and meteorological data. It includes the effect of air and surface temperature and other parameters that impact on human outdoor thermal comfort (SOLWEIG-team, 2015). The advantage of using SOLWEIG is to include parameters that are not measured or modelled using the traditional approaches such as remote sensing and meteorological stations. Also, SOLWEIG enhances the lack of 2D representation of traditional approaches where building's height is not fully included in the calculation of the influencing parameters on UHI formation. Most importantly it is using T_{mrt} as indicator of the presence of UHI for the first time as the major use of T_{mrt} in the literature is to predict the outdoor thermal comfort.

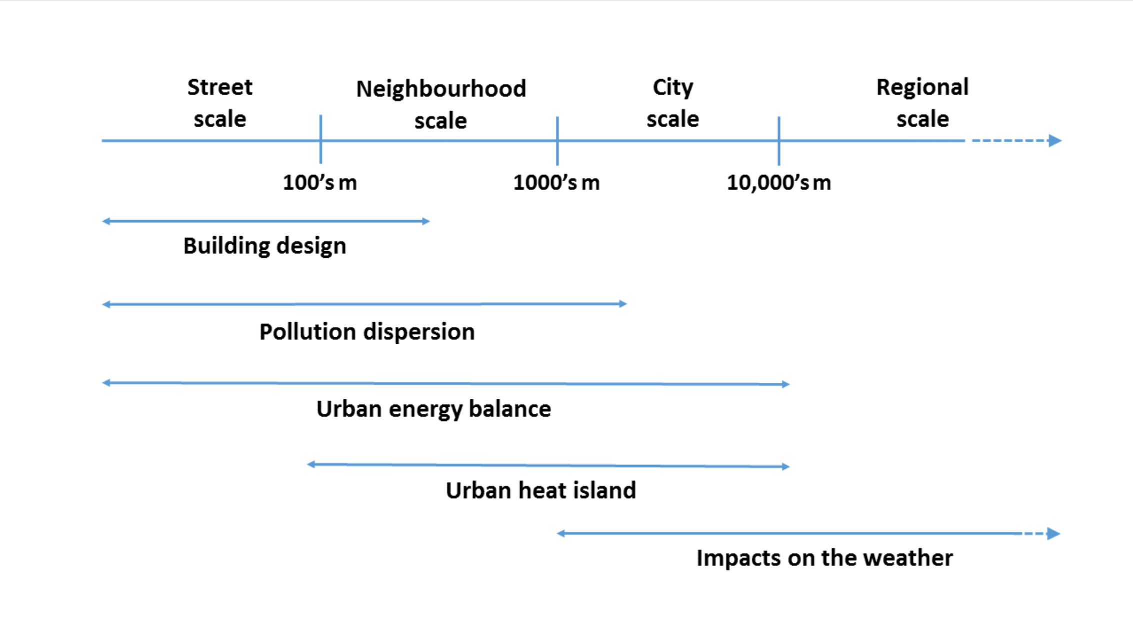

Figure 2.7: Spatial scales and urban climatology topics. Urban surface is heterogeneous and its impact varies on a range of spatial scales. Modified after Britter and Hanna (2003).

2.9. UHI measuring

The temperature and other climatic variables are temporarily and spatially varying, so the already available meteorological stations may not be sufficient to represent the formation of UHI. Earlier studies have used the fixed meteorological stations as an easy way to measure the urban-rural temperature difference (Brazel et al., 2000, Todhunter, 1996). However, Morris and Simmonds (2000) demonstrates that most of the fixed stations are arbitrarily located on high towers and buildings, in which the readings do not represent the canopy layer and the entire morphology of the urban areas. Oke (1988) clarifies that measuring the air temperature above the building's level represents the impact of UHI in the boundary layer above the canopy layer. To overcome these problems, mobile traverses using thermometers have been employed to measure the UHI (Montávez et al., 2000). Nonetheless, this technique cannot capture two readings at two places at the same time unless having two equipments. The difference in time between getting readings at the beginning and end of a pathway might affect the results significantly, since the temperature should be measured at the same time in different locations for better UHI demonstration. To overcome the problems associated with the previous measurement techniques, the current study employs a unique dataset namely HiTemp (High density Temperature measurements), which is a project funded by NERC (the Natural Environment Research Council) within the canopy layer of the urban environment in Birmingham conurbation. Several research groups were involved, but the project was managed by the University of Birmingham Urban Climate Lab (BUCL). The project consists of a network of sensors to record the air temperature and other meteorological parameters such as precipitation, relative humidity, wind speed and direction, pressure, and solar radiation (BUCL, 2014a).

The previous methods can only provide information about climatic variables (such as air temperature), and other techniques are needed to provide information about the surface biophysical characteristics. For example, the type of land use/cover is an essential independent variable to quantify the UHI formation. Hence, the evolution of Remote Sensing (RS) has enabled the scientists to visualise the temperature over large areas as shown in Figure 2.8 with the land use/cover at the same time. The RS systems are able to capture images for visible and invisible energy radiation (Gorsevski, 1998). This equipment can be satellite or airborne, and usually pass over a specific place with a frequent revisit in the case of satellites. Moreover, specialized airplane can be used to measure the temperature in specific times that are not served by other equipment.

The RS systems use sensors that are sensitive to the spectrum of the electromagnetic (EM) radiations. The EM regions are visible (0.4- 0.7 μm), near infrared (0.7- 1.2 μm), mid-infrared (1.2- 8 μm), thermal infrared (8- 14 μm), and microwave (>1 mm) (Chuvieco and Huete, 2010). The infrared and microwave sensors have been used in the literature to detect the LST. Even though the microwave sensors are suitable for different weather conditions; however, they provide lower spatial resolution and precision compared to the infrared sensors. Hence, in this research the focus is on the thermal bands acquired by the infrared sensors. RS does not always provide consistent information, so days with clear weather should be chosen. To retrieve the LST from the raw data of the thermal bands, there are three common algorithms in the literature: the single-channel, split-window, and multichannel algorithms (Kuenzer and Dech, 2013). To serve the aims of this research large number of thermal scenes are required. Thus, high level products are investigated to save the time of LST retrieval from raw data.

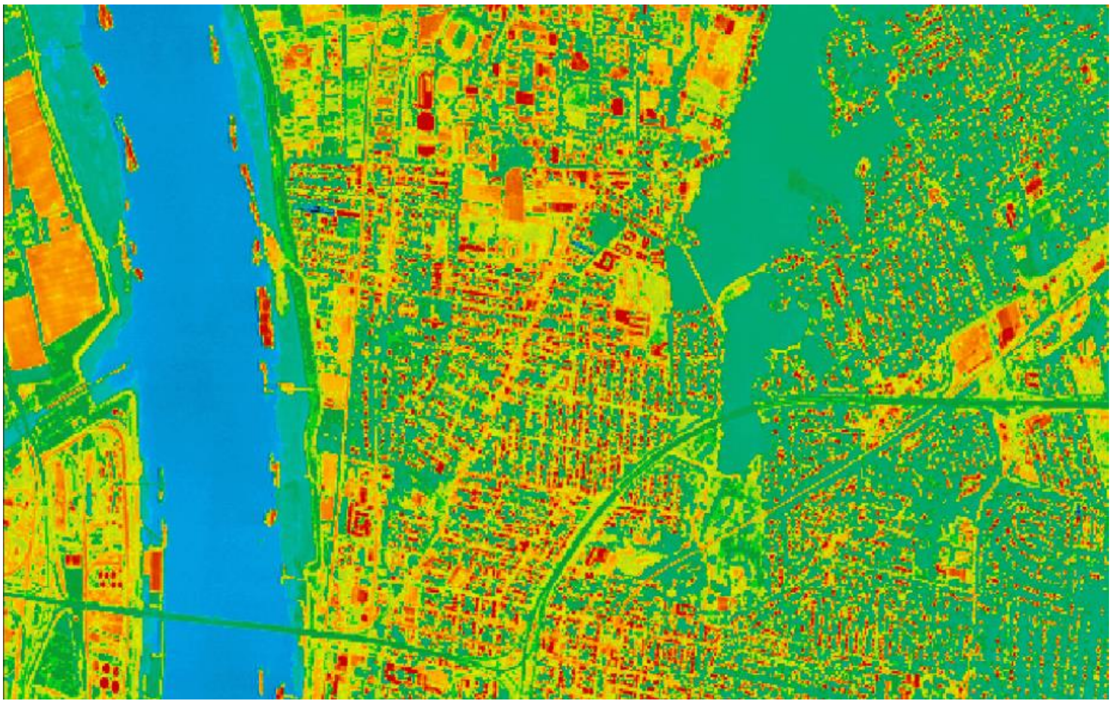

Figure 2.8: Thermal image of downtown Baton Rouge, LA taken about 1:00 p.m. local time on May 11, 1998, estimated 65 °C roof tops and 25 °C vegetation. It was acquired by the NASA Learjet's ATLAS scanner at 10 m spatial resolution with red representing warmer surface temperatures and blue representing cooler surface temperatures. (Gorsevski, 1998).

2.10. UHI modelling

Modelling of the UHI helps to understand the mechanism of the heat island formation, and enables planners to evaluate the impacts of mitigation measures. There are two main approaches of modelling which are physical and mathematical (Tyson et al., 1973). The physical models are carried out at the laboratories under controlled conditions or via onsite small scale experiments. Erell et al. (2011) explains that physical models are hardware models, in which similarity and scaling issues need to be addressed. Therefore, these models are not capable to reproduce the full complexity of an urban site. The mathematical models are more common, and can represent larger scale impacts. There are various types of mathematical models which deal with different ranges of UHIs, the ranges start from the building level to the entire urban region and even larger (Tyson et al., 1973) . However, UHI models are created to solve specific problems and there is no one model that can deal with all the climatic variables and urban features. Table 2.2 lists and compares several UHI models, in which the modelling methods show different approaches to represent the UHI. From the analysis of the existing models, it has been observed that the modelling approach to deal with different scales and can handle large number of variables is the regression analysis. Accordingly, the outputs of the adopted measurement technique will be analysed using the regression models.

Table 2.2: Lists and compares several urban heat islands models based on the modelling method.

Type of model	Application	Limitation	Example (s)	Reference (s)
Meteorological nocturnal models	express the urban-rural temperature difference (dT) as a function of various meteorological factors	do not relate the dT to the land cover and urban design, it estimates the nocturnal dT	dT=1.85-7.4 Y (lapse rate in ºC/millibar over the rural area)	Givoni (1998)
Urban design-oriented nocturnal models	correlate the dT with several features of the urban structure	do not link the urban land use with dT	$dT= P^{1/4}/ (4*U)^{½}$, P(population), U (regional wind speed m/s)	Givoni (1998)
Building energy models	compute the used energy by the buildings for heating and cooling	suffers from problems with calculating the convective heat transfer from the roof	DOE-2 program developed by US department of Energy	Gartland et al. (1996)
Roof energy calculators	estimate the energy and cost that can be saved by using energy roof products	only applied on the roofs	Energy Star Roofing Comparison Calculator, ORNL/DOE Cool Roof Calculator, and Energy Wise Roof Calculator	Gartland (2008)
Canyon and comfort models	study a configuration of buildings surrounding a street	do not estimate the effects of cooling surfaces or adding vegetation	OUTCOMES model	Arnfield (1990)
Ecosystem models	assess the impacts of vegetation areas on UHI in terms of energy saving, air quality and stormwater runoff	do not quantify the impacts of park and green spaces sizes on the UHI	Citygreen & i-Tree	American Forests (2002) & USDA Forest Service (2007)
Regional models	assess the regional influences on air temperature and quality	require meteorological and photochemical modelling techniques, and do not deal with local scales	WRF, MM5, CAMx & MIST	Sailor and Dietsch (2007)
Regression analysis models	evaluate the criteria that are not achieved by other models such as quantifying the cooling impacts of parks on UHI	right now, did not provide consistent results of the park's effects on the UHI	multivariate regression	Cao et al. (2010)

One of the most important objectives in scientific research is the possibility of predicting the value of a dependent random variable based on the values of other independent variables (Sá, 2007). It is commonly known that one independent variable is used to predict values of Y (dependent variable). However, in the real world, it is unlikely that only one variable can influence the dependent values. Therefore, it is necessary to consider many independent variables. A model for predicting change in a dependent variable by using more than one independent variable is called Multiple Regression Model (MRM) as opposed to simple linear model with one independent variable (Orlov, 1996). According to Sá (2007), MRM is one of the most common statistical tools used in scientific research that takes into account more than one independent variable. David Weisburd (2007) points out that MRM is not only based on understanding the relationships among independent variables, but also on specifying why changes occur and what factors are directly responsible for these changes. In MRM, researchers try to separate the various potential factors that have an impact on the dependent variable, to provide an accurate estimation of which variables are in fact most important in causing the change. In addition, the MRM can identify the impact of a specific independent variable while holding constant the impact of other independent variables. This is a very important advantage of MRM over the other regression models (Vanderbei, 2008). So, MRM is used in this study, and wherever regression modelling is mentioned it means MRM.

2.11. Research challenges

The study of climate of cities has not been undertaken in depth by scholars, although cities have been recognised as unique environmental entities (Janković, 2013). Climatology of cities studies the anthropogenic process in urban atmosphere, as cities have different atmospheric regimes due to their various shape, size, materials, function, and social metabolism (Janković, 2013). Webb (2016) identifies that UHI effect is the resultant of climate change, and highlights the high levels of variability of local government policy engagement or non-engagement in the use of urban climatology science worldwide. In spite of the large number of near-surface UHI studies, little substantial progress has been made since Howard's findings more than a century ago (Mills, 2014). Arnfield (2003) explains that the medium sensed (air or surface) and the sensing technique (atmospheric or ground) form the various types of UHI. The profound effects of urbanisation have made the residents more vulnerable to the future environmental changes, which imposes the cities to adopt climate mitigation strategies (Grimmond et al., 2015). Grimmond (2007) emphasises the complexity of the physical causes of UHI, as the dynamics of urban warming differ spatially and temporally.

UHI studies vary in the scales and aims. The scales start from a building size to the entire city. The aims might be to study ventilation, health, comfort, spatial-temporal variation, future forecast, and energy saving (Mirzaei, 2015). The UHI studies' findings sometime contradict with each other, for example the time of the maximum UHI intensity. Arnfield (2003) reported that UHI intensity is greatest at night, while, Ripley et al. (1996) found that the peak UHI might occur in sunny days. Furthermore, Arnfield (2003) stated that the high intensity UHI concentrates in the City Centre, nevertheless, Steinecke (1999) spotted rural area warmer than urban area. Mirzaei and Haghighat (2010) presented the observational approaches to study the UHI, and reviewed the abilities and limitations of each approach. They concluded that field measurements lack the spatial representation, whilst, the thermal remote sensing techniques do not provide reasonable temporal revisit. Mirzaei and Haghighat (2010) added, even when the simulation solved the problem of small scale representation of the physical models, the simulation approaches struggle to provide reliable results.

Accordingly, the use of a specific approach suffers from weaknesses that cannot be overcome without employing other approaches s. This study adopts different approaches to quantify the spatial and temporal change of UHI, and investigates a large set of influencing parameters on the formation of UHI. The scale of this research and the number of approaches employed take it beyond the research reported in the literature. The air, surface and T_{mrt} are used altogether as indictors for the UHI presence, to substitute the lack of using only one of them. Furthermore, RS, GIS, ground measurements and a microclimate modelling technique are employed to improve the spatial and temporal representation of UHI.

Chapter 3: Methodology

3.1. Methods

The procedure of solving the research questions consists of two major stages. The first stage is processing and deriving the dependent and independent variables for the next stage which is statistical and visual interpretation. The first stage includes four main pathways:

- The first one is building geometrical or topographical models such as DSM and DTM for the study site by using different GIS and remotely sensed data such as height information (objectives 3 & 4). The purpose of that is investigating the topography and geometry of the study area as well as deriving these parameters.
- The second is using ground measurements of air temperatures and the thermal data acquired in the thermal infrared region of the electromagnetic spectrum to retrieve the temperature maps (objectives 1 and 2).
- Thirdly, using visible to shortwave remotely sensed data or already available derived GIS layers to characterise the land cover types or surface indices (objective 3).
- The fourth pathway is employing the meteorological variables and climate data to derive the meteorological parameters and identify seasonal patterns (objective 3). Then, derive the radiation fluxes and mean radiant temperature using the microclimate model SOLWEIG (objective 4).

The second stage is the statistical and visual interpretation of the results, and then validating the results using existing studies to investigate the spatiotemporal change of UHI and the influencing parameters on the UHI formation (objectives 1, 2, 3 & 4). Figure 3.1 illustrates a simplified flowchart of the proposed methods to achieve the research objectives. The flowchart describes the major steps and more details are clarified later as each results chapter has its own method. The calculation method of UHI intensity in this study is the same for the various types of UHI. The UHI intensity is calculated by subtracting the pixel value from the minimum values of the temperature within the boundary of each study site. Rural areas are excluded from the analysis and the focus is on intra-urban differences. Martin et al. (2015) excluded the rural areas when calculating the UHI as these areas have different surface energy exchange patterns compared to urban areas, because urban areas are places where people live who are affected by the UHI (Martin et al., 2015).

Stewart and Oke (2009) proposed Urban Climate Zones (UCZs) that can be used to classify the UHI. Nevertheless, these zones are still not easy to use, and complex for risk management or alert systems (Martin et al., 2015). Some studies used the difference in mean or maximum temperature to compare between urban and rural areas for measuring the UHI intensity (Rizwan et al., 2008, Shangming et al., 2010). However, using the mean temperature for a certain area mixes the effects of different land cover types which might have different thermal zones (Martin et al., 2015). Chow et al. (2012) defines the maximum UHI intensity as the largest difference between urban and rural temperatures. Erell and Williamson (2007) used the intra-urban temperature differences to measure the CUHI, as they refer to the characteristics of the sites. This study adopts the difference between the pixel values and the minimum value of temperatures within the city boundary. The rural area should have the lowest temperature when the temperature peaks at the city centre which is the basis of UHI formation. For this reason, the minimum temperature value was subtracted from each pixel to compare the areas of high and low heat gain. Even though the UHI was calculated by subtracting the minimum value across the city, this does not make much difference because the edges of the city were assumed to have similar temperature to the surroundings.

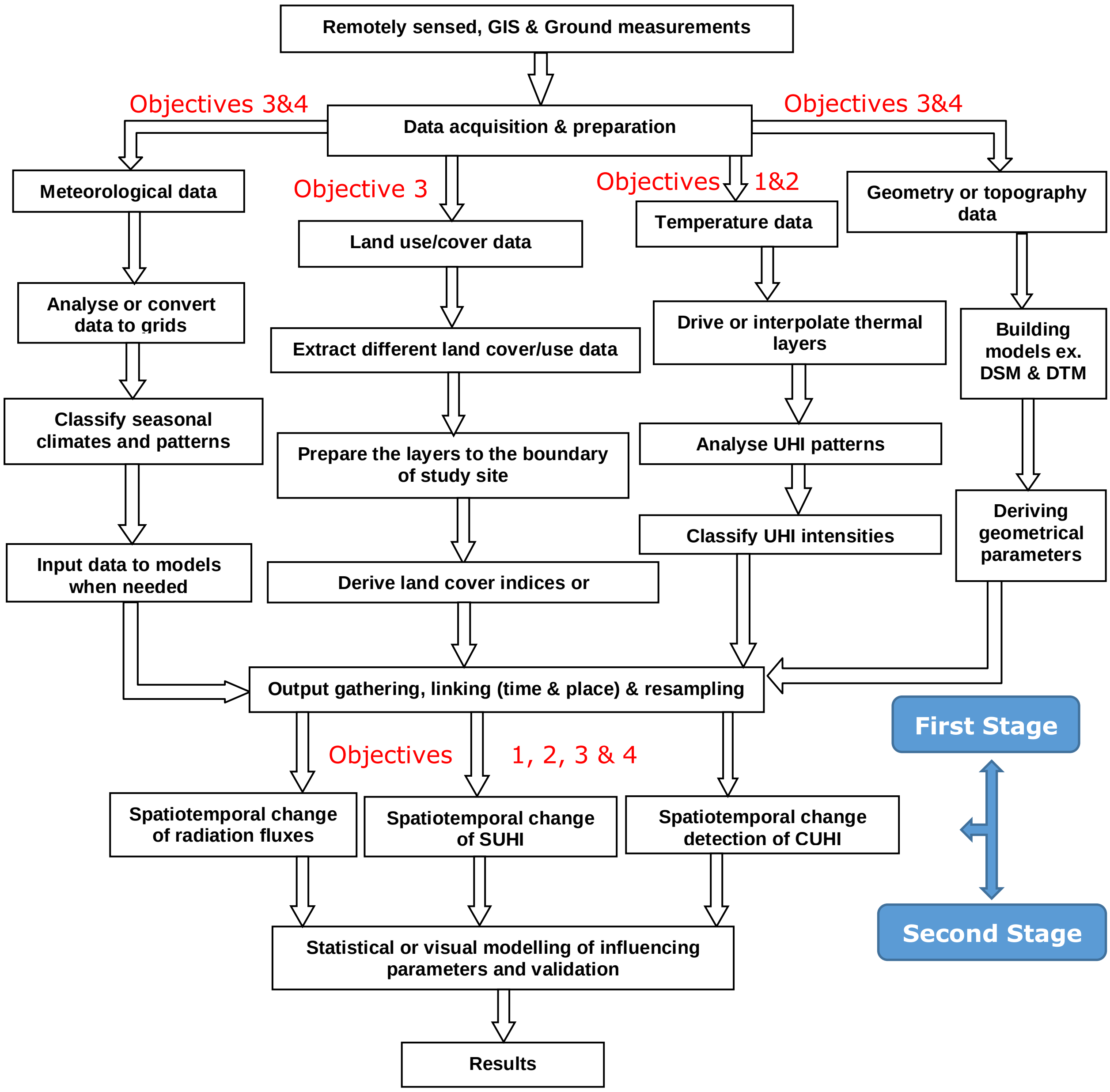

Figure 3.1: Simplified flowchart of the proposed methods to achieve the research objectives.

3.2. Study areas

Baghdad, London and Birmingham were chosen as the study areas for several reasons. Baghdad and London have different geographical location, climatic conditions, and land cover patterns. London is the capital of a developed country (UK) that has practised the UHI mitigation strategies (Greater London Authority, 2006), whereas, Baghdad is the capital of a developing country (Iraq) with a very few studies about UHI (Saleh, 2010). Baghdad had a population of 7,055,200 in 2011 and covers 734 km^2 (City Population, 2013). London; on the other hand; had a population of 8,173,941 in 2011 and extends over 1572 km^2. So, compared with Baghdad, London has higher population by around a million people, while its area is approximately twice that of Baghdad. Baghdad's climate is subtropical arid with hot summers and cold winters, while London's climate is temperate oceanic with warm summers and mild winters (City Population, 2013). Birmingham is the largest populated local authority in the UK by 1,101,400 persons based on the annual mid-year population estimates, 2014 report published by the office for National Statistics (Office for National Statisics, 2015). Its conurbation extends to around 278 km^2 over the West Midlands (Tomlinson et al., 2012).

Tomlinson et al. (2012) highlights that Birmingham used to have only one weather station for urban areas and another station outside in the rural areas, and its UHI studies are limited compared to its size and importance. The previously published research on Birmingham's UHI are highlighted in Chapter 5.The study areas were chosen to have population more than one million, as Akbari (2005) points out that a city with a million or more population can be warmer than its surroundings by about 1-3 ºC. The size of the chosen cities ranges from medium (Birmingham) to large (Baghdad and London) to have a distinctive UHI impacts.

Furthermore, the comparison between Baghdad and London might give typical recommendations for similar cities, as they represent different climatology, morphology, topology and development. Field measurements are crucial in cloudy cities like London and Birmingham due to the difficulty of getting cloud free satellite images. Baghdad's climate offers better sights of the ground from satellites even in the winter. The two UK cities were chosen to represent a sample of a wet environment in different locations with good data availability. Besides, they differ in size and population. However, Baghdad was chosen as a sample of a dry environment that does not have much ground data, which demonstrates the importance of remote sensing and GIS techniques. The SUHI is investigated for the three cities; however, Birmingham is the case study for the other types of UHI because of the availability of HiTemp data.

3.3. Data

This section gives a general description of the data used in the study. However more details are provided for each approach of the three techniques employed in this research when it is relevant.

3.3.1. Remotely sensed data

The best freely available remotely sensed data for this study with their spatial, spectral and temporal resolution that cover a whole city or a large part of it are investigated and summarised as below:

Landsat:

It is a co-operative initiative between the U.S. Geological Survey (USGS) and NASA, which gives the world's longest constantly acquired collection of Spaceborne remotely sensed data. This project has been a source of data for different disciplines such urban mapping and environment for over four decades (USGS, 2013). Table 3.1 summarises the spectral, spatial, and temporal resolution of the historical Landsat missions. The spatial resolution has been improved over time, from 80 metres (m) pixel size for Landsat MSS (Multispectral Scanner System) bands to 30 m for the visible and infrared bands of Landsat 8. Also, the number of bands has increased from 5 bands for Landsat MSS to 11 bands for Landsat 8. However, the temporal revisits of the Landsat missions have not been improved significantly. Figure 3.2 describes the history of the Landsat program to show the temporal availability of each mission. The Landsat 5 and 7 have the longest missions so far, and the Landsat 8 or LDCM (Landsat Data Continuity Mission) has started its mission in 2013.

Table 3.1: A summary of the spectral, spatial, and temporal resolution of the historical Landsat missions (185×185 km spatial coverage). Adapted from USGS (2013).

System	Spectral resolution	Spatial resolution (m)	Temporal resolution	Archive since
Landsat MSS	3 Bands visible 1 Band infrared 1 Band thermal Infrared	80	18	1972
Landsat TM	3 Bands visible 3 Bands infrared 1 Band thermal Infrared	30 - Visible and infrared 60 - thermal infrared	16	1986
Landsat ETM+	3 Bands visible 3 Bands infrared 2 Bands thermal Infrared 1 Band panchromatic	30 - Visible and infrared 60 - thermal infrared 15 - panchromatic	16	1999
Landsat 8	4 Bands visible 4 Bands infrared 2 Bands thermal Infrared 1 Band panchromatic	30 - Visible and infrared 30 (resampled) - thermal infrared 15 - panchromatic	16	2013

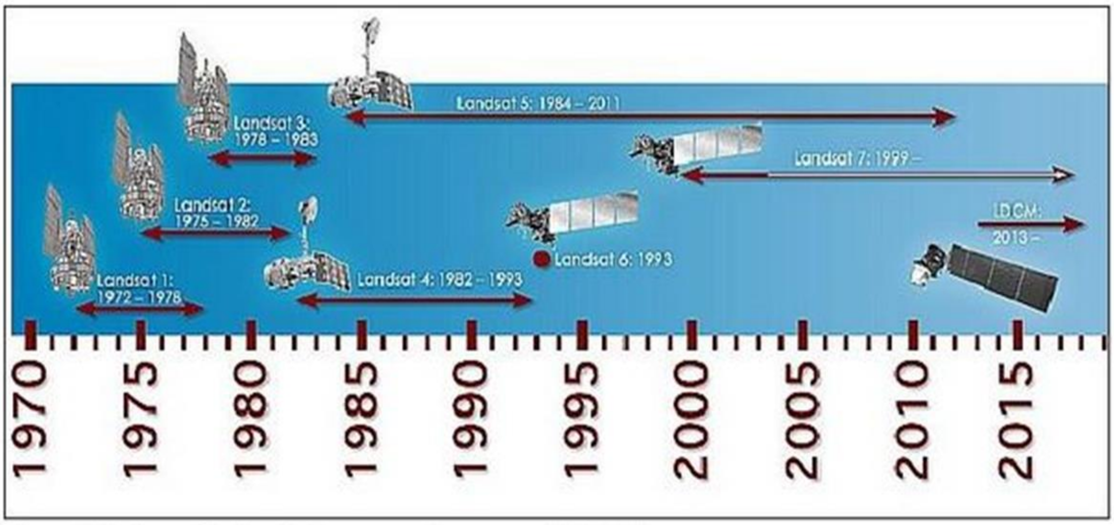

Figure 3.2: History of the Landsat program (USGS, 2013). Credit: U.S. Geological Survey, Department of the Interior/USGS.

ASTER:

Imaging instrument on board of Terra Satellite a joint work between NASA and Japanese institution since 1999, is used to create detailed maps of LST, reflectance, and elevation. It acquires high spatial resolution data in 14 bands, which are 3 visible bands (15m), 6 infrared bands (30m) and 5 thermal infrared bands (90m). The repeating cycle is every 16 days with a day and night time mapping, and the spatial coverage for a scene is 60×60 km. ASTER acquires elevation data using stereo-pair images to create DEM (NASA, 2004).

MODIS:

An instrument aboard the Terra (EOS AM) and Aqua (EOS PM) satellites, it views the entire Earth surface, and acquires data in 36 spectral bands from 250m-1km spatial resolution (visible-thermal spectral resolution). It provides daily night and day time images, also gives direct albedo, emissivity, reflectance and temperature products in moderate resolution. It covers a total spectral range of 0.4 to 14.4 µm. Two bands are captured at a spatial resolution of 250 m at nadir, with five bands at 500 m, and the remaining 29 bands at 1 km (NASA, 2010).

Sentinel-2:

It is part of the Copernicus Earth observation programme, which was mainly initiated by the European Commission (EC) and the European Space Agency (ESA). It provides continuity to services relying on multi-spectral high-resolution optical observations over global terrestrial surfaces. It consists of 13 spectral bands spanning from the visible and the near infrared to the short wave infrared, with a spatial resolution varies from 10 m to 60 m and a 290 km field of view (Drusch et al., 2012).

LIDAR (Light Detection and Ranging):

Active remote sensing technique like RADAR (Radio Detection And Ranging) uses a laser to deliver highly accurate height data. Aerial data is available for 70% of England and Wales from the Environment Agency. They offer a variety of elevation products free of charge for non-commercial use. These products have a vertical accuracy in the range of 5-15 cm, and the spatial resolution ranges from 25cm to 2m (Geomatics, 2014). These data were obtained for the cities of London, Birmingham and Nottingham. However, only the data for Birmingham were used to serve the purpose of this research.

TABI (Thermal Airborne Imagery):

A sensor that is used to distinguish temperature differences at 0.1°C accuracy and spatial resolution of 1- 4 m by measuring the radiation in the 8-12 µm range of the electromagnetic spectrum. These licensed data were obtained for the city of Birmingham from the UK Environment Agency free of charge for non-commercial use (UK Environment Agency, 2014).

OS Master Maps:

A licence has been obtained from the Ordnance Survey (OS), and aerial images for Birmingham were received for the purpose of this research with a spatial resolution of 25 cm and spectral resolution within the visible wavelength (OS, 2015).

3.3.2. GIS data

Geographic information system (GIS) data originates from different types of sources such as RS and ground surveys acquired with their coordinates and thematic information (Brimicombe, 2010). One example is land use/cover data for the UK which are offered by the University of Edinburgh through the Digimap website (EDINA, 2016).

3.3.3. Meteorological data

The main source of UK meteorological data was the Met office, which provides different types of climatic variables. Data from ground stations about temperature grids and other climatic variables were acquired to this research. In particular, MIDAS datasets were used to get the required climatic parameters (MIDAS, 2015).

3.3.4. HiTemp project

It is a NERC-funded project, and several research groups are involved including BUCL at the University of Birmingham. The project consists of a network of two types of sensors, one is to record only the air temperature and the other to capture the air temperature and other meteorological parameters such as (precipitation, relative humidity, wind speed and direction, pressure, and solar radiation). The collection of the data started in June 2012, and they were obtained only until June 2014 even though the project is still ongoing. More information about HiTemp is available in Chapter 5.

Chapter 4: SUHI Spatiotemporal Distribution and Modelling

Part of this chapter has been published as:
ALI, JASIM M., MARSH, STUART H. and SMITH, MARTIN J., 2017. A comparison between London and Baghdad surface urban heat islands and possible engineering mitigation solutions. Sustainable Cities and Society. 29, 159-168.

4.1. Introduction

The Surface Urban Heat Island (SUHI) is primarily measured using thermal RS, by capturing the radiance at the top of atmosphere, then retrieving that to land surface temperature (Hadjimitsis et al., 2013). RS techniques can be used to determine the spatial change of the most important urban biophysical and environmental characteristics. The wide application of RS techniques in urban areas has included urban feature mapping based on their spectral signatures, as a time and cost effective approach compared to traditional methods such as field surveys (Weng, 2012). They also provide quantitative observations about the environment in regions of the electromagnetic spectrum which are outside the visible region, such as temperature (Chuvieco and Huete, 2010). Oke et al. (1999) explain that the surface temperature is not only important to study urban climatology, but it is central to the energy balance of the surfaces. Balling (1988) study was one of the earliest studies to apply thermal remote sensing to examine urban climates; this study concluded that the surface temperature is correlated with the land use and day to day variability of its spatial patterns. Beyond this, a study by Wang et al. (2011) emphasised that surface temperatures and conductive heat fluxes through solid media (roofs, walls, roads and vegetated surfaces) are of major significance not only for outdoors microclimatic conditions, but, also for the comfort of residents indoors.

Sobrino et al. (2013) have evaluated the SUHI influence in the city of Madrid by thermal RS. They employed airborne hyperspectral data and in situ measurements, and the results demonstrated the presence of a night-time SUHI influence with a highest value of 5 K (Kelvin). Deng and Wu (2013) have examined the impacts of urban biophysical compositions on SUHI using normalized difference vegetation index (NDVI), percent green vegetation (%GV), and percent impervious surface area (%ISA). They used a spectral unmixing and thermal mixing approach; the result showed that NDVI and %GV-based regression models perform well in rural areas, while %ISA-based models perform well in urban areas. Furthermore, the influence of temporal aggregation of LST data for SUHI has been studied by Hu and Brunsell (2013). Their study found that the SUHI values in the daytime are larger than during the night-time, and the impacts of aggregation in the spring and summer are higher than in the autumn and winter. Hadjimitsis et al. (2013) used satellite Earth observation data and ground meteorological data to study the effect of SUHI in Cyprus using Artificial Neural networks (ANN). Their findings have revealed that the approach can perform successfully as good correlations between ground and satellite measurements were identified. However, further modification is needed to improve their methodology due to the coarse 1 km resolution of MODIS LST data.

This chapter adopts some of these RS techniques to investigate the formation of areas of high and low temperatures known as SUHI. It investigates and compares the SUHI in Baghdad, Birmingham and London as they represent different climatic conditions, natural environments and levels of urban development. Furthermore, it tests the reported correlation between LST and land cover types under different conditions. Finally, based on the findings, engineering mitigation strategies for each city might be suggested.

4.2. Materials and method

Various satellite and airborne RS data have been used for urban thermal and land cover mapping. Landsat, ASTER and MODIS were employed to provide information about the surface temperature and surface reflectance-derived spectral indices. These data were prepared for the three study areas Baghdad, London and Birmingham based on the availability of cloud free images and full coverage of the study area. Landsat and ASTER were the major source of high spatial resolution data compared to MODIS. However, MODIS data were also acquired as they have night-time coverage and daily revisit to substitute the low temporal coverage of Landsat and ASTER. The time frame for Landsat and ASTER was between 2000 and 2015, and the temporal coverage for MODIS was between 2003 and 2015 for the three cities. The MODIS and ASTER were the sources of only thermal data; nonetheless, Landsat was the source of thermal and land cover data. Therefore, Landsat, ASTER and MODIS were used to investigate the spatial and temporal change of SUHI. Whereas, the correlations between spectral indices (as indicators of land cover types) and LST were modelled using only Landsat data.

Moreover, the MODIS data were used to validate the findings of Landsat and ASTER data in terms of the spatial change of SUHI. The land cover types of the study areas were clarified using already classified maps for London and Birmingham, and Sentinel 2 images after classification for Baghdad. Appendix A. provides detailed information about the Landsat and ASTER images used in this chapter for the three cities as summarised in Tables A.1, A.2, and A3.3. It gives details about the sensor type, date and time of acquisition, cloud cover, path and row, image quality as well as the spatial resolution. Furthermore, MODIS and Sentinel 2 images are clarified in this chapter when it is relevant. On the other hand, the methods to calculate the LST and SUHI as well as the regression modelling are clarified in this section.

4.2.1 Landsat spectral indices

The U.S. Geological Survey (USGS) have funded a project to create higher level data products using the Landsat archive to capture changes of the land surface environment (USGS, 2016c). These data provide the basis to identify the Earth’s historical changes and monitor the current conditions for regional to continental scale. USGS have produced an on demand interface called Earth Resources Observation and Science (EROS)/ Centre Science Processing Architecture (ESPA) to provide terrestrial variables such as brightness temperature and spectral indices (USGS, 2016a). USGS published a document that describes the spectral indices products that are derived from Landsat 4-5 Thematic Mapper (TM), Landsat 7, and Landsat 8 Surface Reflectance data generated at 30-m spatial resolution (USGS, 2016d). The Landsat 4 and

Landsat 6 were not used in this study since only images after 2000 were acquired when these satellites were out of service.

Masek et al. (2006) clarifies that USGS was the original research data source to create surface reflectance scenes by providing 30-m resolution wall-to-wall reflectance coverage for North America epochs centred on 1990 and 2000. Brightness temperature and spectral indices derived from surface reflectance were acquired from ESPA as Landsat high level products (HLPs). This could save the time of raw data processing, and provides large amount of HLPs free of charge for the three cities. The purpose of using spectral indices was to have land cover predictors mapped at the same time of the LST acquisition, which facilities the statistical modelling between them. Furthermore, it overcomes the problem of uncertainty when classifying the land cover types over long periods for the three cities. A reliable thematic map requires ground reference data or any other validation process to have a good accuracy classified map, which is challenging over time due to the land cover change (Foody, 2002). The surface reflectance-derived spectral indices consist of four vegetation indices and another three spectral indices (USGS, 2016d). The vegetation indices include Normalized Difference Vegetation Index (NDVI), Enhanced Vegetation Index (EVI), Soil Adjusted Vegetation Index (SAVI) and Modified Soil Adjusted Vegetation Index (MSAVI). Furthermore, Normalized Difference Moisture Index (NDMI), Normalized Burn Ratio (NBR), Normalized Burn Ratio 2 (NBR2) are derived to produce land cover indices other than vegetation (USGS, 2016d). The seven indices as shown in equations (4.1- 4.7), were adapted from USGS (2016d) which provides more details about the derivation and nature of each index.

$$NDVI = \frac{NIR - R}{NIR + R} \qquad (4.1)$$

$$EVI = G \times \big((NIR - R) \div (NIR + C1 \times R - C2 \times B + L1)\big) \qquad (4.2)$$

$$SAVI = \big((NIR - R) \div (NIR + R + L2)\big) \times (1 + L2) \qquad (4.3)$$

$$MSAVI = \left(2 \times NIR + 1 - \sqrt{(2 \times NIR + 1)^2 - 8 \times (NIR - R)}\right) \div 2 \qquad (4.4)$$

$$NDMI = \frac{NIR - SWIR1}{NIR + SWIR1} \qquad (4.5)$$

$$NBR = \frac{NIR - SWIR2}{NIR + SWIR2} \qquad (4.6)$$

$$NBR2 = \frac{SWIR1 - SWIR2}{SWIR1 + SWIR2} \qquad (4.7)$$

Where:

NIR= near infrared band, B4 in Landsat 4-7 & B5 in Landsat 8.

R= red band, B3 in Landsat 4-7 & B4 in Landsat 8.

B= blue band, B1 in Landsat 4-7 & B2 in Landsat 8.

G= 2.5, C1= 6, C2= 7.5, B= & L1= 1 these enhancements for reducing the background noise, atmospheric noise, and saturation in most cases.

L2= 0.5 which is a soil brightness correction factor.
SWIR1= first shortwave infrared band, B5 in Landsat 4-7 & B6 in Landsat 8.
SWIR2= second shortwave infrared band, B7 in Landsat 4-7 & in Landsat 8.

The spectral indices are calculated from the surface reflectance, and different algorithms of radiometric calibration and atmospheric corrections were applied on Landsat 4- 7 and Landsat 8. The surface reflectance data are generated by a specialised software originally developed through NASA called the Landsat Ecosystem Disturbance Adaptive Processing System (LEDAPS), for Landsat 5 (TM) and Landsat 7 (ETM+) data. LEDAPS applies MODIS atmospheric correction routines to level 1 products (USGS, 2017a). The inputs to the radiative transfer models are the water vapour, ozone, geopotential height, aerosol optical thickness, and digital elevation as well as Landsat data (Masek et al., 2006). On the other hand, for Landsat 8 a different algorithm is applied to generate surface reflectance data, this algorithm is called the Landsat Surface Reflectance Code (LaSRC) (USGS, 2017a). The main difference between LEDAPS and LaSRC is that the later makes use of the coastal aerosol band to perform aerosol inversion tests. Furthermore, the solar zenith and view zenith angles are used by LaSRC as part of the atmospheric correction (Vermote et al., 2016).

The Landsat HLPs provide information about the clouds through Quality Assurance band. It gives the specifications of cloud and cloud shadow derived from the CFMask algorithm. CFMask algorithm re-calculates water values to give high-confidence cloud pixels (USGS, 2017a). That helped to distinguish between cloudy and cloud free pixels. Consequently, cloudy pixels were eliminated to have cloud free images. The spectral indices used in this chapter were limited to the Landsat HLPs, because deriving the spectral indices for the three study areas for the period (2000-2015) is tedious and requires a lot of time. Other spectral indices were investigated in a journal paper published out of this chapter, which compares between London and Baghdad SUHI and suggests possible engineering mitigation solutions. Furthmore, the paper used raw data to derive the spectral indices and more detials about how to convert the digital numbers to reflectance are available in Ali et al. (2017).

4.2.2 Landsat LST

Top of atmosphere Brightness Temperature (BT) for the thermal bands of Landsat was ordered as a separate product through the ESPA interface, but is included with all original products (USGS, 2016b). The general process of converting the digital numbers to radiances then to BT is discussed in Ali et al. (2017). For Landsat 5 and Landsat 7 the thermal band is Band 6, while, Band 10 and Band 11 are the thermal bands of Landsat 8. The BT is derived from the top of atmosphere radiance using LEDAPS for Landsat 5 & 7 and LaSRC for Landsat 8 (USGS, 2017a, USGS, 2017b). The atmospheric effect in the thermal infrared region was considered to be insignificant (Rasul, 2016). Chuvieco and Huete (2010) clarifies that the size of atmospheric small particles such as smoke and biomass burned aerosols are smaller than the thermal infrared wavelengths.

To derive the LST from BT the later needs correction for emissivity due to the strong heterogeneity of land surface characteristics such as vegetation, topography, and soil (Li et al., 2013). There are a number of approaches to retrieve the Land Surface Emissivity (LSE) from satellite data, and a non-unique solution appears during the process of LSE retrieval (Li et al., 2013). Three approaches were implemented based on the availability of emissivity data to derive LST from BT for the three study cities. The ideal emissivity data source should temporally coincide with the BT images overpass, and lies within the same wavelength of the thermal bands. Zhang et al. (2014) explains that LSE is a key physical parameter defined as the ratio of the energy emitted by the land surface to that emitted by a blackbody at the same temperature and wavelength. This why the LSE is referred to as spectral emissivity, as it differs based on wavelength (Zhang et al., 2014). The LST equals the BT when the emissivity value is 1, which is not applicable for land surface studies due to the heterogeneity of the surfaces. Dash et al. (2001) claims that RS is the only means to obtain LST and LSE for a large scale.

The first approach used the emissivity from the ASTER On-Demand L2 Surface Emissivity (AST_05) generated using the five thermal infrared (TIR) bands (acquired either during the day or night time) between 8 and 12 µm spectral range (LPDAAC, 2014b). This approach was employed when there is an emissivity image close to the temperature acquisition's time of Landsat 5 & 7. The emissivity does not vary that much unless the surface properties and moisture change (Jin and Liang, 2006). This method provides an accepted approach of LSE retrieval by the scientific community working in the thermal infrared, as it adopts the TES (Temperature-Emissivity Separation) method (Gillespie et al., 1998). Band 14 (10.95–11.65 µm) of AST_05 was used as its centre wavelength close to the centre wavelength of Band 6 of Landsat 5 & 7 (10.40-12.50 µm).

The second approach was used as a possible alternative to obtain an LSE image from the values of NDVI, in which an emissivity value for the main land cover classes is calculated (Sobrino et al., 2004). The semi-empirical NDVI method is not very operative because it requires a good knowledge of the study area and emissivity measurements of the different land cover classes. However, it was used in this study to estimate the emissivity for satellite data possessing only one thermal channel (Sobrino et al., 2004), when there is no available ASTER emissivity coincident with the Landsat overpass. The NDVI were acquired from the HLPs of Landsat, and certain NDVI values (thresholds) to distinguish between soil pixels, vegetation pixel, and composed pixels of soil and vegetation (Sobrino et al., 2008). The pixel was considered as bare soil if the NDVI is less than 0.2, and the emissivity was obtained from reflectivity values in the red region. And if the NDVI is higher than 0.5, the pixel was assumed fully vegetated and the emissivity value is 0.99. However, for the NDVI values between 0.2 and 0.5, the general equation shown below for composite land cover to retrieve the LSE (ε) was applied as described by (Sobrino et al., 2004).

$$\varepsilon = \varepsilon_v \times P_v + \varepsilon_s(1 - P_v) + d_\varepsilon \qquad (4.8)$$

Where:

ε_v = vegetation emissivity

ε_s = soil emissivity

P_v = vegetation proportion obtained according to (Carlson and Ripley, 1997).

d_ε = includes the effect of the geometrical distribution of the natural surfaces and also the internal reflections obtained according to (Sobrino et al., 2004).

The previous two approaches were adopted for the single thermal channel of Landsat 5 and 7; however, for Landsat 8 Emissivity Normalisation Method (ENM) was applied. ENM calculates the emissivity of the highest temperature for each pixel (Rasul et al., 2015), it assumes a constant emissivity in all N channels for a given pixel (Li et al., 1999). Then, the emissivity-corrected land surface temperature was computed for Landsat 5, 7 and 8 according to Zhang et al. (2013). Appendix B. gives an example of the model builder in ArcGIS used to convert the BT to LST.

$$LST = \frac{BT}{1 + (\lambda \times BT/\alpha)\ ln\varepsilon} \qquad (4.9)$$

LST is land surface temperature (in Kelvin); BT is radiant surface temperature (in Kelvin); λ is the wavelength of emitted radiance; and α = h*c/K = (1.438×10^{-2} m K); where h is Planck's constant (6.26×10^{-34} JS); c is the velocity of light (2.998 × 108 m/s); K is Stefan Boltzmann's constant (1.38×10^{-23} J K^{-1}); and ε is emissivity (Farina, 2012).

4.2.3 ASTER and MODIS LST

ASTER surface kinetic temperature (AST_08) images were acquired; these images contain surface temperatures at 90 m spatial resolution for the land areas only. AST_08 is derived from the TES algorithm, which uses atmospherically corrected ASTER Surface Radiance data (LPDAAS, 2014b). AST_08 products acquired either during the day or night time by the five Thermal Infrared (TIR) bands between 8 and 12 µm spectral range (LPDAAS, 2014b). The TES algorithm first estimates the emissivity in the TIR channels using the ENM, then the LST is derived (LPDAAS, 2014b). These data were requested through the archive record of the Reverb and GloVis as they are on demand products.

MODIS/Aqua level-3 products named MYD11A2, on the other hand, were processed using MODIS Reprojection Tool (MRT) to provide LST 8-day data composed from the daily 1-kilometer LST (LPDAAS, 2014a). Aqua passes over Baghdad at approximately 02:00 and 13:00 local time, and over London and Birmingham at around 01:30 and 13:30 local time. Although, NASA's Aqua and Terra satellites both carry MODIS sensor, only images from Aqua were used for this study. The reason for that is the night-time images of Aqua seem ideal to the formation of maximum UHI. Oke (1988) explains that the maximum UHI magnitude happens (3– 5) hours after sunset.

This period of high intensity UHI is around the time of MODIS/Aqua acquisition; particularly, in the UK summer.

Due to the presence of clouds and low revisit frequency of Landsat and ASTER, MODIS data were used to investigate the temporal change of SUHI as it provides night-time and daytime daily images. Tomlinson et al. (2012) demonstrates that a night image allows a more precise LST quantification as there is no solar irradiation to change the surface energy balance, and night-time MODIS LST accuracy has been found to be better than daytime. MODIS data can produce a better precision in terms of LST retrieval, which attain the 1 K precision required for practical applications when used for homogenous surfaces (Rasul, 2016). Split window and day/night algorithms were used by the producers to retrieve the MODIS LST data, and to maintain the high precision of LST products (Liang et al., 2012).

4.2.4 Data mask, convert, and rescale

The satellite data were masked for the boundary of the study areas, this was undertaken for the spectral indices and LST. Furthermore, the LST was converted from K to ºC. MODIS and ASTER products were rescaled based on scale factors obtained from the Land Processes Distributed Active Archive Centre (LP DAAC) which is one of several discipline-specific data centres within the NASA Earth Observing System Data and Information System (EOSDIS) (LPDAAC, 2014a). Also, they were masked for the study areas. Appendix C. gives an example the process of masking and rescaling undertaken by the model builder in ArcGIS.

4.2.5 Land cover of study areas

To visually investigating the spatial variation of LST related to land cover, high resolution land cover images were acquired for the three cities (Baghdad, London and Birmingham). Land cover images for London and Birmingham were acquired as already classified images, however, Baghdad does not have a classified map that suits the purpose of this study. Therefore, Baghdad land cover map was created by the classification of multispectral (MS) images. For Baghdad, GF-1 (Gaofen-1) satellite data were employed, which is one of the series of the China High-resolution Earth Observation System (CHEOS). Its images for Baghdad were provided in cooperation with Professors LiTao and Guanzhou, Wuhan University, China. GF-1 is configured with two 2 m Pan/8 m MS camera and a four 16 m MS medium-resolution and wide-field camera set (eoPortal, 2016). Figure 4.1 shows the composite red, green and blue bands (RGB) images of Baghdad sensed on the 27th of June 2014, which helps to understand the nature and distribution of the different land features of the city. However, GF-1 data were provided as four bands which are not enough for land cover classification and were used as auxiliary data to choose the training points and test the accuracy of the classification. So, Sentinel-2 satellite launched on the 23th of June 2015 was used to create land cover map for Baghdad as it provides 13 spectral bands (443 nm–2190 nm) with a swath width of 290 km and spatial resolutions of up to 10 m for the visible to near infrared bands (ESA, 2016).

The Sentinel-2 image acquired on the 21 August 2015 was chosen to be in the summer just like the GF-1 image, so the vegetation cover condition would be similar even though they are one year apart. The classification was performed using ArcGIS Maximum Likelihood Classifier (MLC) as described by Dewan and Yamaguchi (2009) and Foody (2004). The accuracy assessment and Kappa index were undertaken using the confusion matrix, and the results were 81.56% and 79.34% for the accuracy assessment and kappa index respectively. Figure 4.2 classifies Baghdad's land cover into seven classes with the domination of developed area, bare lands, vegetation and water.

On the other hand, land cover maps for London and Birmingham were acquired from the Urban Atlas which provides pan-European comparable land use and land cover data (EEA, 2010). The Urban Atlas belongs to The European Environment Agency, and uses data from different sources mainly SPOT 5 images with 2.5 m spatial resolution and city maps with Google Earth dated between 2005 and 2010 (EEA, 2010). Figures 4.3 and 4.4 show the Land Use/Cover (LULC) patterns of London and Birmingham respectively using the Urban Atlas. Urban Atlas provides data for Large Urban Zones with more than 100.000 inhabitants as defined by the Urban Audit (EEA, 2010).

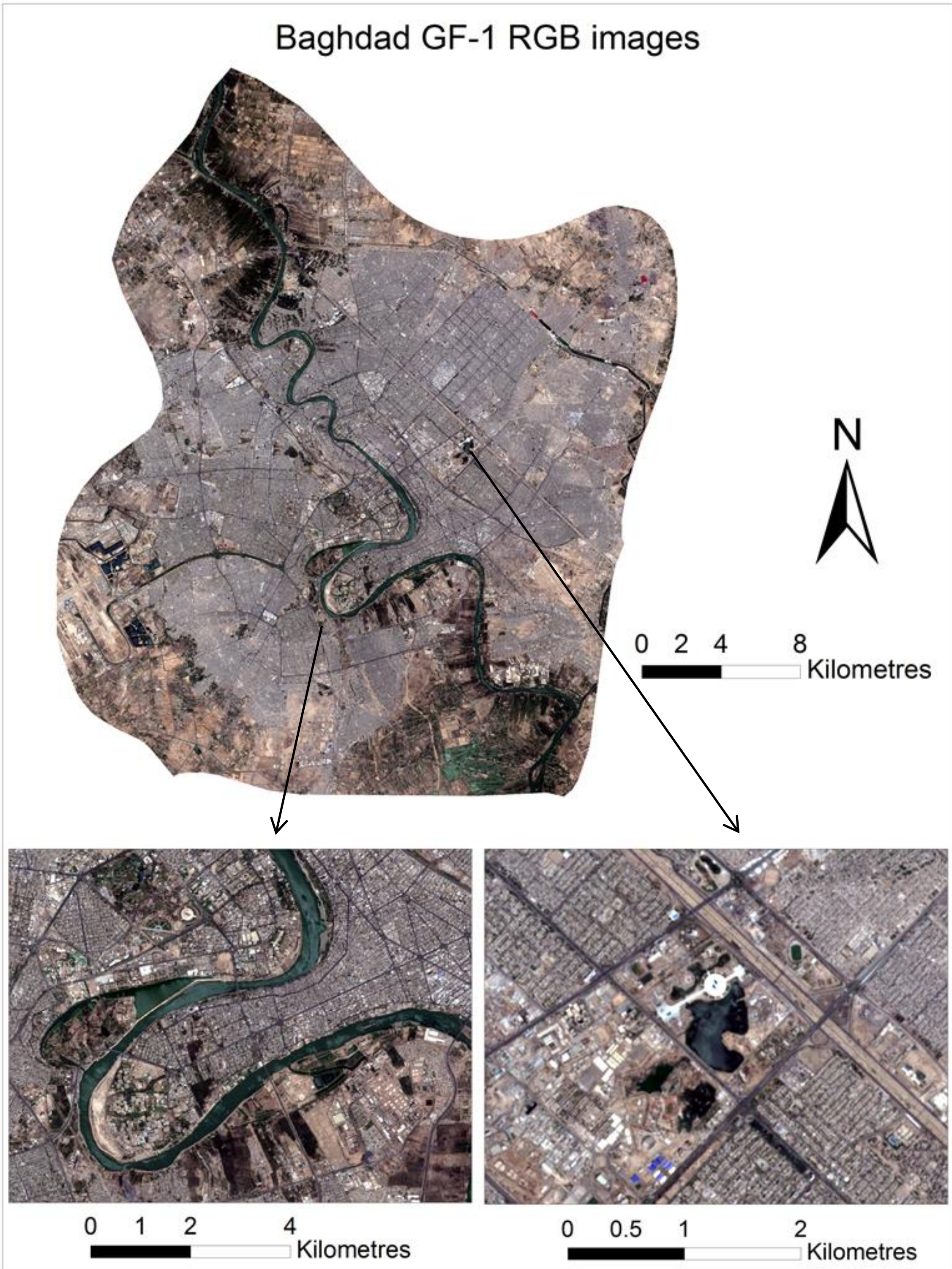

Figure 4.1: Baghdad's true colour (RGB) images of the Chinese GF-1 (Gaofen-1) satellite sensed on the 27th of June 2014 (CHEOS, 2016).

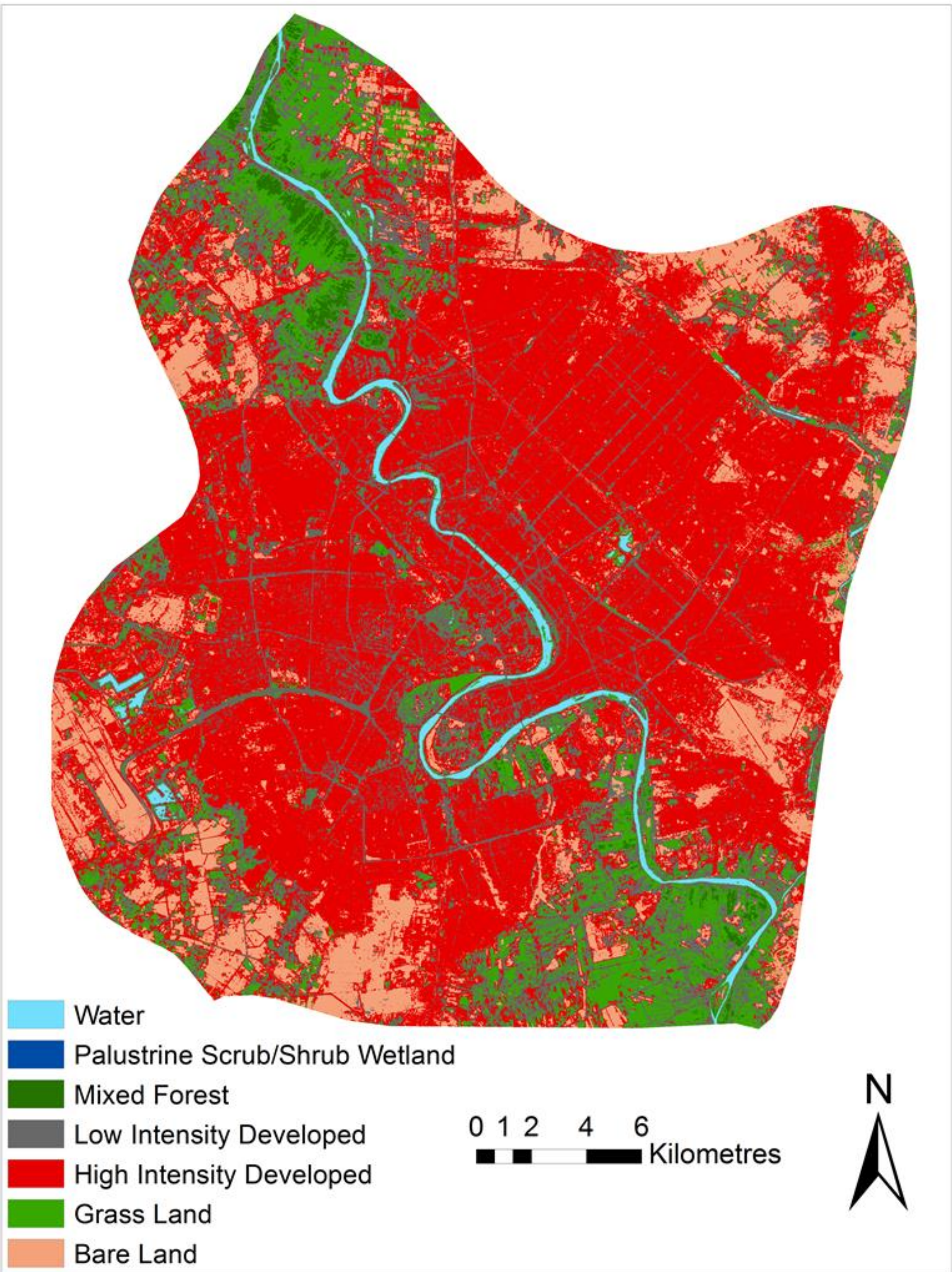

Figure 4.2: Baghdad's land cover classification using Sentinel-2 acquired on the 21 August 2015. The classification was performed using ArcGIS Maximum Likelihood Classifier (MLC).

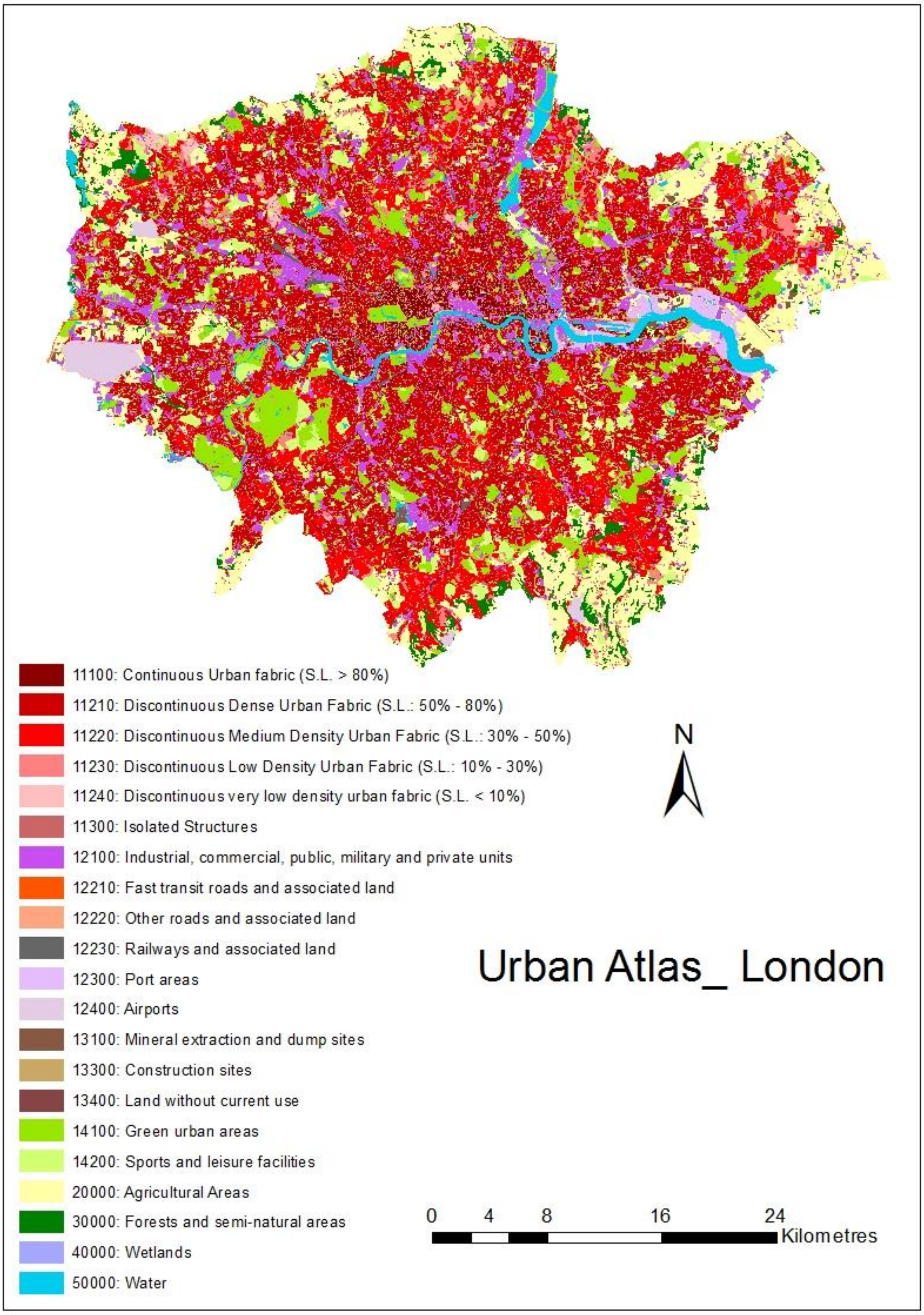

Figure 4.3: London land cover acquired from the Urban Atlas which uses data from different sources (EEA, 2010).

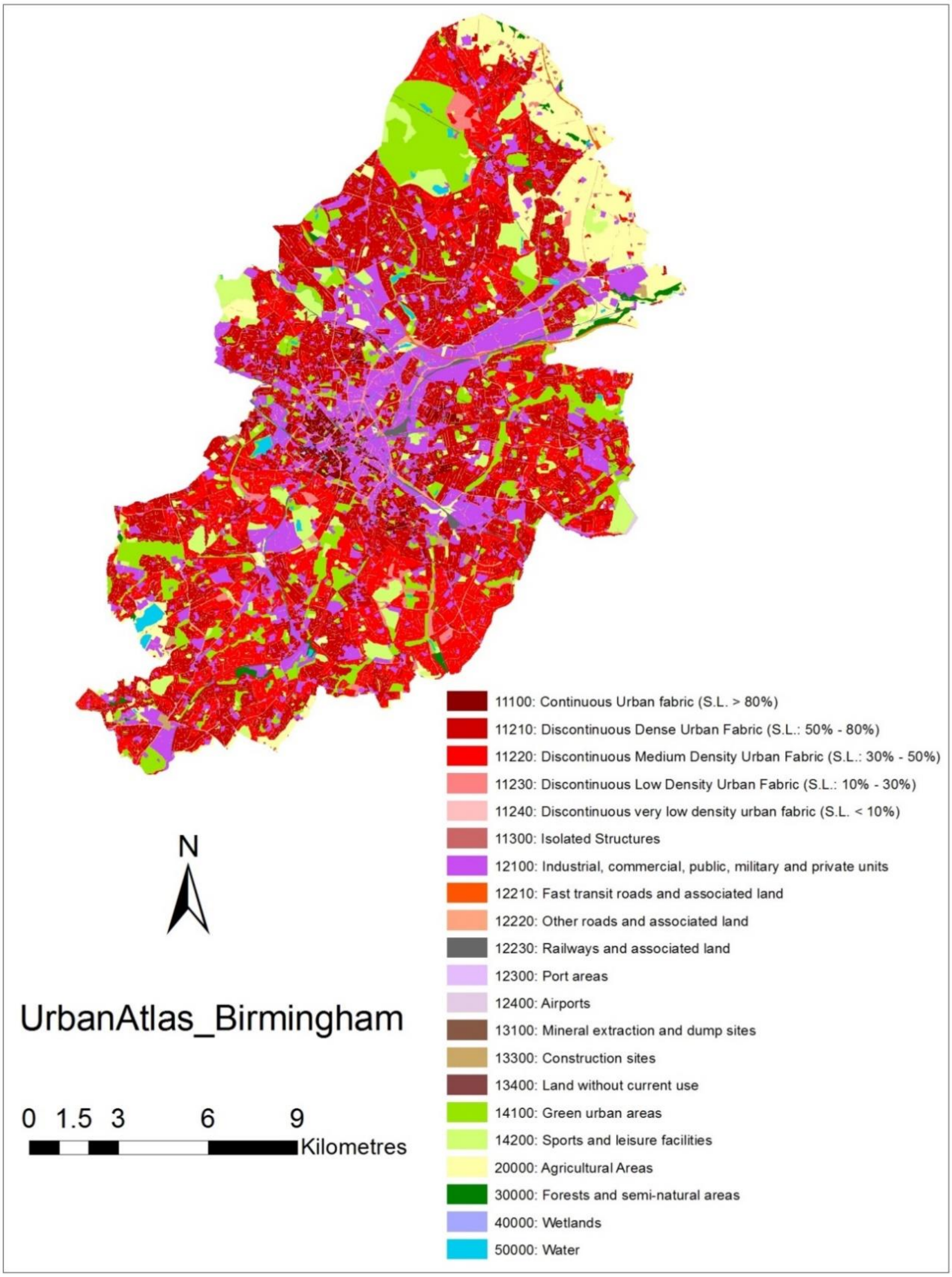

Figure 4.4: Birmingham land cover acquired from the Urban Atlas which uses data from different sources (EEA, 2010).

4.2.6 SUHI and NLST calculation

The magnitude of SUHI was calculated by subtracting the minimum value from the pixel values. Since the study areas were all urban areas and the rural lands were masked, so the SUHI intensity was calculated for each pixel by subtracting the pixel LST from the minimum LST. One of the purposes of UHI studies is to identify the impact of urbanisation on the microclimate. Hence, the urbanisation effects are highlighted by subtracting the minimum LST which is assumed to represent the rural LST. Besides, using the mean LST for certain areas to calculate the SUHI was avoided, because of the mixed pixels where different land cover types maybe present in a small area. For example, Zhang et al. (2010) calculated the SUHI magnitude based on the difference in average LST between urban core and a rural buffer of 20 km² around the city.

In Zhang et al. (2010) study the LST of the urban core was averaged to be subtracted from the rural buffer to calculate the SUHI. Tran et al. (2006) applied a Gaussian approximation to quantify spatial extents and intensity of individual UHIs for inter-city comparison. Their method employed the Gaussian approximation to the quantity SUHI based on the maximum difference in simultaneous temperature between urban and rural areas after the rural LST background has been subtracted. In this study, the rural background was eliminated by subtracting the minimum LST from each pixel value to have the maximum SUHI. The same assumptions were used to calculate the other types of UHI undertaken by this research.

Then the spatial distribution of hot and cold spots was investigated. The spatial change of daytime SUHI was investigated using Landsat, ASTER, and MODIS data. The spatial change of night-time SUHI was investigated using ASTER and MODIS data. However, the temporal change of daytime and night-time SUHI was investigated using MODIS data. The temporal change of SUHI was annually investigated for the period (2003-2015). Furthermore, the available MODIS data for the months (July - December) in 2002 were included. This explains why some monthly figures start from 2003, and others begin in 2002.

Since, the SUHI is the difference between two measurements, it did not need to be normalised. However, temperature values were rescaled between the minimum and maximum values, to calculate the Normalised Land Surface Temperature (NLST). This technique modifies the temperature from satellite images captured in different times, so a temporal comparison would be possible. Amiri et al. (2009) highlights that the normalisation of the temporal analysis could modify the methodology to remove the effect of inter-scene variability. There are various normalisations in statistics, however, a simple technique was used in this study called feature scaling or (Min-max) which brings all values into the range between (0- 1) (Mohamad and Usman, 2013). The calculation of SUHI magnitude was adapted from Schwarz et al. (2011), and the NLST was calculated according to Mohamad and Usman (2013) as below.

$$SUHI = LST_i - LST_{min} \qquad (4.10)$$

$$NLST = \frac{LST_i - LST_{min}}{LST_{max} - LST_{min}} \qquad (4.11)$$

Where:

LST_{max} and LST_{min} = maximum and minimum LST respectively, LST_i= pixel LST

4.2.7 Statistical modelling

This approach assumes that the land cover is the major driver of the LST spatial variation, while the temporal change of SUHI is investigated in different climatic conditions and incident solar radiation. To overcome the need for a classified land cover map for each acquisition due to the land cover change, spectral indices were employed instead, as they are derived at the same time of the thermal maps. Since the spectral indices were derived from Landsat data, so the correlation between LST and these indices represent only the daytime, as Landsat data are acquired mainly in the day. The regression modelling between LST and spectral indices was undertaken by SPSS (Statistical Package for the Social Sciences), and the software was provided by the university of Nottingham as well as a training course on using it. The same regression modelling processes were applied on Baghdad, London and Birmingham.

The significant models were derived by backward elimination of the non-significant predictors, until getting a model with all the predictors having p-values less than 0.001. Moreover, the models were tested for unusual and influential data (particularly Outliers), normality of residuals, heteroscedasticity and collinearity as described in details by IDRE (2016). Although the effects of land cover on urban-rural temperature differences have been extensively documented (Yan et al., 2014), the level of the quantitative effects of intra-urban are debatable. Some researches claim that LULC have strong impact on the LST (Shen et al., 2015, Yan et al., 2014), however, other studies assert that the atmosphere and urban morphology are also of the main drivers of the LST (Scarano and Sobrino, 2015, Materia et al., 2014). Accordingly, the quantitative effects of land cover indices on the LST was investigated, and the spatial and temporal change SUHI.

4.3. Baghdad SUHI

Baghdad is a desert and dry city, was first founded in the year 762 A.D. known as the round city at that time. The city expansion was enabled through the construction of dams on the Tigris River to cope with the growth of population which changed the boundary of the city (Saleh, 2010). Baghdad is the capital city of Iraq, which has hot-dry summers and cold-rainy winters (Awadh and Ahmad, 2010). Awadh and Ahmad (2010) report that about 90% of the annual rainfall occurs between November and April, most of it in the winter months (December - February) when the temperature goes down below freezing in January, while, the average temperature of the hottest summer months (June – August) is about 48 ºC. Generally, the climate of Mesopotamia is semi-arid with a maximum air temperature up to 53 ºC in the summer and minimum temperature of -7 ºC in the winter (Jassim and Goff, 2006). Jassim and Goff (2006) state that the annual precipitation is approximately 150 mm/year, and the prevailing wind is generally North-West. The land cover of Baghdad was clarified by the classified map in Figure 4.2, the Tigris River divides the city into two parts Karkh on the west side of the Tigris River, and Rusafa on the east side of the river. The bare (soil) lands surround the city; whereas, the impervious areas extend on both sides of the river and the vegetation is available alongside the river.

4.3.1 SUHI spatial change

Figure 4.5 shows the daytime spatial change of temperature differences between the pixel value and the minimum of values. The soil areas appear to have the highest LST values, higher than the built-up areas, while the water and vegetation have the lowest LST intensity. The built-up areas inside the city have lower temperature than the bare lands on the boundary of the city, and in this case the city works as Cool Island towards hotter areas. In this case the phenomenon is called Surface Urban Cool Island (SUCI). Some studies have found that built-up areas in semi-arid regions might exhibit lower surface temperatures compared to non-urbanized dry surroundings (Rasul et al., 2015, Frey et al., 2006, Cai and Du, 2009, Shigeta et al., 2009).

The intensity of SUCI varies over different land cover types, to reach over 33 ºC on the 25th of September 2003 for bare lands during the daytime (see Figure 4.5). A study by Al-Lami (2014) found that the maximum difference of LST in Baghdad between the built-up and the surrounding area reach to 11.97 ºC. However, this study only employed one single Landsat-7 ETM+ image on the 18th of March 2001 which could not came up with the temporal variation of LST magnitude. However, during the night-time the SUHI distribution reveals different behaviour compared to daytime as seen in Figure 4.6, where the soil areas have the lowest temperature just lower than the vegetated areas. The built-up areas and water have the highest temperatures during the night-time. So, on the 18th of November 2015 the Tigris River is distinguished on the map with its high temperature (Figure 4.6), where the mean air temperature on that day was 16 ºC (Weather Underground, 2016). On the other hand, the built-up areas give the highest temperature on nights of hot to moderate days, for example, on the 5th of October 2005 when the average air temperature was 26 ºC (Weather Underground, 2016). The higher temperature of water bodies during cold nights maybe attributed to its higher thermal capacity. Gibson (2013) asserts that many natural surfaces (e.g. soil, rock, vegetation) have approximately 0.2 thermal capacity except water which has a thermal capacity of 1. Accordingly, at night-time, Baghdad's built-up areas experience relatively high LST, and the city demonstrates a significant SUHI effect. In contrast, during the daytime densely built-up areas have relatively low LST acting as a SUCI.

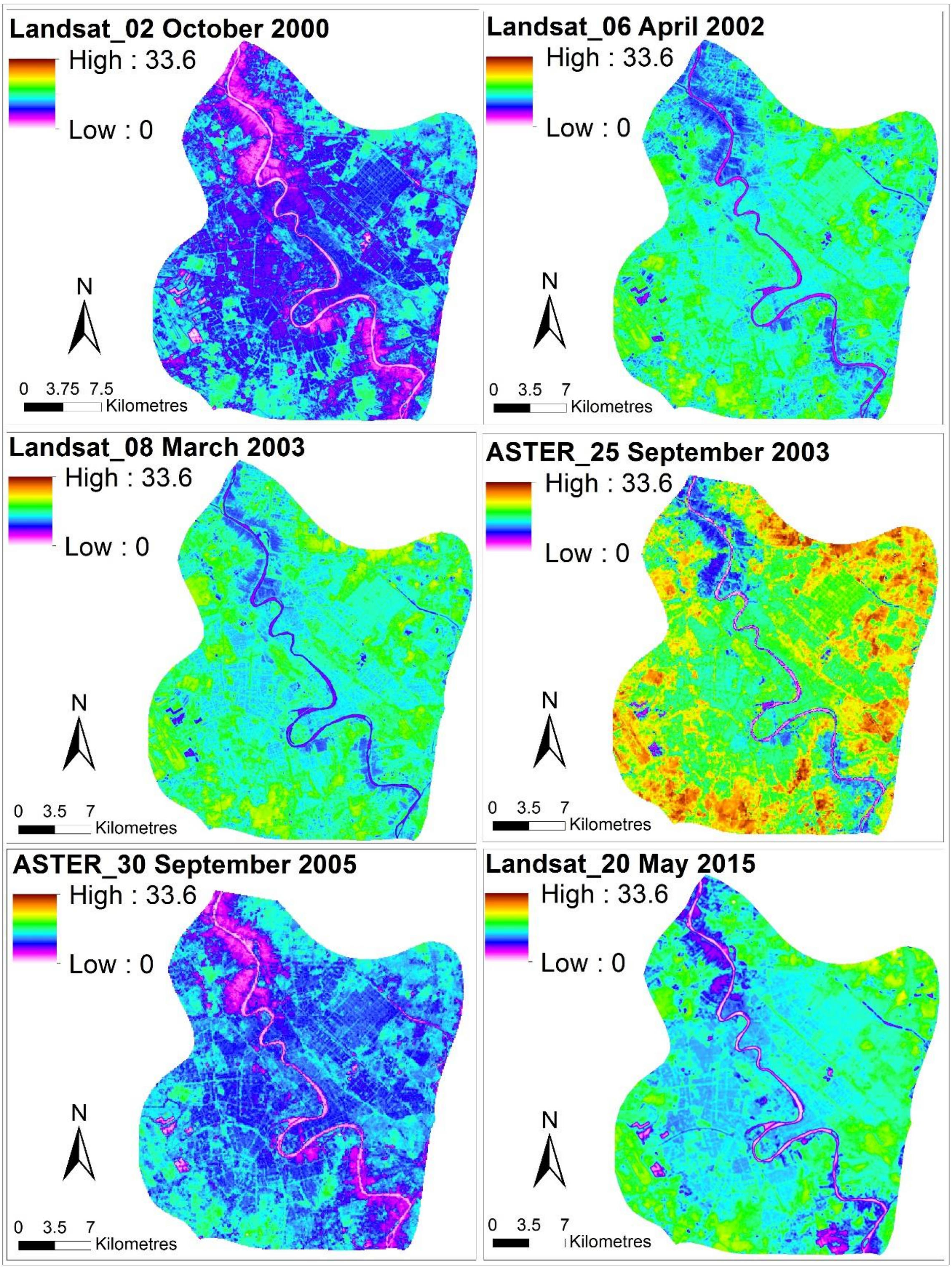

Figure 4.5: Baghdad's daytime SUCI spatial distribution using Landsat and ASTER images (ºC). Derived from the thermal bands of the satellite images acquired between 2000 and 2015.

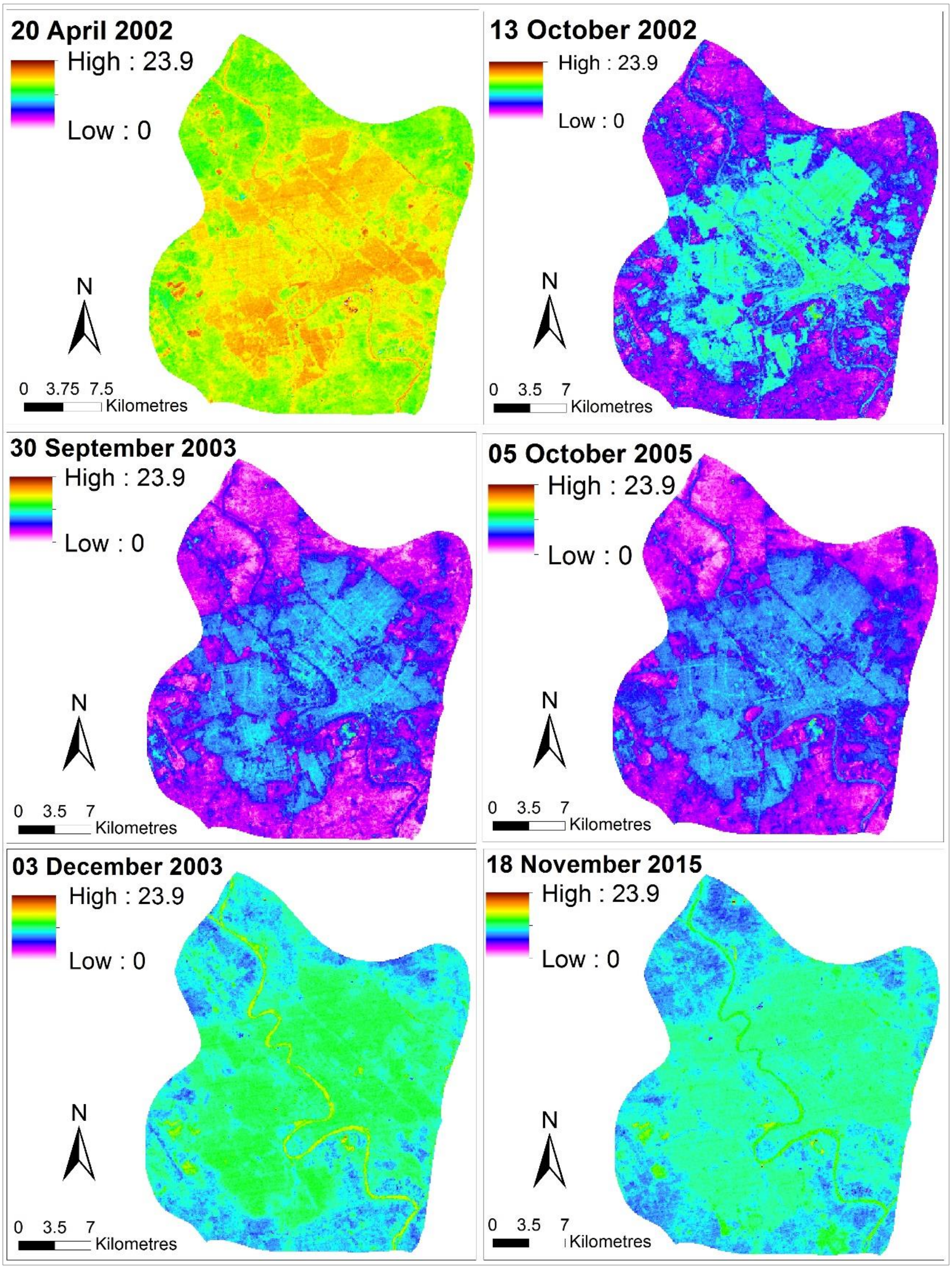

Figure 4.6: Baghdad's night-time SUHI spatial distribution using ASTER images (°C). Derived from the thermal bands of the satellite images acquired between 2002 and 2015.

MODIS images were employed for validating the findings of ASTER and Landsat data as it has more frequent revisits. The average (Ave.) annual images were calculated for the years (2003-2015) based on the data availability by ignoring the no data statistics per pixel. The findings show that during the day the city experiences low SUCI intensity, which means it works as a cooling island except the areas north-east of the Tigris river as shown in Figure 4.7. These results are consistent with the Landsat and ASTER data findings (Figure 4.5). A study by Rasul et al. (2015) employed six Landsat images to examine the spatial formation of the daytime SUCI of the central districts of Erbil city in the north of Iraq. Their results indicated that the urbanised areas have lower LST acting as cool islands, compared to the rural area. Saleh (2011b) studied the mean surface temperatures of Basarah city in the south of Iraq using daytime Landsat images for the years 1990, 2000 and 2002. He found that barren land (dry and wet soil) exhibits highest surface temperature followed by urban, vegetated (orchards) and water areas. However, the hot spots in Figure 4.7 of Baghdad's daytime SUHI have only appeared clearly using MODIS long term data. This implies the importance of using higher temporal resolution images, as some patterns cannot be captured by employing only few images on certain times.

After investigating the high LST spots in the core of the city, they have been found in areas of very high population density where the urban form configurations are mainly attached buildings. Alobaydi et al. (2016) describes the attached urban form configurations as rectangular long urban blocks, gridded street systems, and attached buildings from three sides. In this case, the aspect ratio or building height to street width (H/W) is about 0.6, and the ground is more exposed to the sun radiation with low vegetation and high heat storage of building's mass (Alobaydi et al., 2016). Furthermore, industrial areas as well as attached urban configurations appear to have high SUHI intensity in the daytime, unlike, the night-time images in Figure 4.8 where all the urban areas exhibit higher temperature compared to city periphery. The annual average daytime SUHI reached to 21 °C in 2011, while, the night-time SUHI average peaked in 2013 by about 10.8 °C. The average SUHI were calculated for the whole period (2003 - 2015) to highlight the gross differences between daytime and night-time SUHI as shown in Figure 4.9 with the boundaries of Baghdad's neighbourhoods. The densely populated with attached houses Sadar and Habbibiyah districts (no.27 & 28 in Figure 4.9) have higher daytime SUHI, and industrial areas next to them such as Sheik Omar (no. 7) also have higher SUHI compared to other urban areas.

Due to the limited availability of Iraq's GIS data and the Iraqi governmental units tend to not publish their digital data online, Baghdad neighbourhoods boundaries were obtained from the Empirical Studies of Conflict Project (ESOC) which was initiated in 2009 by a number of practitioners and scholars (ESOC, 2016). The night-time MODIS images in Figures 4.8 and 4.9 have the same spatial SUHI distribution of ASTER images in Figure 4.6 where the urbanised areas exhibited higher LST compared to non-urbanised areas. The only difference is that Tigris River showed distinctive higher temperature than built-up environment in the cold night using ASTER data, while it did not appear in MODIS data due to its course spatial resolution. Similarly, Rasul et al. (2016) found that at night-time Erbil experienced higher LST and demonstrated a significant SUHI effect, their study employed MODIS data to assess the formation of night-time SUHI.

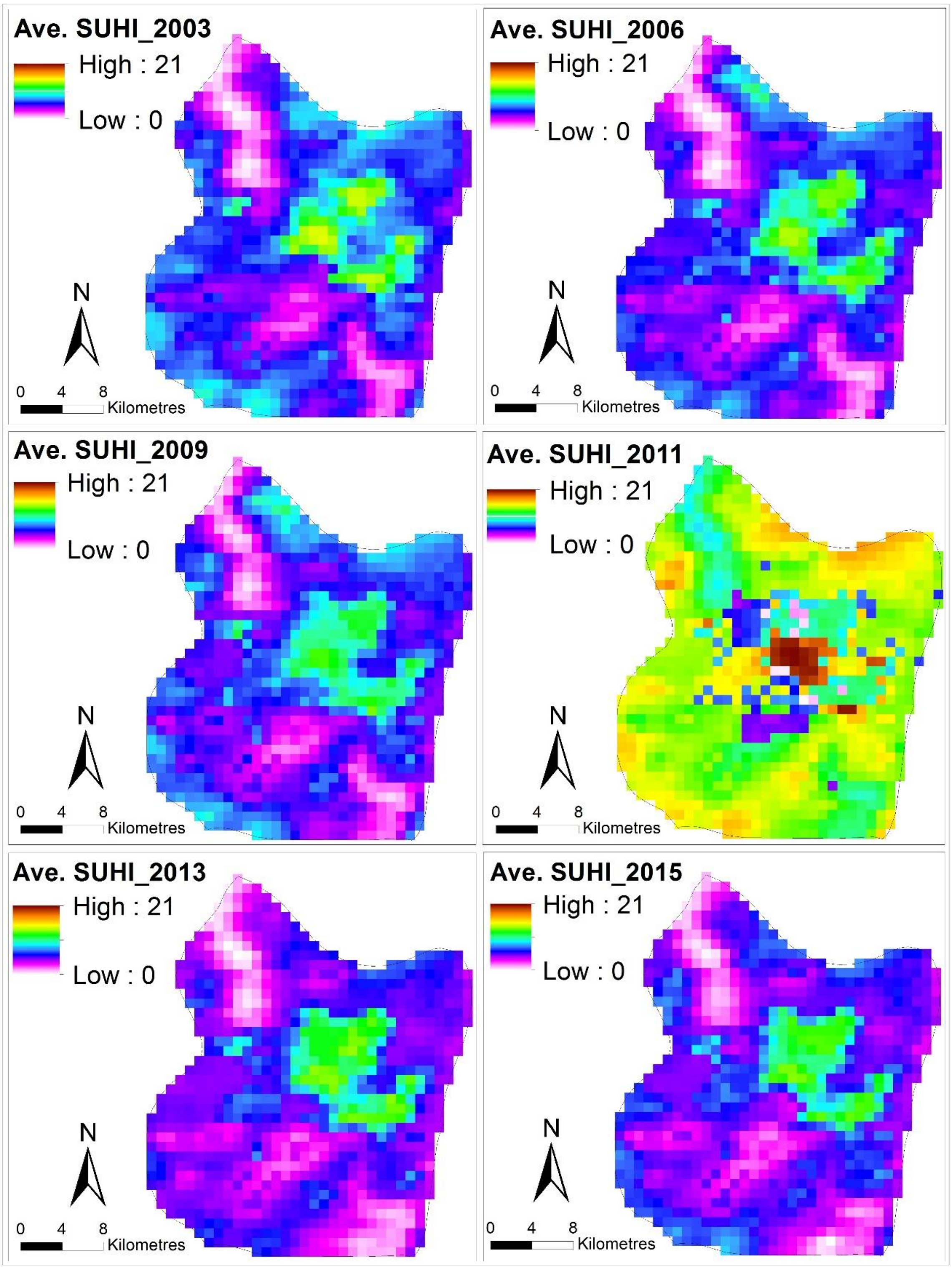

Figure 4.7: Baghdad's daytime SUHI spatial distribution using MODIS images (°C). Derived from the thermal bands of the satellite images acquired between 2003 and 2015.

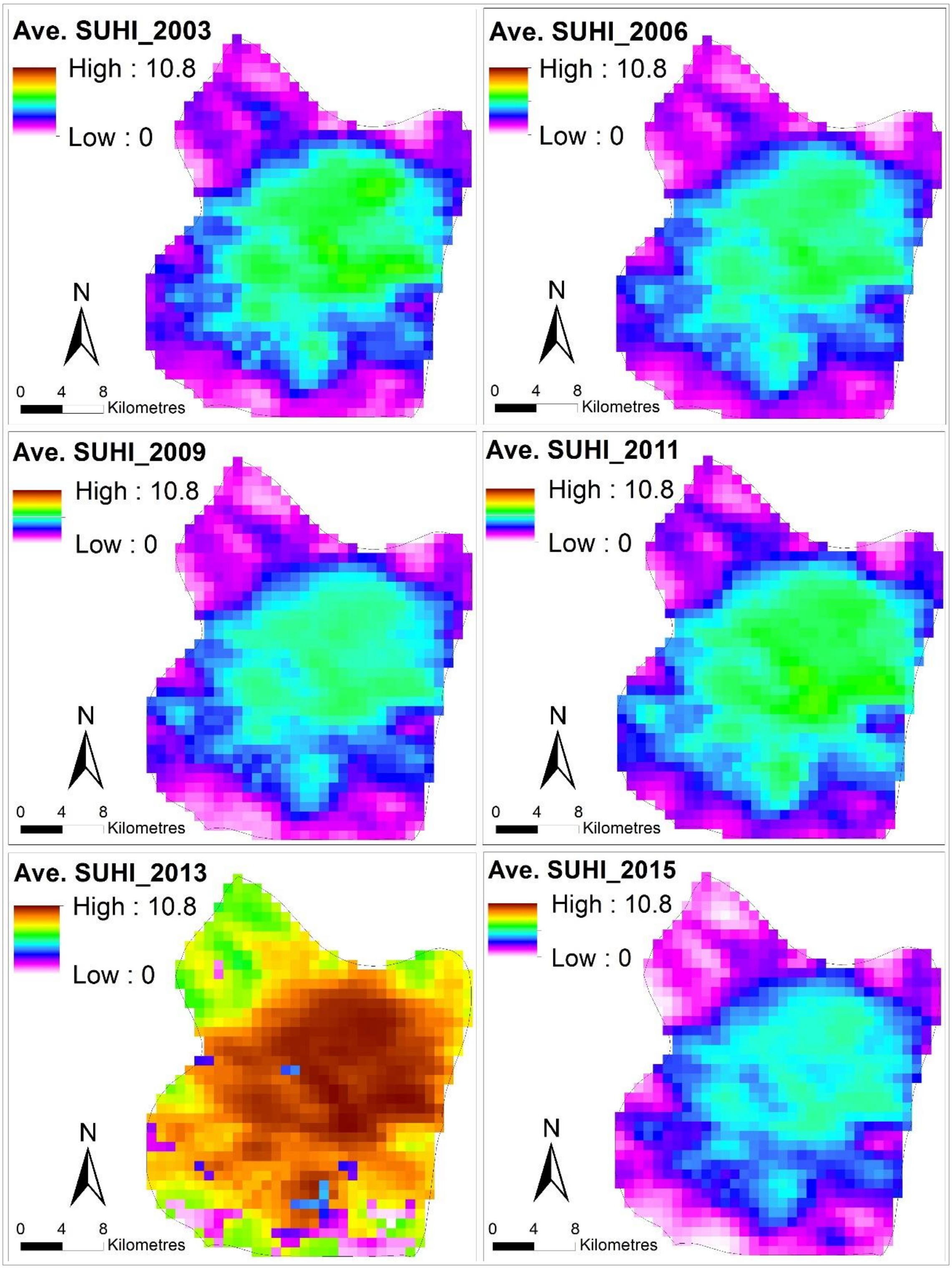

Figure 4.8: Baghdad's night-time SUHI spatial distribution using MODIS images (ºC). Derived from the thermal bands of the satellite images acquired between 2003 and 2015.

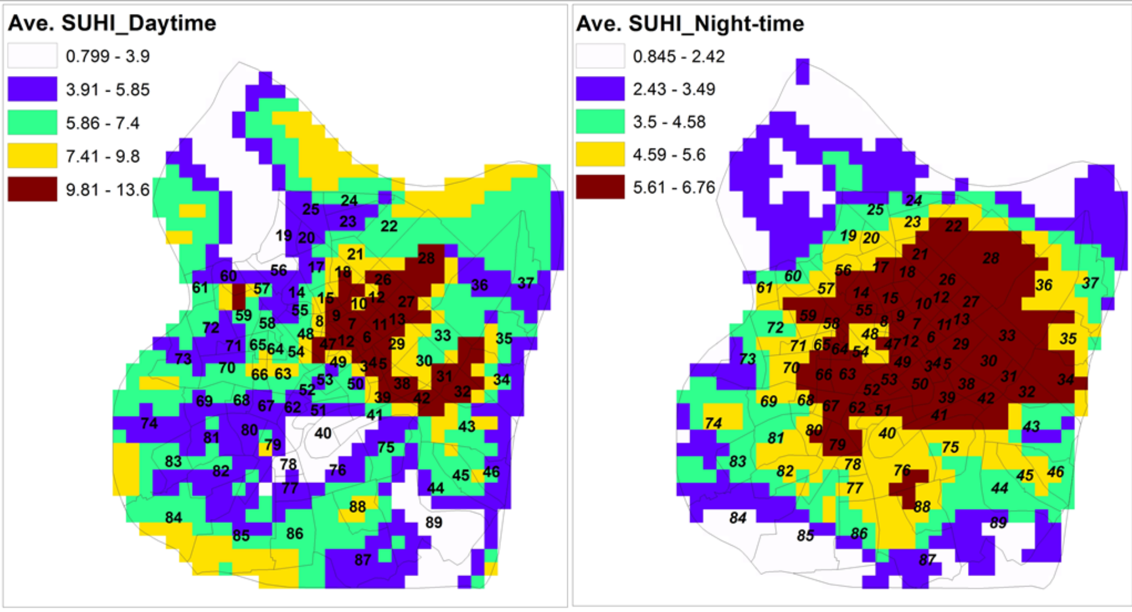

Baghdad Neighbourhoods

1	Sinak	11	Nile	21	Ur	31	Ghadeer	41	Karrada out	51	Um Al Khanzeer	61	Shuala	71	Al-Adil	81	Al Atiba'a
2	Khulani	12	Hay 14 July	22	Shaab East	32	New Baghdad	42	Camp Sarah	52	Harithiya	62	Qadissiya	72	Ghazaliya,E	82	Shurta 4&5
3	Abu Nuwas	13	Idrissi	23	Shaab South	33	Habibiyah	43	Al Rasheed Camp	53	Zawra Park	63	Mansour	73	Ghazaliya,W	83	Al Furat
4	Bataween	14	Adhamiyah	24	Shaab North	34	Mashtal	44	Industrial Zafraniya	54	Old Airport	64	Washash	74	Airport	84	Makasib
5	Saadon Park	15	Waziriya	25	Rashdiya	35	Fedhailia	45	Rabea'a	55	Utayfia	65	Iskan	75	Dora Refinery	85	Resala
6	Camp Gaylani	16	Waziriya Indus.	26	Ishbilya	36	Al Husseinia	46	Zafriniya	56	Kadimiyah 1	66	14 Ramadhan	76	Athureen	86	Ewairij
7	Sheik Omar	17	Maghreb	27	Habbibiyah	37	Obaydi	47	Shawaka	57	Kadimiyah 2	67	Al Yarmuk	77	Saydia1	87	Hour Rejab
8	Medical City	18	Qahira	28	Sadar City	38	Alwiya	48	Sheik Maaruf	58	Ali Al-Saleh	68	Kafa'at	78	Saydia	88	Mechanic
9	Bab AlMuadham	19	Krai'at	29	Shaab Stadium	39	Karrada In	49	Salhia	59	Hurriyah,1-5	69	Al Amriya	79	Bajas, Amil	89	Bo'altha
10	Mustansiriya	20	Tunis	30	Zayonna	40	Jadiriya	50	Karadat Maryam	60	Dabbash	70	Al Jamia'a	80	Jihad		

Figure 4.9: Daytime & night-time average SUHI of Baghdad's neighbourhoods over the period (2003- 2015) using MODIS images (ºC). Different SUHI scales are used for daytime and night-time.

4.3.2 SUHI temporal change

Figure 4.10 shows the total diurnal (day and night), daytime and night-time LST for the whole study period (2003-2015) with their Standard Deviation (SD). It can be seen clearly that the average of the LST has increased for both normal and normalised values. By comparing the normal and normalised values in Figure 4.10, there is no noticeable difference in the trends in spite the ranges were modified through normalisation. The averages of NLST range between 0.56 - 0.58 for the diurnal, daytime and night-time NLST. The average of diurnal LST magnitude is 17 ºC with SD of 1.74 as shown in Figure 4.10. The average of daytime LST fluctuates around 35.83 ºC with SD of 1.9 which is higher than the night-time as it is about 17 ºC with 1.63 SD.

The increase of the diurnal LST is a consequence of the rise in trends of night-time LST, as daytime LST has not increased over time. The reason of night-time LST increase might be attributed to the increase of anthropogenic heat due to population growth. Baghdad's population jumped from 5,423,964 in 1997 to 7,055,200 in 2011, and peaked to 7,665,300 in 2014 (Brinkhoff, 2016). Rabee (2014) reports that Baghdad's population formed approximately 10% of Iraq's total population in 1947; however, Saleh (2011a) states that the density has increased to form nearly 25% of the country population in 2011. The population density of Baghdad City reached

5233 persons / km^2 by 2011; nonetheless, it is between 6 and 190 persons / km^2 for other Iraqi cities (Saleh, 2011a). This explains the increase in the total LST night-time LST as daytime LST is more affected by the sun's radiation which might include the effect of global climate change. However, the heat gained during the day is usually released back to the atmosphere in the night. The stable daytime LST might reveal that the urban expansion has not contributed to increase the diurnal LST, and the increase of population density has positively contributed to the night-time LST.

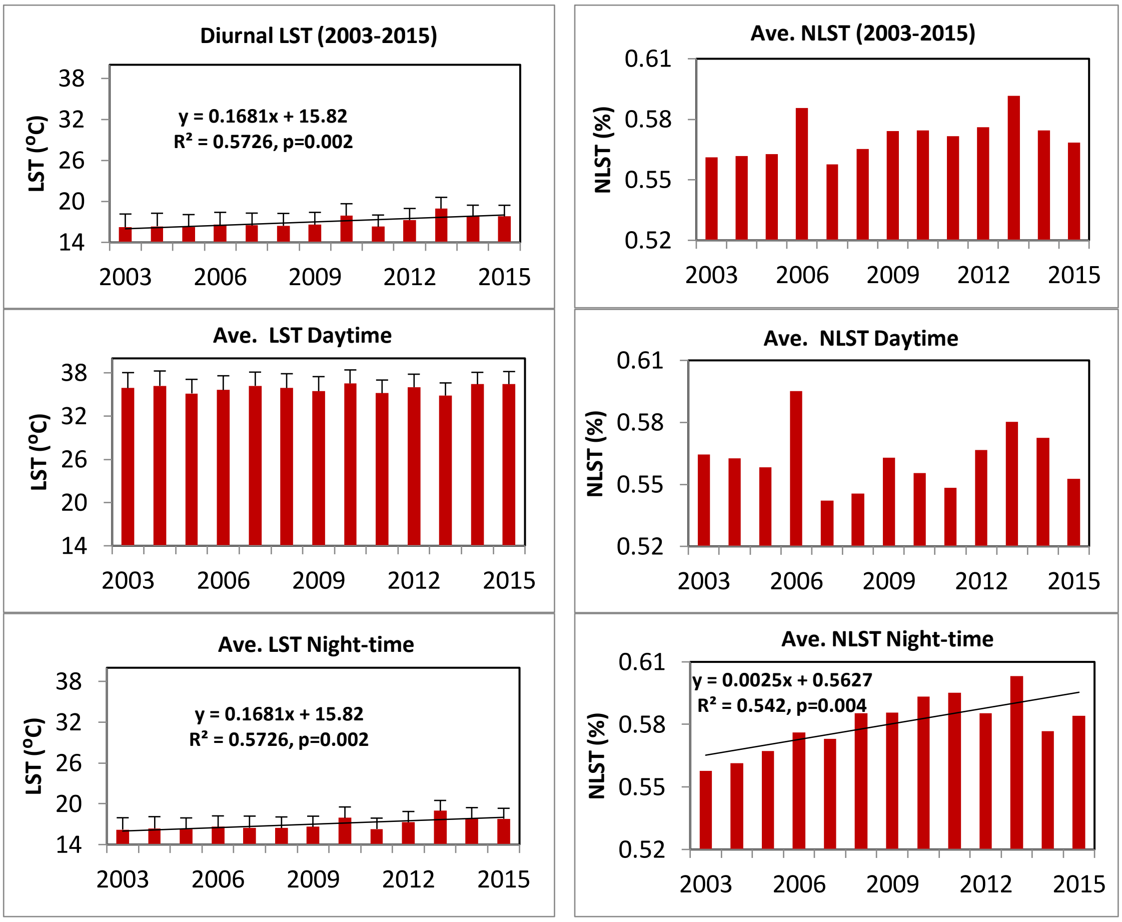

Figure 4.10: Baghdad's diurnal, daytime & nigh-time of LST change derived from MODIS data over the period (2003-2015), left (Normal) & right (Normalised). Only significant trend lines are shown.

The average of diurnal SUHI magnitude is 9.41 ºC with SD of 3.09 as shown in Figure 4.11. The average of daytime SUHI fluctuates around 11.56 ºC with SD of 2.8 which is higher than the night-time SUHI as it is about 7.26 ºC with 1.38 SD. Although the trend of daytime SUHI went down, the magnitude of the daytime SUHI is still high compared with the night-time. The overall trends of diurnal, daytime and night-time SUHI have decreased between (2003- 2015).

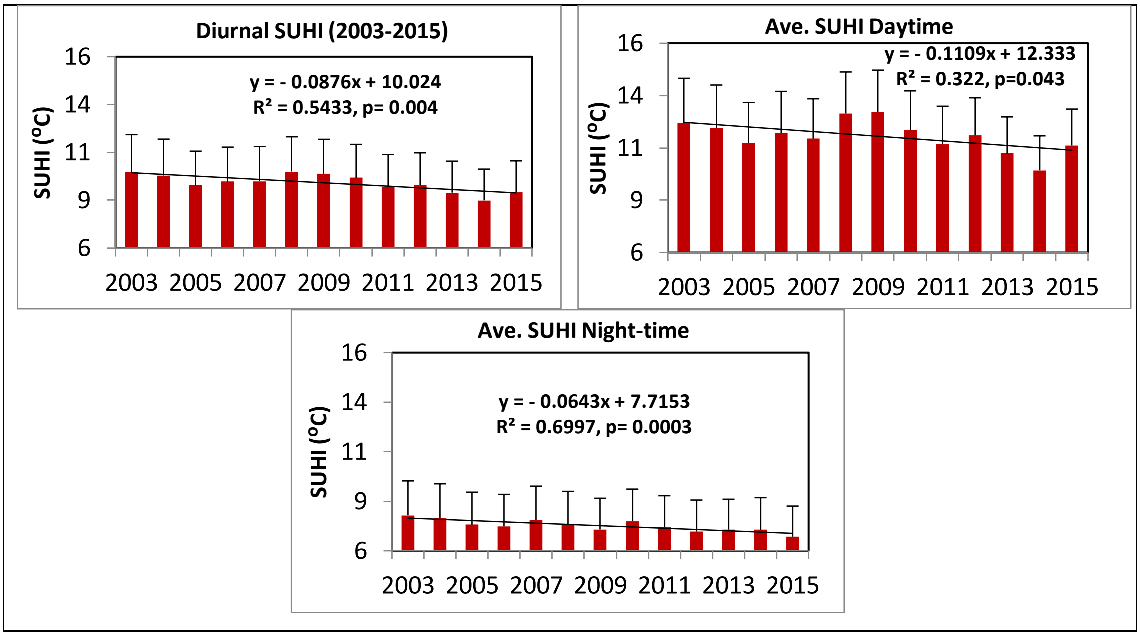

Figure 4.11: Baghdad's diurnal, daytime & nigh-time average SUHI change derived from MODIS data over the period (2003-2015).

Iraq has four seasons in the year, therefore, the incoming four figures include the months of each season. Figure 4.12 contains the winter's months which do not show obvious increase in the trends for the study's period. The LST averages for winter's months range between 12 – 16 ºC, and for the NLST the ranges are between 0.56 – 0.58. There is no noticeable difference between the trends of LST and NLST for the winter's months (see Figure 4.12). Furthermore, Figure 4.13 includes the spring's months which fluctuate in the trends over the study's period. The LST averages for spring months range between 21 – 32 ºC, and for the NLST the ranges are between 0.56 – 0.57. There is a noticeable difference between the trends of LST and NLST for the spring's months as shown in Figure 4.13. So, March LST average shows an increase for the LST values and does not show the same increase for the NLST values. April LST does not have the same decrease in the trend as the NLST. Similarly, May LST does not have the same increase of NLST.

On the other hand, Figure 4.14 contains the summer months which show different increases in the trends for the study's period. The LST averages for summer's months range between 37 – 39 ºC, and for the NLST the ranges are between 0.58 – 0.59. There is no noticeable difference between the trends of LST and NLST except for August. Hence, the NLST has significantly increased (R^2= 0.67, p= 0.0003) compared to the very low increase (R^2 = 0.17) for the LST (see Figure 4.14). Moreover, Figure 4.15 contains the autumn months which do not show clear increase in the trends of LST and NLST for the study's period. The LST averages for the autumn months range between 18 – 33 ºC, and for the NLST the ranges are between 0.55 – 0.57. There is no noticeable difference between the trends of LST and NLST for the autumn months (see Figure 4.15). In total, most months show different degrees of LST increase over the study period, and spring has the more noticeable rise. Furthermore, for some months the LST and NLST do not have the same trends direction, and in few cases, they have opposite behaviour.

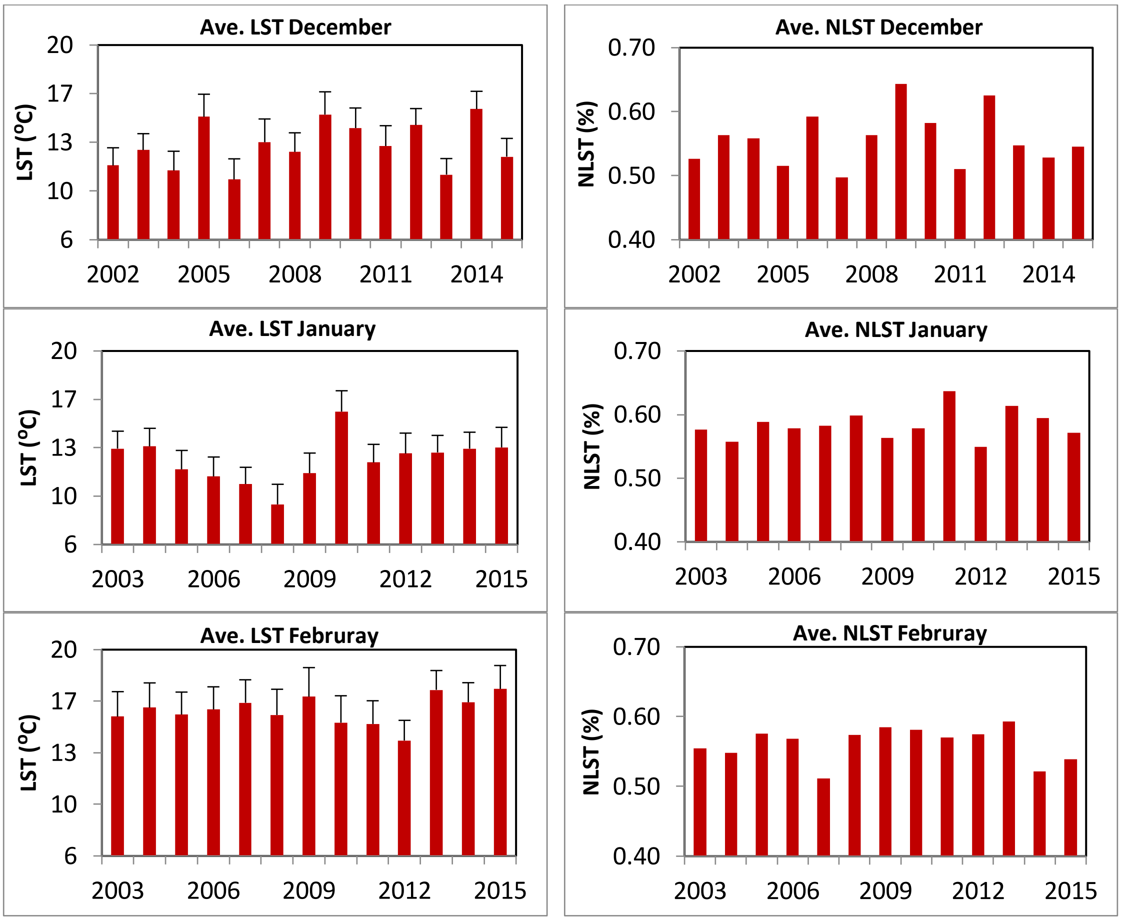

Figure 4.12: The temporal change of the winter's months LST and NLST in Baghdad derived from MODIS data, left (Normal) & right (Normalised) between 2002 and 2015.

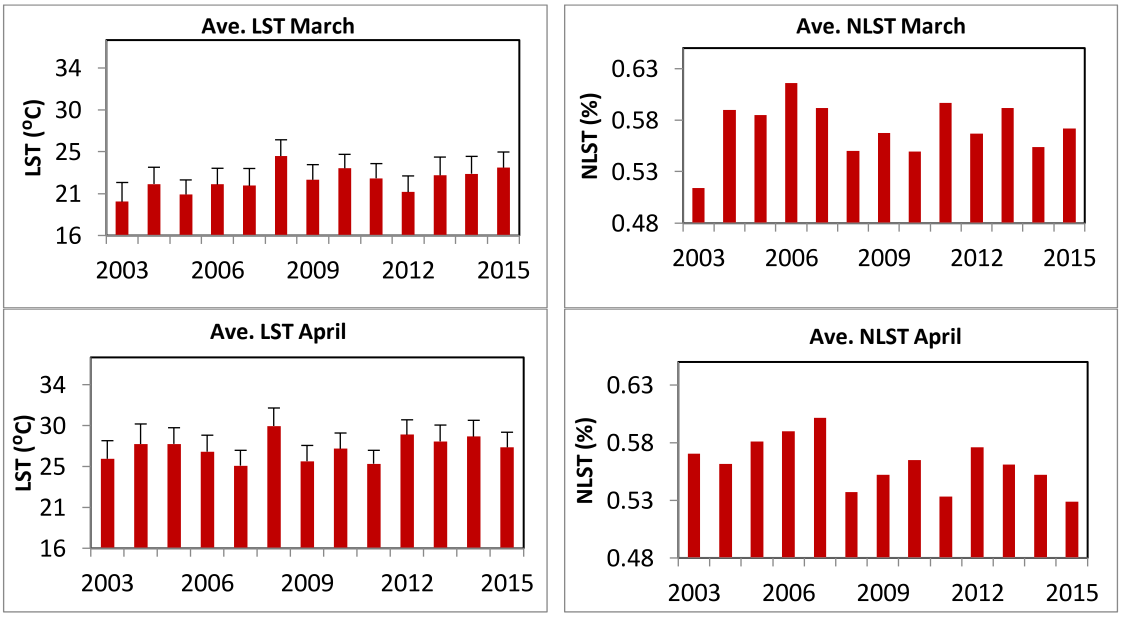

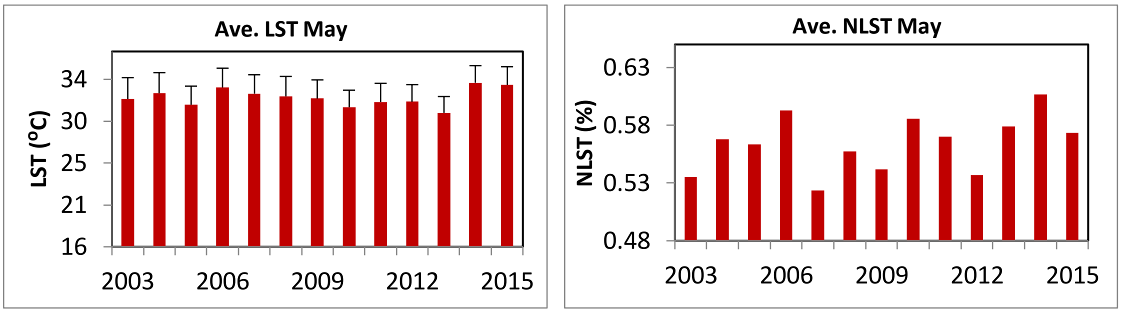

Figure 4.13: The temporal change of the spring's months LST and NLST in Baghdad derived from MODIS data, left (Normal) & right (Normalised) between 2003 and 2015.

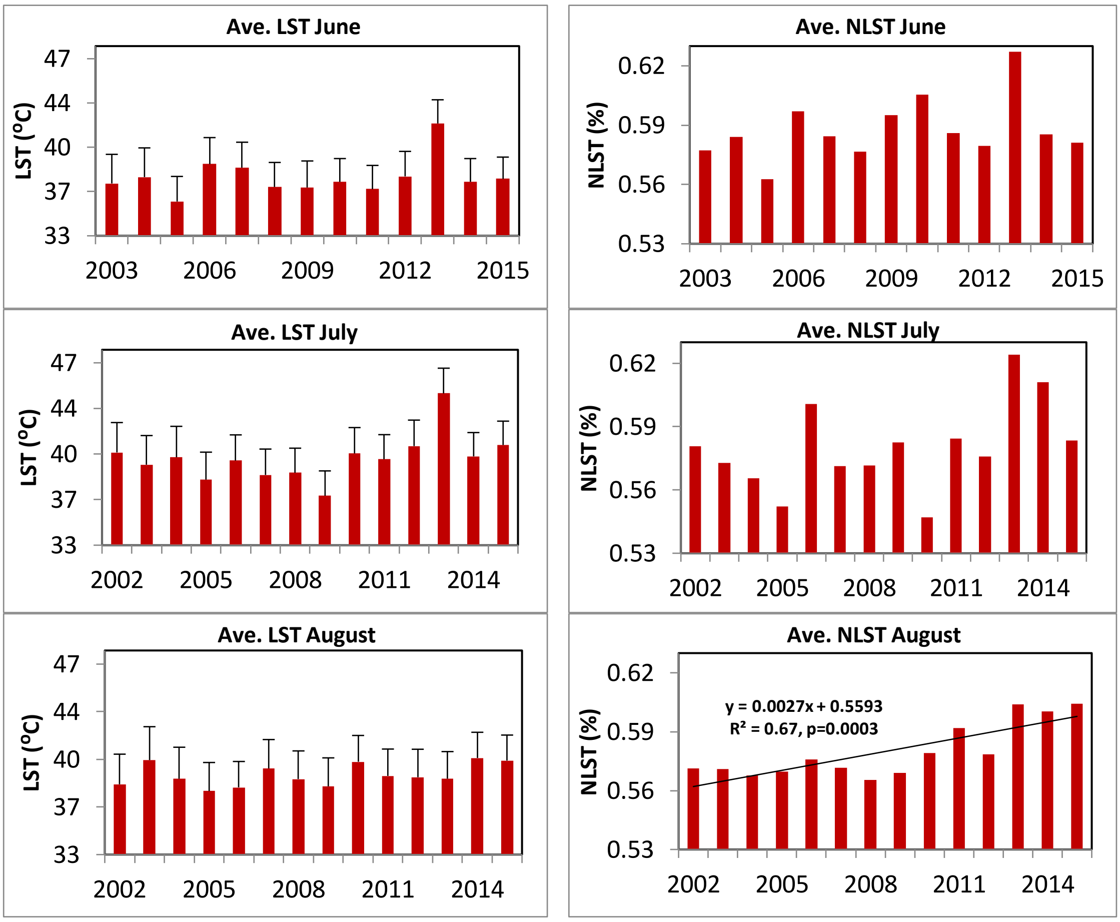

Figure 4.14: The temporal change of the summer's months LST and NLST in Baghdad derived from MODIS data, left (Normal) & right (Normalised) between 2002 and 2015. Only significant trend lines are shown.

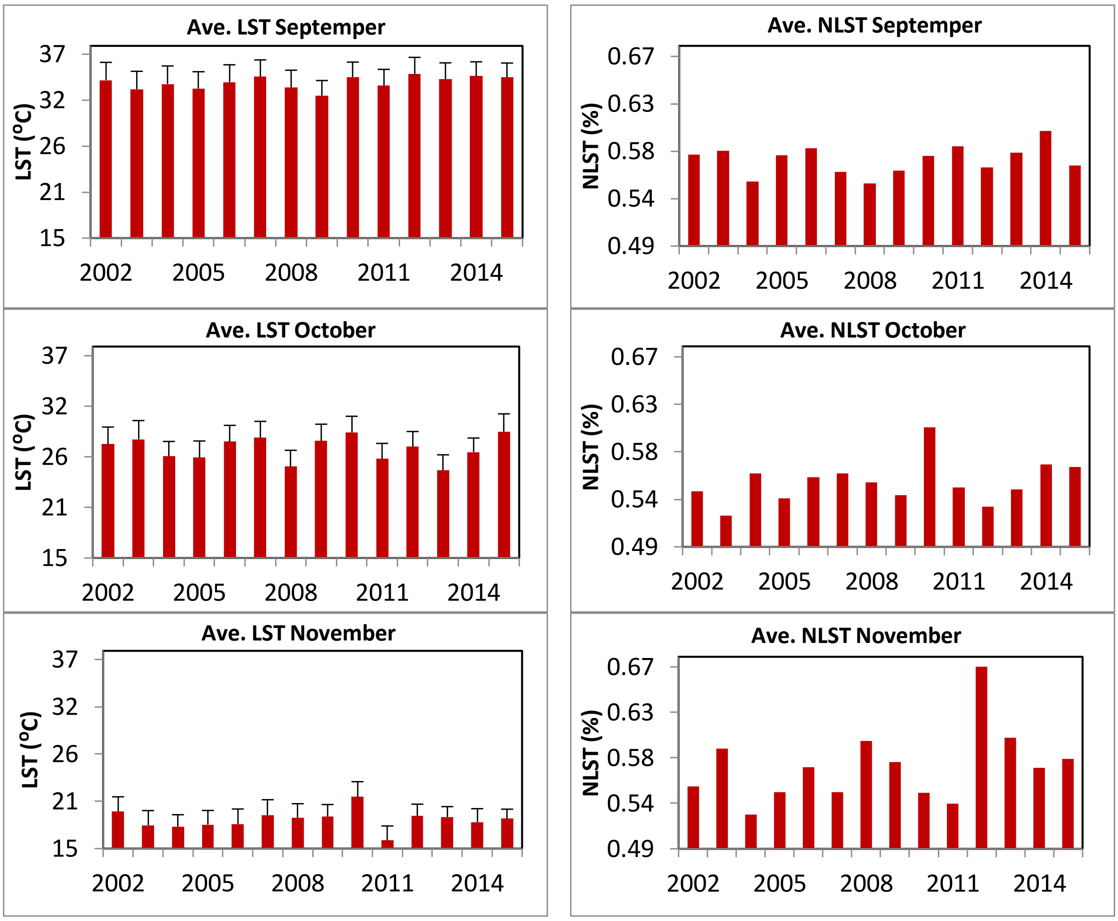

Figure 4.15: The temporal change of the autumn's months LST and NLST in Baghdad derived from MODIS data, left (Normal) & right (Normalised) between 2002 and 2014.

The monthly averages of SUHI for the whole study period range between 8.06 – 10.51 ºC as detailed in Figure 4.16. The average SUHI intensity fluctuated from about 8.05 ºC with SD of 2.35 ºC for December to around 10.51 ºC with 3.63 SD for May. Almost all the monthly trends decreased, with a higher percentage of decrease identified by R-square (R^2) more than 0.3 from (April – September). These months have the higher temperature averages compared to other months in the year, as their average LST ranges between 27 – 40 ºC. However, these months (April – September) still have the highest magnitudes of SUHI intensity. The relationship between LST and SUHI over the study period (2003 – 2015) is negative. And the high averages of SUHI coincided with months of high LST averages during the year (Figure 4.16). Hence, the increase of annual LST over 12 years has not enhanced the SUHI. Nevertheless, the seasonal differences might have maximised the average SUHI. This agrees with Kumi-Baoteng et al. (2015) findings when they studied the effects of urban growth on urban thermal environment of Sekondi-Takoradi metropolis of Ghana. Their results suggested that urban expansion has a certain effect on the monthly average surface temperature as well the seasonal average temperature changes of the Metropolis. Furthermore, Du et al. (2016a) assessed the surface UHI and its relationship with types of land cover and other influencing parameters. Their results indicated that average temperature is one of the positive contributors to SUHI intensity. Overall, the average SUHI intensity fluctuated from about 8.05 ºC for December to around 10.51 ºC for May. The next section explores the influencing parameters on the formation of SUHI, land cover types.

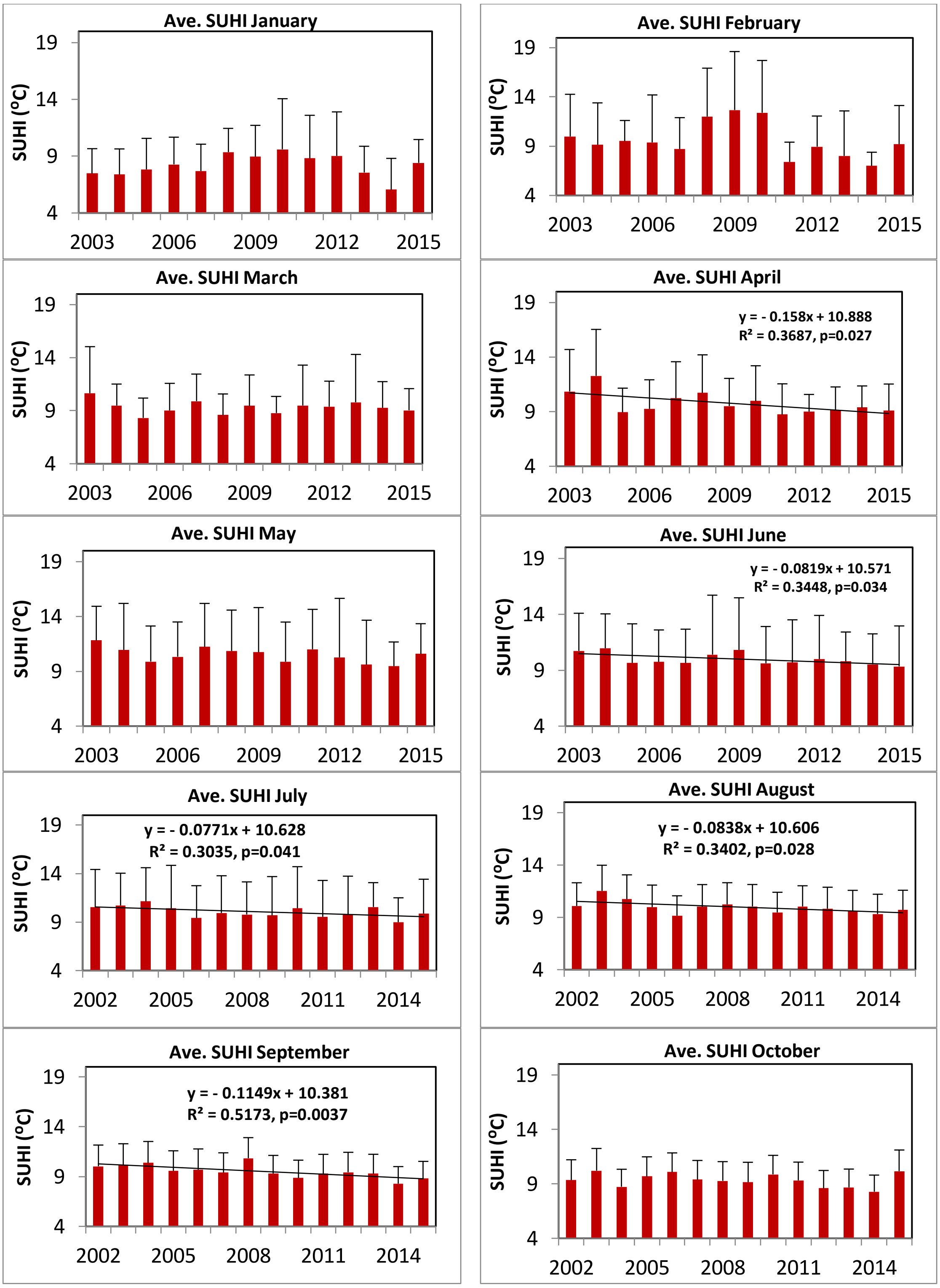

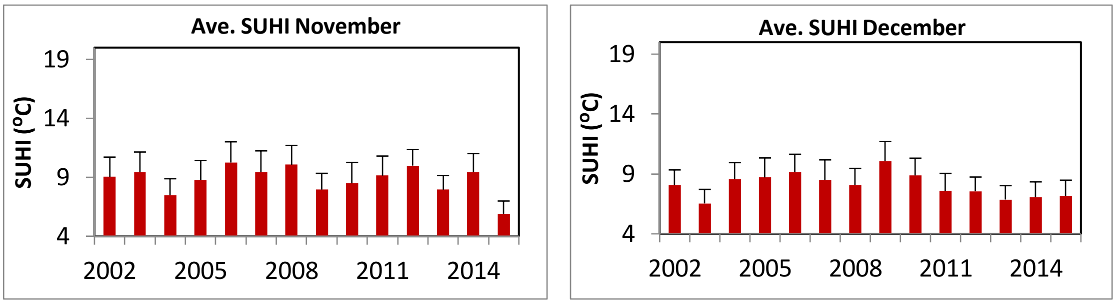

Figure 4.16: The monthly averages of Baghdad's SUHI derived from MODIS data over the period (2003-2015). Only significant trend lines are shown.

4.3.3 LST and land cover

The correlation between land cover types and LST is evident in the literature. Aminipouri and Knudby (2014) found a strong negative relationship (R^2= 0.834) between mean LST and NDVI values, suggesting that vegetation can effectively reduce the LST. Wang et al. (2015) asserts that to determine effective mitigation and adaptation strategies, the hotspots should be more analysed with land surface composition. The land cover composition refers to the variety and relative abundance of patch types within the landscape, typically quantified using the proportions of different land cover types (Du et al., 2016b). Accordingly, the land cover types were set to be the main contributors (predictors) to SUHI intensity.

Table 4.1 gives the results of the highly significant models ($p < 0.01$) where the LST was the dependant variable and land cover indices were the predictors. Most of the vegetation indices (NDVI, EVI, SAVI and MSAVI) seem to have clear significant negative correlation with LST for Baghdad (Table 4.1). Furthermore, NDMI has a noticeable negative correlation with LST. Both of NBR and NBR2 indices have negative correlation with LST. NDVI is a good indicator of vegetation activity derived from the infrared and near-infrared bands of remote sensing imagery (Li et al., 2016). So, higher NDVI values refer to denser presence of vegetation which has lower LST compared to soil and built-up lands. Similarly, the other vegetation indices (EVI, SAVI & MSAVI) indicate the intensity of greenness; however, they are derived to overcome the weaknesses in the NDVI. NDMI index contrasts the near-infrared index (NDVI), which is sensitive to the reflectance of shortwave-infrared to identify the moisture content of an object (Duran, 2015). Duran (2015) concluded that NDMI values higher than 0.1 are symbolised as high humidity level, and vice versa.

NBR and NBR2 have been found to be highly correlated with field estimates of burn severity which is the degree of environmental change caused by fire, and consequently with organic soils (Epting et al., 2005). Therefore, the benefit of using NBR and NBR2 is to investigate the presence of soils since the other indices only give information about the vegetation and moisture (water). This would help identifying the impervious surfaces when all the indices have low values which means that pixel might be impervious area. All the derived land cover indices correlated negatively with LST, with different degrees of significance based on the nature of the index. Thus, low SUHI intensity is associated with more vegetation and moisture during the day. And high SUHI intensity is associated with more soil lands and built-up areas. This explains the high SUHI of Baghdad's barren and built-up areas compared to the vegetation and water lands. Unfortunately, there are no high-level products using Landsat database to derive LST images and land cover indices at night-time for the three cities.

Table 4.1: Correlation between LST and land cover indices of Baghdad city. Derived from Landsat high level products between 2000 and 2015.

Date	Pearson correlation coefficients							Regression equations	R Square
	NDVI	EVI	SAVI	MSAVI	NDMI	NBR	NBR2		
8 September 2000	0	0	0	-0.57	-0.72	0	-0.58	37.9-36.2NDMI-6.1NBR2+16.2MSAVI	0.53
1 October 2000	0	0	0	-0.57	-0.70	0	-0.53	30.4-28.3NDMI+7.6NBR2+5.6MSAVI	0.52
2 October 2000	0	0	-0.60	0	-0.72	0	0	32.2+6.8SAVI-28.2NDMI	0.52
25 October 2000	0	-0.50	0	0	-0.62	0	0	25.4-17.6NDMI+5.2EVI	0.40
8 July 2001	0	0	0	0	-0.67	0	-0.56	44.2-25.1NDMI-3.8NBR2	0.45
6 April 2002	-0.56	0	0	0	-0.72	0	0	26.8+6.5NDVI-29.3NDMI	0.54
22 April 2002	0	0	0	-0.62	-0.72	0	-0.60	26.6-18.1NDMI+7.7NBR2-6.1MSAVI	0.53
15 October 2002	0	0	0	-0.49	-0.54	0	-0.71	30.8+8.4NDMI-38.4NBR2+12.9MSAVI	0.54
8 March 2003	-0.39	0	0	0	-0.57	0	0	22.3+4.1NDVI-19.5NDMI	0.34
2 April 2003	-.055	0	0	0	.060	0	0	24.2-7.6NDVI+8.4NDMI	.019
14 June 2006	-0.31	0	0	0	-0.74	0	-0.55	38.2+9.4NDVI-45.6NDMI-22.1NBR2	0.62
14 July 2006	-0.53	0	0	0	-0.67	0	-0.56	39.9+15.1NDVI-30.7NDMI-15.5NBR2	0.49
22 March 2014	0	0	0	0	-0.70	0	-0.40	26.4-13.8NDMI+5.5NBR2	0.51
20 May 2015	-0.38	0	0	0	-0.65	0	-0.31	37.7+7.4NDVI-58.7NDMI+31.4NBR2	0.57
21 May 2015	0	0	0	-0.40	-0.70	0	0	40.6-57.6NDMI+23.7MSAVI	0.50
13 November 2015	0	0	0	0	-0.59	-0.53	0	19.9-8.2NDMI+1.6NBR	0.36
20 November 2015	0	0	0	0	-0.48	-0.40	0	19.7-13.1NDMI+4.2NBR	0.26

4.4. London SUHI

London has 32 boroughs subdivided into electoral wards with a status similar to metropolitan districts, and also the City of London, which is a City Corporation and has a number of additional roles (ONS, 2016). The River Thames flows across Greater London, which is the major river system flowing through southern England, and supplies about two thirds of London's water (Jin et al., 2012). The catchment of the River Thames is densely populated and highly vulnerable to changes in climate, land use and population, and the river basin drains approximately 10,000 km^2 (Jin et al., 2012). London has eight Royal Parks covering over 5,000 acres (20.23 km^2) of historic parkland, which provide green spaces right in the heart of the capital (RPF, 2016). The UK summer climate is expected to increase by 2.7 ºC by the 2050s (central estimate) in London based on The UKCP09 Climate Projections (Virk et al., 2015). While, in the sustainable development of buildings, summertime overheating is increasingly being recognised as a major design issue, Virk et al. (2015) assert. London's climate is temperate with an average annual temperature of 11.1 °C, and 621 mm rainfall per year. February is the driest month with

39 mm of rainfall, whereas, November has the greatest amount of precipitation with an average of 61 mm rainfall (Climate-Data, 2016). July is the warmest month with an average temperature of 18.7 °C, while, January has the lowest average temperature of 4.9 °C per the year (Climate-Data, 2016).

4.4.1 SUHI spatial change

The SUHI distribution of London in Figure 4.17 shows the daytime spatial change of temperature differences. The high daytime SUHI can be clearly seen in the heart of the city where the built-up areas are dominant, with an intensity of SUHI reaching to 24.2 ºC on the 27th of May 2015 over the urban fabric. The land cover was shown earlier in Figure 4.3. The water areas have the lowest SUHI, so, the River Thames is recognised on most of the maps in Figure 4.17 with its low SUHI intensity. Furthermore, the vegetated areas and bare lands have moderate SUHI intensity, with low intensity for high trees. A study by Zhang (2015) found that in central London areas the high SUHI decreases towards the surrounding areas. On the other hand, the water areas have the highest SUHI during the night-time, particularly, in the cold months as shown in Figure 4.18. The night-time images reveal the same SUHI distribution of daytime images decreasing towards the surrounding areas, except for water areas at cold nights. This introduces a new type of UHI, when the water areas record the highest LST. The water areas had a SUHI reaching to 15.5 ºC on the 19th of October 2007 (Figure 4.18). In this case, the heat island belongs to water, and can be called Water Urban Heat Island (WUHI). WUHI seems to be beneficial in terms of energy consumption as opposed to SUHI and CUHI. Because it appears in the cold nights when the average temperatures are low and the indoors heating loads are high. Which would reduce the electricity demand if that building were affected by the convective heat from the adjacent water areas.

However, during the hot months such as July, the urban areas are still dominant to have the highest SUHI with the water as shown on the image of the 12th of July 2006 (Figure 4.18). The SUHI intensity for built-up and water areas ranged between 8 - 11.2 ºC on the 12th of July 2006. Zhang (2015) detected an urban warming in London of up to 7.34 °C for the average of 39 cloudless nights using thermal satellite images. However, Zhang (2015) study did not consider the impact of water bodies, so, the finding only referred to the urbanised areas. Also, it did not account for the diurnal and seasonal variation of SUHI. The high temperature of water bodies is a concerning issue, since it exerts major effects on biological activities and water chemistry. USGS (2016e) explains that temperature governs the kinds of organisms that can live in water, higher temperature increases the rate of chemical reactions, and it is related to the dissolved-oxygen concentration in water. Accordingly, the temperature of the River Thames should be monitored in the cold nights, as when the temperature changes either by a natural event or by a human-induced event, there could be impact on the aquatic organisms. Also, the same thing for Baghdad as the Tigris River showed higher temperature in cold nights.

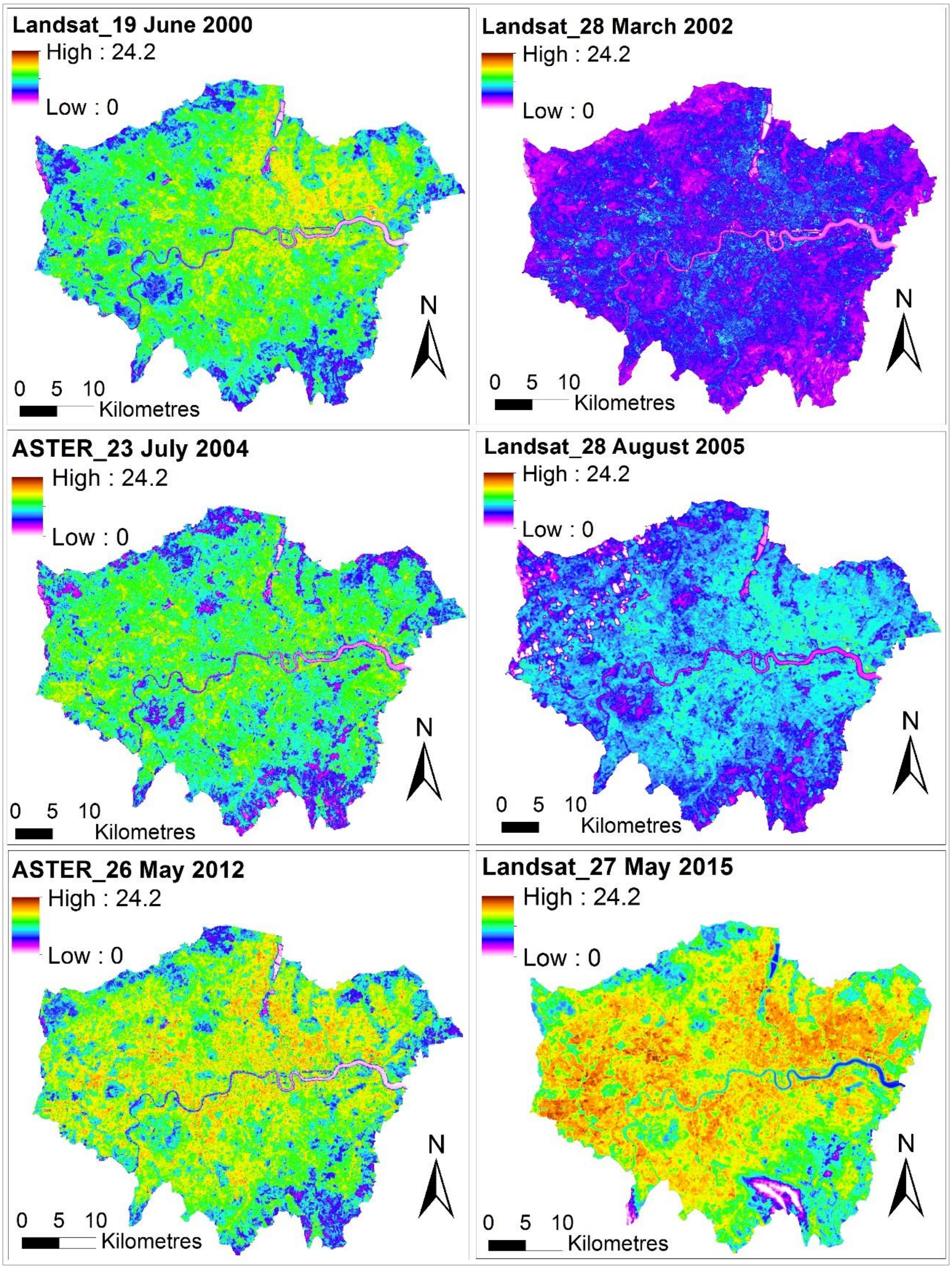

Figure 4.17: London's daytime SUHI spatial distribution using Landsat and ASTER images (ºC). Derived from the thermal bands of the satellite images between 2000 and 2015.

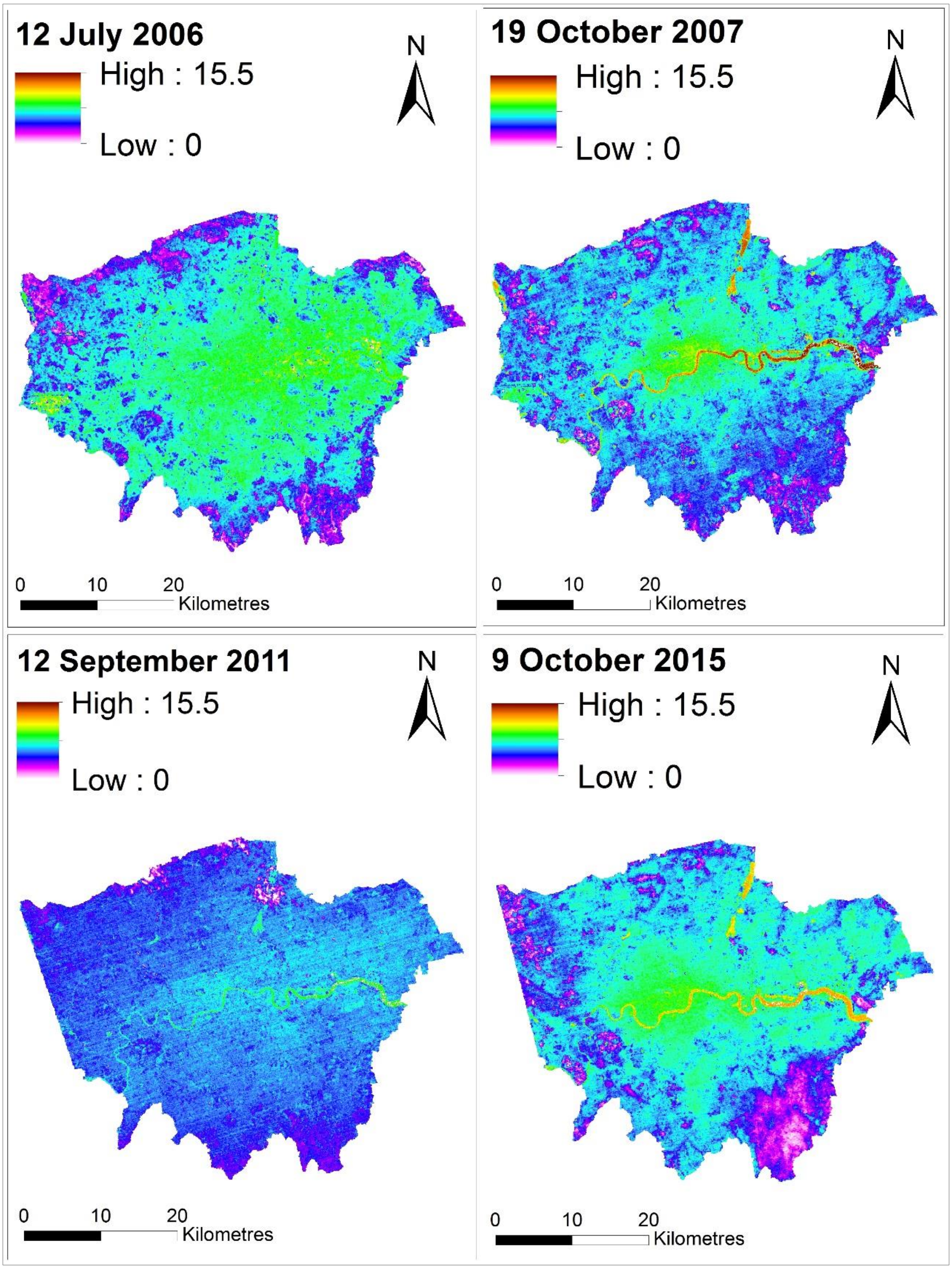

Figure 4.18: London's night-time SUHI spatial distribution using ASTER images (ºC). Derived from the thermal bands of the satellite images between 2006 and 2015.

MODIS daytime and night-time findings give slightly different spatial patterns to those of ASTER and Landsat as shown in Figures 4.19 & 4.20. So, the SUHI intensity is concentrated in the London City and its surroundings to reach 13.7 °C in 2013 as shown in Figure 4.19. Although, there are only 9,000 residents living within the Square Mile of the City of London, however, over 300,000 people work in the City and almost 30,000 go there to study every day (City of London Corporation, 2007). Iamarino et al. (2012) computed the annual mean anthropogenic heat flux for Greater London, they found that the highest peaks in the central activities zone (CAZ) associated with extensive industry services. The anthropogenic heat flux decreases towards the outskirts of the city, with the domination of emissions from the domestic sector and road traffic. Therefore, the city has the highest SUHI in the daytime comparing with other urban areas. The founder of the UHI Howard (2007), concluded that the mean air temperature of London, is approximately 9.17 °C (48.50 °F), however, in the denser parts of the metropolis, it is raised to 10.28 °C (50.50 °F) by the effect of the population and fires. Also, Chandler (1965) found an intense heat island in the City of London by normal daytime standards. His results exhibited that temperatures in central London during the spring reached a minimum of 11 °C, whereas, in the suburbs they dropped to 5 °C, under clear skies and light winds.

In Figure 4.20, the MODIS night-time SUHI distribution resembles the findings using ASTER images in Figure 4.18, where the water bodies have high LST. The SUHI reached 5.32 °C in 2011 over water to stretch to the adjacent built-up areas, and decreases gradually when moving to outer London. Unlike Baghdad, London does not invert the SUHI spatial distribution between the daytime and night-time. Figure 4.21 gives the averages of daytime and night-time SUHI for the period (2003 - 2015) for Greater London Boroughs. The boundaries of London Boroughs were acquired from the Digimap EDINA which is the Jisc-designated centre for digital expertise and online service delivery at the University of Edinburgh (EDINA, 2016). The average daytime SUHI reached to 12.6 °C for the City of London, while, the night-time SUHI average peaked over the River Thames and adjacent areas by about 5.06 °C. By looking at the boroughs with high night-time SUHI adjacent to the River Thames, they have been found to have only between 0.1 - 17.6 % of domestic gardens (Greater London.Authority, 2016). With the lowest percentage of domestic gardens is for the City of London by 0.1 % out of the total land use. Also, the City of London has the second highest percentage of roads by about 23.8 % just after Westminster which has the highest percentage by 23.9 % out of the total land use (Greater London.Authority, 2016). It reflects the amount of anthropogenic heat flux emitted by the vehicle, as well as metabolic heat. Boroughs like Tower Hamlets, Newham, Hammersmith & Fulham, and Kensington & Chelsea have low percentage of domestic gardens and consequently low greenness compared to other boroughs at the outskirt of London (Greater London.Authority, 2016). Accordingly, the high intensity SUHI is associated with low percentage of green spaces. Furthermore, the River Thames does not appear to have mitigation role on the SUHI formation.

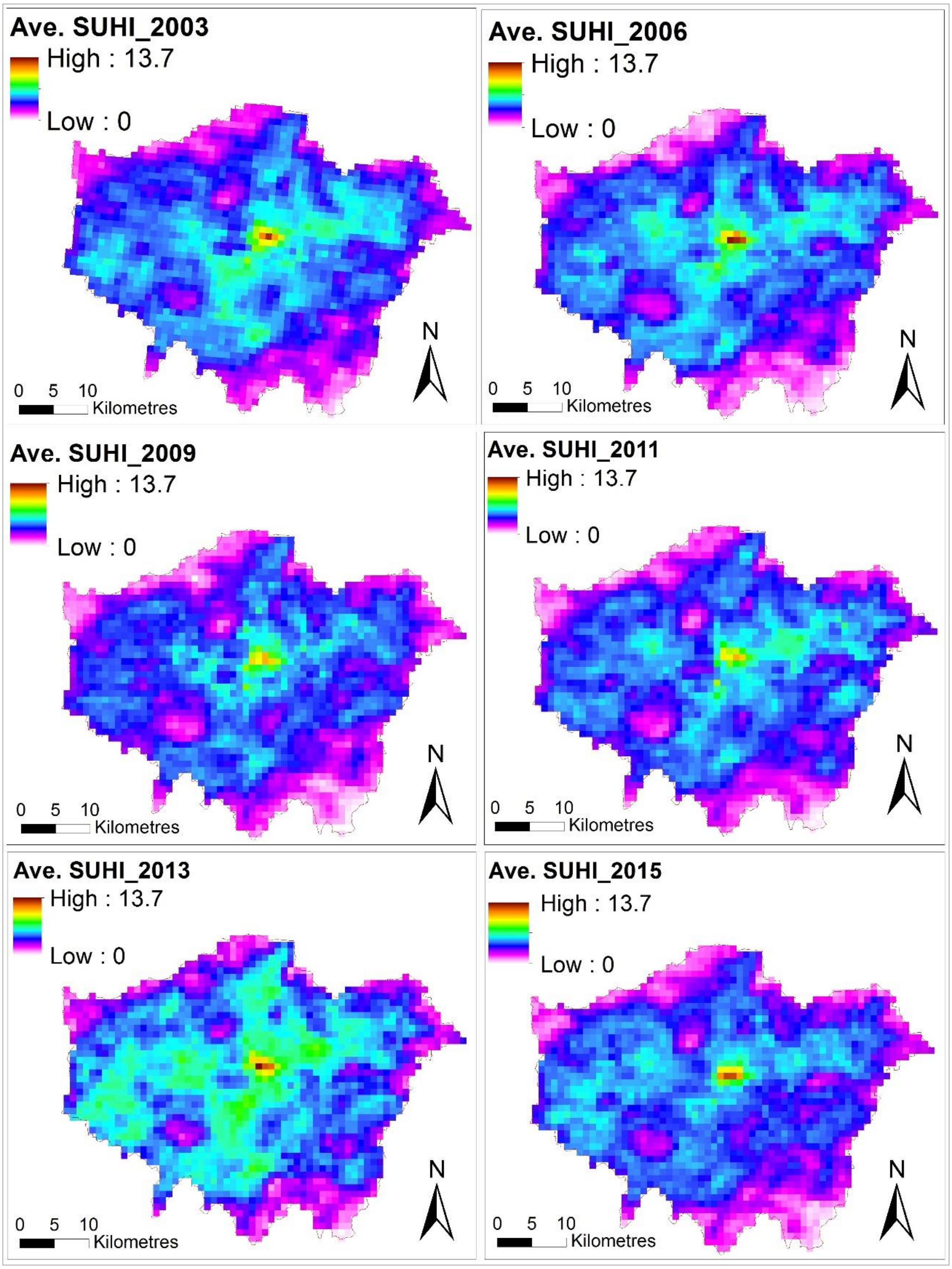

Figure 4.19: London's daytime SUHI spatial distribution using MODIS images (ºC). Derived from the thermal bands of the satellite images between 2003 and 2015.

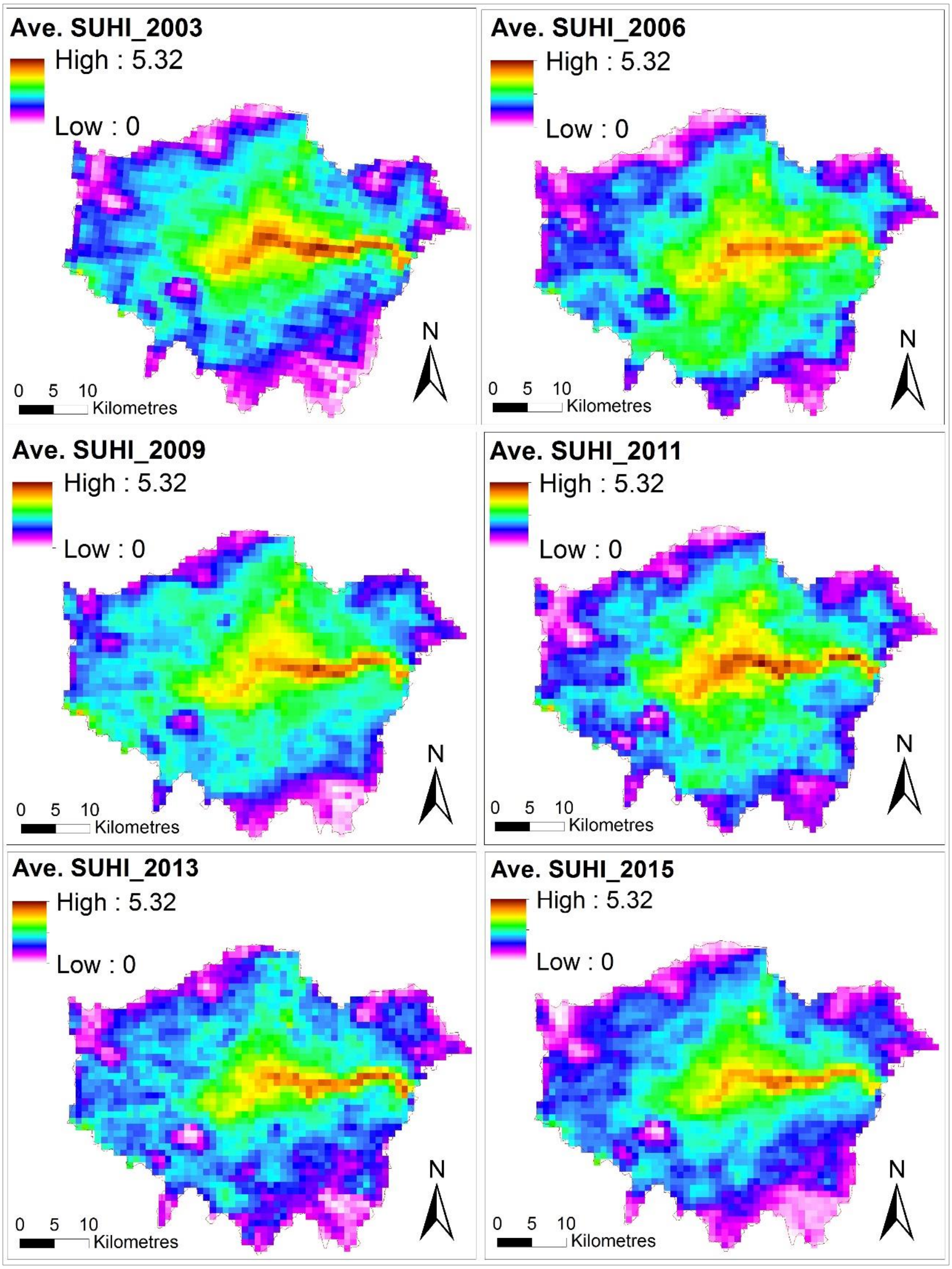

Figure 4.20 London's night-time SUHI spatial distribution using MODIS images (ºC). Derived from the thermal bands of the satellite images between 2003 and 2015.

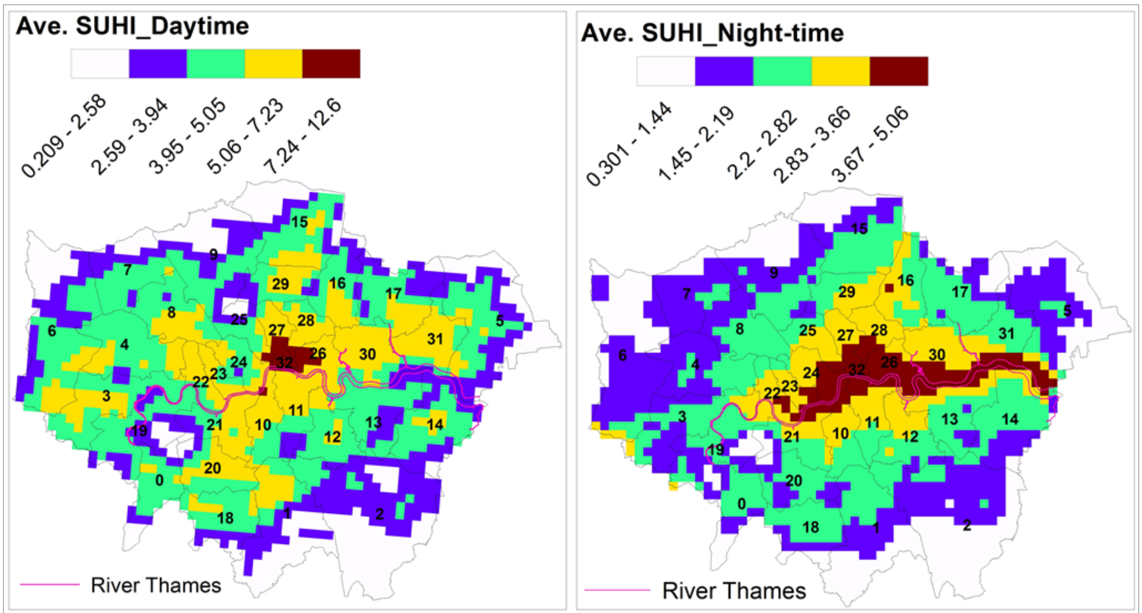

0	Kingston upon Thames	9	Barnet	18	Sutton	27	Islington
1	Croydon	10	Lambeth	19	Richmond upon Thames	28	Hackney
2	Bromley	11	Southwark	20	Merton	29	Haringey
3	Hounslow	12	Lewisham	21	Wandsworth	30	Newham
4	Ealing	13	Greenwich	22	Hammersmith and Fulham	31	Barking and Dagenham
5	Havering	14	Bexley	23	Kensington and Chelsea	32	The City of London
6	Hillingdon	15	Enfield	24	City of Westminster		
7	Harrow	16	Waltham Forest	25	Camden		
8	Brent	17	Redbridge	26	Tower Hamlets		

Figure 4.21: Daytime & night-time average SUHI of London's boroughs over the period (2003-2015) using MODIS images (°C). Different SUHI scales are used for daytime and night-time.

4.4.2 SUHI temporal change

The average diurnal LST of Greater London did not show significant change from 2003 to 2015 as shown in Figure 4.22, the average diurnal LST is 11.72 °C with 1.76 SD. The averages of diurnal LST, daytime LST, and night-time LST have very low R^2 (< 0.1). The average of daytime LST is 17.46 °C with 2.13 SD, and the average of night-time LST is 6.02 °C with 1.39 SD. The averages of NLST range between 0.41 - 0.48 for the diurnal, daytime and night-time NLST. The NLST showed similar trends to the LST with some difference in the value of R-square (Figure 4.22). Similarly, the average diurnal SUHI did not change over the study period, and its average magnitude was about 11.29 °C with 5.21 SD. The reason of the steady average SUHI is that the slight increase in the average daytime SUHI was equalised by the slight decrease in the average of night-time SUHI as shown in Figure 4.23. The average of daytime SUHI is 13.52 °C with 5.90 SD, and the average of night-time SUHI is 9.07 °C with 3.01 SD. Accordingly, the overall temporal change of LST and SUHI do not show significant change; unlike Baghdad, which experienced an increase in LST and decrease in SUHI averages.

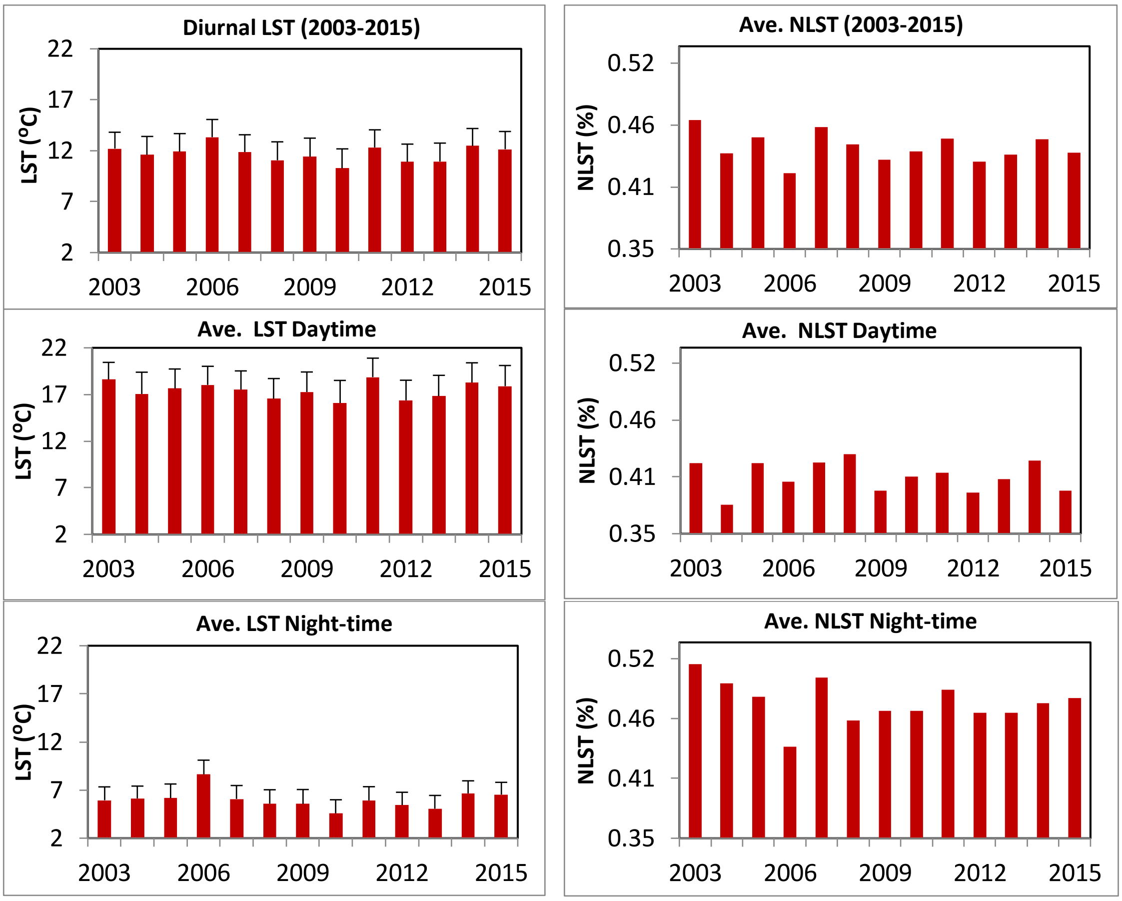

Figure 4.22: The temporal change of the diurnal, daytime & nigh-time LST in London derived from MODIS data over the period (2003-2015), left (Normal) & right (Normalised).

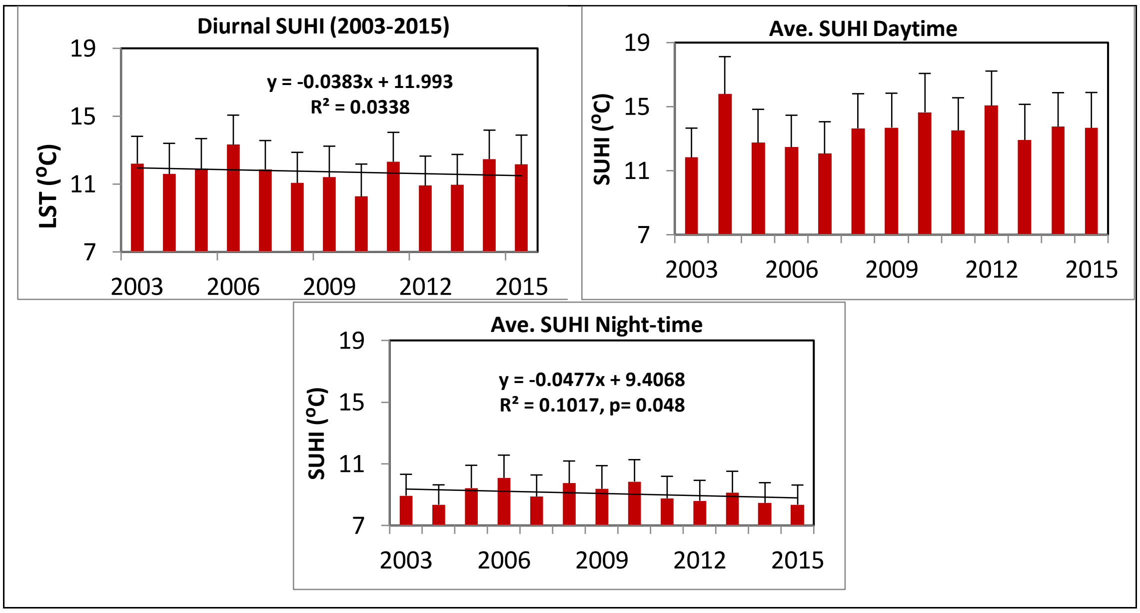

Figure 4.23: The temporal change of the diurnal, daytime & night-time average SUHI in London derived from MODIS data over the period (2003-2015). Only significant trend lines are shown.

UK has four seasons in the year just like Iraq, therefore, the incoming four figures include the months of each season. Figure 4.24 contains the winter months which do not show obvious increase in the trends for the study's period, as most of R-squares are low (< 0.1). The LST averages for the winter months range between 3.14 – 4.56 ºC, and the NLST ranges between 0.41 – 0.44. There is a slight difference between the trends of LST and NLST for the winter months, in particular for December (see Figure 4.24). Furthermore, Figure 4.25 includes the spring months which reveal a very small decrease in the trends over the study's period, except for the NLST in March. The LST averages for the spring months range between 9.20 – 15.55 ºC, and the NLST ranges between 0.44 – 0.46. There are some differences between the trends of LST and NLST for the spring months, in particular for March, as shown in Figure 4.25. March LST averages show weak decrease, while, they give significant increase for the NLST. However, the LST has the same trend as the NLS for both of April and May.

On the other hand, Figure 4.26 contains the summer months which show low decreases in the trends for the study's period. The LST averages for the summer months range between 19.17 – 20.60 ºC, and the NLST ranges between 0.43 – 0.45. There are no noticeable differences between the trends of LST and NLST. Figure 4.27 contains the autumn months which show slight increases in the trends for the study's period. The LST averages for the autumn months range between 6.55 – 15.53 ºC, and the NLST ranges between 0.42 – 0.47. There is no noticeable difference between the trends of the LST and NLST for the autumn months (see Figure 4.27). All in all, the spring and summer showed a slight decrease in LST, whereas, the autumn and winter reflected a bit of increase. The NLST for some months gave opposite trends to the LST, especially, for December and March.

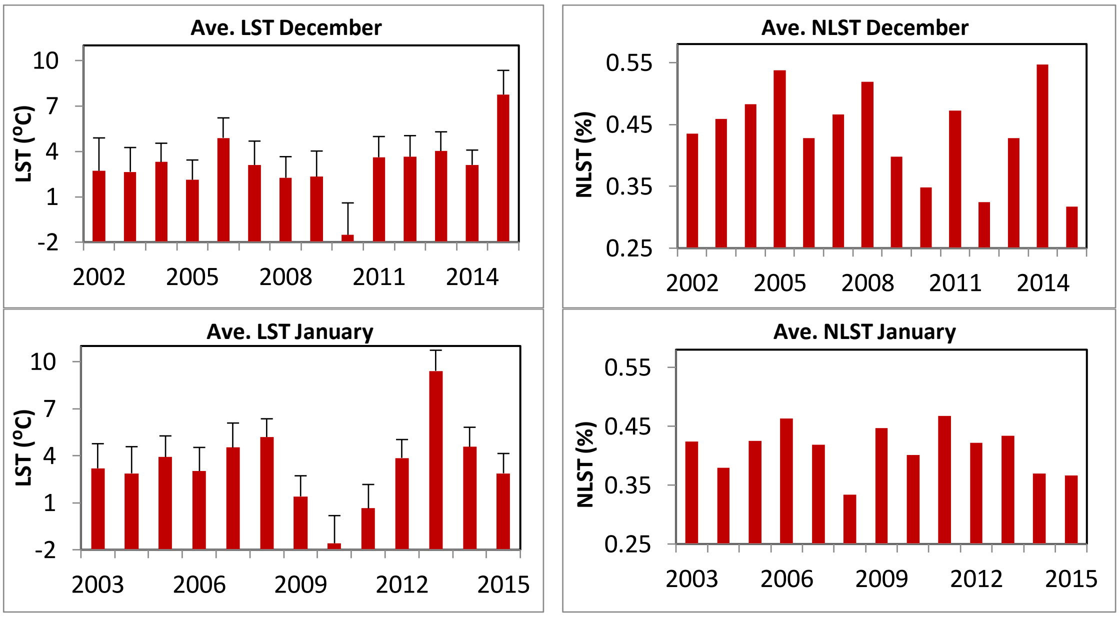

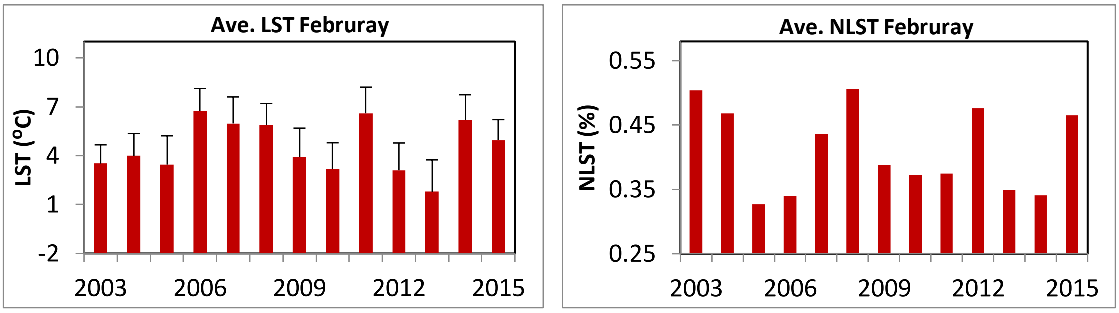

Figure 4.24: The temporal change of the winter's months LST and NLST in London derived from MODIS data, left (Normal) & right (Normalised) between 2002 and 2015.

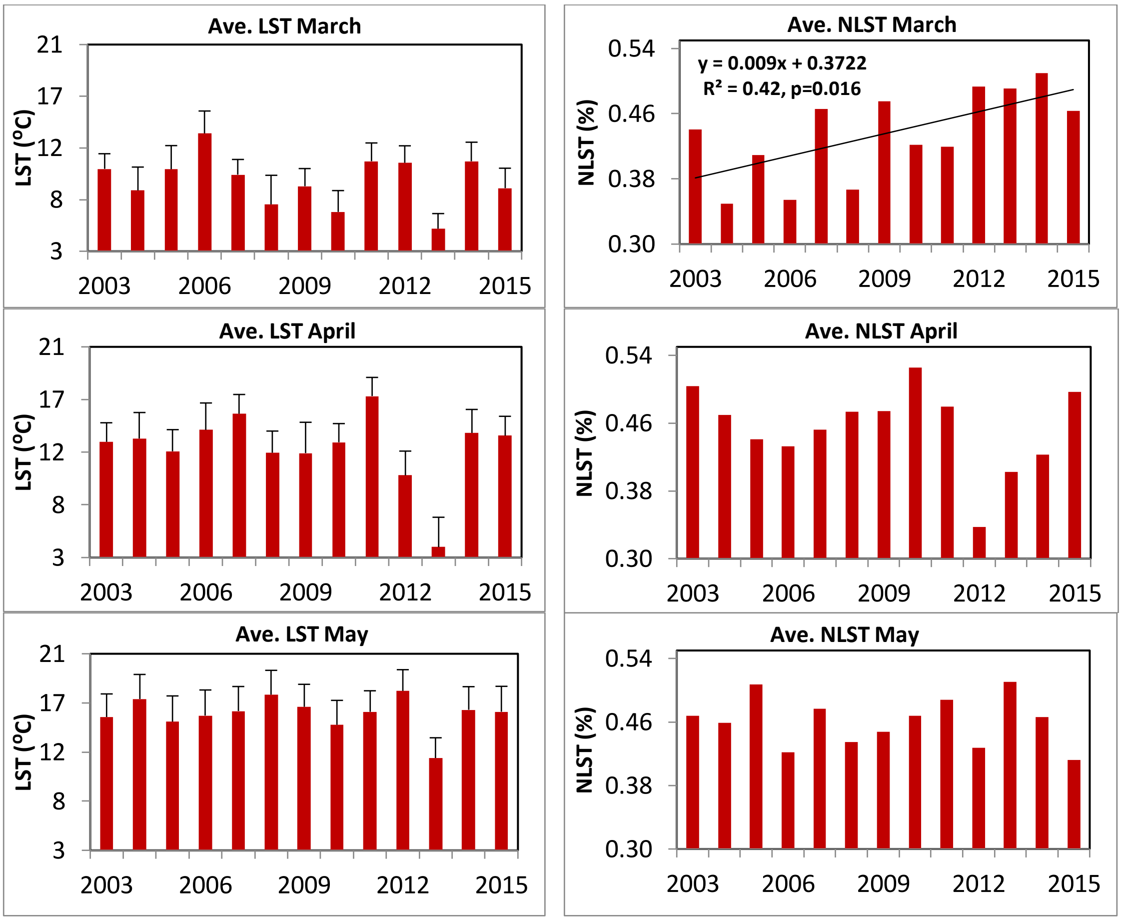

Figure 4.25: The temporal change of the spring's months LST and NLST in London derived from MODIS data, left (Normal) & right (Normalised) between 2003 and 2015. Only significant trend lines are shown.

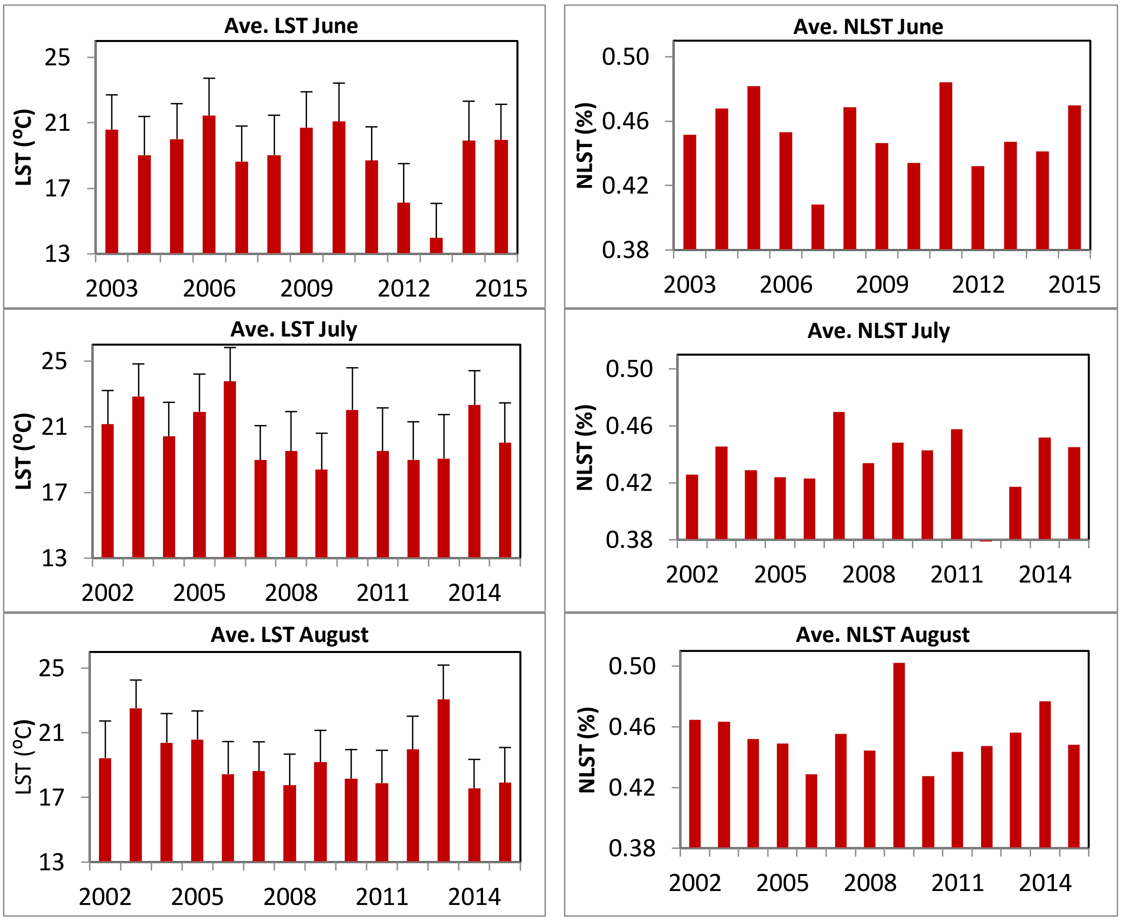

Figure 4.26: The temporal change of the summer's months LST and NLST in London derived from MODIS data, left (Normal) & right (Normalised) between 2002 and 2015.

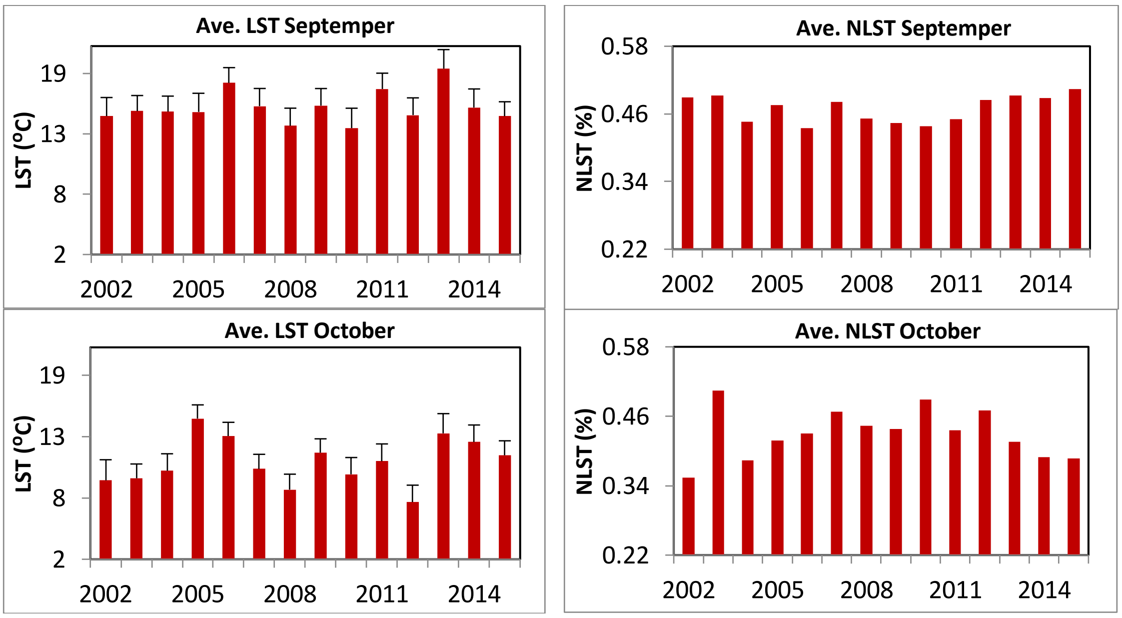

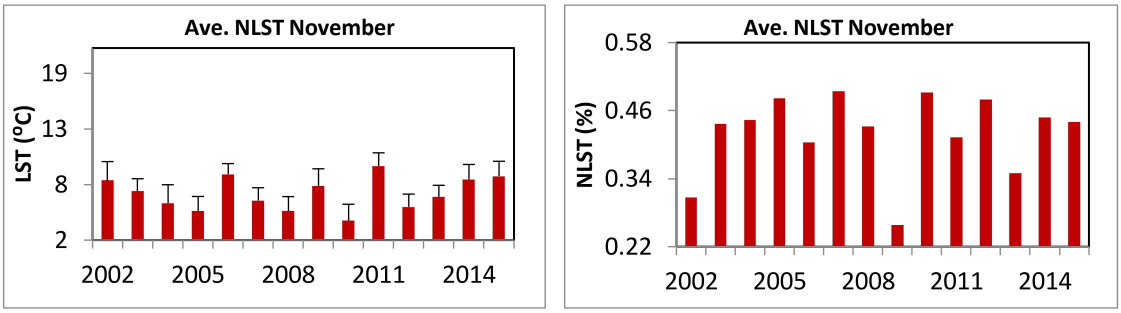

Figure 4.27: The temporal change of the autumn's months LST and NLST in London derived from MODIS data, left (Normal) & right (Normalised) between 2002 and 2014.

The monthly averages of SUHI for the whole study period range between 9.29 – 13.99 ºC as detailed in Figure 4.28. The average SUHI intensity fluctuated from about 9.29 ºC with 3.49 SD for December to around 13.99 ºC with 6.19 SD for July. Months from June to September showed weak increase in the trends with R^2 less than 0.16. These months (June – September) have higher temperatures compared to the rest in the year, as their average LST ranges between 15.53 – 20.60 ºC. Lee (1992) tested the assumption that population expansion is usually accompanied by increases in the impervious surfaces such as housing, roads and public transport. He examined the claim in the literature that most of the cities experienced long-term increases in UHI intensity; cities also have been subjected to large population growth. His study area was London over the period 1962 to 1988 when the population has fallen from just over 8 million to about 6.8 million. The study results showed that the daytime UHI have decreased over time and night-time UHI have increased. However, since then the population of London has grown to reach approximately 8.66 million in 2015 which is just over its peak in 1939 when it was 8.62 million (Aldridge et al., 2015). This might explain the slight increase of daytime SUHI and the weak decrease in night-time SUHI in this study. Nevertheless, this is tested against the land cover types using different indices in the next section.

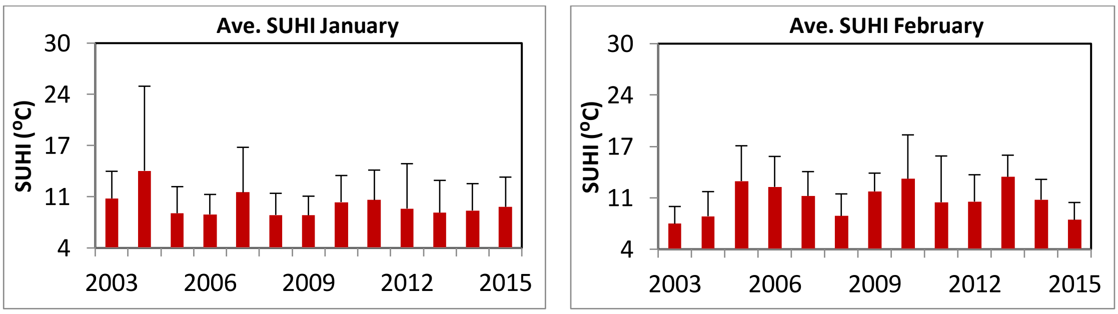

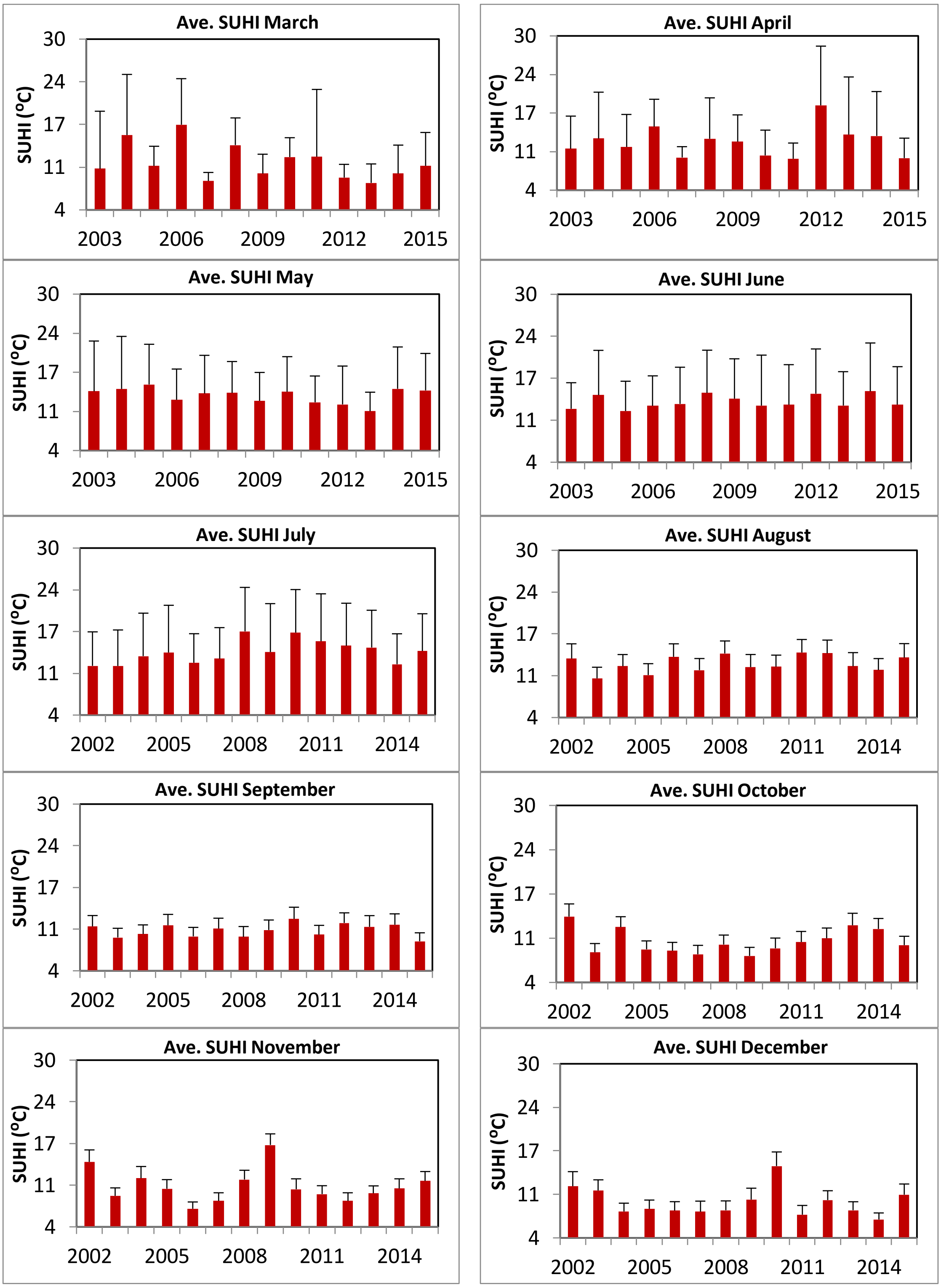

Figure 4.28: The monthly averages of London's SUHI derived from MODIS data over the period (2003-2015).

4.4.3 LST and land cover

Table 4.2 gives the regression results of the very significant models ($p < 0.01$), where the LST is the dependant variable and land cover indices are the explanatory variables. The correlations reveal the importance of vegetation in reducing the LST. So, vegetation indices (especially NDVI & MSAVI) played a major role to relieve the LST with up to 0.81 R^2 for NDVI on the 19 of June 2000. Furthermore, NDMI contributed negatively to most of the LST models in Table 4.2 with up to 0.82 R^2. This reflects the importance of water bodies to reduce the LST; however, the River Thames did not play a significant role to reduce the spatial variability of SUHI. Hence, a specific land feature might have different impact on the LST and SUHI. Since the SUHI is the difference in temperature between the pixel LST value and the minimum LST within the scene. So, the land cover feature might have influences on the local area and the area of the minimum LST value that do not lead to SUHI reduction. Also, NBR2 gave significant negative correlation with nearly 70% of the models.

The Mayor of London published a report on London's UHI Authority, and it proved the association between high surface temperatures and high density continuously developed areas across London. The report results showed that the relatively cool areas to the southwest of the core of high surface temperatures coincide with the large open and green spaces of Richmond Park (Greater London Authority, 2006). Furthermore, an ARUP (2016) report determined that London's land cover has not been altered significantly from 2000 to 2015. Since, the increase of green areas, agricultural land and water bodies during this period was less than 2%, and these areas form around 31% of London's surface. The report also investigated the effect of green spaces and water bodies on LST in the heatwave events. The results emphasised the importance of green spaces and water bodies in a city to cool the high LST areas during heatwave events in a summer day (ARUP, 2016). Consequently, this study findings agree with ARUP (2016) report conclusions about the role of green spaces and water bodies to minimise the effect of SUHI. However, this reduction exists in all high temperature days not only during the heatwaves. Therefore, the high significant models ($R^2 > 0.3$) coincided with summer months to reach 0.7 R^2 on the 19 of June 2000 as described in Table 4.2. SAVI and NBR indices did not show any significant regression correlation with LST.

Table 4.2: Correlation between LST and land cover indices of London city. Derived from Landsat high level products between 2000 and 2015.

Date	Pearson correlation coefficients							Regression equations	R Square
	NDVI	EVI	SAVI	MSAVI	NDMI	NBR	NBR2		
7 April 2000	-0.34	-0.31	0	0	-0.43	0	-0.45	16.6+1.4NDVI-3.3NDMI+5.9EVI-17.1NBR2	0.26
19 June 2000	-0.81	0	0	0	-0.82	0	0	36.5-5.7NDVI-11NDMI	0.70
12 May 2001	0	0	0	0	-0.71	0	-0.76	30.4-1.4NDMI-19.2NBR2	0.58
28 March 2002	-0.58	0	0	0	-0.52	0	-0.61	15.7-1.04NDVI+0.7NDMI-7.9NBR2	0.37
16 April 2003	0	0	0	-0.39	-0.52	0	-0.50	27.2-8NDMI-16.5NBR2+9.8MSAVI	0.34
24 September 2003	-0.47	0	0	0	-0.58	0	-0.48	16.7+1.3NDVI-6.6NDMI-5.7NBR2	0.37
28 August 2005	0	-0.40	0	0	-0.38	0	-0.45	23-1.9NDMI-10.3NBR2+0.9EVI	0.21
10 May 2006	-0.73	0	0	0	-0.76	0	0	23.5-2.3NDVI-11NDMI	0.59
11 May 2006	-0.42	0	0	0	-0.55	0	0	23.6+7.8NDVI-30.4NDMI	0.33
12 June 2006	0	0	0	-0.73	0	0	-0.74	31.8-10NBR-4.4MSAVI	0.57
2 November 2006	-0.43	0	0	-0.26	-0.43	0	0	7.6-1.3NDVI-3.1NDMI+2.51MSAVI	0.32
20 September 2008	0	0	0	-0.57	-0.69	0	-0.65	19.7-7.9NDMI+0.61MSAVI	0.50
29 September 2011	0	0	0	-0.32	-0.63	0	-0.47	24.5+0.53NDVI-9.72NDMI+2.1MSAVI	0.43
30 September 2011	0	0	0	-0.37	-0.57	0	-0.48	23.7-5.4NDMI-4.3NBR2+3MSAVI	0.34
11 November 2012	-0.21	0	0	-0.1	-0.24	0	-0.22	6.9-1.7NDVI-1.9NDMI-2.3NBR2+5.2MSAVI	0.23
18 November 2012	-0.14	0	0	-0.1	-0.19	0	-0.15	5.7-1.3NDVI-2.3NDMI-2NBR2+4.9MSAVI	0.12
20 April 2013	-0.58	0	0	0	-0.43	0	-0.61	21-1.19NDVI+3.3NDMI-15.9NBR2	0.39
8 July 2013	-0.70	0	0	0	-0.78	0	-0.77	29.2+4.2NDVI-8.8NDMI-14.8NBR2	0.65
17 July 2013	-0.58	0	0	0	-0.66	0	-0.64	32.4+5.7NDVI-12.3NDMI-18.3NBR2	0.48
1 February 2014	0.1	0	0	0.01	-0.1	0	0.1	2.2+0.9NDVI-1.9NDMI+2.7NBR2-1.1MSAVI	0.1
4 July 2014	-0.28	0	0	0	-0.48	0	-0.38	24.5+12.9NDVI-20.9NDMI-13.6NBR2	0.33
9 April 2015	-0.51	0	0	-0.44	-0.48	0	-0.56	20.4-3.6NDVI-0.1NDMI-19.9NBR2+10.1MSAVI	0.37
27 May 2015	-0.64	0	0	0	-0.73	0	0	24.9+4NDVI-21.8NDMI	0.53
2 October 2015	0	0	0	-0.55	-0.67	0	0	16.7-5.5NDMI+0.1MSAVI	0.44

4.5. Birmingham SUHI

Birmingham is the geographical heart of England, and it is the UK's second largest student city (The Complete University Guide, 2016). Birmingham has a various land use types such as urban fabric, industrial areas, and large green spaces as shown earlier in Figure 4.4. The urban fabric concentrates in the middle of the city and stretches towards the periphery in all directions, the industrial areas mainly in the east, with some parks around the city (Azevedo et al., 2016b). The climate is warm and temperate, and the average annual air temperature is about 9.2 °C with 705 mm of rainfall (Climate Data, 2016). February is the driest month with 49 mm rainfall, and the greatest 70 mm rainfall happens in December. July has the highest average temperature with 15.7 °C, and the coldest is January with 3.2 °C (Climate Data, 2016). The change of SUHI in time and space is discussed in the incoming sections with its correlation with land cover types.

4.5.1 SUHI spatial change

The daytime SUHI distribution of Birmingham is shown in Figure 4.29, which gives the spatial change of temperature differences using Landsat and ASTER data. Unfortunately, ASTER cloud free images are not available at night-time for Birmingham during the study period. Accordingly, an airborne image acquired in March 2009 was employed. It was supplied by the UK Environment Agency (UK Environemnt Agency, 2014), and has 1 m pixel size and 0.1 ºC temperature accuracy (Figure 4.30). The airborne TABI image was a part of the aerial survey undertaken by the UK OS to capture the thermal losses of urban areas, in particular the buildings. It measures heat loss from rooftops, which have been used to advise local authorities where to target climate change mitigation strategies (UK Environment Agency, 2014). The airborne images were acquired on two missions to cover the entire Birmingham City. Both were at about the midnight, the first one started on the 10th of March 2009 at about 23:10 and ended on the 11th of March 2009 at about 01:27. The second fly started on the 26th of March 2009 at about 22:44 and ended on the 27th of March 2009 at about 00:01. The two missions were undertaken at times close to midnight when the air temperatures ranged between 2- 4 ºC in clear and calm weather (MIDAS, 2015). It seems that the acquisition times were chosen to have similar weather conditions, so the captured temperatures would not be biased. Therefore, the two images that represent the two missions were merged to have one image covers the entire Birmingham City.

The daytime SUHI in Figure 4.29 concentrates in the urban fabric and industrial and commercial units (see land cover map in Figure 4.4), and stretches to the suburbs specifically the north-east ones. The maximum intensity of SUHI reached 22.8 ºC on the 1st of June 2009, and the lowest intensity was on the 19th of January 2015 at 4.5 ºC. On the other hand, the night-time image (Figure 4.30) gives a more detailed spatial SUHI change, as it has much higher spatial resolution (1 m) compared to Landsat and ASTER thermal images. Like Baghdad and London, Birmingham water bodies have the highest temperature with a maximum of 5.6 ºC in cold nights. However, in Birmingham trees seem to have the second highest temperature, which did not clearly appear in the other two cities. The high temperature of water surface enhances evaporation to release large amounts of water vapour (Hughes, 2000). Monteith (1981) explains that when water evaporates from a wet surface to the atmosphere, an equilibrium status tends to happen to compensate the local loss of latent heat by the net supply of heat. The same mechanism applies in the transpiration process when the moisture leaves the leaf, as the water has relatively higher temperature due to interactions and higher storage capacity. It happens particularly during the cold nights where the temperature of other surfaces is low compared to water in ponds and trees. This can be seen clearly in Figure 4.30 when the trees and water areas in Sutton Park have higher temperature than bare lands and grass. The high canopy of the trees traps more energy in the daytime to be released at night-time and enhances the transpiration process.

Moving to the City Centre in Figure 4.30, the streets enclosed by high buildings also have higher temperature, where the sky view factor is low. The streets outside the city showed lower temperature than the ones located inside the city. In this case, the geometry played a major role in inducing the SUHI, not the only the land cover, as built-up areas exhibited lower temperature than grass in some places. The low temperature of built-up areas demonstrates the high insulation of buildings, which means minimum heat loss and high energy saving. The high spatial resolution of the night-time airborne thermal image (Figure 4.30) has enabled this study to highlight unprecedented SUHI patterns (the trees high LST), which urges the crucial need for high spatial resolution thermal images to study the SUHI. The 1 meter spatial resolution appears to be ideal for SUHI studies, because of the high heterogeneity of the urban surfaces and the presence of small width objects such as narrow streets. Zhang and Liang (2012) identify that the different types of urban surface features will greatly impact the brightness temperature. They also determine that different ground objects with the same spectrum still exist. Consequently, monitoring the LST should consider employing multi channels of spectrum with different observation time.

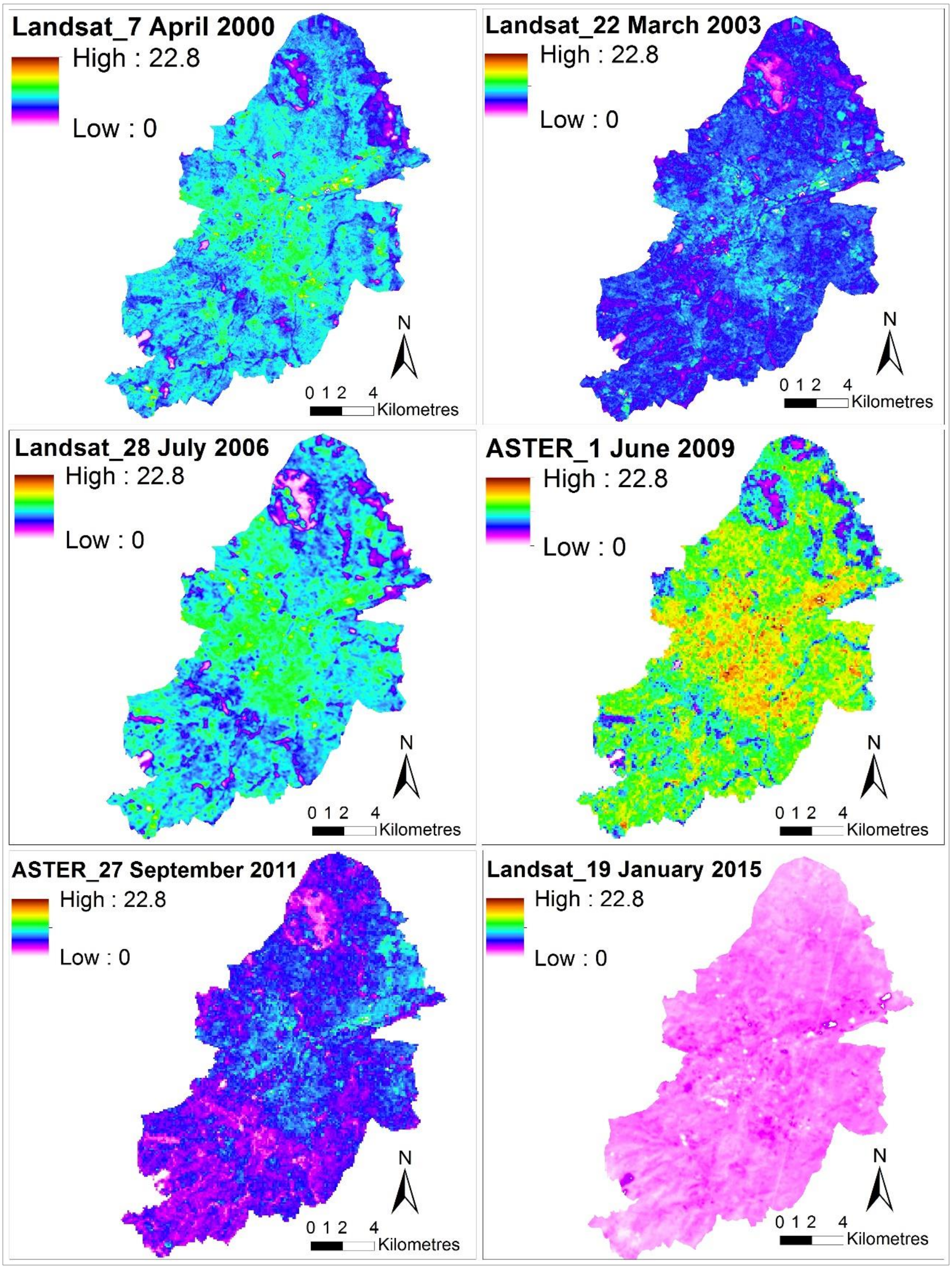

Figure 4.29: Birmingham's daytime SUHI spatial distribution using Landsat and ASTER images (ºC). Derived from the thermal bands of the satellite images acquired between 2000 and 2015.

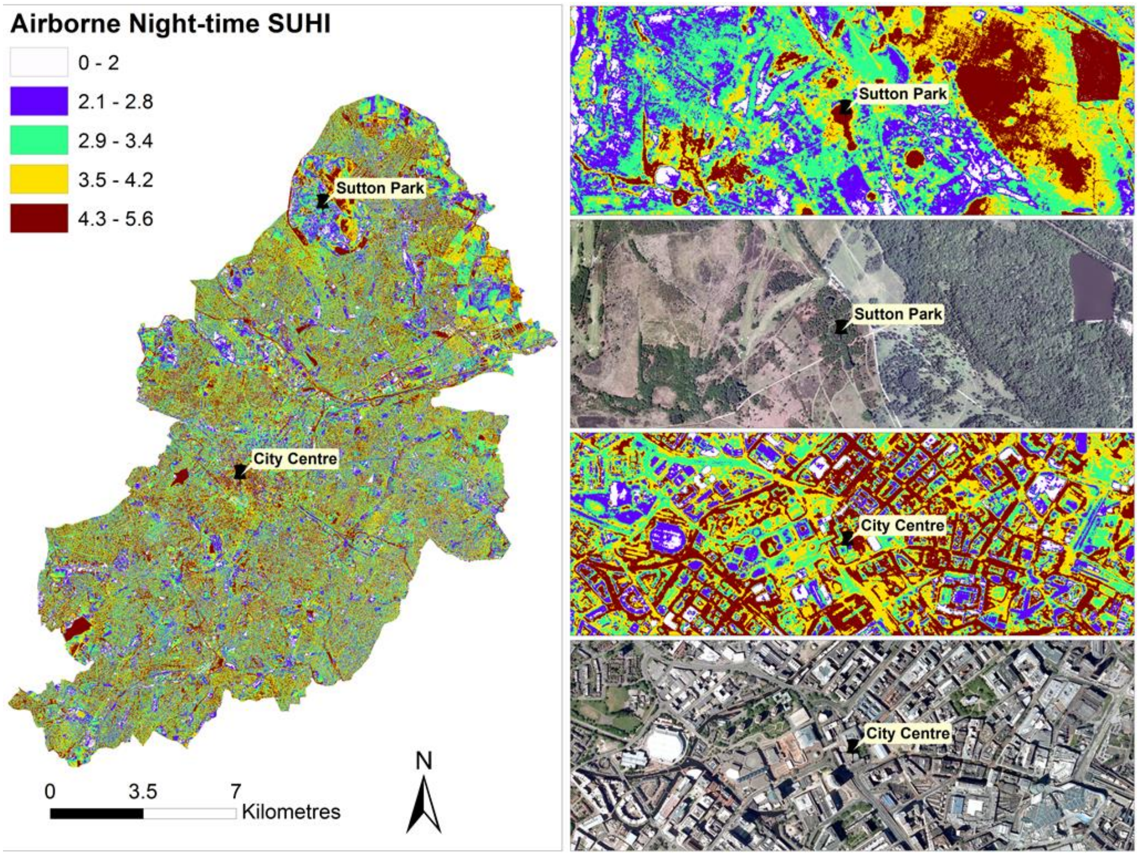

Figure 4.30: Birmingham's night-time SUHI spatial distribution using airborne image (left), City Centre and Sutton Park SUHI distribution and overlaid OS maps (right) (ºC).

On the other hand, MODIS annually averaged SUHI has provided daytime and night-time long-term records. The average maximum daytime SUHI ranged from 19.4 ºC in 2015 to 22.2 ºC in 2009 as shown in Figure 4.31. The City Centre is the core of the maximum daytime SUHI intensity, and the lowest intensity can be seen in Sutton Park. Similarly, the night-time average SUHI peaked at the City Centre to extend to the adjacent suburban's areas (Figure 4.32). The average maximum night-time SUHI ranged from 5.73 ºC in 2003 to 6.79 ºC in 2006. Hence, both of daytime and night-time SUHI peaked at the City Centre, and extended to the surrounding areas. However, the difference is between the magnitudes of the SUHI intensity, as the daytime is much higher than the night-time SUHI. Also, the spatial dimension of the highest intensity SUHI class is different for each time. Azevedo et al. (2016b) found that the average SUHI of Birmingham in 2006 peaked in the City Centre and was significantly lower in the urban green areas. They also indicated that the average daytime SUHI is higher than night-time, because of the solar heating during the daytime. Interestingly, the Sutton Park can be a heat island and cool island at the same time, because it includes dense trees and grass as shown in Figure 4.30. The trees look hot as they trap more radiation compared to the cold grass which has higher SVF. This reflects the importance of the geometrical parameters as the various features of the same land cover (vegetation) might give different thermal behaviour. These patterns cannot be identified using coarse spatial resolution images due to the problem of mixed pixels.

To visualise the averages of SUHI for the whole study period, daytime and night-time SUHI were calculated and overlaid on the wards of Birmingham District. Birmingham is divided into ten parliamentary constituencies, each constituency is divided into four wards (Council, 2003). The digital boundaries of Birmingham's Wards were acquired from Digimap EDINA (EDINA, 2016), and adapted to be consistent with the description of the wards by Birmingham City Council (Council, 2003). Figure 4.33 demonstrates the daytime and night-time average SUHI for the entire study period (2003 – 2015). The maximum average daytime SUHI intensity is 19.9 ºC, and the maximum average night-time SUHI intensity is 5.77 ºC.

There are five common wards that most of their areas recorded the maximum average daytime and night-time SUHI as shown in Figure 4.33. They are Laywood (19), Nechells (3), Aston (34), Sparkbrook (26), and Washwood Heath (4.35). The population of each of these five wards was more than 30000 residents in 2011 (Council, 2011). The major land uses of these wards are as follow: Ladywood (residential), Nechells (residential (west), industrial & commercial (north & east)), Aston (residential (centre & west), industrial & commercial (north & east)), Sparkbrook (residential), and Washwood Heath (industrial & trading estates (north), residential (west & east)) (Axinte, 2015). Accordingly, the high daytime and night-time SUHI intensity presents in the densely populated areas, which is used for residential, industrial, and commercial purposes. On the other hand, the lowest intensity of daytime and night-time SUHI appears in Sutton Park, which works as a cool island towards the urbanised areas. Sutton Park is one of the largest urban parks in Europe, extending over about 9.7 km^2 (Council, 2016). It is located 9.6 Km north of the City Centre, and a site of special scientific interest, as it has open heathland, woodlands, seven lakes, wetlands, marshes, and ancient monuments (Council, 2016). It is evident that large green areas in Birmingham have cooling effects, with a significant temperature gradient extending northwards from the City Centre to Sutton Park (Tomlinson et al., 2013). The temperature decreases through the suburbs and urban green spaces, where the City Centre can be (7 - 8 ºC) hotter than the Sutton Park under heatwave conditions (Tomlinson et al., 2013).

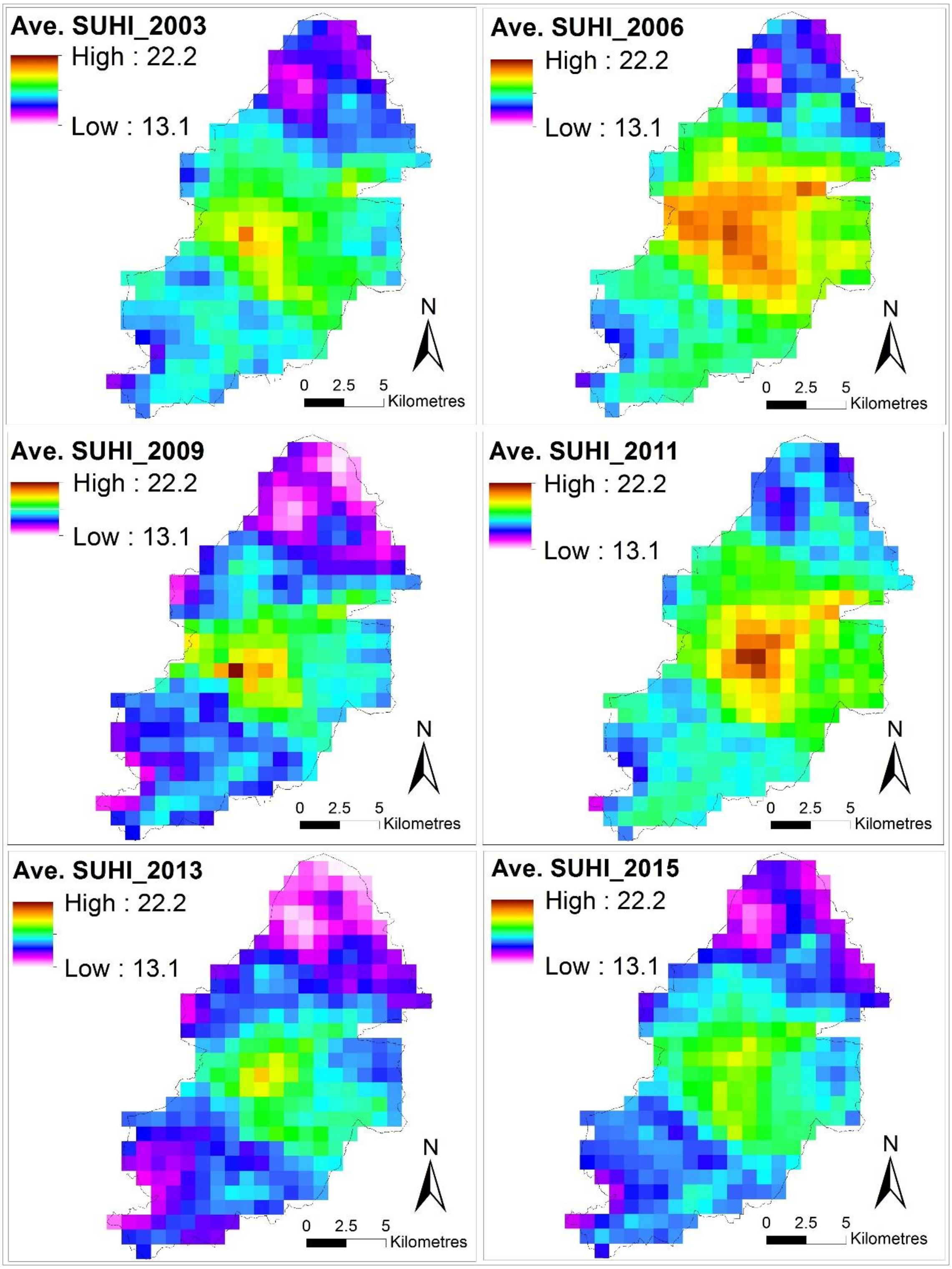

Figure 4.31: Birmingham's daytime SUHI spatial distribution using MODIS images (ºC). Derived from the thermal bands of the satellite images acquired between 2003 and 2015.

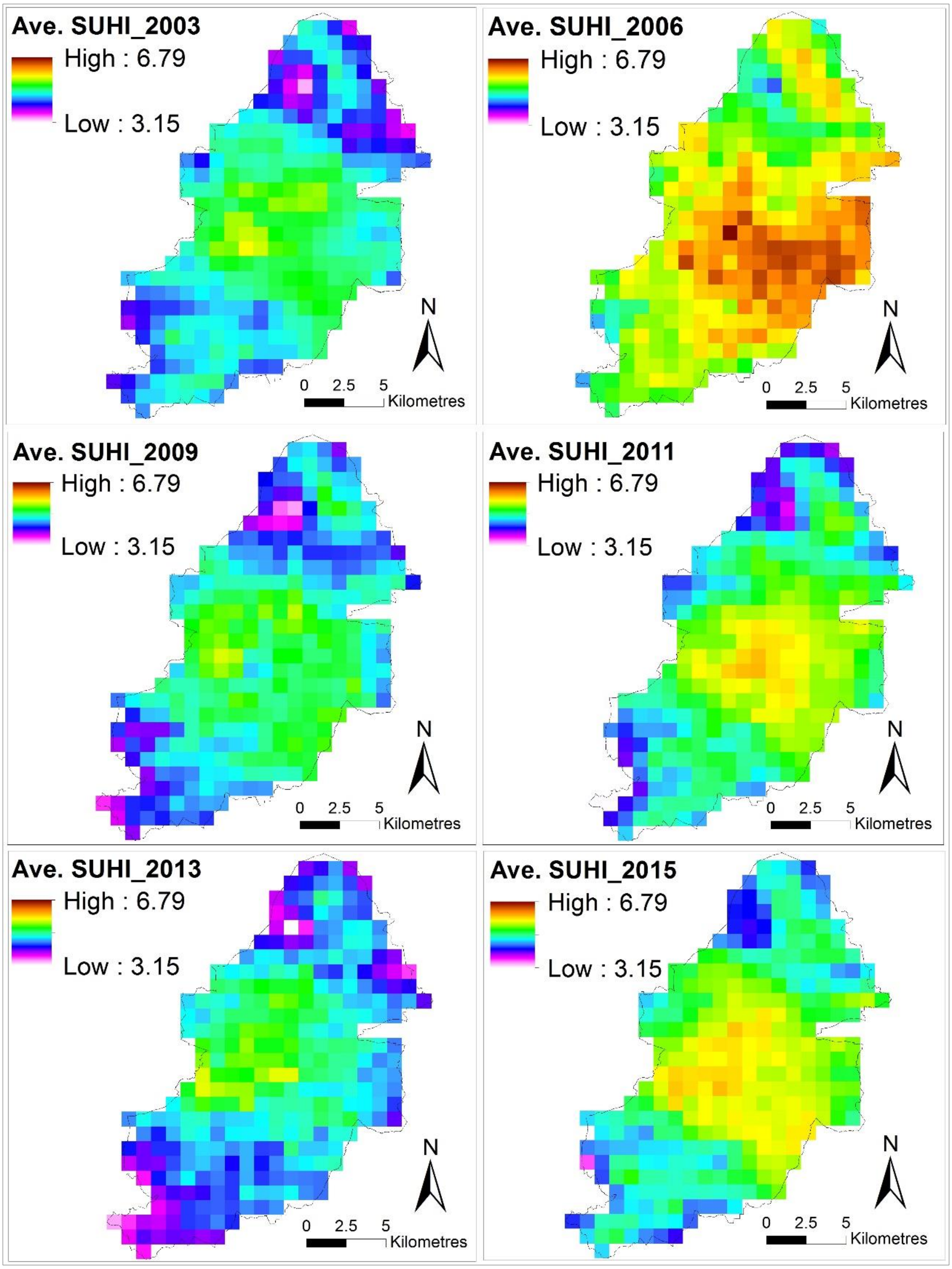

Figure 4.32: Birmingham's night-time SUHI spatial distribution using MODIS images (ºC). Derived from the thermal bands of the satellite images acquired between 2003 and 2015.

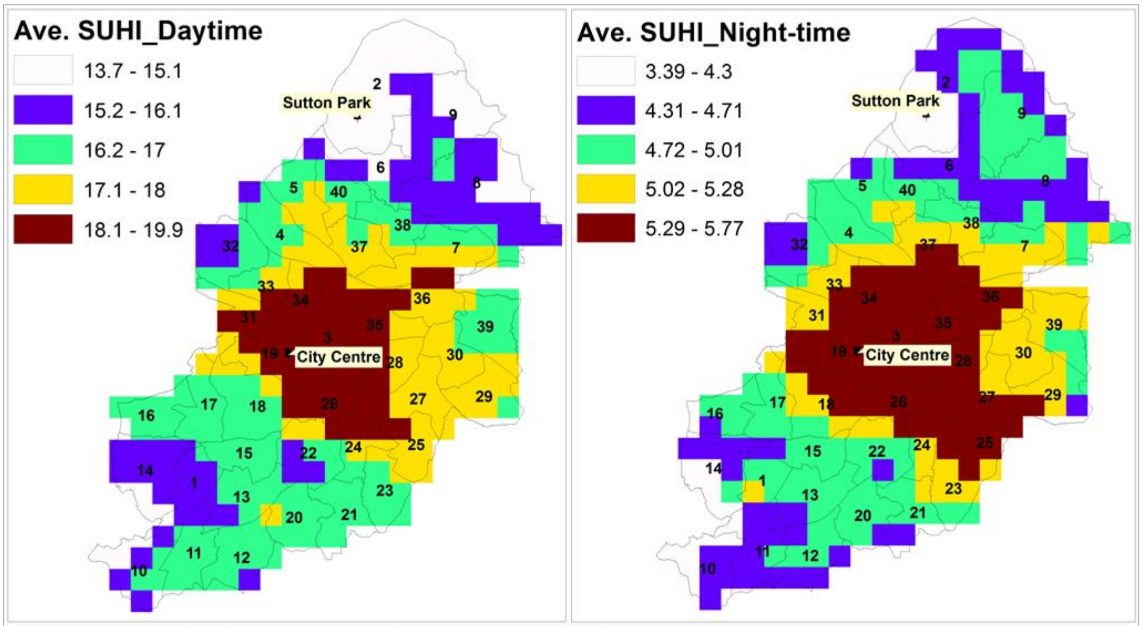

1	Weoley	9	Sutton Trinity	17	Harborne	25	Acocks Green	33	Lozells and East Handsworth
2	Sutton Four Oaks	10	Longbridge	18	Edgbaston	26	Sparkbrook	34	Aston
3	Nechells	11	Northfield	19	Ladywood	27	South Yardley	35	Washwood Heath
4	Perry Barr	12	Kings Norton	20	Brandwood	28	Bordesley Green	36	Hodge Hill
5	Oscott	13	Bournville	21	Billesley	29	Sheldon	37	Stockland Green
6	Sutton Vesey	14	Bartley Green	22	Moseley and Kings Heath	30	Stechford and Yardley North	38	Erdington
7	Tyburn	15	Selly Oak	23	Hall Green	31	Soho	39	Shard End
8	Sutton New Hall	16	Quinton	24	Springfield	32	Handsworth Wood	40	Kingstanding

Figure 4.33: Daytime & night-time average SUHI of Birmingham's wards over the period (2003-2015) using MODIS images (ºC). Different SUHI scales are used for daytime and night-time.

4.5.2 SUHI temporal change

The average LST of Birmingham does not show significant change from 2003 to 2015 as shown in Figure 4.34, and the diurnal LST is 10.58 °C with 1.48 SD. The steady trend of average diurnal LST is as a result of the stability of the night-time LST and daytime average LST which all have R^2 less than 0.1 for the entire study period (2003 – 2015). Johnson (1985a) studied heating and cooling rates of the heat island, and found that the most important changes occur at sunrise and sunset. The reason behind that is the change of the radiation budget of the urban surface, which highlights the importance of investigating the daytime and night-time SUHI separately. The average of daytime LST is 16.31 °C with 1.98 SD, and the average of night-time LST 4.86 is °C with 0.99 SD. The averages of NLST range between 0.39 - 0.43 for the diurnal, daytime and night-time NLST. The NLST showed similar trends to the LST without noticeable differences in the values of R^2 (Figure 4.34).

Like the LST, the average diurnal SUHI has not considerably changed over the study period, and its average magnitude was about 7.63 °C with 4.74 SD. The average daytime SUHI and the average night-time SUHI did show important alteration as shown in Figure 4.35. The average of daytime SUHI is 10.14 °C with 5.14 SD, and the average of night-time SUHI 5.13 °C with 2.41 SD. A study by Tomlinson et al. (2012) investigated the summer (June, July, August) night-time UHI of Birmingham between (2003-2009) using night-time MODIS imagery. They identified that during periods of high atmospheric stability, the SUHI intensity in Birmingham can reach up to 5 – 7 ºC, with a clear peak in the central business district and relatively lower temperature in the Sutton Park. Generally, the temporal change of average LST and SUHI of Birmingham did not show significant changes over the study period (2003-2015) just like London, however, they both gave high spatial variability.

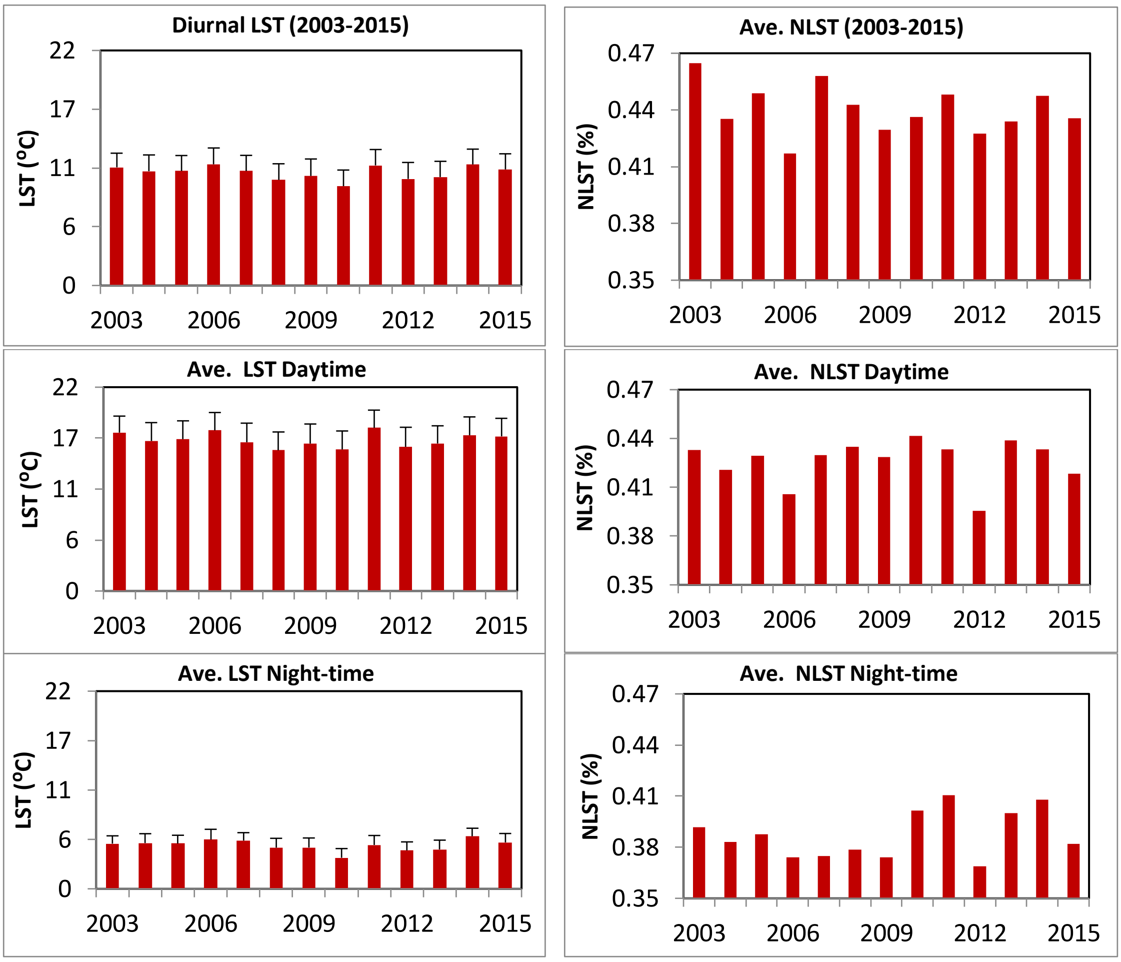

Figure 4.34: Birmingham's diurnal, daytime & night-time LST derived from MODIS data over the period (2003-2015), left (Normal) & right (Normalised).

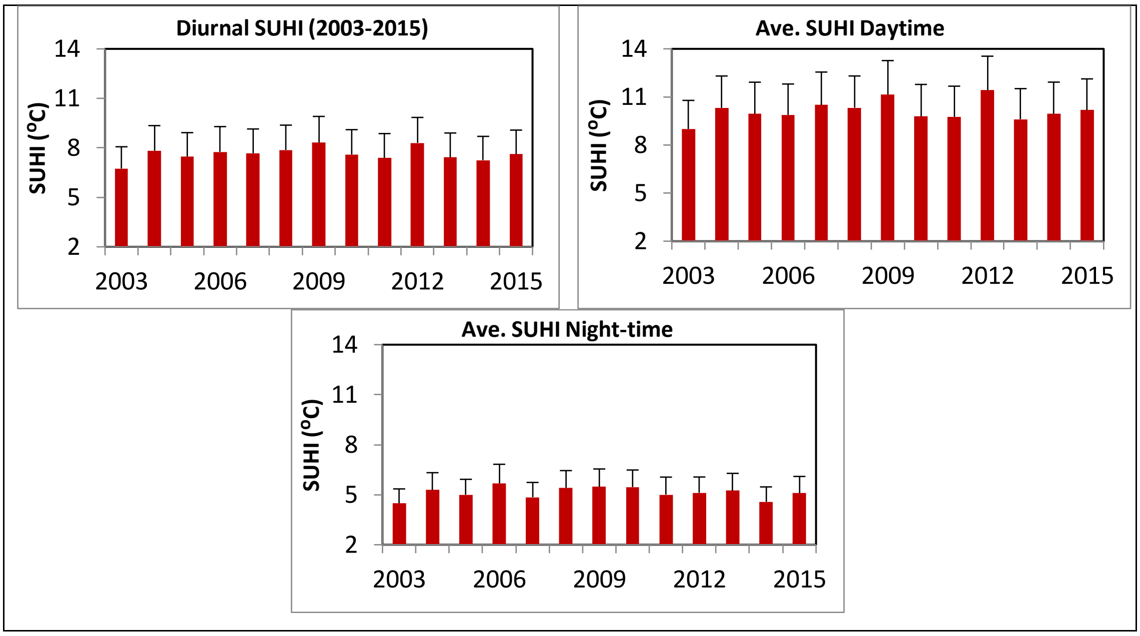

Figure 4.35: Birmingham's diurnal, daytime & night-time average SUHI change derived from MODIS data over the period (2003-2015).

Figure 4.36 contains the winter's months which do not show obvious increase in the trends for the study's period, as all the R^2 are low (< 0.1). The LST averages for the winter months range between 2.23 – 3.57 ºC, and for the NLST the ranges are between 0.39 – 0.41. There is a slight difference between the trends of the LST and NLST for the winter months, in particular for December and January (see Figure 4.36). Furthermore, Figure 4.37 includes the spring months which reveal a very small change in the trends over the study's period, except for March NLST. The LST averages for the spring months range between 7.56 – 14.53 ºC, and for the NLST the ranges are between 0.41 – 0.42. There are some differences between the trends of the LST and NLST for the spring months, in particular for March, as shown in Figure 4.37. March LST averages show weak decrease for the LST values, while, they give significant increase for the NLST values (R^2= 0.21). However, the LST has the same the trend as the NLST for May, with a slight difference for April.

On the other hand, Figure 4.38 contains the summer months which show low decreases in the trends for the study's period. The LST averages for the summer months range between 17.66 – 19.5 ºC, and for the NLST the ranges are between 0.40 – 0.41. There are some small differences between the trends of the LST and NLST, especially for June and July. Moreover, Figure 4.39 contains the autumn months which show slight increases in the trends for the study's period. The LST averages for the autumn months range between 5.39 – 14.12 ºC, and for the NLST the ranges are between 0.40 – 0.42. There is no noticeable difference between the trends of LST and NLST for the autumn months, except for September (see Figure 4.39). In summary, the summer showed a slight decrease in LST, whereas, the autumn and spring reflected a bit of increase to moderate winter temporal change. The NLST for some months gave opposite trends to the LST, especially, for September and March.

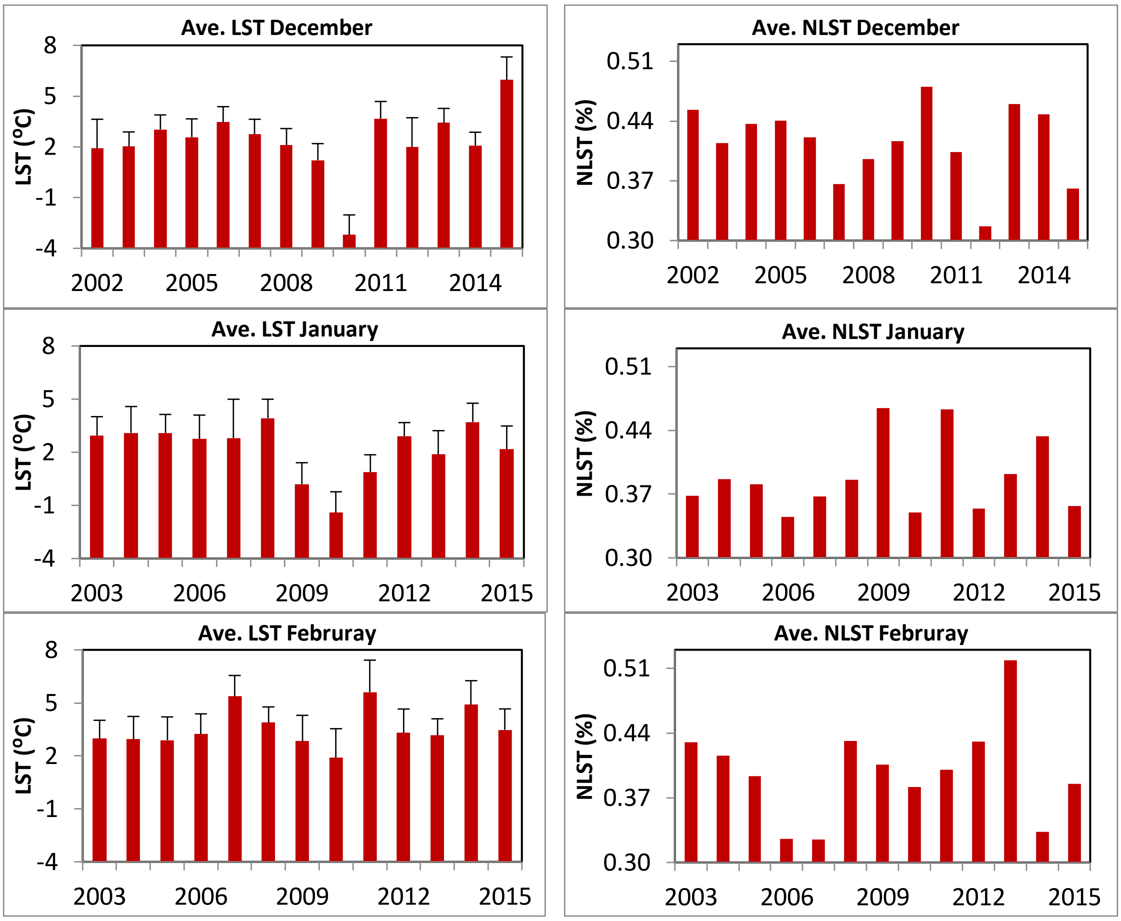

Figure 4.36: The temporal change of the winter's months LST and NLST in Birmingham derived from MODIS data, left (Normal) & right (Normalised) between 2002 and 2015.

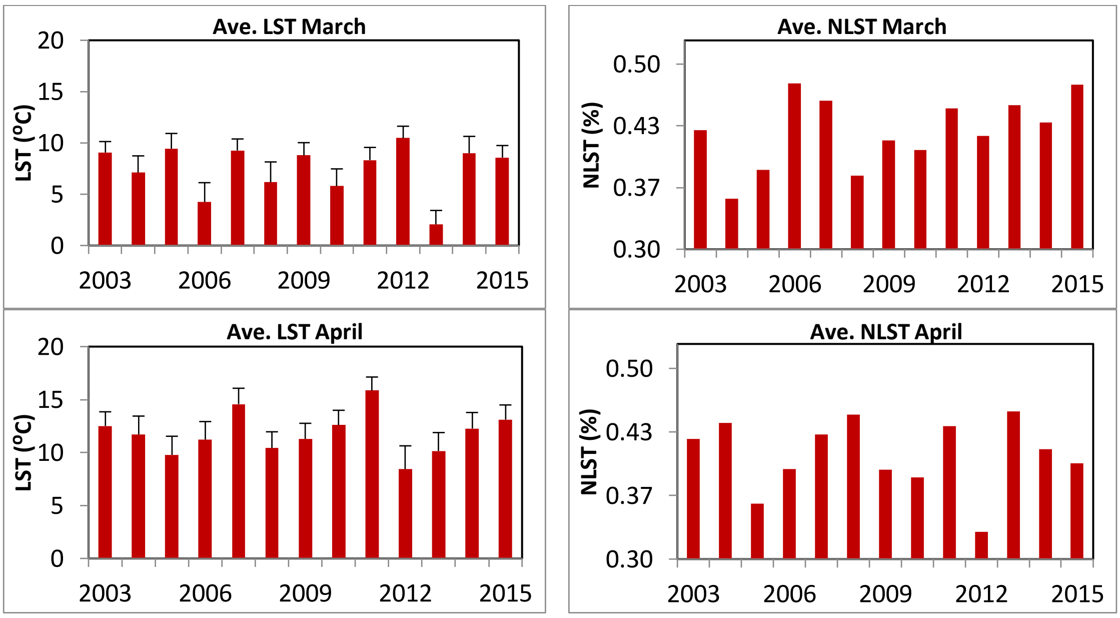

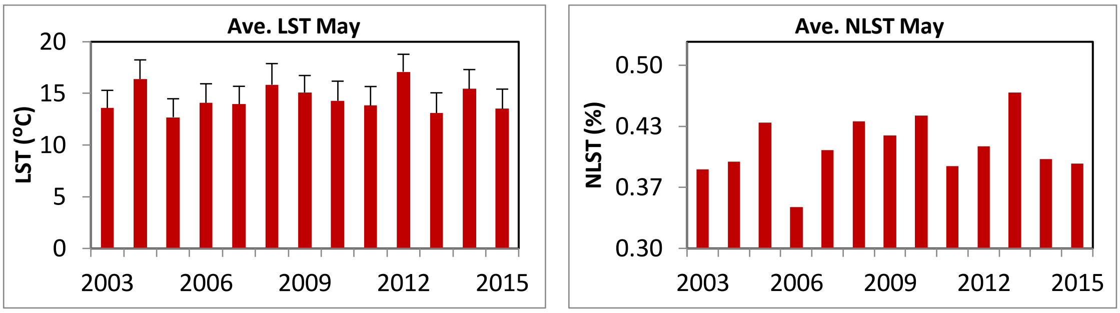

Figure 4.37: The temporal change of the spring's months LST and NLST in Birmingham derived from MODIS data, left (Normal) & right (Normalised) between 2003 and 2015.

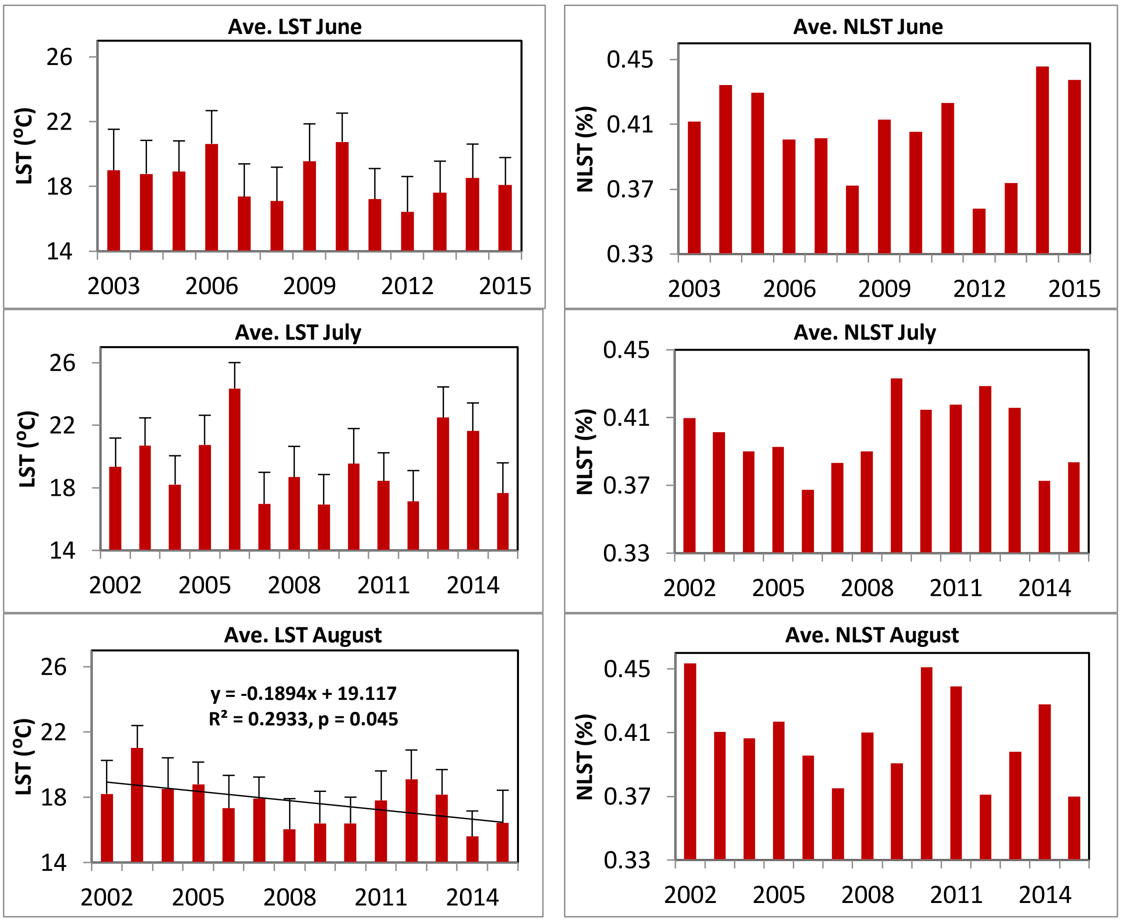

Figure 4.38: The temporal change of the summer's months LST and NLST in Birmingham derived from MODIS data, left (Normal) & right (Normalised) between 2002 and 2015. Only significant trend lines are shown.

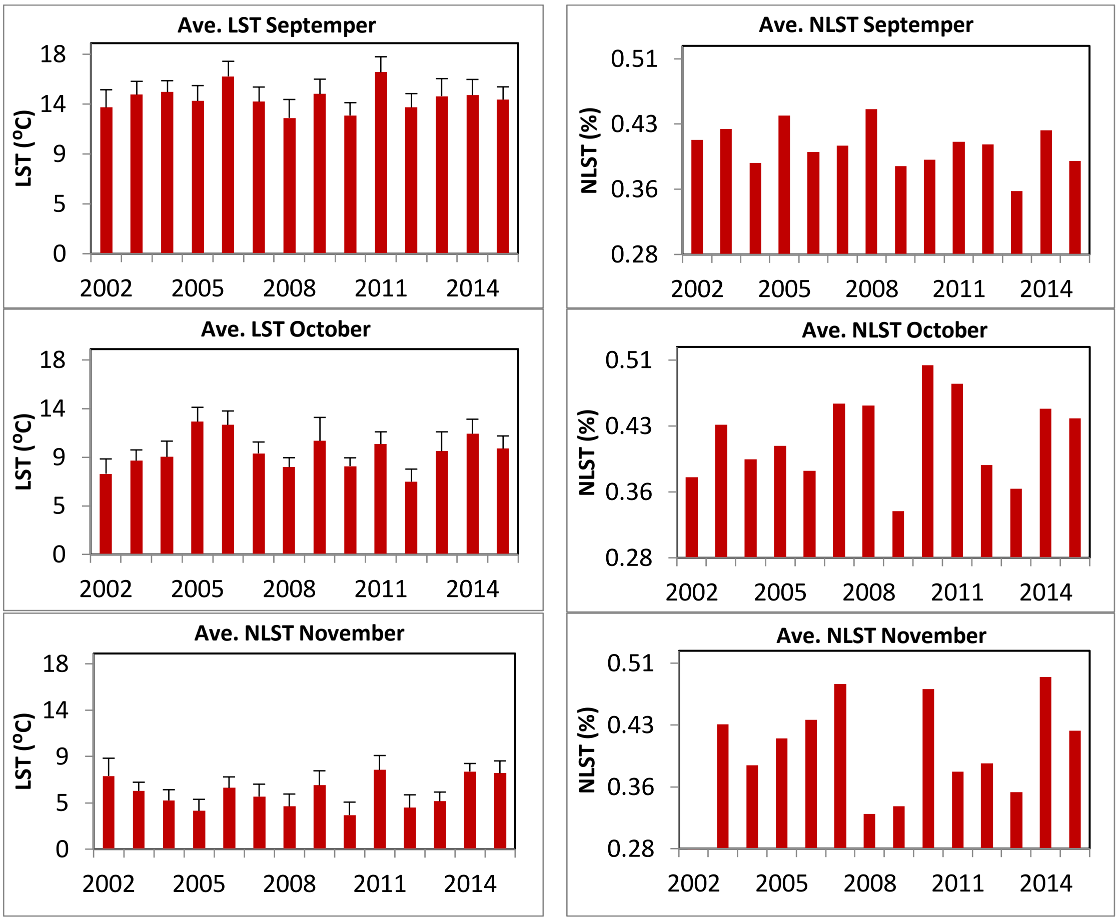

Figure 4.39: The temporal change of the autumn's months LST and NLST in Birmingham derived from MODIS data, left (Normal) & right (Normalised) between 2002 and 2014.

The monthly averages of SUHI for the whole study period range between 5.39 – 10.28 ºC as detailed in Figure 4.40. The average SUHI intensity fluctuated from about 5.39 ºC with 2.67 SD for December to around 10.28 ºC with 6.21 SD for June. Months from July to December showed weak increase in the trends with R^2 less than 0.1. The monthly temporal change of SUHI appears to fluctuate for the different months, thus, the weak increase (July – December) moderated by the weak decrease of (January, March, April & June). This might explain the slight increase of the average daytime SUHI, which was equalised by the weak decrease in the night-time SUHI over the study period to have neutral SUHI over time. Azevedo et al. (2016a) used MODIS LST to identify the spatial pattern of the daytime and night-time UHI in Birmingham for June, July and August 2013. They demonstrated that the distribution of the surface UHI appears to be clearly linked to land use, and considered this as a significant finding of their work. Accordingly, the next section quantifies and identifies the role of land cover types in the formation of SUHI.

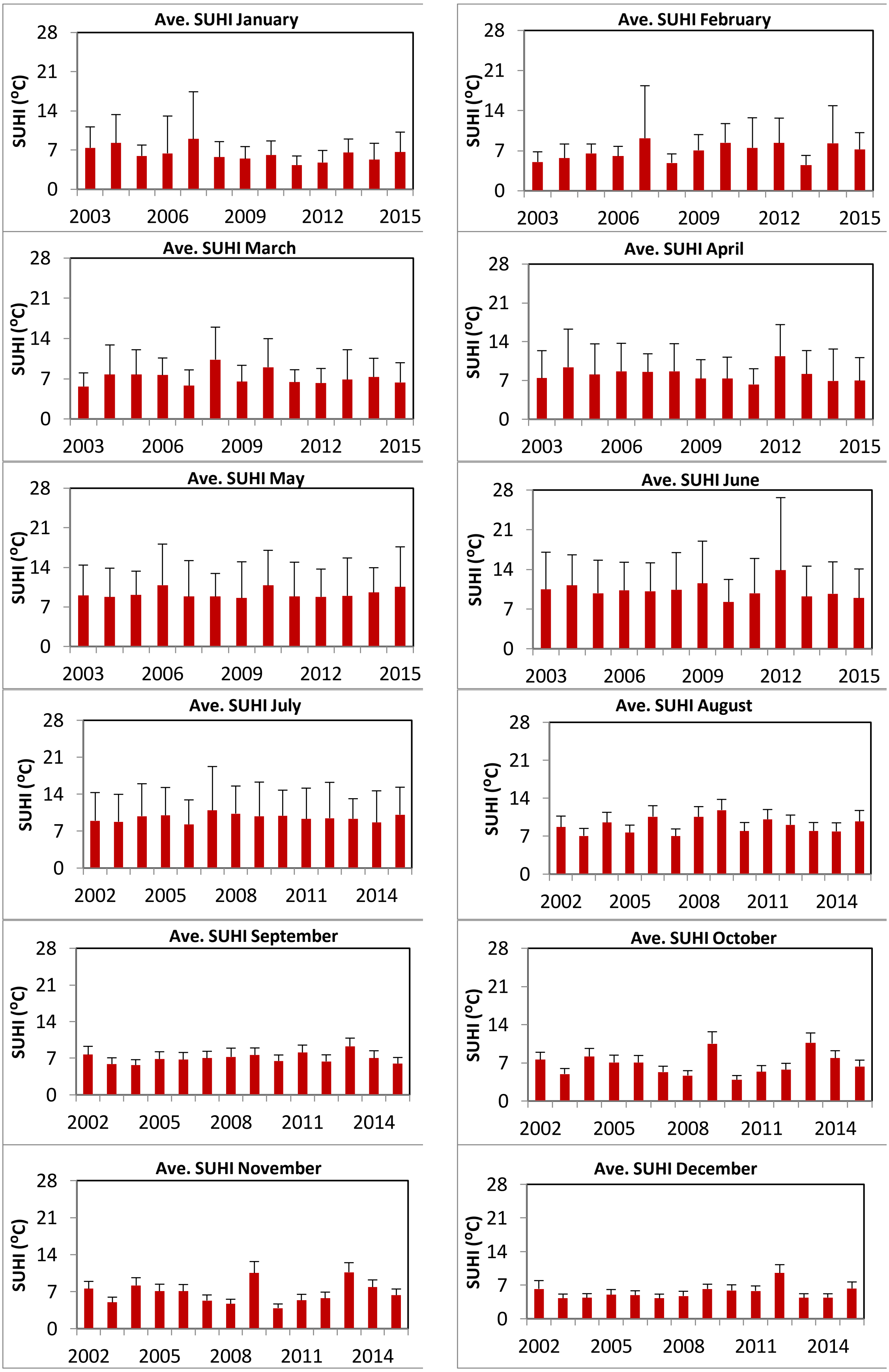

Figure: 4.40 The monthly averages of Birmingham's SUHI derived from MODIS data over the period (2003-2015).

4.5.3 LST and land cover

Table 4.3 gives the regression results of the very significant models ($p < 0.01$), where the LST is the dependant variable and land cover indices are the predictors. The correlations reflect the importance of NDMI and NBR2 in reducing the LST. Hence, NDMI contributed negatively to about 85% of the LST models in Table 4.3 with R^2 up to 0.75. Also, NBR2 gave significant negative correlation with nearly 89% of the models. The NBR2 could explain 82% of the LST variation on the 10th June 2006. Furthermore, vegetation indices (especially NDVI & MSAVI) played a major role to relieve the LST with up to 0.77 R^2 for NDVI on the 12th of May 2001. The NDVI could explain 77% of the LST variation on the 10th June 2006, and negatively contributed to about 67% of the LST models. Also, the MSAVI relieved the temperature for about 63 % of the LST models with up to 0.62 R^2 on the 16th of April 2003.

The high significance models ($p < 0.01$) with ($R^2 > 0.4$) formed about 55% of the total models, and the highest R^2 (0.67) was on 10th of June 2006. SAVI and NBR indices did not show any significant regression correlation with LST. Azevedo et al. (2016b) demonstrated that a strong negative correlation between LST and NDVI exists, with the strongest relationship evident during the daytime with −0.78 R (not R^2) compared to night-time with −0.69 R. The difference between R^2 and R is that R^2 means the coefficient of determination, while, R is the coefficient of correlation (Bansal, 2015). R^2 shows the percentage of variation in y (LST here) which is explained by all the x variables (land cover indices) together. Bansal (2015) clarified that it is easy to explain the regression in terms of R^2, however, it is not easy to explain the regression in terms of R. Accordingly, the LST of Birmingham can be dramatically reduced by enhancing the vegetation and moisture of the surface cover, which shows a similar behaviour to London. Moreover, the correlation between LST and NBR2 is considerably negative for both of London and Birmingham. It was explained earlier that NBR2 is correlated with the presence of organic soils; consequently, the LST is negatively correlated with organic soils.

Table 4.3: Correlation between LST and land cover indices of Birmingham. Derived from Landsat high level products between 2000 and 2015.

Date	Pearson correlation coefficients							Regression equations	R Square
	NDVI	EVI	SAVI	MSAVI	NDMI	NBR	NBR2		
7 April 2000	-0.62	0	0	-0.52	-0.54	0	-0.60	17.8-7.8NDVI-1.6NDMI-9.7NBR2+9.4MSAVI	0.43
12 May 2001	-0.77	0	0	0	0	0	-0.76	30.8-5.9NDVI-9.1NBR2	0.61
28 March 2002	-0.66	0	0	-0.55	-0.52	0	-0.61	16.5-8.5NDVI+NDMI-7.9NBR2+8.3MSAVI	0.48
4 April 2002	-0.69	0	0	0	-0.61	0	-0.65	20.1-4.1NDVI-1.9NDMI-3.3NBR2	0.49
11 September 2002	0	0	0	-0.60	-0.64	0	-0.66	22.8-5.1NDMI-8.4NBR2+1.3MSAVI	0.48
22 March 2003	-0.44	0	0	-0.31	-0.33	0	-0.40	14.3-7.9NDVI-0.5NDMI-5.6NBR2+10.8MSAVI	0.27
16 April 2003	0	0	0	-0.62	-0.63	0	-0.64	28.1-6.9NDMI-8.5NBR2-0.2MSAVI	0.45
13 July 2003	-0.68	0	0	0	-0.67	0	-0.74	30.6+1.6NDVI-4.6NDMI-15NBR2	0.56
19 November 2004	0.57	-0.26	0	0	0	0	0.29	-2.4+7.5NDVI+2.8NBR2-11.9EVI	0.65
10 May 2006	-0.75	0	0	0	-0.72	0	-0.75	24.5-3.5NDVI-4NDMI-6.8NBR2	0.59
10 June 2006	0	0	0	0	-0.75	0	-0.82	32.3-2.8NDMI-15.9NBR2	0.67
20 July 2006	-0.07	-0.31	0	0	-0.32	0	0	21.4-17.1NDMI-82.9EVI+64.6NDVI	0.53
21 July 2006	0	0	0	0	-0.29	0	-0.18	24.6-12.2NDMI-0.3NBR2	0.09
28 July 2006	-0.57	0	0	0	-0.56	0	-0.64	30.9+3NDVI-7.3NDMI-17.2NBR2	0.46
2 November 2006	-0.41	0	0	-0.29	-0.38	0	-0.39	6.9-2.6NDVI-0.7NDMI-2NBR2+3.1MSAVI	0.22
18 November 2006	0.168	0	0	0.21	0	0	0	4.2-0.2NDVI+1.2MSAVI	0.1
20 September 2008	0	-0.37	0	0	-0.33	0	-0.31	12.1-2.3NDMI+5.7NBR2-7.3EVI	0.14
22 June 2010	0	0	0	0	-0.43	0	-0.33	18.3-31NDMI+15NBR2	0.20
20 October 2010	-0.42	0	0	-0.35	-0.37	0	-0.42	7.1-2.1NDVI-0.3NDMI-2.6NBR2+2.5MSAVI	0.21
30 April 2011	-0.64	0	0	0	-0.62	0	-0.64	20-1.3NDVI-4NDMI-4.7NBR2	0.44
28 September 2011	0	0	0	-0.41	-0.50	0	-0.48	21.3-3.1NDMI-3.2NBR2-MSAVI	0.28
29 September 2011	-0.46	0	0	0	-0.56	0	-0.45	23.8-0.3NDVI-6.2NDMI+0.3NBR2	0.32
18 November 2012	0	0	0	0	-0.13	0	-0.1	3.1-NDMI-0.1NBR2	0.02
18 November 2013	0	0	0	0	-0.13	0	-0.07	3.1-1.3NDMI+0.1NBR2	0.02
19 January 2015	-0.22	0	0	0	-0.25	0	0	-1.4-0.2NDVI-0.8NDMI	0.07
9 April 2015	-0.63	0	0	-0.59	0	0	-0.62	21.7-4.5NDVI-6.9NBR2+2.7MSAVI	0.42
8 July 2015	-0.65	0	0	0	-0.71	0	-0.72	28.5+2.5NDVI-7.6NDMI-12.5NBR2	0.54

4.6 Discussion and analysis

The SUHI showed different behaviour for the three cities (Baghdad, London & Birmingham), as these cities gave different spatial and temporal SUHI change. The various SUHI distributions might be attributed to the specific LULC features of each city, the climatic and geographical condition or population density. For Baghdad using Landsat and ASTER data, built-up areas recorded relatively higher LST at night-time compared to other land cover types, while, during the daytime densely built-up areas had lower LST to act as a cool island. The high spatial resolution of Landsat and ASTER images has made the higher temperature of water bodies visible during the cold nights, which is probably due to its high thermal capacity. On the other hand, MODIS data provided higher temporal coverage compared to Landsat and ASTER images, and could be used to recognise the Industrial areas, and the highly populated attached urban configurations as high daytime SUHI intensity spots. Unlike the night-time SUHI, where all the urban areas exhibited higher temperature compared to the city boundary.

London, on the other hand, experienced high daytime SUHI in the heart of the city where the built-up areas are dominant using Landsat and ASTER data. The night-time SUHI also peaked in the city to decrease towards the surrounding areas, except for water bodies at cold nights. Similarly using MODIS images, the City of London had the highest SUHI at daytime comparing with other urban areas. At night-time, the water bodies and adjacent areas had the peak SUHI. The high intensity of SUHI over water was evident for the three cities during cold nights. Thus, the term WUHI was initiated to describe this phenomenon as a unique finding of this study.

Birmingham high intensity daytime SUHI showed similar patterns to London, concentrated in the urban fabric and industrial and commercial units. However, the high spatial resolution of the airborne night-time thermal image could identify the trees to have the second highest temperature after the water bodies, which did not appear in London and Baghdad. Birmingham daytime SUHI intensity peaked at the City Centre using MODIS data, and the lowest intensity could be seen in Sutton Park. Furthermore, the night-time SUHI maximised at the City Centre to extend to the adjacent suburban’s areas.

Figure 4.41 shows the overall averages of diurnal (day and night) SUHI for the entire study period (2003 – 2015) using MODIS data. The high intensity SUHI can be seen clearly in the heart of the three cities, and its magnitude reduces towards the boundaries. Consequently, the spatiotemporal distribution of SUHI gives similar patterns in general for the three cities, in spite of the specific characteristics of each city. Baghdad and London both have a major river that divides the cities, while Birmingham does not have a large water body; however, it does have a large park (Sutton Park). Table 4.4 provides a comparison of the summary statistics among the three cities of the LST, SUHI and NLST magnitudes for the entire study period. The diurnal average SUHI are 9.41, 11.29, and 7.63 ºC for Baghdad, London, and Birmingham respectively. The daytime average SUHI are 11.56, 13.52, and 10.14 ºC for Baghdad, London, and Birmingham respectively. The night-time average SUHI 7.26, 9.07, and 5.13 ºC for Baghdad, London, and Birmingham respectively. Despite the higher diurnal, daytime and night-time LST of Baghdad compared to London and Birmingham, the SUHI values of London are higher than those of Baghdad. Furthermore, the high magnitude of Baghdad’s NLST is compatible with the high averages of LST compared to other cities, whereas, London’s NLST has much variation in the range to enhance the SUHI.

Although, London has vegetation cover much higher than Baghdad, London SUHI intensity is higher than Baghdad. Therefore, the size of the city in terms of population and anthropogenic fluxes are of the main contributors to SUHI besides the LULC. All the derived land cover indices correlated negatively with LST for the three cities, with different degrees based on the nature of the index. Some of the indices such as NDVI, MSAVI, NDMI and NBR2 showed very significant negative correlation with LST. The land cover indices could explain up to 70 % of the LST variation for the significant models. The correlation between SUHI and LST was negative for the three cities over the study period (2003-2015) as detailed in Figure 4.42. This might suggest that the increase of global temperature might not be the cause of SUHI rise; however, the local biophysical parameters enhance the SUHI. And the elevating SUHI of the urban cities is one of the contributors to the global warming. Accordingly, the local climate for the neighbouring cities creates the regional climate which forms the global climate. Gartland (2008) explains that the UHI is one of the global warming causes, and on top of its negative effect it reduces the habitability of urban and suburban areas. In spite of some scientists are still doubtful about the effect of UHI, nevertheless, most scientists agree that the global warming observed in recent years is at least partially due to UHI (Stein, 2001). Although, this chapter focuses on the SUHI formation using LST as an indicator; however, the typical definition of UHI employs the air temperature to measure the CUHI.

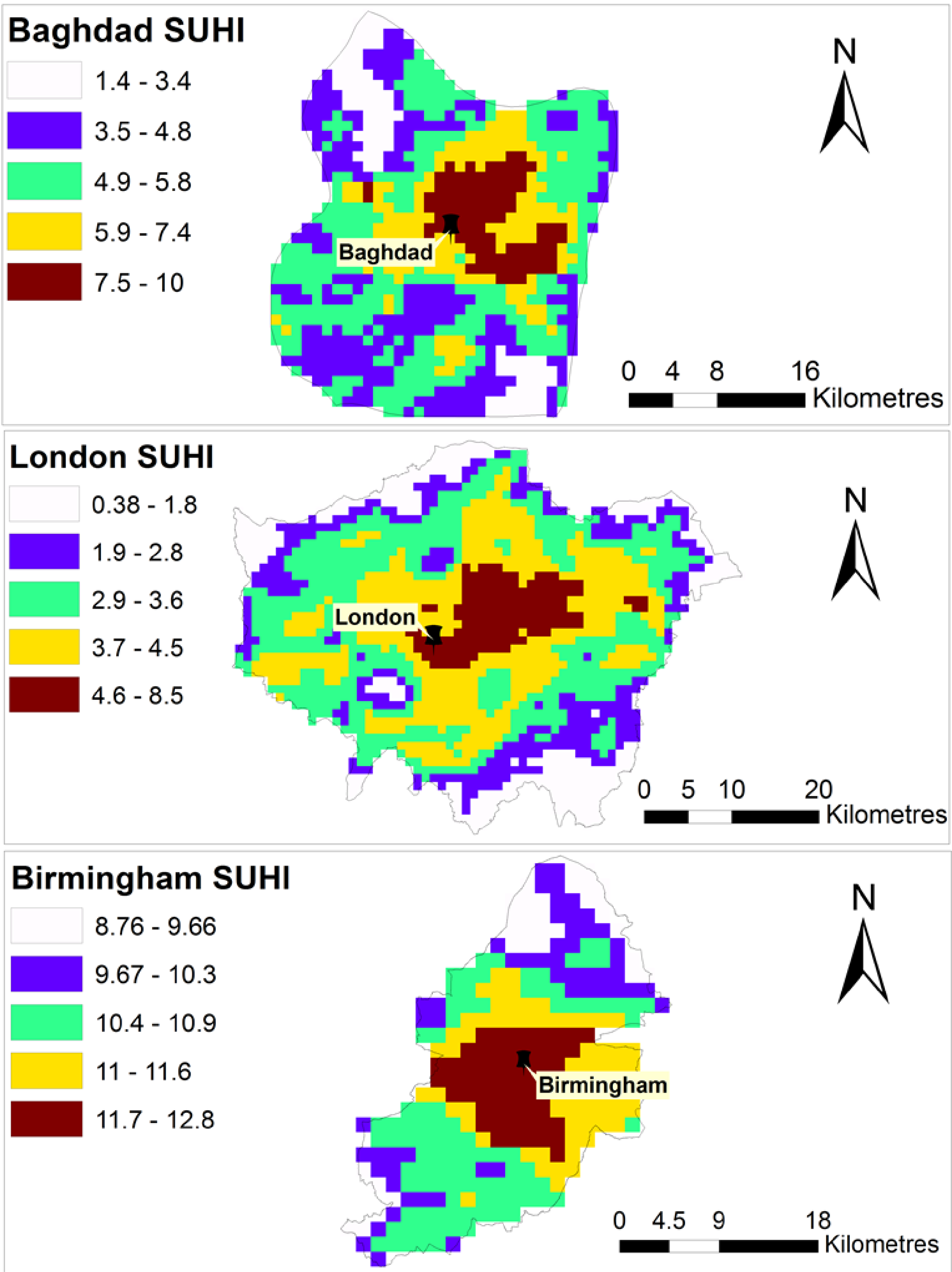

Figure 4.41: Diurnal averages SUHI of Baghdad, London and Birmingham derived from MODIS data over the period (2003 - 2015) (ºC). Different SUHI scales are used for daytime and night-time.

Table 4.4: Summary statistics of LST, SUHI and NLST for Baghdad, London and Birmingham calculated from MODIS data over the period (2003-2015).

City	Ave. diurnal LST (°C)	Ave. daytime LST (°C)	Ave. night-time LST (°C)	Ave. diurnal SUHI (°C)	Ave. daytime SUHI (°C)	Ave. night-time SUHI (°C)	NLST range
Baghdad	17	35.83	17	9.41	11.56	7.26	0.56 - 0.58
London	11.72	17.46	6.02	11.29	13.52	9.07	0.41 - 0.48
Birmingham	10.58	16.31	4.86	7.63	10.14	5.13	0.39 - 0.43

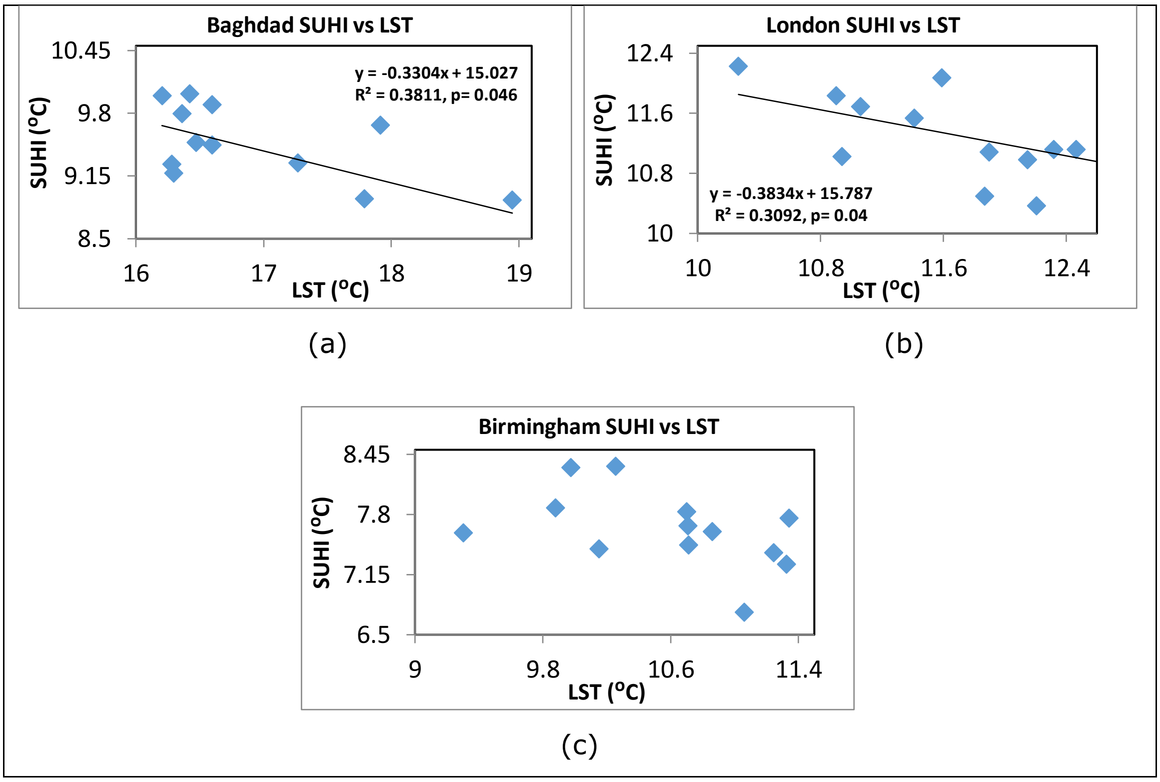

Figure 4.42: Correlations between SUHI and LST of (a) Baghdad, (b) London and (c) Birmingham derived from MODIS data over the period (2003 - 2015). Different axes scales are used for the three cities and only significant trend lines are shown.

4.7 Conclusions

The spatial and temporal change of SUHI was investigated in this chapter as well as the contributing parameters to the SUHI, in particular land cover. The study areas were Baghdad and London as large cities, as well as Birmingham as a medium size city. The different climatic conditions and land cover patterns for the cities provided the opportunity of investigating various SUHI behaviours in time and space. Baghdad is a dry city surrounded by soil lands, while, London and Birmingham are vegetated environments with a considerable amount of rainfall. The spatial distribution of SUHI in Baghdad slightly differs from London, even though, both cities have a large river crosses approximately in the middle. However, some soil lands in Baghdad exhibited higher LST than the densely built-up areas; unlike, London which has only small fraction of bare lands.

The vegetation and water classes had the lower temperatures during the daytime for the three cities. The densely built-up areas and the business districts recorded the largest temperatures at times of high anthropogenic activities. The water bodies were distinguished by their high thermal capacity to have the peak LST during cold nights. The trees were also highlighted to have high LST using high resolution airborne thermal images, which did not appear using moderate resolution images. The derived land cover indices negatively correlated with LST, and could explain up to 70 % of the LST variation for the significant models.

The temporal change of SUHI negatively responded to the elevated LST. The SUHI had its maximum overall intensity in London, in spite of Baghdad having the highest average LST. Consequently, the mitigation techniques for London and Birmingham might not be the same for Baghdad. As the soil lands around Baghdad when it is replaced by concrete, asphalt or vegetation might relieve the SUHI if the expansion considered a strategy of low density sprawl. Nevertheless, the green areas surrounding London and Birmingham work as cool islands. Therefore, the key solution is less anthropogenic fluxes with higher moisturised surfaces. These findings are applicable to mitigate the SUHI; however, the next chapter will investigate the CUHI using air temperature by ground measurements. This will provide meaningful comparisons for the different measuring techniques of UHI, and Birmingham will be the study site of the CUHI. Then the differences and similarities can be drawn by applying different techniques on the same city.

Chapter 5: CUHI Spatiotemporal Distribution and Modelling

Parts of this chapter have been published as:
ALI, JASIM M., MARSH, STUART H. and SMITH, MARTIN J., 2016. Modelling the spatiotemporal change of canopy urban heat islands. Building and Environment. 107, 64-78.

5.1 Introduction

A common measurement technique of the UHI is using air (canopy) temperature to monitor the CUHI, while, satellites measure the LST to map the SUHI (Tomlinson et al., 2013). Tomlinson et al. (2013) argues that the relationship between the CUHI and SUHI is especially complex across an urban area. The traditional approach to measure the CUHI is using a meteorological station in the City Centre and another one outside the city in a rural area (Gartland, 2008). However, due to the heterogeneity of the urban environment, the city climate requires a dense network of sensors to study its microclimate (Muller et al., 2013). Muller et al. (2013) investigated the relation between the spatial scales and climate networks, and found that a dense climate network covering an entire city or neighbourhood is required to monitor and model the UHI. Birmingham has adopted one of the densest climate monitoring systems worldwide, with 107 sensors.

The advantages of using a dense climate network over only pairs of stations were addressed by Stewart (2007). On top of the benefits of using a dense network of sensors is the ability to study the intra-urban differences of the climate patterns, and even to compare between different cities with a similar monitoring system, Stewart (2007) remarks. Lelovics et al. (2016) note that the air temperatures in the city differ based on the properties of the urban environment and the characteristics of the regional climate. There were not many city scale (local scale) urban climate monitoring networks in Europe and in other parts of the world in service in 2016. Table 5.1 provides a review of the past and current local scale climate monitoring networks around the world, and compares them in terms of the number of sites, area covered, operating time period, and the aim of the project with the types of the installed instrument and method of communication.

Table 5.1: A review of the past and current city scale urban climate monitoring systems worldwide.

Country	City	Number of Sites	Area (km^2)	Time Period	Aim, Instruments, & Communication	References
England	Birmingham	107	278	2012-present	meteorological data, 25 AWS & 82 ASM, Wi-Fi transmission	(Ali et al., 2016)
England	London	91	1572	2009-present	Education, different survey sensors, Wi-Fi transmission	(Davies et al., 2011)
Finland	Helsinki	102	150	2005-present	Mesoscale observation, Vaisala AWS, Mobile phone network	(Dabberdt et al., 2005)
Finland	Turku	63	206	2002-2007	Urban Climate Research, temperature loggers, not provided	(Hjort et al., 2011)

Germany	Berlin	10	892	2000-present	Research data, different sensors, Ethernet cable	(Fenner et al., 2001)
Italy	Florence	35	102.41	2004-present	intra-urban monitoring, temperature & humidity sensors, onsite collection	(Petralli et al., 2011)
USA	Washington DC	16	177	2003-present	Dispersion of hazards, various instruments, not provided,	(Honjo et al., 2015)
USA	Oklahoma	40	1440	2007-2010	atmospheric monitoring, 4 Mesonet & 36 micronet stations, traffic signals	(Basara et al., 2011)
USA	St. Louise, Missouri	50	170	2008-present	Real time weather forecast, different sensors, Wireless	(Muller et al., 2013)
USA	Cambridge, MA	25	18.47	2006-2010	Weather monitoring, various sensors, Dual Wi-Fi	(Murty et al., 2008)
USA	Madison, Wisconsin	151	243.54	2012-present	Urban climate, temperature/RH dataloggers, not provided	(Yang et al., 2013)
USA	Detroit, Michigan	32	370	2009-2010	urban–rural temperature difference, multiple networks, multiple	(Oswald et al., 2012)
USA	Minneapolis–St. Paul	170	5000	2011-present	Urban climate, temperature sensors, not provided	(Smoliak et al., 2015)
USA	Barrow, Alaska	68	55.2	2001-2002	UHI studies, HoboPro two-channel data loggers, onsite computers	(Hinkel and Nelson, 2007)
USA	New York, NY	75	1,214	1997-1998	mesoscale analysis UHI, meteorological stations, phone cables	(Gedzelman et al., 2003)
USA	Orlando, Florida	75	287	1999-2001	Urban-rural climate, HOBO loggers, not provided	(Yow and Carbone, 2006)
Japan	Tokyo	120	2187	2002-2005	Observation system, temperature and precipitation equipment, not provided	(Yamato et al., 2009)
Taiwan	Taipei	60	271.79	2003-present	Education, different sensors, school Wi-Fi	(Chang et al., 2010)
China	Hong Kong	105	1104	2007-present	Public weather education, various instruments, Wireless or LAN	(Hung and Wo, 2012)
China	Shanghai	200	6340.5	NA-present	Multi-purpose, different instruments, various methods	(Tan et al., 2015)
China	Beijing	185	300	2007-present	Weather monitoring, AWS, Wi-Fi transmission	(Yang et al., 2013)
Serbia	Novi Sad	27	112	2013-present	urban climate monitoring, weather stations, not provided	(Šećerov et al., 2015)
Hungary	Szeged	24	280	2013-present	intra-urban excess heat patterns, weather stations, onsite	(Gál et al., 2016)

Sweden	Göteborg	30	172.88	1998-2000	spatial air temperature variations, temperature stations, not provided	(Eliasson and Svensson, 2003)
S. Korea	Seoul	11	606	1999–2002	UHI studies, weather stations, onsite collection	(Lee and Baik, 2010)
Singapore	Singapore	35	700	2003-2008	CUHI Spatial change, HOBO ONSET, not provided	(Li and Roth, 2007)

The UHI studies that employ the air temperature within the canopy layer presented in the literature either lack the high spatial and temporal resolution of temperature measurements, or they choose specific climatic conditions and ignore others. The reviewed climatic networks in Table 5.1 have been employed by the researchers for different purposes, and not much attention was paid to deeply study the UHI. Furthermore, they have not modelled all the important controllable factors that potentially affect the development of UHI. For example, Busato et al. (2014) reported their experimental results for three years of mobile traverses, which covered prefixed paths in the city of Padua in Italy. However, this traversing approach does not fully explain the impacts of topography and the effects of different land covers. Doick et al. (2014) investigated the impact of Kensington Gardens, a park land area in London, and the findings showed the importance of vegetation in UHI mitigation. Nevertheless, the study also revealed the uncertainty over the variables that govern the extent of UHI. This result supports Ivajnšič et al. (2014) who concluded that local and regional variables have a very important role in explaining spatial variation in mean air temperature.

Whilst, large scale studies of UHI have been based mainly on remotely sensed satellite images, they lack the temporal variation of real time LST (Sismanidis et al., Weng and Fu, 2014, Rogan et al., 2013, Zhang et al., 2013). A study by Ho et al. (2014) assessed the ability of three remote sensing-based regression models to map the peak daytime air temperature using dense observation weather stations. However, this study was very limited temporarily as it used only six satellite images and focused on extreme events of air temperature. To address this deficiency, HiTemp has been carried out by the BUCL, funded by NERC (BUCL, 2014a). It has provided near real time data from one of the densest urban meteorological networks of automatic weather stations worldwide (Chapman et al., 2015a).

The HiTemp project is still ongoing since June 2012, and covers the entire conurbation of Birmingham. A study by Azevedo et al. (2016a) employed the HiTemp data to compare between the LST and high resolution air temperature observations. Their findings have concluded that the spatial change of LST is strongly linked to land use, whereas, the CUHI is more affected by the advective process. Another finding of their study is the tendency for a larger core of CUHI to spread to the east of Birmingham City; whilst, SUHI extends more to the west of the city. Also, they found that the relationship between SUHI and CUHI is strong at a neighbourhood scale, and limited at the city scale (Azevedo et al., 2016a). Nevertheless, this study was limited to the time of the satellite over pass and did not fully include the whole air temperature observations in the analysis which leaves gaps in understanding the spatiotemporal change of CUHI at times other than satellite overpass. Furthermore, the influencing parameters on the CUHI development were limited to specific factors.

Accordingly, the aim of this chapter is to model the spatial and temporal variation of UHI using a dense network of meteorological sensors, and to investigate the influence of a number of important influencing parameters on the CUHI formation. The temporal resolution of the data starts from hourly basis to monthly time increment, whereas, the spatial resolution relies on the distribution of HiTemp stations' locations. The influencing parameters are grouped into LULC, geometrical and meteorological factors and these parameters are tested to investigate their impact on the CUHI.

5.2 Study area and Data

5.2.1 Study area

Birmingham was chosen as a study area as it has experienced the deployment of a dense network of air temperature sensors and automated weather stations. Tomlinson et al. (2012) highlighted that the city used to have only one weather station for urban areas and another station outside the city in the rural areas. The UHI studies on Birmingham are limited compared to its size and importance. Unwin (1980) did one of the earliest studies about Birmingham UHI by comparing the temperature measurements between a site in the city and a rural area. A maximum of 5 ºC UHI intensity was observed in settled anticyclonic conditions. Similarly, Johnson (1985b) found a maximum of 4.5 ºC UHI intensity using a mobile traverse technique. After that, Bradley et al. (2001) used a 1-dimesional energy balance model to capture a maximum of 4.7 ºC SUHI.

Recently, Tomlinson et al. (2012) identified a maximum of 5 ºC in the central business district during high atmospheric pressure periods, and also recorded cold spots in one park of up to 7 ºC lower than the City Centre. On the other hand, the influencing parameters on the CUHI development have been quantified by very few studies. One of them was Azevedo et al. (2016a) study as discussed earlier, however, this study did not include the influence of the geometrical parameters and anthropogenic activities on the formation of CUHI. The influencing parameters were limited to the atmospheric conditions, land use, and advective process. Another one is Bassett et al. (2016) study which was one of the very few studies to quantify the horizontal wind impact on the spatial distribution of CUHI in a process called Urban Heat Advection (UHA). Their results indicated the mean contribution of UHA to the warming of areas downwind of Birmingham city can be up to 1.2 ºC. Consequently, Birmingham was considered a good site to investigate the biophysical effects on the UHI intensity, as it provides the required data to look into the change of CUHI in space and time with identifying and quantifying unprecedented number of influencing parameters.

5.2.2 Data

The air temperature data from the HiTemp project was provided by NERC for the purposes of this study. The climate network consists of two main types of sensors. Over 80 wireless Aginova Sentinel Micro (ASM) sensors record only air temperature, while, another 25 Automatic Weather Stations (AWS) record the main meteorological variables (Chapman et al., 2015a). All these stations capture the meteorological data per minute, and the data obtained for this study is from June 2012 to June 2014. Figure 5.1 shows the HiTemp distribution of stations inside the boundary of the city, and the stations' locations were obtained from the Metadata of the project. AWS and ASM are denoted with the prefix W and S respectively as shown in Figure 5.1. Schools were selected to host the majority of sensors as they are relatively secure and representative of their local environment (Chapman et al., 2015a). Also, Birmingham's schools have a good coverage of the city, and are mostly connected to Wi-Fi networks for data transmission. Furthermore, the sensors are installed more than 20 m away from heat sources, and the ASM sensors have approximately 3 km average spacing (Chapman et al., 2015a). ASM provide only temperature data, however, AWS give other meteorological data such as wind speed and direction which are considered alongside the analysis of the temperature data (BUCL, 2014a).

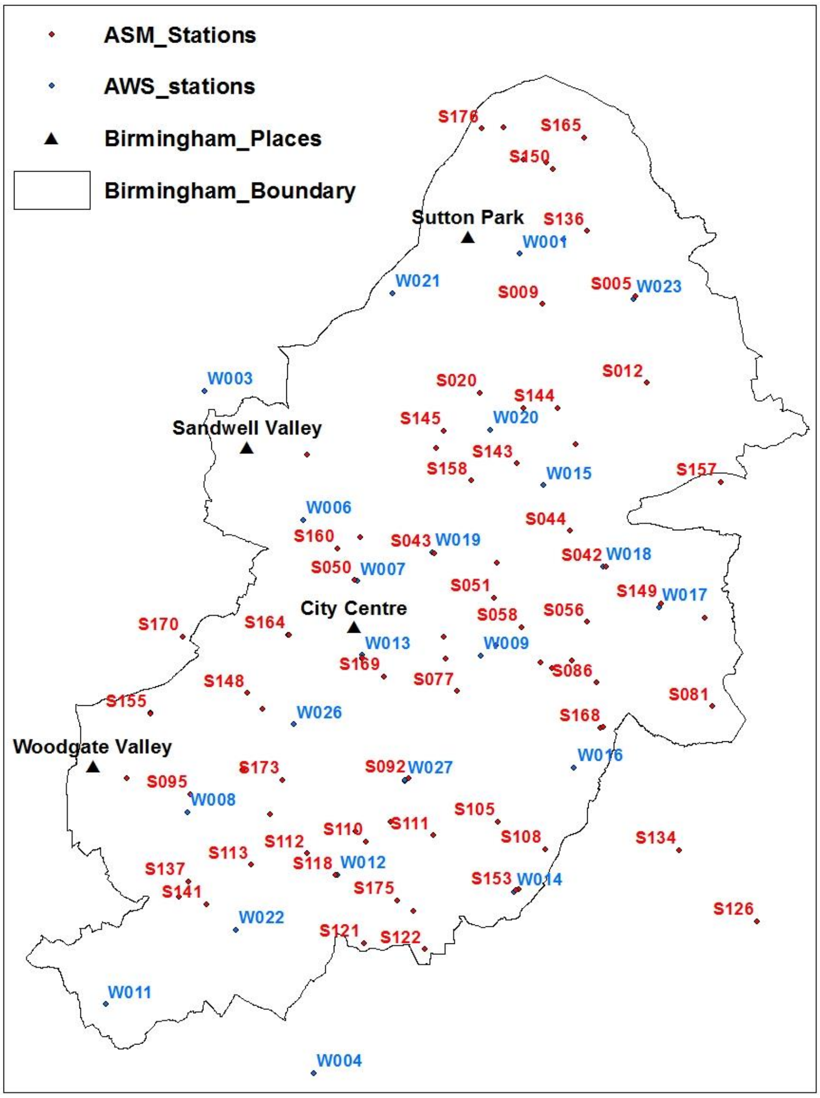

Figure 5.1: HiTemp Stations' locations in Birmingham obtained from the Metadata of the project. AWS and ASM are denoted with the prefix W and S respectively.

The air temperature is used as an indicator of UHI, and it is the dependent variable that is analysed and investigated against the predicting variables of the influencing parameters. The influencing parameters on the formation of UHI that are used in this study can be grouped into three main categories: LULC, urban geometry and meteorology. There are other influencing parameters not modelled in this chapter such as the radiation fluxes, which will be investigated in the next chapter.

5.2.2.1 LULC

Four LULC data sets of Birmingham City were used to capture all the variations of the physical environment such as buildings, pavements, parks and water. The first set of urban data is the OS Master Map Topography Layer which contains information about the objects on the ground divided into themes and descriptive groups (Ordnance Survey, 2015). The version of the

OS vector data updated in June 2015 has been used as it includes data stored in geodatabases useful for GIS urban mapping as detailed in Figure 5.2 and Figure 5.3. The descriptive groups are more detailed collections of the generalised themes, and it is feasible to examine the influence of both. A descriptive group is the primary classification attribute of a feature, which assigns a feature to one or more of 21 groups (EDINA, 2015). A theme is a set of features that have been grouped together for the convenience of customers, and to provide a high-level means of dividing the data on the layer coherently or logically. As a result, one classification might be more sensitive to air temperature change than the other.

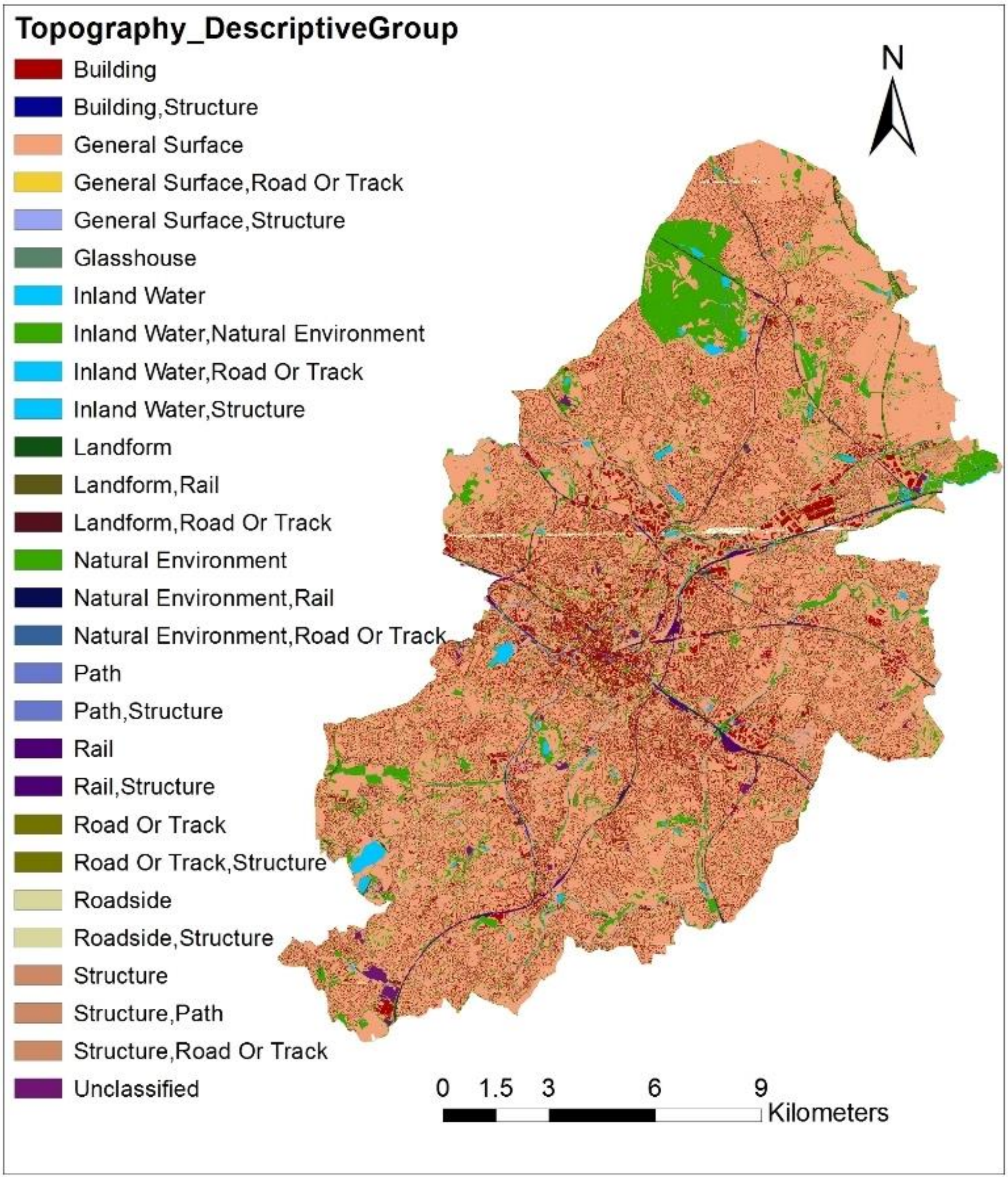

Figure 5.2: Descriptive group of Birmingham's topography layer derived from OS vector data updated in June 2015 (EDINA, 2016).

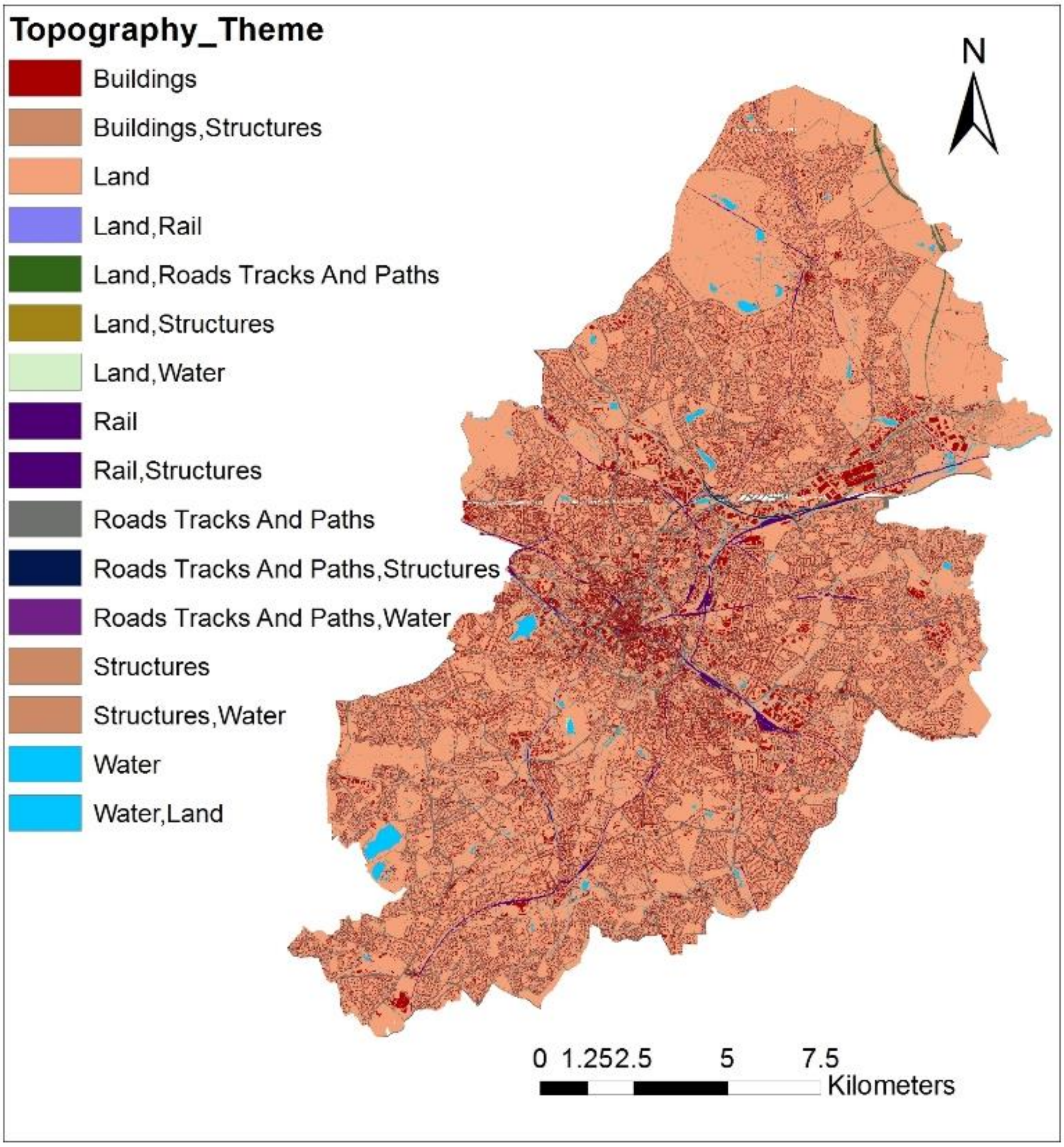

Figure 5.3: Themes of Birmingham's topography layer derived from OS vector data updated in June 2015 (EDINA, 2016).

The second set of data is the land use map including low density urban fabric classified by the European Environment Agency based on SPOT 5 images (2010) and city map (2008). These high resolution classes as shown in Figure 5.4 were downloaded from the European Urban Atlas available for large urban zones with more than 100000 inhabitants, as defined by the Urban Audit (EEA, 2014).

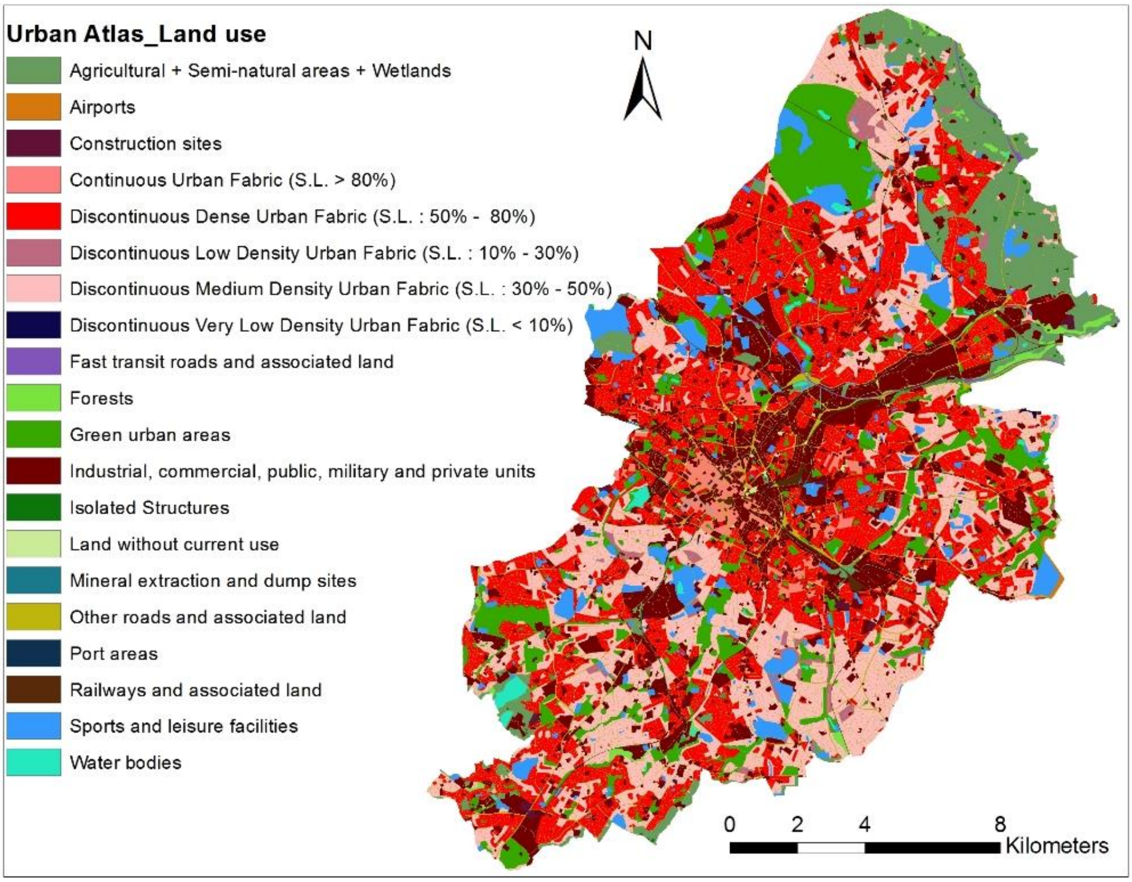

Figure 5.4: Urban Atlas of Birmingham's land use classified by the European Environment Agency based on SPOT 5 images (2010) and city map (2008) adapted from (Zhang et al., 2013).

The third set of data classifies the differing urban land use to eight categories, and it splits the urban fabric into multiple categories allowing more in depth comparison (Tomlinson et al., 2012). It uses data from OS and the UK Centre for Ecology and Hydrology (CEH) classified by a Principle Component Analysis (PCA) and cluster analysis (Owen et al., 2006). The classification scheme was based on 27 different input attributes and the output spatial resolution is a 1 km^2 grid showing similar urban land morphology (for more details see (Owen et al., 2006)). The result map of this approach is shown in Figure 5.5 and consists of eight categories of urban land use classification derived per pixel based on their common land use. It can be seen that the City Centre is classified as urban or transport, and most of the villages and farms are close to the city's boundary.

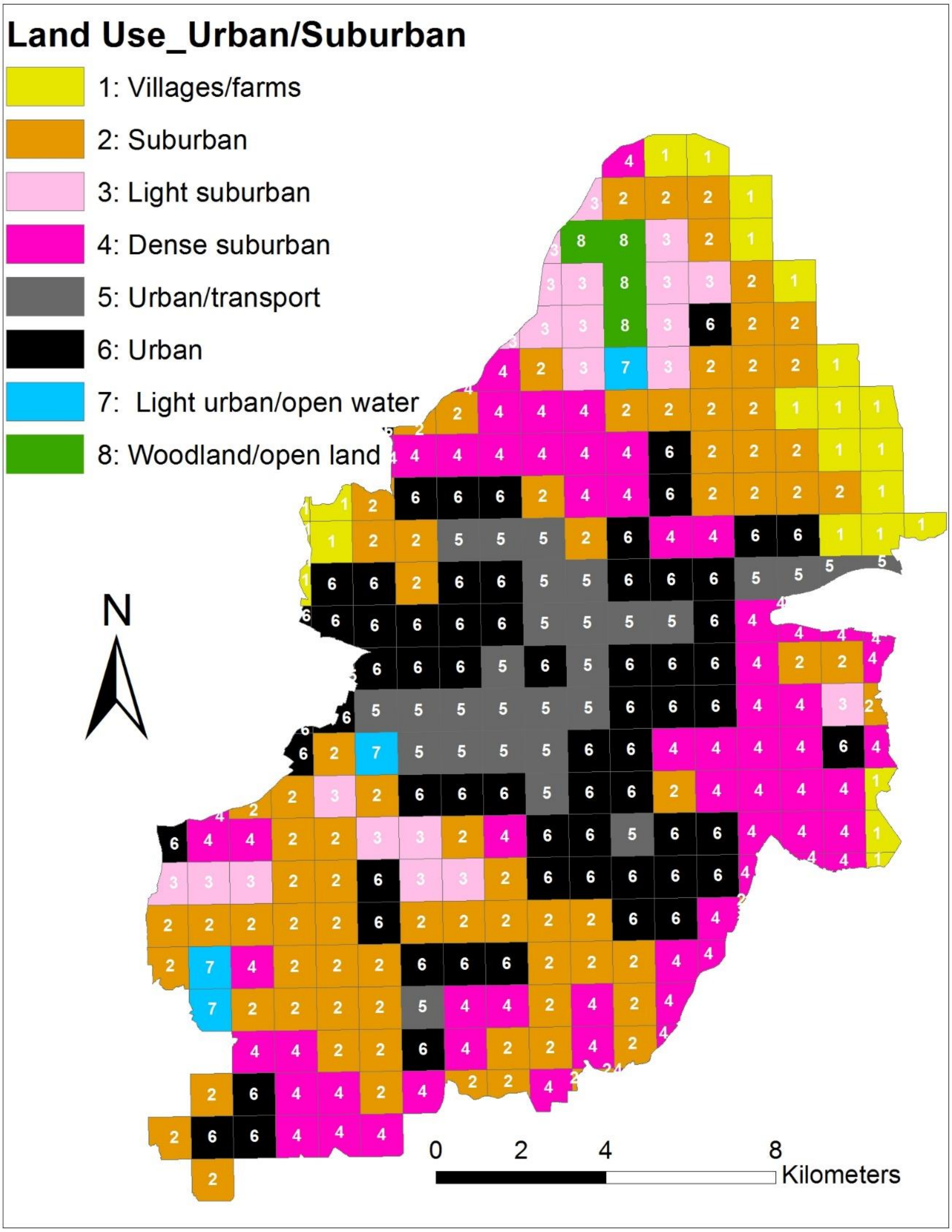

Figure 5.5: Spatial distribution of land use classification. It uses data from OS and the UK Centre for Ecology and Hydrology (CEH) classified by a Principle Component Analysis (PCA) and cluster analysis (Tomlinson et al., 2012).

The fourth data set is the high resolution raster images (25 cm) obtained from the OS based on a licensed agreement for the purpose of this study (Ordnance Survey, 2014). This dataset is employed to georeference other data layers and interpret the classification of the mentioned LULC maps with the help of the ArcGIS online basemap. These basemaps and reference layers are freely available to anyone and include World Imagery, World Street Map, World Topographic, Ocean Basemap, and more (Esri, 2015). Figure 5.6 gives examples of images for specific locations identified in Figure 5.1 using the high-resolution OS images.

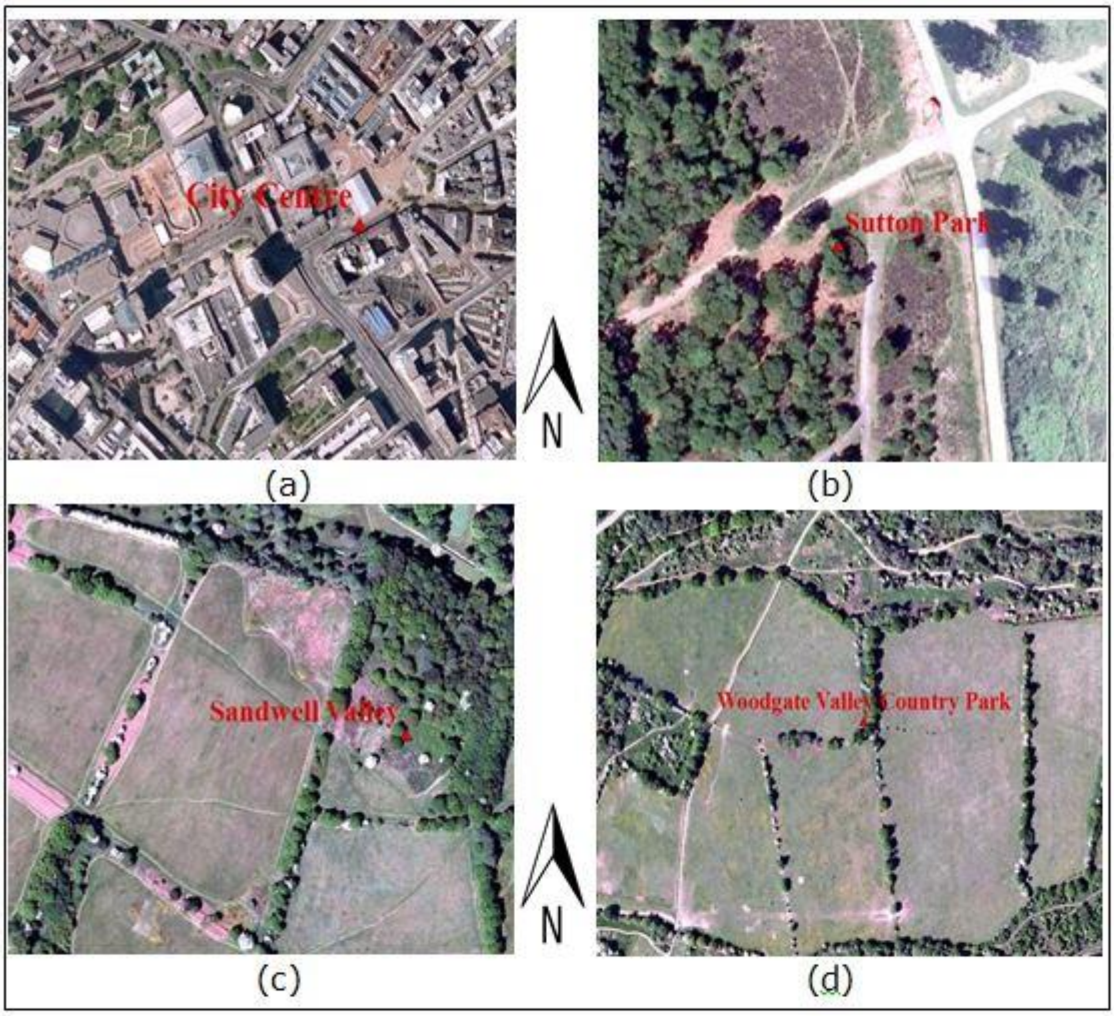

Figure 5.6: OS high resolution (25 cm) aerial photographs of Birmingham (a) City Centre, (b) Sutton Park, (c) Sandwell Valley and (d) Woodgate Valley Country Park at 1:2500 scales.

5.2.2.2 Urban Geometry

Two digital elevation models were prepared to derive the geometrical factors (such as sky view factor and shadow patterns); the DSM and DTM as shown in Figure 5.7. The 1m resolution DSM was obtained from the UK Environment Agency free of charge for academic purposes. It provides height data of buildings and other features on the ground using airborne LiDAR technology (Geomatics, 2014). On the other hand, OS Terrain 5 DTM is a 5 m resolution product captured as a triangulated irregular network (TIN), which is a three dimensional model edited to exclude buildings, trees and other above ground features created within a photogrammetric environment (EDINA, 2015).

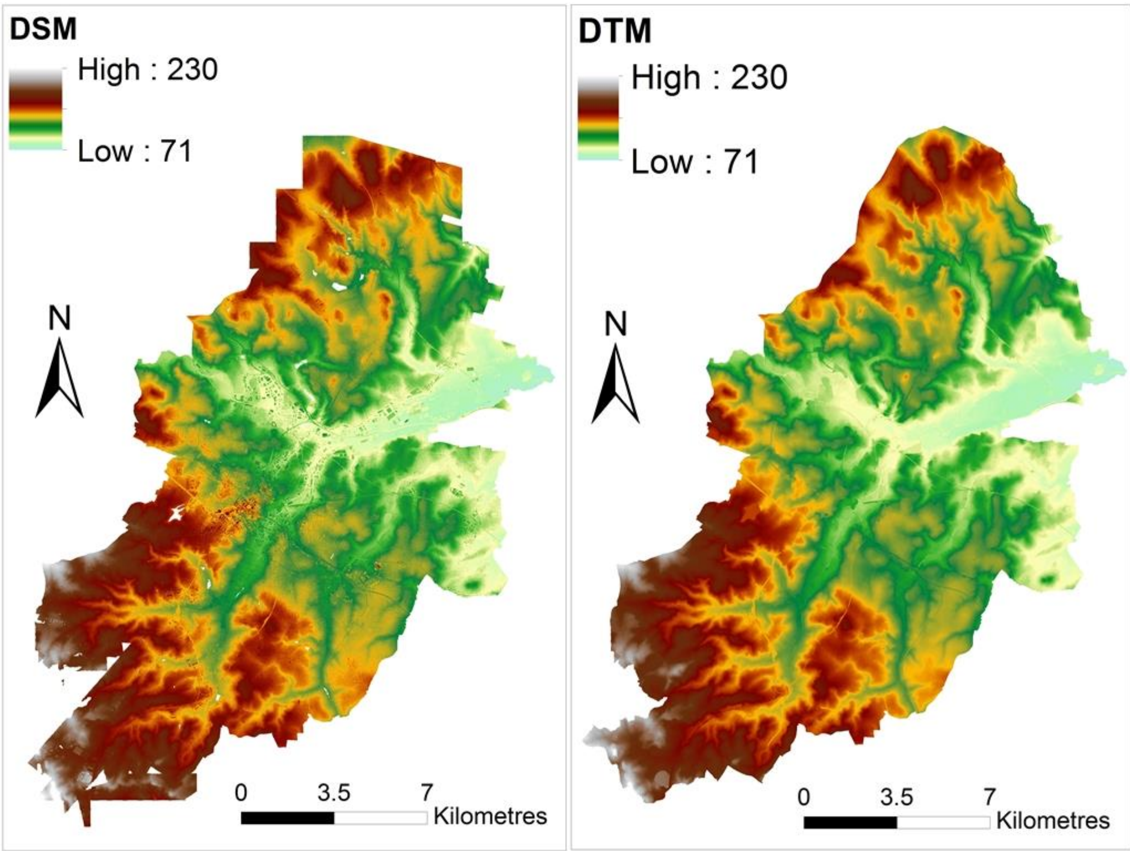

Figure 5.7: DSM and DTM models (metres). DSM is 1m spatial resolution derived from LIDAR data, and DTM is 5m pixel size captured as a triangulated irregular network.

5.2.2.3 Meteorological data

The hourly meteorological variables not available from the HiTemp were acquired from The Centre for Environmental Data Archival (CEDA). CEDA is a data centre for the atmospheric sciences run by NERC. Rainfall, cloud cover and solar radiation data for ground stations in Birmingham were downloaded from the Met office Integrated Data Archive System (MIDAS) catalogue (MIDAS, 2015).

5.3 Method

Most of the input data required format conversion, extent extraction and resampling to be handled and overlaid with other layers in ArcGIS and other software. GIS applications have been commonly used to represent the current status and plan the future of the urban environment, as they are well suited to address spatial data and visualization issues associated with multiscale geographical data (Xu and Coors, 2012). Wong et al. (2016) employed the integration of GIS, GPS and logging sensors in microclimate monitoring to study impacts of environmental and human factors on UHI in Hong Kong. Furthermore, ArcGIS and ENVI (an acronym for "Environment for Visualizing Images") were coupled to investigate and identify land use types which had the most influence to the increase of ambient temperature in Singapore (Jusuf et al., 2007).

Initially, the air temperature data are raw data divided into daily files for individual stations. Erroneous readings were identified from flags assigned to each observation provided by the Birmingham Urban Climate Lab (BUCL) guide, and omitted. Temperature records and other meteorological parameters were extracted from each station for a specific time with the coordinates and elevation. The process of cleaning the data and extracting them was undertaken by a MATLAB code as described in Appendix D. These text files were exported to ArcGIS to be converted to feature class and raster images by Inverse Distance Weighting (IDW). The spatial resolution of the air temperature raster following IDW interpolation of the point measurements is 84.15 m. This spatial resolution is similar to the topography layers pixel size in Figures 5.2 and 5.3 that were used to process the IDW. A statistical and spatial analysis was then performed to find the high intensity UHI hours. The hourly time scale is sufficient for the purpose of this study, and any unexpected values were investigated. Some studies used filtration schemes to investigate the UHI events for certain weather conditions or specific times of the year. Tomlinson et al. (2012) employed an atmospheric stability approach named Pasquill-Gifford stability to classify the weather conditions from extremely unstable to extremely stable. Their results averaged UHI events over four Pasquill-Gifford stability classes which are neutral, slightly stable, moderately stable, and extremely stable. Azevedo et al. (2016a) quantified the daytime and night-time UHI in Birmingham using LST data obtained for only June, July and August (JJA). Nevertheless, this study has not set any assumptions, so all the HiTemp data were included in the analysis. Accordingly, the underlying assumption is that the CUHI might happen in any weather condition and during the day and time throughout the whole year.

The land cover data were extracted to the extent of the study site after converting its format to raster images. Also, a data extractor tool called CEDA Web Processing Service (WPS) was used to extract the meteorological data from MIDAS for the time period and spatial range of the study. The high-resolution DSM model and OS Mastermap were built by mosaicking the 1 km2 grids and converting the formats to raster images.

The next stage is processing and modelling the influencing parameters. Land cover data were extracted to include all the various physical parameters. Then, geometrical factors such as Sky View Factor (SVF), Visible Sky (VS) and Terrain View Factor (TVF) were derived using the

DSM as input to the free and open source Quantum GIS (QGIS). The SVF algorithm in QGIS was used to derive the SVF, VS, and TVF by using the DSM as the elevation model and choosing the default parameters of the maximum search radius and method. Shadow patterns and illumination images were constructed for the days of high UHI intensity. The last stage of the method was building multiple linear regressions, where the relationship between air temperature and the variables (influencing parameters) could be explored. After building and running the regression models using SPSS, the models were enhanced using the backward elimination method until a significant model was found. The backward elimination method is an economical procedure to choose the best regression equation by removing the variable being investigated that has the highest P value until the model becomes significant (Draper, 1998). The P value (or the observed significance level) is the smallest fixed level at which the null hypothesis can be rejected (Dallal, 2000). A variable is considered significant if its p-value is less than 0.05 at a confidence level 95%, and the relationship becomes highly significant if the p-value is less than 0.01.

5.4 Results and discussion

This section discusses the temporal and spatial change of CUHI. Also, it shows the derived geometrical parameters as well as some of the shadow patterns. These parameters and others are the inputs to the regression analysis to identify the correlation between the CUHI and influencing parameters.

5.4.1 CUHI temporal change

The historical air temperature data (1990- 2014) for the City Centre of Birmingham were acquired from the Met Office (MIDAS, 2015) for the purpose of validating the use of HiTemp data from June 2012- June 2014. Figure 5.8 draws the averages of the maximum and minimum air temperatures with their trends for the period (1990- 2014). The means of the maximum and minimum for the 25 years are 13.01 and 6.91 ºC, respectively, with SD of 0.75 for the maximum temperature and 0.77 for the minimum. The HiTemp means of the maximum temperature for the 2012, 2013 and 2014 years are 12.83, 12.40 and 13.30 ºC, and for the minimum are 6.36, 6.96 and 7.52 respectively. Therefore, the averages of the temperatures during the period 2012- 2014 lie within the mean and the standard deviation of the 25 years historical data. So, this 2 years (HiTemp Project) period can be considered typical for the period covered by the historical data (1990- 2014). The averages of the maximum and minimum air temperatures during the whole (2012-2014) period of the collected data are 12.19 and 9.68 ºC with SD 5.30 and 5.72 respectively.

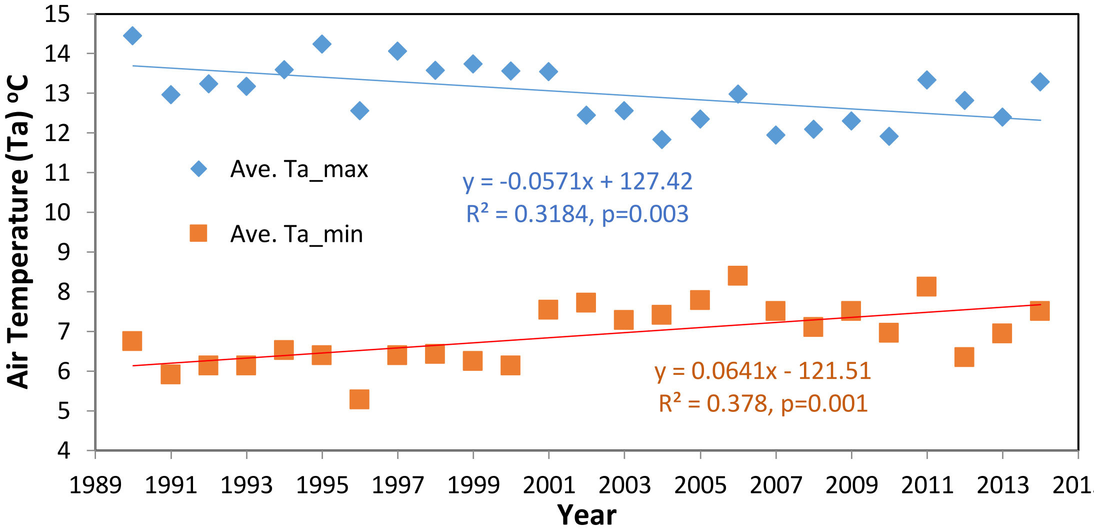

Figure 5.8: Historical air temperatures of Birmingham City acquired from the Met Office over the period (1990- 2014).

Next, the data were analysed per hour to summarise the variation of CUHI, then monthly statistics were calculated to show the seasonal change of temperature patterns as shown in Table 5.2. Also, extreme events were identified with the climatic condition, and the spatial distribution of hot spots was extracted. The CUHI was derived from the air temperature measurements by subtracting the maximum value from the pixel value per hour. The hourly statistical analysis of CUHI for 2 years of measurements has demonstrated that around 56% of total 17520 hours gave an air temperature variation more than 1.5 °C in the City of Birmingham. This was used to set a threshold of 1.5 ºC difference in temperature as a minimum variation to indicate the CUHI's presence. Interestingly, the maximum CUHI intensity was in September, at 13.5 °C, and the lowest intensity 5 °C was in January. However, the monthly highest average CUHI 3.9 °C was monitored in July, whereas, the lowest average was in January by 2.3 °C. Besides, the longest hours of CUHI occurrence were in June by 1323 hours, and the shortest, 471 hours of occurrence were in February.

Table: 5.2: Statistical summary of CUHI analysis calculated from HiTemp data of Birmingham.

Statistics\Month	Dec.	Nov.	Oct.	Sep.	Aug.	Jul.	Jun.	May	Apr.	Mar.	Feb.	Jan.
Count (hr)	719	853	715	806	727	686	1323	1184	1104	854	471	476
Ave. CUHI (°C)	2.5	2.6	2.5	3.5	3.3	3.9	3	3	2.8	2.8	2.4	2.3
Max. CUHI (°C)	9.1	6.3	6.8	13.5	7.6	13.4	9.6	10.7	7.9	12.4	6.7	5

Moreover, CUHI events with intensity over 10 °C showed that it can happen in the evening, night or early morning times as detailed in Table 5.3. Table 5.3 includes the date and time of the highest CUHI events over 10 °C with the averages of wind speed, also the times of sunrise and sunset were added to distinguish between the day and night (Time and Date, 2013). The extreme events (over 10 °C) are listed in Table 5.3 in descending order, regardless, of the dates of occurrence, to show their magnitude and time. It is important to notice that none of the highest intensity CUHI (over 10 °C) coincided with the heat wave that affected most of the UK from 3 to 23 July 2013. This might be due to the local instant effect of the CUHI, while the heat waves have larger regional influence.

The UHI induces more intense heat waves through the global warming in the long term, and the former is being referred to as either a cause or consequence of the later (Alcoforado and Andrade, 2008). The Met office has declared the July 2013 heat wave as the third warmest on record, and this month as the warmest and sunniest for the whole UK since 2006 (Met Office, 2015). Nevertheless, the highest temperature in 2013 recorded by the Met Office stations in Birmingham was 30.5 °C on the 1 August 2013 at 3 p.m. (MIDAS, 2015), while, using HiTemp network the highest temperature in Birmingham at the same time was 31.2 °C. Furthermore, it was not the highest temperature recorded by HiTemp on that day, as it recorded 32.34 °C on the same day (1 August 2013) at 5 p.m. This difference between Met Office and HiTemp' readings might be due to the height of the sensors. HiTemp sensors were installed at 3 m (with exceptions no more than 0.5 m higher or lower), while Met Office sensors were installed almost 5 m above the ground level (Chapman et al., 2015b). The 3m high sensors will be more affected by surrounding surface heat, as they are closer to the energy sources (Chapman et al., 2015b). Furthermore, the Met Office stations do not cover the full variation of the temperature due to the limited number of stations. On the other hand, most of the extreme events in Table 5.3 coincided with calm (< 1 m/s) or light air (1- 2 m/s) wind speed as described by the Beaufort wind force scale (Met Office, 2016). This agrees with Roth (2012), that the heat island is greatest under light wind conditions.

The CUHI events with intensity over 10 °C were investigated to figure out where they had peaked. Figure 5.9 gives some examples of CUHI events with intensity over 10 °C in the form of (year_ month_ day_ hour), also some important features included to have a spatial reference of the peak temperature patterns. The peak events concentrated in two main places. The first place lies about 6 km to the south of the City Centre, and the air temperature sensor in this area is S110. The HiTemp project's metadata states that the surface cover below the sensor S110 is grass and asphalt (BUCL, 2014b). The sensor S110 is in a school within a dense suburban area as shown in Figure 5.10, and it is adjacent to urban area. The second place that the CUHI over 10 °C peaked at, is located around 6 km south-east of the Sutton Park (see Figure 5.9). Two sensors are available in this area, S144 and S025 which are located at school sites. S025 is in a dense suburban area, while, S144 is in a suburban just next to an urban area (see Figure 5.10). The surface cover below the S025 sensor is made of asphalt, grass, soft asphalt, wood, and metal. Whereas, the surface cover below the S144 sensor is made of asphalt, canvas, astroturf and soft asphalt (BUCL, 2014b). The important finding in this case (CUHI > 10 °C) is that the temperature patterns peaked at suburban areas far from the City Centre during out of working hours. The occurring time of the CUHI over 10 °C events are between 4 p.m. and 6 a.m., and the locations are almost suburban areas. The explanation of this phenomena is that when people are at home, they increase the anthropogenic heat release which elevates the air temperature.

However, when people go to work which is mostly moving towards the City Centre this limits the human activities in the suburban areas.

Furthermore, the sensors are located at schools, and the working hours for the schools are usually from 9 a.m. to 4p.m. However, anthropogenic fluxes released from student's activities and school's energy consumption do not appear to have significant effect on the temperature magnitude. Because the temperature values did not peak at working time, and the surrounding areas effect seems more dominant than the impact of the local environment on a specific point of measurement. This highlights the success of the network configuration, as sensors where installed at a distance from the sources of energy. So, the high intensity fluxes from specific sources will not highly influence the readings of temperature, which insures no bias in the monitoring system.

Table 5.3: Birmingham's CUHI intensity over 10 °C events and average wind speed listed in descending order, and Calculated from HiTemp data.

Date	Hour	Sunrise	Sunset	CUHI Intensity (°C)	Ave. Wind Speed (m/sec.)
04/09/2013	19	06:25	19:47	13.53	0.44
05/09/2013	17	06:26	19:45	13.46	1.52
01/07/2013	21	04:50	21:33	13.37	0.53
01/07/2013	20	04:50	21:33	13.22	0.88
01/07/2013	22	04:50	21:33	13.17	0.54
05/09/2013	18	06:26	19:45	12.74	2.04
04/09/2013	20	06:25	19:47	11.83	0.39
04/09/2013	18	06:25	19:47	11.68	0.92
03/09/2013	19	06:23	19:49	11.60	0.36
07/09/2013	18	06:30	19:40	11.56	1.13
03/09/2013	18	06:23	19:49	11.27	0.53
01/07/2013	19	04:50	21:33	11.26	1.31
01/07/2013	16	04:50	21:33	11.20	1.85
05/09/2013	19	06:26	19:45	11.04	2.13
04/09/2013	21	06:25	19:47	11.02	0.31
05/09/2013	05	06:26	19:45	10.72	0.40
05/09/2013	01	06:26	19:45	10.70	0.62
24/05/2013	11	04:57	21:11	10.67	2.31
01/07/2013	17	04:50	21:33	10.64	1.85
05/09/2013	04	06:26	19:45	10.63	0.36
05/09/2013	03	06:26	19:45	10.60	0.47
05/09/2013	02	06:26	19:45	10.56	0.47
01/07/2013	18	04:50	21:33	10.45	1.84
04/09/2013	17	06:25	19:47	10.38	0.97
04/09/2013	22	06:25	19:47	10.33	0.45
05/09/2013	00	06:26	19:45	10.25	0.67
16/09/2013	17	06:45	19:19	10.18	2.33
05/09/2013	06	06:26	19:45	10.18	0.67
04/09/2013	23	06:25	19:47	10.01	0.43

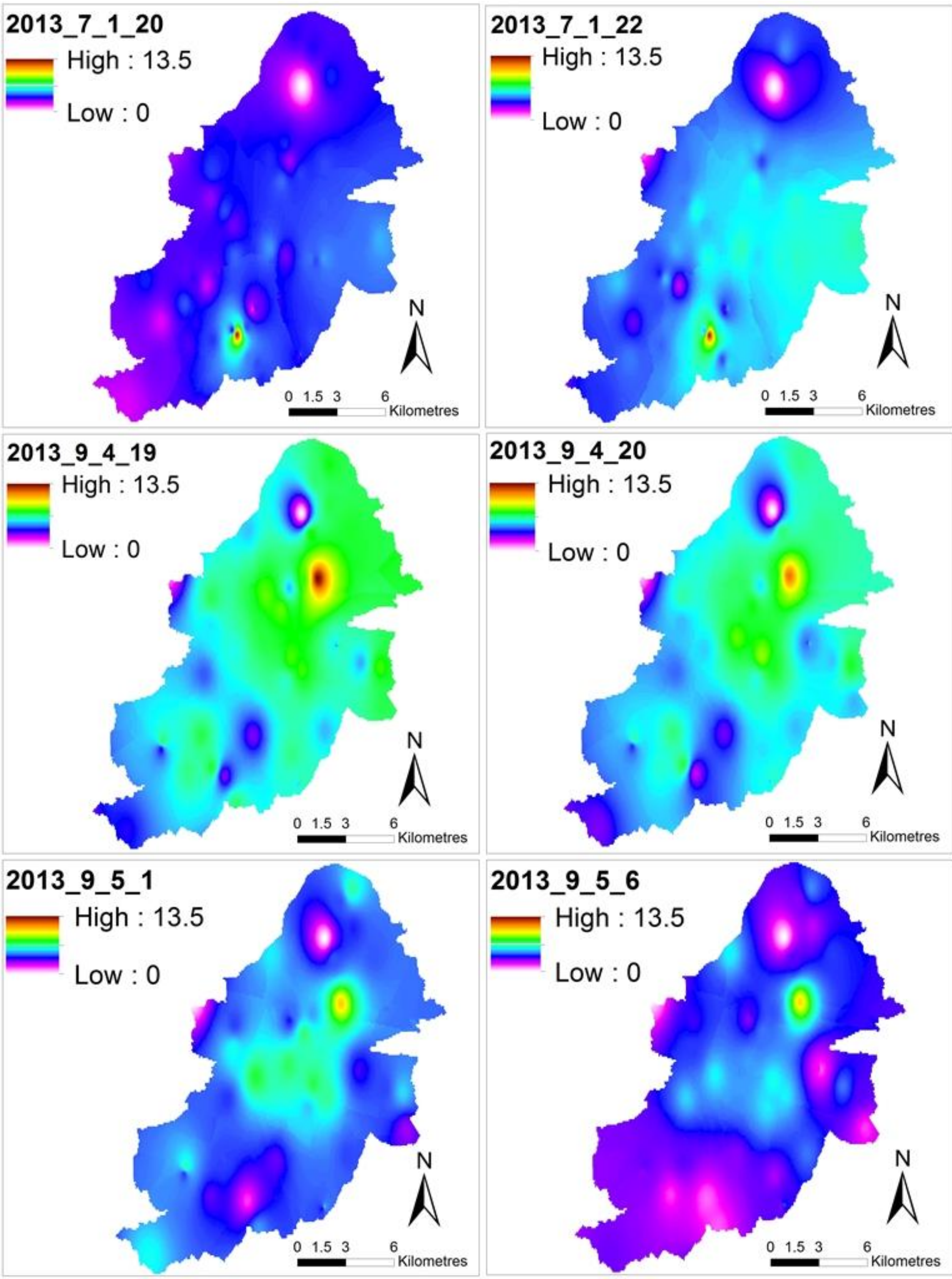

Figure 5.9: Examples of Birmingham's CUHI events with intensity over 10 °C, and the legend title in the form of (year_ month_ day_ hour).

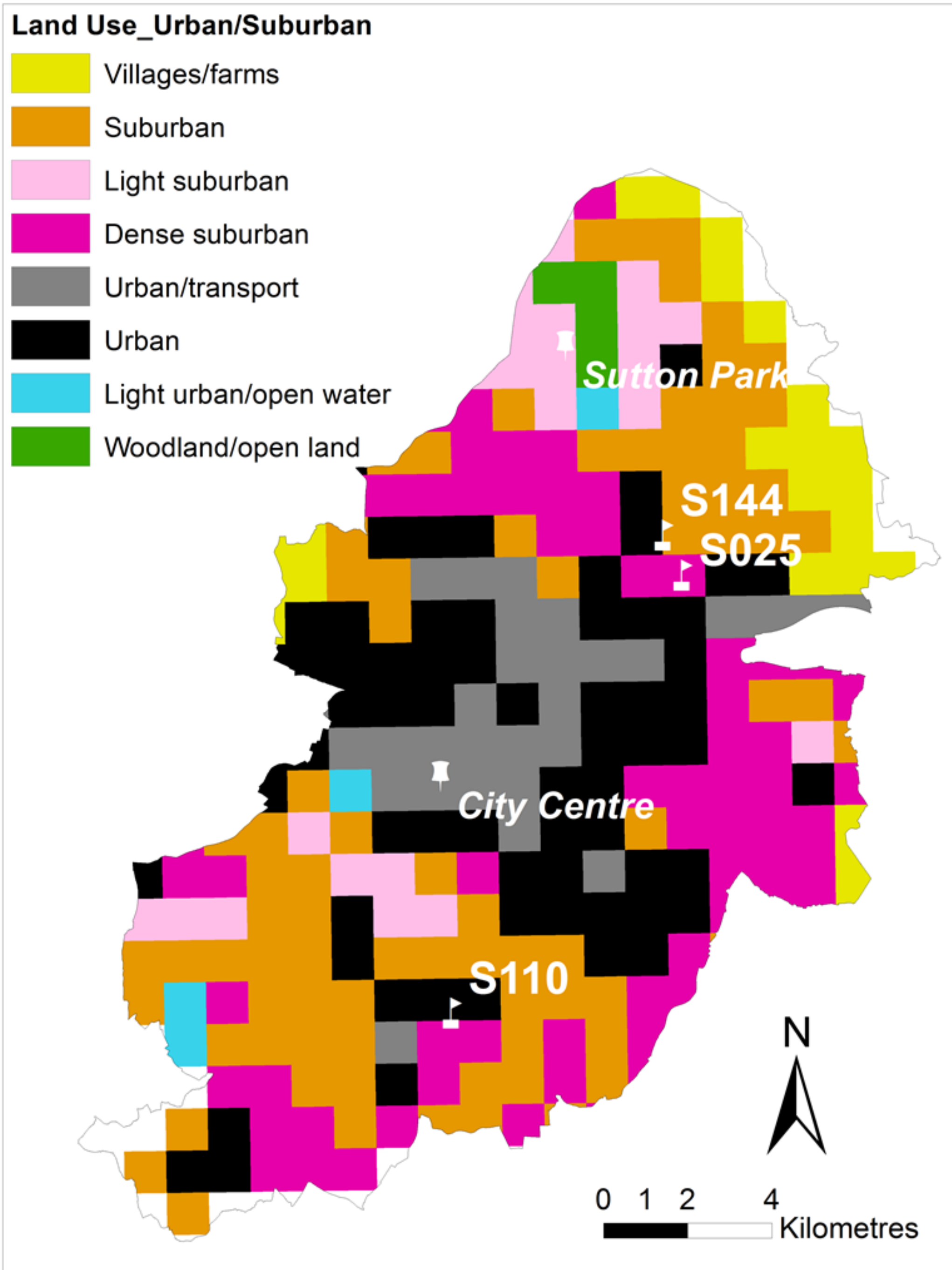

Figure 5.10: Birmingham's land use, urban features, and specific sensors. The land use classes adapted from Tomlinson et al. (2012), and the locations of the sensors obtained from the HiTemp project metadata.

5.4.2 CUHI spatial change

The CUHI was found to be concentrated in the City Centre when its intensity is close to the mean values; however, the extreme intensities were seen to stretch to the suburban areas due to the weather parameters in particular, the wind. Oke (1988) states that the maximum AUHI develops (3- 5) hours after the sunset in clear and calm weather. The analysis of HiTemp data supports Oke's claim. However, high CUHI intensity can happen in the early morning, before sunset, or during the day in a cloudy weather when not much of the sun's radiation reaches the ground to change the surface energy balance. The higher spatial resolution of the HiTemp air temperature measurements compared to the data used by Oke (1988) were able to detect that high CUHI intensity can occur at almost any time of the day. Figure 5.11 gives examples of strong CUHI's at the City Centre for each season, and the layer name in the legend provides the date and time of the image in the format of year, month, day and hour. The highest intensities of CUHI appear in or around the City Centre, and the size of the red spot reveals the extent of the coverage. However, there are some spots of high intensity CUHI away from the City Centre; this is mainly due to the wind speed and direction as shown in Figure 5.12. Furthermore, the lower temperature areas clearly appear over the grass of the Sutton Park which is the largest park in Birmingham that has vegetation and trees.

Figure 5.12 shows the wind speed and direction at the same dates and time of Figure 5.11, and on average for the entire Birmingham area the low wind speed coincides with high CUHI intensity. Local wind speed is relatively high when the hot spots are concentrated in and around the City Centre, however, the average wind speed for the entire city is low. Because the presence of high buildings traps the release of heat into the atmosphere and increases the speed of the air flow. Whilst, the wind direction does not impact on the CUHI intensity, it affects the size and distribution of the hot and cold spots. So, the CUHI intensity is high for different wind directions, however, the size and distribution of hot spots are fluctuated for the dates and times in Figure 5.11 especially for (2013_9_5_7). Which shows high wind speeds outside the city and its patterns change in direction around the city, to create sparse hot spots in the city and away from it.

To investigate the daily change of CUHI, Figure 5.13 shows the movement of hot and cold spots over the city in different times for a selected day when the CUHI intensities are close to the average, as detailed in Table 5.2. The heat islands concentrate in and around the City Centre during the night and early morning, and they move clockwise to Sutton Park to return to the City Centre after the sunset. Sunrise and sunset on the 6th October 2013 were 4:53 and 21:31 respectively (Time and Date, 2013), with 1.33 m/s average wind speed. When Sutton Park becomes a heat island, the City Centre works as a cool island compared with their adjacent areas. The daily wind speed and direction as shown in Figure 5.14 matches the same date and times of the daily CUHI distribution in Birmingham shown in Figure 5.13. The CUHI peaks at the City Centre when the wind speed is lower than 2 m/s (light air), and its direction above the city is heading towards the north. Usually, the wind direction is described based on where it comes from, so when the wind moves to the north it is called the south wind (Cermak et al., 1995). This agrees with the finding of Bassett et al. (2016) who indicate that the UHA can contribute to a maximum of 1.2 ºC to the warming of areas downwind of Birmingham City. Other influencing parameters on the formation of UHI are investigated later in this Chapter.

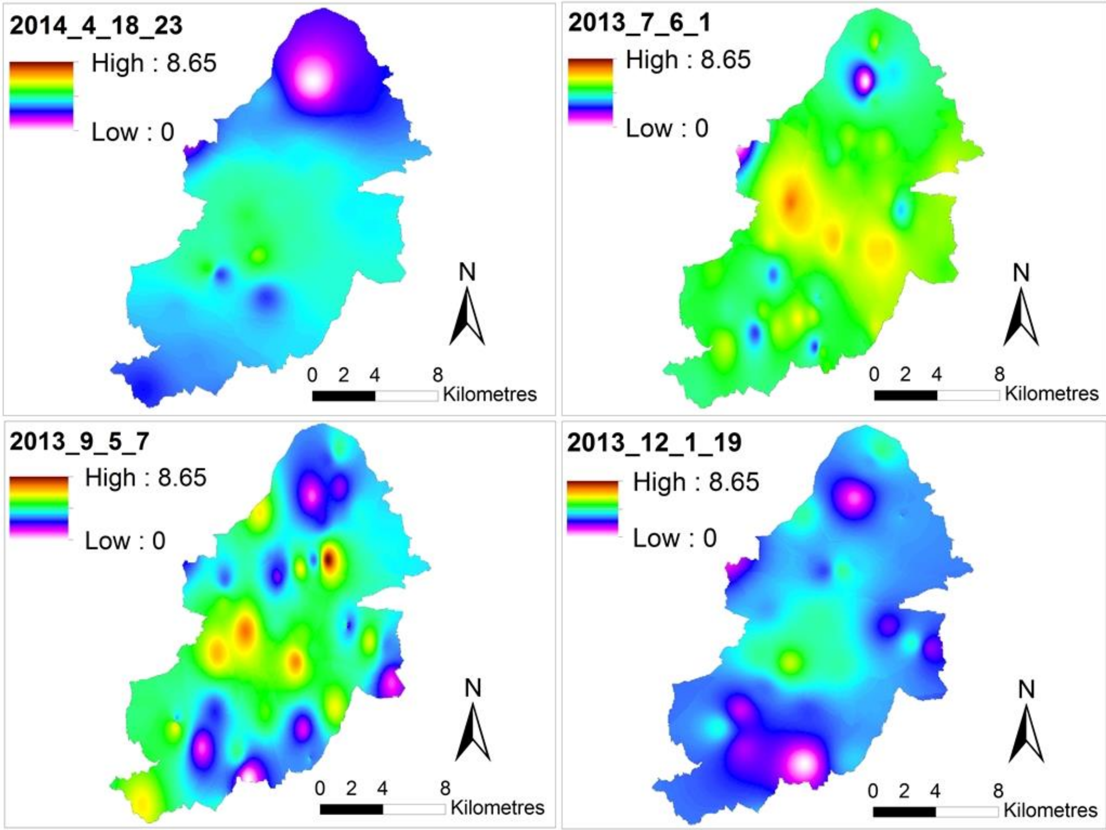

Figure 5.11: Seasonal examples of strong CUHI's at the City Centre of Birmingham (°C).

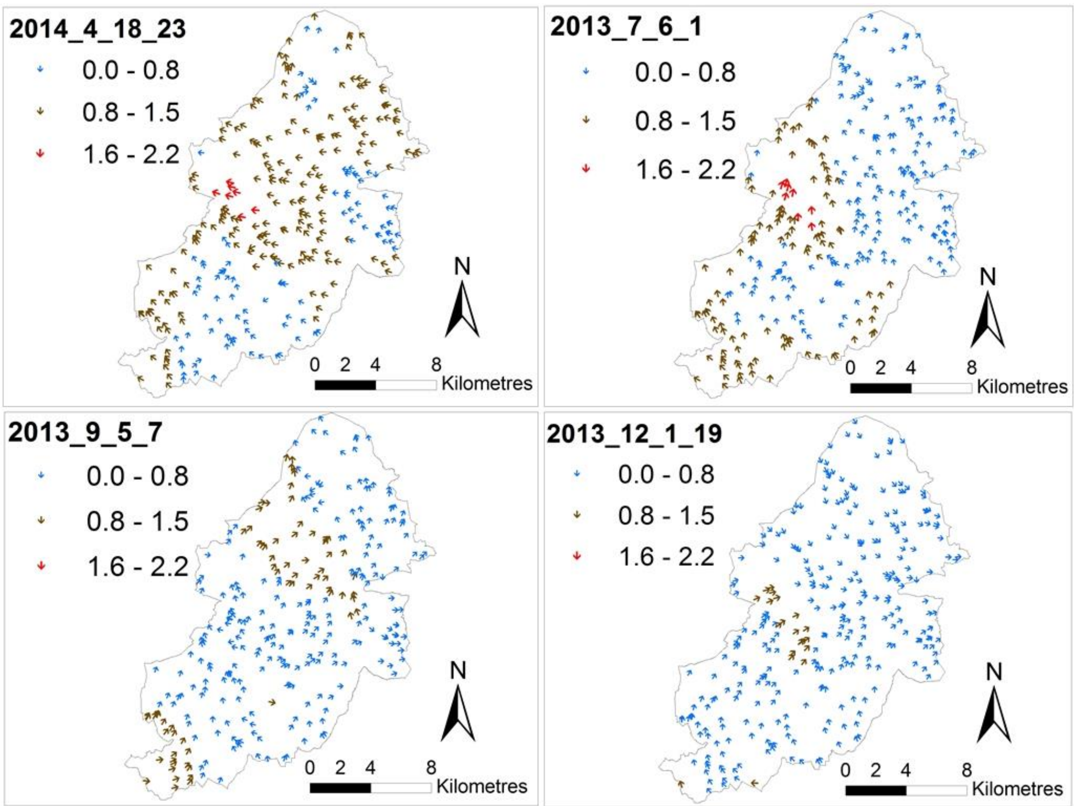

Figure 5.12: Seasonal wind speeds (m/s) and directions in Birmingham at the same dates and time of Figure 5.11.

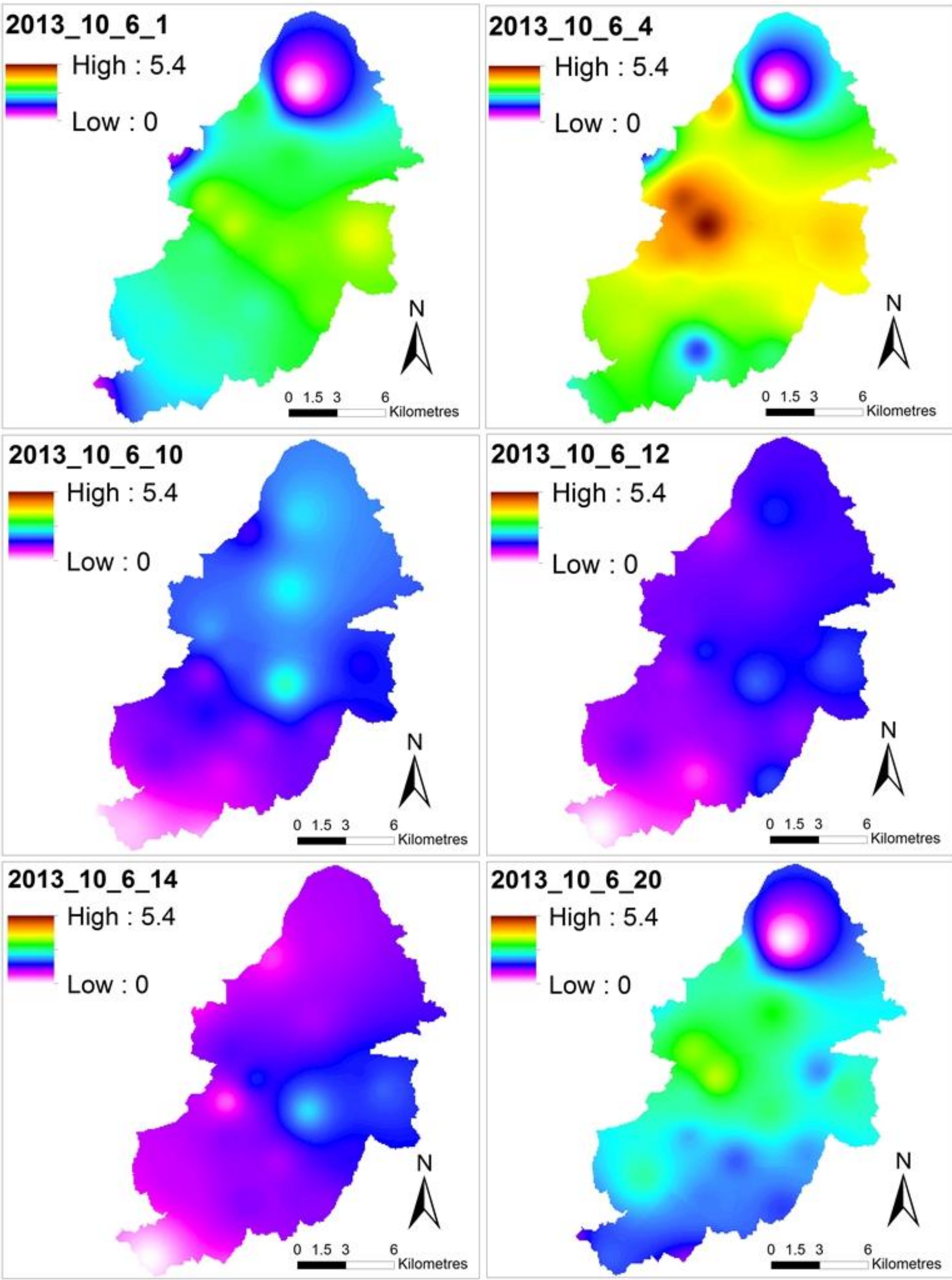

Figure 5.13: Example of daily CUHI change over the city of Birmingham when the CUHI intensity is close to the average (°C).

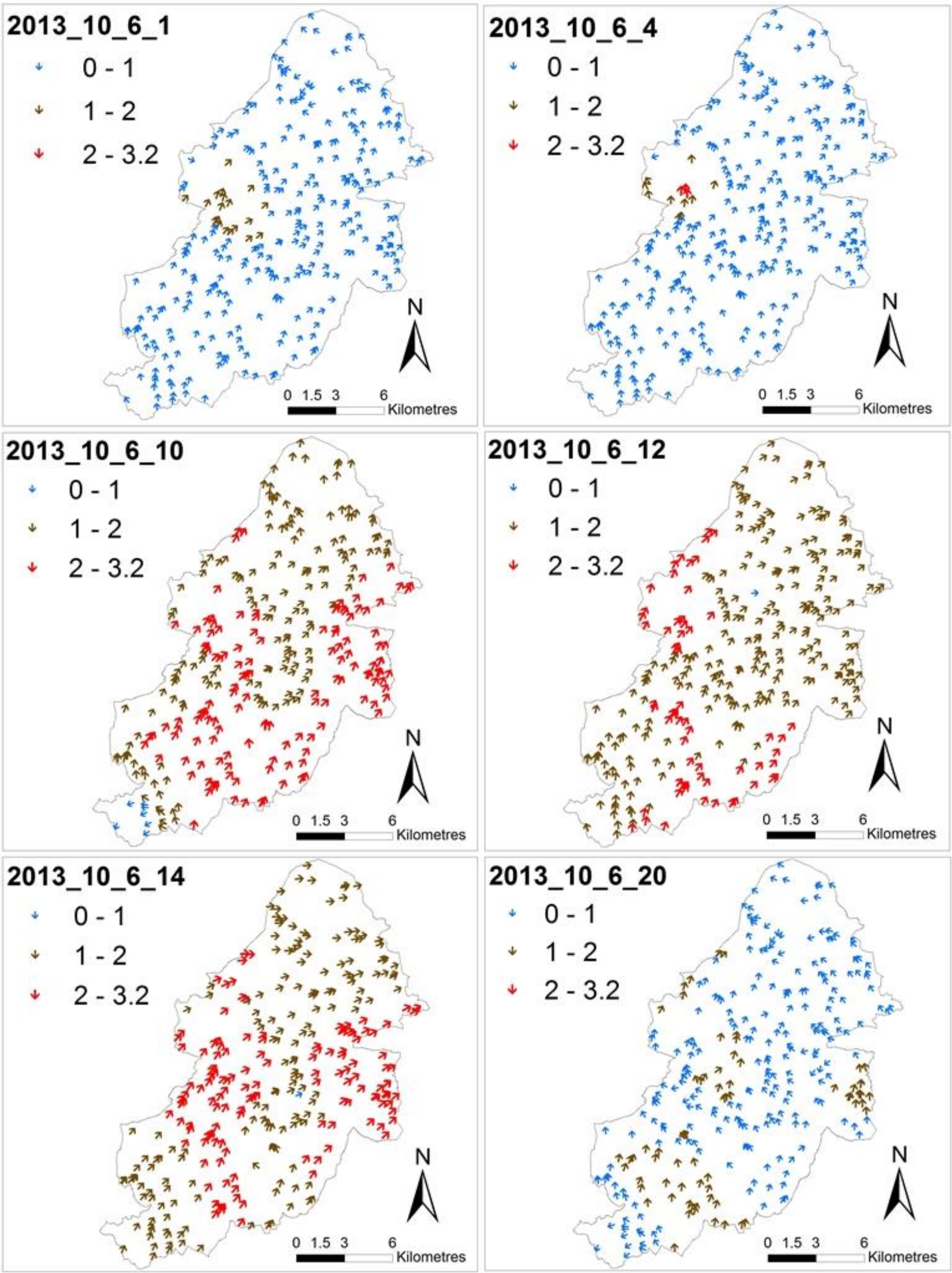

Figure 5.14: Example of daily wind speed (m/sec) and direction in Birmingham at the same dates and time of Figure 5.13.

5.4.3 Geometrical parameters derivation

The derivation of the geometrical parameters provided layers of Sky View Factor (SVF), Visible Sky (VS) and Terrain View Factor (TVF). The SVF and VS are dimensionless measures to estimate the visible area of the sky from an earth viewpoint (Souza et al., 2003), while, TVF is the opposite to them (Böhner and Antonić, 2009). Figure 5.15 shows the variation of SVF, VS and TVF through the entire city of Birmingham. Gal et al. (2009) verifies that the use of high resolution DEM is very useful to obtain a general picture of the geometrical size and shape of an urban environment. The derived parameters in Figure 5.15 show that the SVF (0-1) and VS (1.9-100) values are low in the City Centre and within the dense trees areas but high in the open spaces. Conversely, the values of TVF are high in the City Centre and low in the open spaces, due to the presence of high buildings in the City Centre which do not exist in the open areas.

Pairs of stations close to each other were chosen to investigate the impact of shadow patterns on air temperature. To be sure that no other functions are responsible for the variations in temperature, it is necessary to compare stations that are close to each other, thus eliminating other variables. Another challenge is that the shadow is time dependant and varies significantly during the day. For these reasons, the effect of shadow on CUHI formation has been investigated separately from other parameters. The hill-shade tool in ArcGIS creates a shaded relief from a surface raster by considering the illumination source angle and shadows (ArcGIS Resource Center, 2011). The shadow areas can be distinguished by the black colour (Figure 5.16), and the areas of minimal or no shadows are scaled in shades of grey between (1- 254). The analysis of level of shadow did not show significant correlation with the air temperature. However, the presence of shade reduced the air temperature by up to 2 °C, by comparing the air temperature of a station in the shade and with one in no shade. Stations in Figure 5.16 a & b recorded lower temperatures when they are under shade compared to those exposed to the sunshine. Figure 5.16 c & d give examples when the shade moves from one station to another, and in both cases the station under the shade was slightly cooler than the one exposed to the sunshine. Moreover, all the pairs of stations in Figure 5.16 did not show significant variation of temperature measurements when they are both under the shade or exposed to the sunshine at the same time. So, the degree of illumination does not have a noticeable impact on the temperature’s readings.

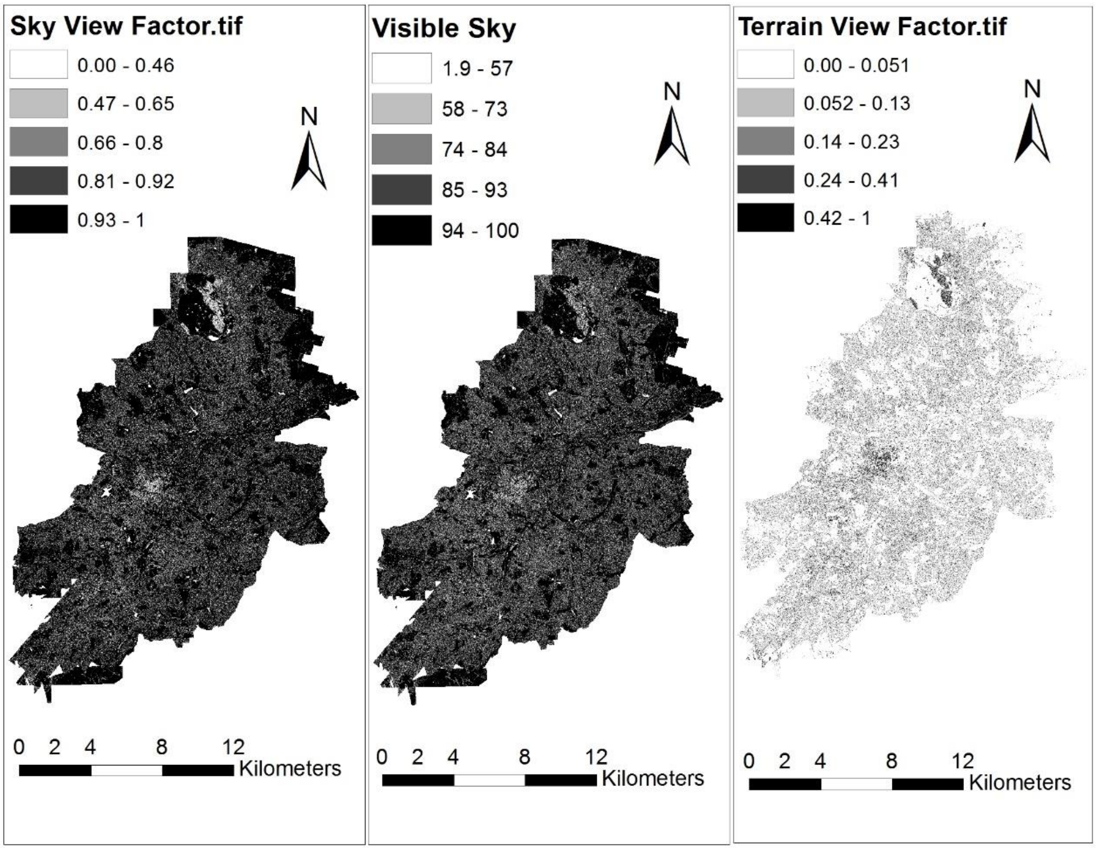

Figure 5.15: Birmingham's Sky View Factor (SVF), Visible Sky (VS) and Terrain View Factor (TVF) derived from the DSM (Dimensionless).

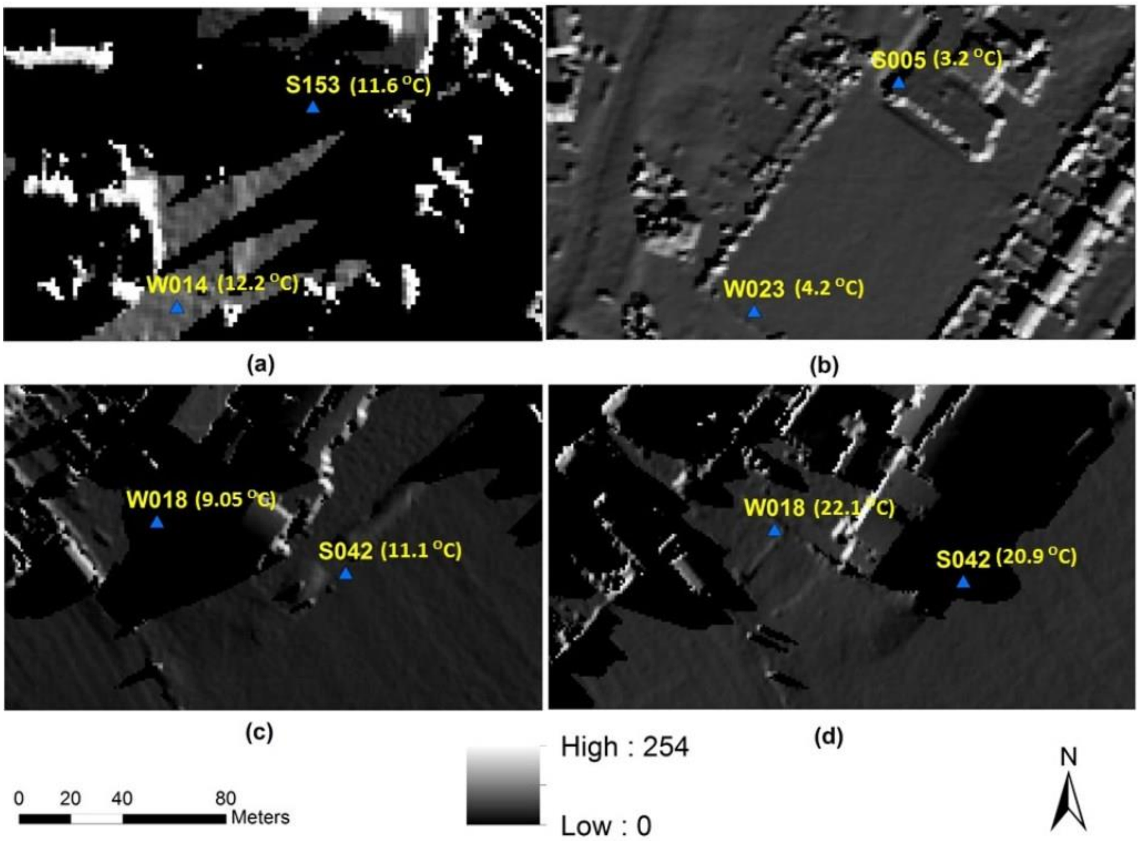

Figure 5.16: Birmingham's shadow and illumination patterns for pairs of stations and the corresponding air temperatures on the (a) 1st July 2013 at 6 am, (b) 30th November 2013 at 10 am, (c) 11th July 2013 at 5 am, and (d) 11th July 2013 at 7 p.m.

5.4.4 Identifying influencing parameters

The influencing parameters on the generation of CUHI could be broadly characterised into two classes: controllable and uncontrollable (Rizwan et al., 2008). Rizwan et al. (2008) further characterised these classes into permanent, temporary and cyclic effects variables. The controllable variables which appear to be more permanent can be either urban design and structure related factors such as land cover and SVF, or population related such as anthropogenic heat and air pollutants (Cheung, 2011). The uncontrollable factors are environment and nature related which seem to have temporary effects such as anticyclone conditions, seasons, wind speed and cloud cover (Cheung, 2011). Shalaby (2012) clarifies that the controllable factors can be humanly controlled to some extent, while, the uncontrollable factors are normally beyond people's control. On the other hand, solar irradiation has cyclic effects on both controllable and uncontrollable factors, Shishegar (2014) asserts. Accordingly, this study models both the controllable and uncontrollable influencing parameters.

Four days were selected to represent the four seasons in Birmingham. These days were chosen to have CUHI intensity between the average and the maximum monthly values as detailed earlier in Table 5.2, and their CUHI spatial distributions for specific times are shown in Figure

5.11. The independent controllable parameters are VS, Urban Atlas (UA), Topographic Themes (TT), Topographic Groups (TG), TVF, SVF, Land Classes (LC), DTM, DSM, and Population (PO). The uncontrollable independent parameters are Solar Radiation (SR), Wind Speed (WS), Relative Humidity (RH), and Atmospheric Pressure (PR). Accordingly, the input predictors were 14 in total, 10 of them are controllable and 4 uncontrollable. The population parameter can refer to the anthropogenic heat, as more people in a place means more energy consumption. Rizwan et al. (2008) reports that the UHI positively correlated with the city population. Another study by Tran et al. (2006) assessed the effects of UHI with satellite data in twelve Asian mega cities, and stated that the UHI intensity positively correlated with city population.

The dependent parameter is the air temperature (Ta) which indicates the presence of CUHI. The modelling of the relationship between Ta and influencing parameters was carried out using SPSS multiple linear regressions by stepwise elimination of non-significant parameters. The Ta was regressed against the influencing parameters on hourly basis. A model was significant if the p values were less than 0.01 for the whole model and individual parameters. Furthermore, the models were tested for collinearity, heteroscedacity, outliers, and normality of residuals as described by IDRE (2016).

Table 5.4 gives summary statistics of the output significant regression models on the 4th of April 2014, when the season is spring in Birmingham. The outputs include the Pearson correlation coefficients of the significant individual parameters as well as the R^2 values for the entire model for each hour of the modelled day. Furthermore, the averages of hourly weather data were included to identify any significant weather patterns that coincide with the presence of significant entire models or individual parameters. The weather averages were calculated based on the data acquired from AWS sensors of the HiTemp project, as they record the main meteorological variables. Tables 5.5, 5.6 and 5.7 contain similar information to those in Table 5.4, however, each table represent a sample of one of the four seasons in Birmingham. The Pearson coefficients are dimensionless values ranging between-1 to 1. The positive signs of the coefficients mean positive correlation between that parameter and the Ta. And the negative sign of the coefficients means negative correlation between that parameter and the Ta. The zero fields in the tables mean that parameter did not show significant correlation with the Ta, or sometimes specific parameters have collinearity and the less important ones were eliminated from the regression. For instance, DTM and DSM almost have high correlation between them (over 70%), as the only difference between them is that the DTM is derived without the manmade objects on the ground. Furthermore, other sets of highly correlated parameters were SVF and VS, DTM and PR. These were found to be highly correlated, and consequently they do not frequently appear all together in significant models. The reason for including these parameters in the regression process is that their relative influence was unknown. So, the only way to investigate their effects was to include them and test their importance. It is important to note that the land cover maps, DSM, DTM were produced a few years prior to the air temperature measurements and this might be a possible source of errors in the fit of the regression models.

Table 5.4 highlights the importance of the selected parameters to predict the Ta as some of the models have R^2 just over 90%. Most of the controllable and uncontrollable parameters showed high significant correlation with Ta over the 24 hours on the 18th of April 2014. The uncontrollable parameters (SR, WS, RH, & PR) showed higher influence on the Ta than the controllable ones. The lowest R^2 was 0.30, and the highest was 0.91, which means the influencing parameters could predict up to 91% of the Ta variation. Nearly all the uncontrollable parameters participated to form the highly significant models. The SR and PR positively contributed to Ta, while WS and RH negatively contributed to Ta. The RH was the biggest contributor to Ta among the uncontrollable parameters. On the other hand, PO was the biggest contributor to Ta among the controllable parameters. Most of the controllable parameters positively contributed to Ta. The models with the highest R^2 (0.91) were predicted after the sunset, when the WS was less than 1 m/sec and the air was moist. Lawrence (2005) explains that the air is called moist when its RH is more that 50%. The most important LULC predictors were LC and TG. The TG appeared to have more effects during the night-time than the daytime. The SR values can give indication about the presence of clouds during the daytime, as SR is zero or close to it at night-time and in the case of clouds. From the temporal variation of SR values throughout the day on the 18th of April 2018, it is almost a clear day. Also, the weather data in Table 5.4 shows that there is a negative correlation between the SR and RH, and WS is weaker during the night. These conditions are typical for the formation of high intensity UHI as described by Oke (1981). The highest Ta was 11.9 ºC at 15:00, and SR peaked at 13:00 by 71.4 w/m^2.

Table 5.5 gives the summary statistics of regression modelling on the 6th of July 2013 when it is summer in Birmingham. The highest R^2 was 0.71, and the lowest was 0.34. The uncontrollable parameters are still dominant in the significant models, with new controllable parameters appearing that were not significant in Table 5.4. So, DTM and DSM appeared in few models to negatively contribute to Ta. In general, most of the important correlations with Ta and the significant parameters were the same as in Table 5.4. However, a small shift towards the controllable parameters having more influence can be seen in Table 5.5 compared to Table 5.4. In addition to DTM and DSM, UA and TVF negatively contributed to the Ta. The most important LULC predictors were LC and UA. The LC seems to have more effects during the night-time, whereas, the WS noticeably affected the models during the daytime. The R^2 values show a pattern; they decreased with the time. So, they were relatively higher at the beginning of the day (00:00) in Table 5.5, and went down at the end of the day (23:00). From the weather averages, the Ta increased after the sun rise, while, the RH decreased, and the WS increased. The highest Ta was 25.2 ºC at 17:00 and 18:00, while the highest irradiance was 80 W/m^2 at 12:00 (see Table 5.5).

Table 5.6 shows the outputs of modelling the influencing parameters on the 5th of September 2013, when it is autumn. The R^2 values fluctuated from 0.24 to 0.84. The most dominant controllable parameter is PO, whereas, RH is still on top of the uncontrollable parameters. Table 5.6 reflects more role for the controllable parameters to form the significant models compared to Tables 5.5 & 5.4. The most important LULC predictor was LC, while, DTM was the most important topographic parameter. The DTM appeared to influence the models during the daytime more than the night-time. The highest Ta was 21.7 ºC at 16:00 and 18:00, while the highest irradiance was 64.4 W/m^2 at 11:00. The PR recorded low values in Table 5.6 compared to Tables 5.4, 5.5, and 5.7, as it did not cross 1000 hPa (HectoPascals). The standard PR at sea level is 1013 hPa, and the ascending and descending air causes areas of high and low pressure on the Earth' surface (Met Office, 2013). So, the air ascends when it is warm leading to low pressure at the surface, which leads to unsettled weather conditions (Met Office, 2013). The WS went over 2 m/s for two hours (19:00 & 20:00), and its correlation with Ta fluctuated from negative to positive.

On the other hand, a winter day on the 1st of December 2013 was modelled, and the regression outputs are summarised in Table 5.7. The regression models could explain up to 95% of the T_a variation, as the R^2 at 16:00 was 0.95. And at least 40% of the dependant variable (T_a) could be explained by the predictors, which reveals the significance of the influencing parameters entered the regression process. The uncontrollable parameters were dominant in the significant models. PO, LC, and TT dominated the controllable parameters. The highest Ta was 9.4 ºC at 14:00, and the lowest was 4.4 ºC at 20:00. The solar irradiation did not last for long, and peaked at 13:00 by 13.4 w/m^2. The RH did not go below 74%, and the WS was over 1 m/s during the first half of the day. Accordingly, this day was a typical winter day, with a little sunshine and a lot of moisture in the cold air. Nearly 60% of the significant models in Table 5.7 have R^2 values over 0.7, and more than half of them with R^2 over 0.8.

Table 5.4: A summary of the regression models of the controllable and uncontrollable influencing parameters on the formation of Birmimgham' CUHI on the 18th of April 2014.

hr.	Pearson correlation coefficients														Regression equations	R Square	Hourly weather data averages				
	VS	UA	TT	TG	TVF	SVF	LC	DTM	DSM	PO	SR	WS	RH	PR			Ta (°C)	SR (W m^{-2})	PR (hPa)	RH (%)	WS (m s^{-1})
0	0	0	0	0	0.07	0	0.34	0	0	0.50	0	0	-0.33	0	$7.1+2\times10^{-5}PO+0.01LC+0.1TVF-0.01RH$	0.30	6.5	0.0	1003.6	76.1	1.8
1	0	0	0	0.01	0	-0.08	0.36	0	0	0.54	0	-0.16	-0.50	0	$12.7+2.6\times10^{-5}PO+0.01LC-0.07SVF+0.004TG-0.01RH-0.01WS$	0.51	6.0	0.0	1003.5	79.8	1.8
2	0	0	0	0.09	0.09	0	0.32	0	0	0.49	0	-0.32	-0.54	0.19	$20+1.3\times10^{-5}PO+0.02LC+0.1TVF+0.0TG-0.8RH+0.05PR-0.08WS$	0.62	5.6	0.0	1003.7	83.7	1.5
3	0	0	0	0	0	0	0	0	0	0.39	0	-0.38	-0.78	0.14	$38.7+4.1\times10^{-6}PO-0.2RH-0.02PR-0.2WS$	0.67	5.0	0.0	1004.2	83.6	1.1
4	0	0	0	0	0	0	0	0	0	0.39	0	-0.28	-0.58	0.13	$-5.4-1.3.1\times10^{-5}PO-0.2RH+0.03PR-0.3WS$	0.53	4.5	0.0	1004.1	85.2	0.9
5	0	0	0	0.09	0	0	0	0	0	0.41	-0.02	-0.1	-0.83	0.30	$61.9+2.4\times10^{-5}PO+0.004TG-1.9SR-0.2RH-0.04PR+0.2WS$	0.85	4.1	3	1004.4	83.2	0.8
6	0	0	0	0	0	0	0	0	0	0.34	0.26	0	-0.88	0.31	$44.9+1.9\times10^{-5}PO-0.16RH-0.03PR+0.007SR$	0.83	4.4	64	1005.0	81.4	0.7
7	0	0	0	0	0	0.06	0.13	0	0	0	0.79	-0.11	-0.69	0.78	$-33.3+0.008LC+0.03SVF-0.06RH+0.04PR+0.03SR-0.07WS$	0.86	6.0	193	1005.5	71.5	1.5
8	0	-0.05	0	0	0	0	0.37	-0.65	0	0	0.60	0	-0.44	0	$11.1-0.004DTM+0.02LC-0.002UA-0.07RH-0.01SR$	0.70	7.0	351	1007.7	59.7	1.9
9	0	0	0	0	0	0	0	0	0	-0.15	0.62	-0.08	0.08	0.68	$-67.1-2.3\times10^{-5}PO+0.08PR+0.009SR-0.04RH-0.08WS$	0.68	8.0	491	1006.4	53.7	2.0
10	0	0	0	-0.03	0	0	-0.06	0	0	0	0.46	-0.31	-0.50	0.50	$-31.2-0.04LC-0.005TG-0.13RH+0.05PR+0.02SR-0.1WS$	0.61	8.9	618	1006.4	50.4	1.8
11	0	0	0	0	0	0	0	0	0	0.19	0.15	-0.03	-0.72	0	$19.1+2.6\times10^{-5}-0.2RH-0.28WS+0.01SR$	0.77	9.9	615	1006.3	45.9	2.0
12	0	0	0	0	0	0	0.23	0	0	0.31	0.55	-0.17	-0.72	0.48	$-54.1-1.5\times10^{-5}PO-0.01LC-0.1RH-0.39WS+0.07PR-0.004SR$	0.63	10.8	691	1006.2	40.2	1.9
13	0	0	0	0	0	0	0.22	0	0	0.32	-0.05	-0.06	-0.76	-0.03	$-35.6-1.4\times10^{-5}PO-0.01LC-0.2RH+0.06PR-0.1WS+0.006SR$	0.74	11.3	714	1006.1	38.7	1.8
14	0	0	0	0	0.11	0	0.20	0	0	0.25	0.05	-0.35	-0.69	-0.02	$-3.4-1.7\times10^{-5}PO+0.08TVF-0.0LC-0.2RH-0.3WS+0.02PR+0.00SR$	0.58	11.7	611	1005.9	39.0	1.5
15	0	0	0.11	0	0	0	0.50	0	0	0.63	0	-0.27	-0.68	0.33	$-39.5+7.9\times10^{-6}PO+0.02LC+0.008TT-0.1RH+0.06PR-0.1WS$	0.79	11.9	486	1005.6	39.1	1.7
16	0	-0.07	0	0	0	0	0	-0.26	0	0	0.13	-0.08	-0.83	0	$18.9-0.002DTM-0.002UA-0.2RH-0.007SR-0.08WS$	0.77	11.8	379	1005.2	40.1	1.9
17	0	0	0	0	0.11	0	0.26	0	0	0.38	0	-0.28	-0.72	0.12	$-21.7-7.6\times10^{-6}PO+0.04TVF-0.007LC-0.2RH+0.04PR+0.02WS$	0.68	11.6	234	1004.9	41.3	1.5
18	0	0	0	0.09	0.07	0	0	0	0	0.44	0.11	-0.01	-0.63	0.49	$-26.7+3.8\times10^{-6}PO+0.1TVF+0.0TG-0.2RH+0.04PR-0.1WS+0.1SR$	0.68	11.0	83	1004.9	44.6	1.5
19	0	0	0	0.11	0	0	0	0	0	0	-0.05	0	-0.89	0.25	$-21.7+0.002TG-0.16RH+0.04PR-0.6SR$	0.86	9.9	9	1005.0	48.2	1.2
20	0	0	0	0	0	0	0	0	0	0	0.18	0.35	-0.91	0.20	$-48.6+3\times10^{-6}PO-0.2RH+0.07PR-0.18WS-3SR$	0.91	8.8	0.0	1005.3	53.5	0.9
21	0	0	0	0	0	0	0	0	0	0	0	0.40	-0.95	0.18	$1.5-0.24RH-0.14WS+0.02PR$	0.91	7.6	0.0	1005.3	60.1	0.9
22	0	0	0	0.12	0	0	0.52	0	0	0.64	0	0.53	-0.04	0	$6.8+6.1\times10^{-5}PO+0.08LC+0.01TG+0.9WS-0.04RH$	0.57	6.7	0.0	1005.2	77.8	1.0
23	0	0	0	0	0	0	0	0	0	0.66	0	0.41	-0.94	0.15	$-8.5+2.9\times10^{-6}PO-0.2RH+0.03PR-0.1WS$	0.90	5.8	0.0	1005.2	70.9	0.9

Table 5.5: A summary of the regression models of the controllable and uncontrollable influencing parameters on the formation of Birmimgham' CUHI on the 6th of July 2013.

hr.	Pearson correlation coefficients														Regression equations	R Square	Hourly weather data averages				
	VS	UA	TT	TG	TVF	SVF	LC	DTM	DSM	PO	SR	WS	RH	PR			Ta (°C)	SR (W m^{-2})	PR (hPa)	RH (%)	WS (m s^{-1})
0	0	0	0.14	0	0	0	0.52	-0.39	0	0.65	0	0	-0.73	0	$21.1+4\times10^{-5}PO+0.06LC-0.003DTM+0.04TT-0.07RH$	0.61	16.9	0.0	1015.0	75.3	0.5
1	0	0	0	0	0	0	0.57	0	0	0.70	0	0	-0.80	0.35	$-28.1+4\times10^{-5}PO+0.06LC-0.1RH+0.05PR$	0.71	16.4	0.0	1012.2	77.9	0.8
2	0	0	0	0	0	0	0.52	0	0	0.63	0	0	-0.80	0	$24.7+1.7\times10^{-5}PO+0.04LC-0.1RH$	0.67	15.8	0.0	1012.1	83.1	0.8
3	0	0	0	0	0	0	-0.25	-0.20	0	-0.29	0	0	0.59	0.03	$89.3+2.4\times10^{-5}PO-0.01DTM-0.03LC+0.2RH-0.09PR$	0.46	13.7	0.0	1012.2	85.1	0.9
4	0	0	0	0	0	0	0.53	0	0	0.66	0.29	0	-0.76	0.17	$5.9+2.4\times10^{-5}PO+0.05LC-0.09RH+0.65SR+0.02PR$	0.68	14.9	4	1012.2	84.8	0.7
5	0	0	0	0	0.09	0	0.50	0	0	0.65	0	0.58	0	-0.01	$66.6+5.4\times10^{-5}PO+0.07LC+0.2TVF+0.7WS-0.05PR$	0.61	14.5	44	1012.5	94.0	0.7
6	0	0	0	0	0	0	0.42	-0.01	0	0.62	0.22	-0.01	-0.75	0	$25+2.8\times10^{-5}PO+0.003DTM+0.02LC-0.13RH-0.67WS-0.03SR$	0.71	14.9	158	1012.6	78.6	0.9
7	0	0	0	0	0	0	0	0	0	0.56	0.11	0.11	-0.64	0.31	$-56.4+4.7\times10^{-5}PO-0.2RH+0.09PR-0.06SR-0.79WS$	0.59	16.6	333	1012.7	23.0	1.2
8	0	-0.01	0	0	0	0	0	0	0	0.56	0.27	0.46	-0.69	0	$23.9+3\times10^{-5}PO-0.006UA-0.13RH+0.32WS+0.02SR$	0.58	18.3	491	1012.8	61.5	1.3
9	0	0	0	0	0	0	0.28	0	-0.55	0	0.4	0.01	-0.74	0	$30.1-0.004DSM+0.009LC-0.19RH+0.33WS+0.01SR$	0.67	19.5	604	1012.9	59.6	1.4
10	0	0	0.09	0	0	0	0	0	0	0.34	0.41	0	-0.69	0.79	$-202+1.9\times10^{-5}PO+0.02TT+0.22PR+0.007SR+0.03RH$	0.66	20.4	619	1012.7	57.5	1.4
11	0	0	0	0	0	0	0	0	0	0.35	0.46	-0.04	0	0.71	$-109.3+1.8\times10^{-5}PO+0.13PR+0.006SR-0.14WS$	0.55	21.2	773	1012.7	52.9	1.7
12	0	0	0	0	0	0	0	0	0	0.40	0.47	-0.21	0	0.67	$-91.1+1.9\times10^{-5}PO+0.11PR+0.006SR+0.15WS$	0.54	22.2	800	1012.6	50.5	1.1
13	0	0	0.1	0	0	0	0	0	0	0.39	0.28	0.13	-0.52	0.72	$-114.3+1.9\times10^{-5}PO+0.01TT+0.14PR-0.2WS+0.004SR-0.04RH$	0.59	23.2	760	1012.1	47.7	1.8
14	0	0	0.08	0	0	0	0	0	0	0.33	0.53	0.22	-0.59	0.60	$-46+1\times10^{-5}PO+0.01TT-0.07RH+0.02SR+0.07PR-0.06WS$	0.57	23.8	766	1011.9	45.0	1.6
15	0	0	0	0	0	0	0	0	0	0.38	0.52	0.34	-0.60	0.63	$-87.4+1.4\times10^{-5}PO+0.1PR+0.03SR-0.03RH+0.04WS$	0.63	24.6	645	1011.7	41.9	1.4
16	0	-0.04	0	0	-0.04	0	0	0	0	0	0.40	0	0	0.60	$-80.4-0.002UA-0.09TVF+0.1PR+0.02SR$	0.43	24.9	545	1011.6	41.0	1.2
17	0	-0.04	0	0	0	0	0	0	-0.58	0	0.35	-0.03	-0.32	0.75	$-149-0.001DSM-0.002UA+0.2PR+0.02SR-0.2WS-0.007RH$	0.64	25.2	405	1011.6	40.6	1.0
18	0	0	0	0	0	0	0	0	0	0.07	0.43	0	-0.27	0.63	$-100.5-1.3\times10^{-5}PO+0.13PR+0.02SR-0.03RH$	0.51	25.2	214	1011.8	40.8	1.1
19	0.03	-0.03	0	0	0	0	0.27	0	-0.56	0.1	0.42	0	-0.54	0	$30.2-3\times10^{-5}PO -0.008DSM+0.03LC-0.005UA+0.001VS-0.1RH+0.02SR$	0.53	24.8	79	1012.1	43.1	0.9
20	0	0	0	0	0	0	0.31	0	-0.55	0.21	0.45	0	-0.42	0.44	$-37.4-2.5\times10^{-5}PO -0.006DSM+0.03LC-0.05RH+0.67SR+0.06PR$	0.52	23.9	16	1012.4	50.0	0.7
21	0	0	0	0	0	0	0.28	0	0	0	0.31	0.5	0	0.40	$-34.3+0.07LC+0.66WS+10.4SR+0.06PR$	0.34	22.4	0.0	1013.2	84.0	1.0
22	0	0	0	0	-0.05	0	0.21	-0.58	0	0	0	0.24	0	0	$22.5-0.02DTM+0.04LC-0.3TVF+0.12WS$	0.35	20.6	0.0	1013.7	84.0	1.2
23	0	0	0	-0.03	-0.06	0	0	-0.46	0	0.01	0	-0.15	-0.28	0	$37.3-0.01DTM-6.4\times10^{-5}PO-0.32TVF-0.01TG-0.2RH-0.5WS$	0.39	18.8	0.0	1014.2	75.7	1.2

Table 5.6: A summary of the regression models of the controllable and uncontrollable influencing parameters on the formation of Birmimgham' CUHI on the 5th of September 2013.

	Pearson correlation coefficients																Hourly weather data averages				
hr.	VS	UA	TT	TG	TVF	SVF	LC	DTM	DSM	PO	SR	WS	RH	PR	Regression equations	R Square	Ta (^oC)	SR (W m^{-2})	PR (hPa)	RH (%)	WS (m s^{-1})
0	0	0	0	0	0	0	0.38	0	0	0.59	0	0.53	-0.69	0.26	$-60.5+6\times10^{-5}PO+0.02LC-0.09RH+0.08PR+0.5WS$	0.59	16.7	0.0	996.7	70.9	0.7
1	0	0	0	0	0	0	0	0	0	0.56	0	0	-0.71	0.20	$-76.8+3.3\times10^{-5}PO-0.13RH+0.1PR$	0.57	16.0	0.0	996.3	73.4	0.6
2	0	0	0	0	0	0	0.29	0	0	0.50	0	0.29	-0.76	0.19	$-10.4+2.5\times10^{-5}PO-0.03LC-0.2RH-0.96WS+0.04PR$	0.61	15.0	0.0	995.8	76.0	0.4
3	0	0	0	0	0	0	0.28	0	0	0	0.11	0	-0.80	0.25	$-78.8-0.05LC-0.19RH+0.1PR+56.07SR$	0.65	14.0	0.0	995.3	79.9	0.4
4	0	0	0	0	0	0	0	-0.31	0	0	0	0.1	-0.73	0	$31.5-0.004DTM-0.21RH-1.5WS$	0.59	13.2	0.0	994.5	82.6	0.3
5	0	0	0	0	0	0	0.31	-0.43	0	0.46	0.52	0.41	-0.80	0	$26.5+4.7\times10^{-5}PO-0.001DTM-0.027LC-0.19RH+1.33WS+10.5SR$	0.70	12.4	0.0	994.4	85.7	0.4
6	0	0	0	0.11	0	0	0.38	0	0	0.57	0	-0.13	-0.78	0.25	$92+4.8\times10^{-5}PO+0.03LC+0.01TG-0.2RH-0.06PR-0.7WS$	0.67	12.1	31	994.3	85.4	0.4
7	0	0	0	0.13	0.01	0	0.40	-0.01	0	0.57	0	-0.02	-0.63	0	$20.8+9.2\times10^{-5}PO+0.01DTM+0.1LC+0.03TG+0.35TVF-0.16RH+0.5WS$	0.53	13.5	150	994.6	78.0	0.7
8	0	0	0	0.01	0	0	0.37	-0.03	0	0.48	0.12	0	0	0	$11+9.6\times10^{-5}PO+0.1LC+0.005DTM+0.02TG+0.05SR$	0.30	16.3	310	994.7	92.8	1.3
9	0	0	0	0.09	0	0	0.41	0	0	0	0.13	-0.27	-0.69	0.45	$-41.7+0.05LC+0.007TG-0.13RH+0.07PR+0.06SR+0.07WS$	0.56	18.3	482	994.6	63.6	1.4
10	0	-0.06	0.11	0	0.09	0	0.41	-0.23	0	0.59	0	-0.59	-0.70	0	$24+1.5\times10^{-5}PO+0.05LC+0.001DTM+0.2TVF+0.03TT-0.004UA-0.1RH-0.3WS$	0.60	19.5	576	994.4	60.4	1.3
11	0	0	0	0	0	0	0.23	-0.49	0	0.32	0.31	0	-0.87	0	$28.2-0.001DTM-4.4\times10^{-6}PO+0.03LC-0.14RH+0.001SR$	0.76	20.0	644	994.0	60.0	1.5
12	0	0	0	0	0	0	0	-0.45	0	0.22	0.04	0	-0.76	0.45	$-128.4-0.003DTM-1.1\times10^{-5}PO-0.14RH+0.16PR-0.005SR$	0.75	20.5	537	993.4	58.2	1.7
13	0	0	0	0	0	0	0	0	0	0.31	-0.32	0	-0.83	0	$36.8-2.6\times10^{-5}PO-0.26RH-0.02SR$	0.84	20.7	524	993.5	56.5	1.7
14	0	0	0	0	0	0	0	-0.44	0	0	-0.52	0.07	-0.14	0	$22.8-0.004DTM-0.02SR+0.1WS-0.009RH$	0.32	21.1	396	993.1	49.6	1.4
15	0	0	0	0.05	0	0	0.13	-0.45	0	0.01	0	0.02	0	0	$23.7-0.01DTM-2.6\times10^{-5}PO+0.03LC+0.009TG-0.14WS$	0.24	21.6	519	992.7	44.6	1.6
16	0	0	0	0	0	0	0.09	-0.55	0	-0.06	0.23	0.26	-0.25	0	$25.5-0.01DTM-3.2\times10^{-5}PO+0.03LC+0.13WS-0.03RH+0.005SR$	0.37	21.7	292	992.4	46.7	1.7
17	0	0	0	0	0	0	0	0	-0.50	-0.18	0.38	0.26	-0.07	0	$27.3-0.02DSM-6.8\times10^{-5}PO+0.68-0.1RH+0.2SR$	0.41	21.2	122	992.3	52.4	1.5
18	0.05	0	0	0	0	0	-0.08	0	-0.50	-0.20	0.37	0	-0.17	0	$33.4-0.01DSM-9.3\times10^{-5}PO+0.003VS-0.03LC-0.17RH+0.29SR$	0.41	19.6	40	992.4	62.2	1.9
19	0.06	0	0	0	0	0	-0.15	-0.49	0	-0.26	-0.13	0	0	0	$25.3-0.03DTM-9.7\times10^{-5}PO-0.05LC+0.002VS-25.4SR$	0.47	17.1	1	992.9	74.2	2.1
20	0.05	0	0	0	0	0	-0.1	0	-0.52	-0.25	0	0.05	-0.28	0	$30.4-0.01DSM-7.8\times10^{-5}PO-0.04LC+0.002VS-0.15RH+0.07WS$	0.45	14.9	0.0	993.2	76.5	2.1
21	0.04	0.01	0	0	0	0	0	0	-0.58	-0.09	0	-0.07	-0.20	0	$23.7-0.01DSM-4.4\times10^{-5}PO+0.002VS-0.006UA-0.09RH+0.04WS$	0.43	14.0	0.0	993.0	74.6	1.8
22	0.04	0.01	0	0	0	0	0	0	-0.58	-0.10	0	-0.11	-0.22	0	$22.9-0.01DSM-4\times10^{-5}PO-0.005UA+0.002VS-0.09RH+0.04WS$	0.45	13.6	0.0	992.7	74.2	1.5
23	0	0.01	0	0	0	0	0.06	-0.56	0	-0.09	0	0.13	-0.11	0	$19-0.01DTM-3.2\times10^{-5}PO+0.008LC-0.002UA-0.05RH+0.08WS$	0.41	13.4	0.0	992.6	72.4	1.7

Table 5.7: A summary of the regression models of the controllable and uncontrollable influencing parameters on the formation of Birmimgham’ CUHI on the 1st of December 2013.

hr.	Pearson correlation coefficients														Regression equations	R Square	Hourly weather data averages				
	VS	UA	TT	TG	TVF	SVF	LC	DTM	DSM	PO	SR	WS	RH	PR			Ta (°C)	SR (W m^{-2})	PR (hPa)	RH (%)	WS (m s^{-1})
0	0	0	0	0	0	0	0	0	0	0.15	0	0.51	-0.62	0.84	-127.5+8.3×10^{-6}PO+0.12PR+0.39WS+0.1RH	0.91	6.2	0.0	1014.6	82.8	1.3
1	0	0	0	0	0	0	0.22	0	0	0	0	0	-0.83	0.78	-75.7-0.004LC-0.32RH+0.1PR	0.84	6.7	0.0	1014.5	80.1	1.5
2	0	0	0.07	0	0	0	0.33	0	0	0	0	0.49	-0.94	0	31.5+9.6×10^{-6}PO+0.008LC+0.008TT-0.31RH+0.06WS	0.90	7.2	0.0	1014.4	79.0	1.7
3	0	0	0	0	0	0	0	0	0	0.47	0	0.28	-0.85	0.32	9.5-1.1×10^{-5}PO-0.24RH+0.016PR-0.012WS	0.77	7.4	0.0	1014.4	78.5	1.8
4	0	-0.07	0	0	0	0	0.35	-0.05	0	0.42	0	0.11	-0.80	0	21.6+3×10^{-6}PO+0.013LC-0.002DTM-0.001UA-0.18RH+0.05WS	0.78	7.4	0.0	1014.4	78.6	1.7
5	0	0	0	0	0	0	0.40	0	-0.18	0.42	0	-0.08	-0.86	0	20.7-3.2×10^{-6}PO+0.005LC-0.001DSM-0.17RH+0.04WS	0.80	7.4	0.0	1014.4	78.5	1.9
6	0	0	0	0	0	0	0.39	0	0	0.45	0	0.28	-0.91	-0.13	-10-4.6×10^{-6}PO+0.003LC-0.19RH+0.03PR+0.07WS	0.89	7.4	0.0	1014.4	76.8	1.9
7	0	0	0	0	0	0	0.46	0	0	0.45	0	0.38	-0.82	0.35	-13+0.003LC+1.52×10^{-6}PO-0.12RH+0.03PR+0.1WS	0.84	7.2	0.0	1014.8	77.0	1.5
8	0	0	0	0	0	0	0.26	0	0	0.26	0	0.15	-0.83	-0.16	-24.9-7.16×10^{-6}PO+0.003LC-0.18RH+0.05PR+0.1WS	0.84	7.5	4	1015.4	76.2	1.3
9	0	0	0	0	0	0	0	0	-0.25	0	0.23	0	-0.49	0	14.4-0.002DSM-0.09RH+0.12SR	0.60	7.7	31	1015.0	75.6	1.0
10	0	0	0	0	0	0	0.35	0	0	0.35	-0.08	0.27	-0.52	0.56	-28.8-7×10^{-6}PO+0.003LC+0.043PR-0.083RH+0.038WS-0.012SR	0.65	8.3	61	1016.4	74.1	1.0
11	0	0	0	0	0	0	0.21	0	0	0.27	-0.09	-0.12	-0.42	0.59	-49.9-5.8×10^{-6}PO+0.002LC+0.064PR-0.088RH+0.038WS-0.013SR	0.74	8.4	65	1016.7	77.8	1.5
12	0	0	-0.03	0	0	0	-0.03	0	0	0.04	-0.18	0	-0.43	0.24	-35.2-5.62×10^{-6}PO-0.006LC-0.005TT-0.092RH+0.05PR+0.017SR	0.66	8.6	50	1016.4	79.1	1.4
13	0	0	0	0	0	0	0	0	0	0.35	0.31	0.08	-0.84	0	25.9-1.13×10^{-5}PO-0.22RH+0.013SR+0.023WS	0.74	9.3	134	1016.3	75.7	1.3
14	0	0	0	0	0	0	0	0	0	0.13	0.02	0.29	-0.84	0	22.3-1.6×10^{-5}PO-0.17RH+0.02SR+0.037WS	0.79	9.4	85	1016.4	74.2	0.8
15	0	-0.08	0	0	0	0	0.47	0	0	0.50	0.39	0.45	-0.84	0.19	25.4+7.2×10^{-6}PO+0.02LC-0.001UA-0.11RH+0.13WS+0.03SR-0.008PR	0.78	9.2	39	1016.4	74.1	0.7
16	0	0	0	0	0	0	0.40	0.14	0	0.60	-0.21	0.36	-0.94	0	22.42+1.42×10^{-5}PO+0.002DTM-0.006LC-0.19RH+0.28WS-0.65SR	0.95	8.0	07	1016.7	78.2	0.6
17	0	0	0.12	0	0	0	0.29	0	0	0.53	0	0.46	-0.68	-0.01	1.5+3×10^{-5}PO+0.03TT-0.01LC-0.15RH+0.24WS+0.02PR	0.53	6.5	0.0	1017.2	83.5	0.5
18	0	0	0.12	0	0	0	0.34	0	0	0.56	0	0.35	-0.64	0.24	-77.4+3.4×10^{-5}PO-0.02LC+0.04TT-0.22RH+0.1PR+0.46WS	0.58	5.6	0.0	1017.5	86.2	0.6
19	0	0	0.13	0	0	0	0.33	0	0	0.58	0	0.33	0	0.24	-42.9+7.7×10^{-5}PO+0.08TT+0.02LC+0.62WS+0.04PR	0.40	4.6	0.0	1018.2	92.0	0.5
20	0	0	0	0	0	0	0.28	0	0	0.46	0.45	0.49	-0.60	0.35	-89.4+3.1×10^{-5}PO-0.03LC-0.3RH+0.12PR+18.6SR+0.56WS	0.60	4.4	0.0	1018.6	90.0	0.7
21	0	0	0.01	0	0	0	0.31	0	0	0.42	0	0.02	-0.58	0.60	-228.7+2.2×10^{-5}PO-0.02LC+0.04TT+0.26PR-0.34RH+0.93WS	0.65	4.6	0.0	1018.7	90.6	0.7
22	0	0	0.01	0	0	0	0	0	0	0.45	0	0.02	-0.67	0.59	-99.5+8.3×10^{-6}PO+0.02TT+0.12PR-0.23RH+0.3WS	0.66	5.2	0.0	1018.9	89.6	0.5
23	0	0	0	0.11	0	0	0	0	0	0.45	0	0	-0.63	0	-51.1+6.6×10^{-6}PO+0.005TG+0.07PR-0.15RH	0.59	5.5	0.0	1019.3	89.6	0.3

The ability of the regression models to predict the Ta means that they are applicable to identify the excessive heat intensity (CUHI). As the CUHI is just the difference in Ta between two points, however, it was better to use the individual Ta as dependant parameters. This is because the magnitude of influencing parameters is local and changes spatially. So, it was not logical to use the CUHI magnitude instead of Ta, as the CUHI includes the influence of two different points.

The derived models could explain the variation in Ta day and night-time, and consequently they are able to predict the day and night CUHI. If the sky is cloudy during the day preventing the sunshine from reaching the ground, the situation during the day will be like the night-time, and the only difference is the light which does not have noticeable impact on the CUHI, as proved earlier. From Tables (5.4- 5.7), the influencing parameters do not have the same influence during the day and night time. So, some parameters have shown to have notable impact during the night, and others dominated during the day-time. These outcomes agree with the results of Ryu and Baik (2012) that in the daytime the impervious surfaces contribute positively to the UHI, and the 3D urban geometry contributes negatively.

Furthermore, the uncontrollable parameters were dominant over the controllable parameters in the significant models. The RH is the most distinguished uncontrollable predictor, and the PO is the highly significant controllable predictor. The importance of weather conditions in the formation of CUHI agrees with the derivation of thermal indices discussed earlier in the literature such as HI and wind chill. Heat index and wind chill combine the humidity and wind speed respectively with other weather and physiological parameters, to assess the thermal stress on human bodies (Steadman, 1979, Steadman, 1971). In general, the 14 predictors could explain up to 0.91, 0.71, 0.84 and 0.95 of the Ta in spring, summer, autumn and winter respectively. Moreover, the weather averages gave an indication about the climatic condition for each hourly regression model. This highlighted the importance of the synoptic weather to model the CUHI, though the changeable (controllable) hourly parameters played a major role to make up the significant models after the uncontrollable ones.

5.5 Conclusions

The use of HiTemp data has improved the spatiotemporal modelling of CUHI, with its high-density network of sensors which enabled the production of high spatial and temporal resolution CUHI images. Furthermore, the height of the stations provided information about the canopy layer under the level of buildings close to the energy sources. This chapter provided unprecedented in-depth modelling of the CUHI, though the reasonable number of past and current dense meteorological network worldwide reviewed in Table 5.1. Nevertheless, none of the recent or past UHI studies within the canopy layer presented in the literature have used such a high spatial and temporal resolution of temperature measurements to study the CUHI in different climatic conditions. Furthermore, the number of controllable and uncontrollable parameters are unprecedented to be used in a single study.

It was found that the CUHI occurs in all seasons, day and night based on the climate condition. However, the high intensity CUHI happens during the clear and calm weather. The CUHI was found in approximately 56% of the total hours during the study period (June 2012 – June 2014). The maximum CUHI intensity in Birmingham during the period of the study was 13.53 °C. The wind speed and direction have important impact on the spatial distribution of the hot spots, as well as the extent of the CUHI. The CUHI occurred in the suburban areas as well as the urban areas due to the presence of impervious surfaces and anthropogenic activities. The extreme CUHI events (UHI > 10 °C) happened at suburban areas far from the City Centre during the period of out of working hours. The occurring time of the UHI over 10 °C events were between 4 p.m. and 6 am, and the locations are almost all suburban areas.

The City Centre showed the lowest values of SVF and VS due to high buildings, which provided the shade to reduce the air temperature by up to 2 °C. Fourteen parameters were derived to have large number of layers, enabling the regression analysis to pick up significant relationships with Ta. The influencing parameters were grouped into controllable and uncontrollable factors. They could effectively predict the day and night CUHI. The regression models could explain up to 95% of the air temperature variations when laid under the components of LULC, geometrical factors, and synoptic weather factors. Though the uncontrollable parameters dominated the significant models, some controllable ones were constantly participating in forming the highly significant models. The 14 predictors could explain up to 0.91, 0.71, 0.84 and 0.95 of the Ta in the spring, summer, autumn and winter respectively.

Moreover, the weather averages gave an indication about the climatic condition for each hourly regression model. This highlighted the importance of the synoptic weather to model the CUHI, though the controllable hourly parameters played a significant role to make up the significant models. However, other influencing parameters could not be included when modelling the CUHI such shortwave and longwave radiations, as these radiation fluxes need many inputs and a microclimate model to be simulated for a large scale. Therefore, the Ta seems not to be enough as a predictor to derive all the influencing parameters on the formation of UHI, and likewise the LST. Accordingly, the next chapter adopts a new indictor of UHI and employs a microclimate model.

Chapter 6: RUHI Spatiotemporal Modelling and 3D Radiative Fluxes

6.1. Introduction

An excessive heat has been observed in urban and suburban areas as detailed in the previous two chapters where air and surface temperature are higher than their adjacent rural areas to form heat islands above the city. The SUHI and CUHI were investigated using surface temperature and air temperature respectively as indictors. There is no single indicator can fully investigate the spatiotemporal change of different types of UHI, because, there is no particular cause of the UHI, and many factors contribute to UHI formation (Gartland, 2008). The complexity of urban settings makes it difficult to have a specific measure of climatic variables (Lindberg and Thorsson, 2009), so different UHI types should be investigated separately. Accordingly, T_{mrt} is used as a new indicator of the UHI formation, which combines the effects of many influencing parameters on the UHI. T_{mrt} is derived using SOLWEIG microclimate model, and there are other different methods to obtain the T_{mrt} in the literature such as Rayman software (Thorsson et al., 2007). The first version of SOLWEIG was developed by Lindberg et al. (2008) to predict the outdoor thermal comfort. However, SOLWEIG model is used for the first time to study the UHI in this research. Also, the T_{mrt} is used for the first time to model the UHI as a new indictor, which upgrades the 2D UHI using LST and air temperature to 3D UHI simulation

However, SOLWEIG was evaluated using 3D integral radiation measurements at different sites with various building geometries. And the results of the evaluation gave about 0.94 (R^2) agreement between the modelled and measured values with p values less than 0.01 and RMSE (Root Mean Square Error) about 4.8 K (Lindberg et al., 2008). The model used to require a limited number of inputs such as meteorological data, shortwave radiations, urban geometry, and geographical location (Lindberg et al., 2008). However, the recent developments of the model by Lindberg et al. (2016a) have incorporated the land cover, wall height and wall aspect grids as well as other modifications. SOLWEIG is able to model the *K* and *L* radiations, shadow patterns as well as the T_{mrt} that a standing or sitting person might receive in an outdoor environment (Lindberg et al., 2016a). The modelled Tmrt is used to investigate the presence of a new type of UHI which differs from SUHI and CUHI. In a physical sense the T_{mrt} is the uniform temperature of a hypothetical spherical surface surrounding a subject that would result in the same net radiation energy exchange with the subject as the actual (Walikewitz et al., 2015). The term Radiant Urban Heat Island (RUHI) is introduced for the first time to measure the difference between the pixel T_{mrt} and minimum T_{mrt} within the city of Birmingham. The spatiotemporal change of RUHI is explored to compare it with the SUHI and CUHI. Furthermore, the *K* and *L* upward and downwards radiations are modelled to identify their effects on the RUHI formation as influencing parameters.

6.2. Calculation and application of T_{mrt}

The calculation of T_{mrt} can be undertaken by several measuring and modelling techniques. Ali-Toudert et al. (2005) used integral radiation measurements and angular factors, which is a costly and complex technique. A cheap and simple measurement technique, the globe thermometer was used for indoor measurement, which was later developed for outdoor comfort studies (Nikolopoulou et al., 2001). A three dimensional fluid dynamic coupled with an energy balance model formed the base of a software called ENVI-met, which models the microclimate including the T_{mrt} (Bruse, 2006). The Rayman software is able to calculate the T_{mrt} and thermal indices (Matzarakis et al., 2000), which requires input information similar to SOLWEIG model. However, Rayman software is a site-specific measurement, and does not require information about building geometry and vegetation (Thorsson et al., 2007). So, Rayman software cannot be used for large scale studies. Then, SOLWEIG 1.0 was released to model the spatial variations of 3D radiant fluxes and T_{mrt} in complex urban settings including building geometry and vegetation (Lindberg et al., 2008). The calculation of T_{mrt} requires the determination of the mean radiant flux density (S_{str}), which sums up the long and shortwave radiation in three dimensions as shown below (Lindberg et al., 2008) .

$$S_{str} = \zeta_k \sum_{i=1}^{6} K_i F_i + \varepsilon_p \sum_{i=1}^{6} L_i F_i \qquad (6.1)$$

$$T_{mrt} = \sqrt[4]{S_{str}/\varepsilon_p \sigma} - 273.15 \qquad (6.2)$$

S_{str} = the mean radiant flux density (Wm^{-2}).

K_i & L_i = the short and longwave radiation fluxes respectively (i=1-6) (Wm^{-2}).

F_i = the angular factors between a person and the surrounding surfaces (0.22 for radiation fluxes from the four cardinal points and 0.06 for radiation fluxes from above and below).

ζ_k = the absorption coefficient of a person for shortwave radiation (typically 0.7).

ε_p = the emissivity of the human body (typically 0.97).

σ = the Stefan-Boltzmann constant ($5.67 * 10^{-8}$ Wm^{-2} K^{-4}).

The applications of T_{mrt} have been used to investigate the outdoor thermal comfort, heat stress, and heat related mortality. Krüger et al. (2014) states that T_{mrt} plays an important role in human energy balance, and can be used as input to derive other thermal indices to monitor the urban microclimate. The simulation of T_{mrt} showed that urban geometry has significant impact on its intensity in the summer daytime, and the open spaces are warmer than adjacent narrow street canyons (Lau et al., 2016). Furthermore, Lau et al. (2016) found that high T_{mrt} in high density sub-tropical urban environments causes severe thermal discomfort in the summer. This study raised a caution about over shadowing the dense urban environments which reduces the air ventilation. Lindberg et al. (2016b) evaluated the impact of urban planning strategies on heat stress, and found that the highest T_{mrt} occurs close to sun-exposed, south facing walls during clear and warm weather. Though, their results showed that the highest average daytime T_{mrt} happen at open location, because open areas have the highest frequency of sunlit occasions.

Furthermore, the intra-urban differences of T_{mrt} were found high in Shanghai due to the varying building density and height, street orientation and vegetation. T_{mrt} peaked to over 60 ºC during daytime when simulating a heat wave in 2013. On the other hand, Thorsson et al. (2014)

suggests T_{mrt} be used as a predictor of heat related mortality instead of T_a (air temperature), because T_{mrt} models gave a better fit than T_a models for daily mortality which makes it a good measure to identify urban hot spots. Their study chose a typical built-up area (100 m × 200 m) in Stockholm County, Sweden. Accordingly, the calculation of T_{mrt} is not a straight forward process and requires many inputs to give robust outputs that are critical for a wide range of urban planning, thermal comfort, and heat stress applications.

6.3. Method and materials

SOLWEIG is a separate computer software model, that has a graphical user-friendly interface written in MATLAB programming language (SOLWEIG-team, 2015). It is an open source software, which makes use of a runtime engine called the MCR (MATLAB Compiler Runtime) to run the interface outside the MATLAB environment (SOLWEIG-team, 2015). However, the recent version is available in the larger tool package, UMEP (Urban Multi-Scale Environmental Predictor). UMEP is an open source climate service tool accessed through QGIS, and the feature development is to provide the user with the ability to interact with spatial information, improve and extend the modelling capabilities (Lindberg et al., 2016a). QGIS is written in C++, but it has bindings to the Python language that was exploited in the development of UMEP (Lindberg et al., 2016a). The UMEP plugin contains pre-processors, processors and post-processors, and SOLWEIG is one of the processors. The pre-processors prepare the data for the processors, and the later include all the main models for the calculations (Lindberg et al., 2016a). Then, the post-processors provide an initial quick look of the results; however, in this study, the post-processing was undertaken using ArcMap as it provides simple and more powerful tools compared to QGIS. The work flow of the pre-processor, processor and analyser is summarised in Figure 6.1, and several inputs were prepared using the pre-processors SVF, wall height and aspect, and meteorological data. Nevertheless, other input layers such as DEM, ground and building DSM, vegetation DSM and the land cover were created using ArcMap. Birmingham was chosen as the study site to apply SOLWEIG, so the results could be compared with SUHI and CUHI. Furthermore, the HiTemp project provided the required meteorological data with unprecedented spatial and temporal resolution.

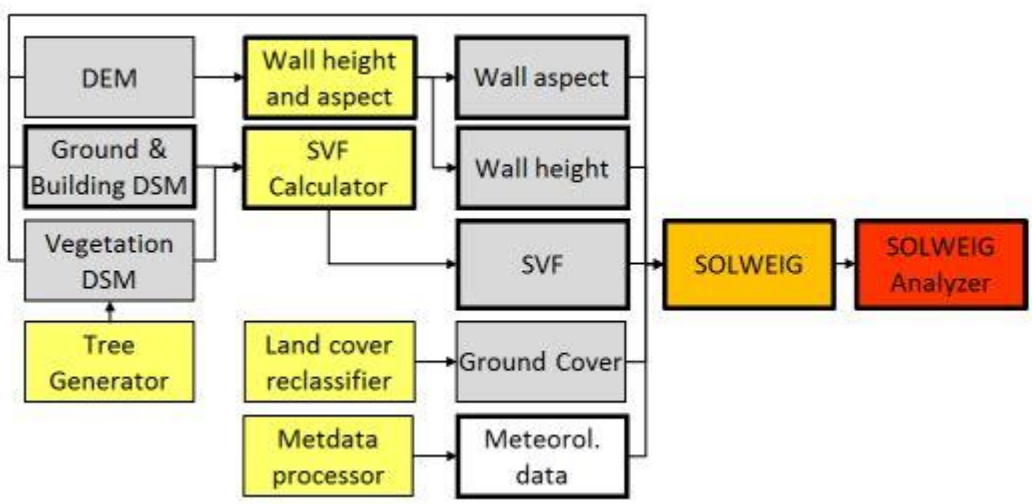

Figure 6.1: Workflow and geodata for SOLWEIG. Bold outlines (Mandatory items), yellow (pre-processor), orange (processor), red (post-processor), and grey boxes (geodatasets) (Lindberg et al., 2016a).

6.3.1 Pre-processing

The pre-processing included preparing all the data in the yellow and grey boxes shown in Figure 6.1. The ground and building DSM was made by combining the DTM (in Figure 5.7) with building's footprints downloaded from the Digimap of the OS (EDINA, 2015). The ground and building DSM merges the elevation of the ground with the height of the buildings, however, it does not include the vegetation. Therefore, the vegetation DSM consists of pixels with vegetation canopy height (almost trees) above the ground where the ground represents the zero level. This layer has gaps on the map as it shows only the trees, while zero values are assigned for other features. The vegetation DSM was masked out of the LIDAR DSM derived earlier in Figure 5.7. On the other hand, the land cover types were classified into five classes (paved, building, grass, bare soil, and water) according to the land cover scheme described by Lindberg and Grimmond (2011a). The land cover classes exclude the trees as they are already represented by the vegetation DSM. The land cover classes were reclassified from the descriptive groups of the topographic map in Figure 5.2. The land cover map of Birmingham in Figure 6.2 appears to be dominated by the grass because the general surfaces and vegetation surfaces in Figure 5.2 were classified as grass. Furthermore, the grass class includes the mixed pixels of grass and soil when the grass is dominated the pixel area. However, the map is not that green when zoomed in due to the scale issue, and the other surfaces can be seen among the grass areas when the ratio of the distance on the map to the corresponding distance on the ground is increased. The ground and building DSM, vegetation DSM, and the classified land cover are shown in Figure 6.2, and these layers were processed using ArcMap based on the SOLWEIG model requirements described by Lindberg et al. (2016a).

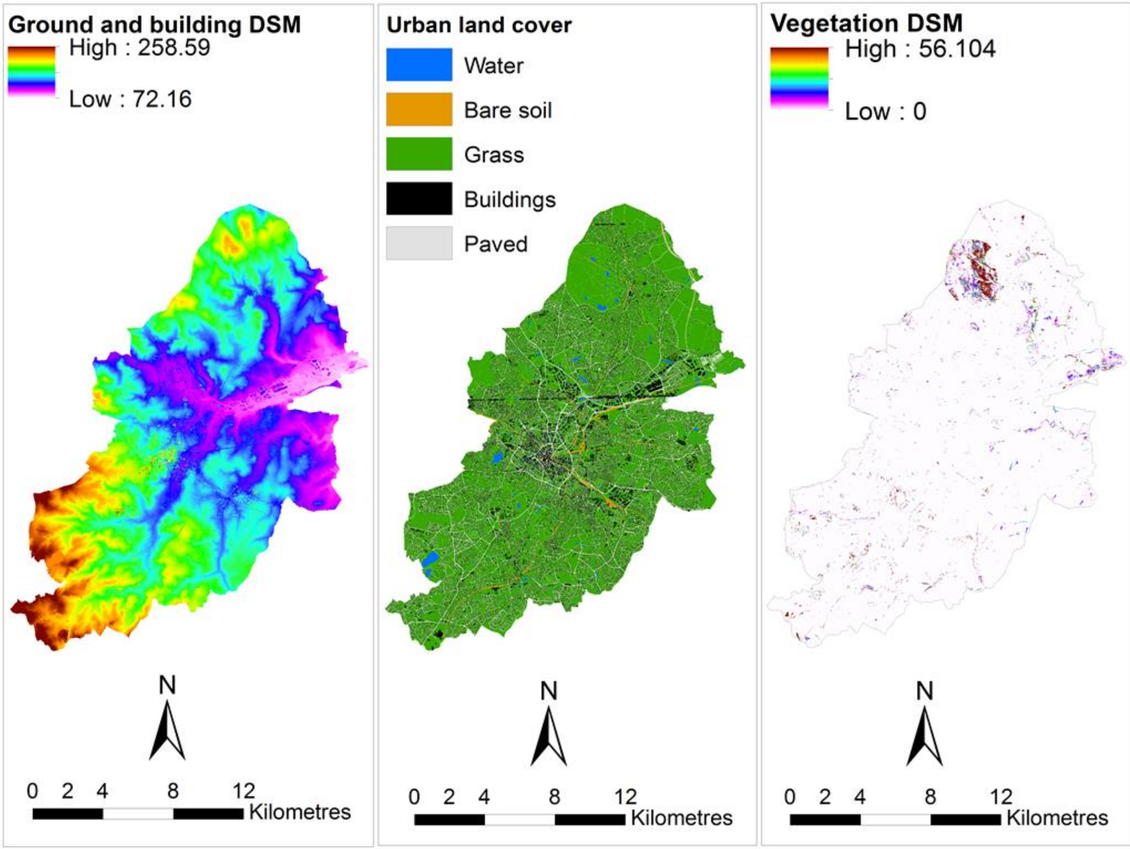

Figure 6.2: Birmingham's ground and building DSM (metres), land cover, and vegetation DSM (metres).

The pre-processors of UMEP were used to derive the SVF, walls height and aspect, as well as the meteorological inputs to the format that suits the model. The SVF is the ratio of the radiation received to the emitted on a planar surface by the entire hemispheric environment, and the methodology to derive it is described by Lindberg and Grimmond (2010). The SVF plugin was used to generate the SVF per pixel using the ground and building DSM and vegetation DSM (Lindberg et al., 2016a). The SVF values in Figure 6.3 range between 0 and 1, and the lowest values can be seen in Sutton Park, which are even lower than the SVF values of the City Centre. Sutton Park contains dense trees, which obscure the ground visions more than the buildings in the City Centre (see Figures 6.4 and 5.6 to understand the places' location and land cover respectively).

The wall height was generated by identifying wall pixels and their height from ground and building DSM. Similarly, the wall aspect was estimated by the same plugin that derives the height (wall height and aspect pre-processor) using specific filters as described by Lindberg et al. (2015a). The values of wall aspect range between (0- 360) degrees where a north facing wall pixel has a value of zero. The wall height and aspect layers in Figure 6.3 contain gaps, as they only represent the wall pixels by ignoring the other surfaces. On the other hand, the MetPreprocessor was used to transform required temporal meteorological data into the format used in UMEP. The input variables were air temperature, relative humidity, barometric pressure, wind speed, wind direction, and incoming shortwave radiation. Furthermore, the date and time of the meteorological data were specified for each of the input days, and more details about MetPreprocessor can be found in (Lindberg et al., 2016a). The meteorological data was acquired from the HiTemp project using AWS station (see Figure 6.4) as they provide the required input variables.

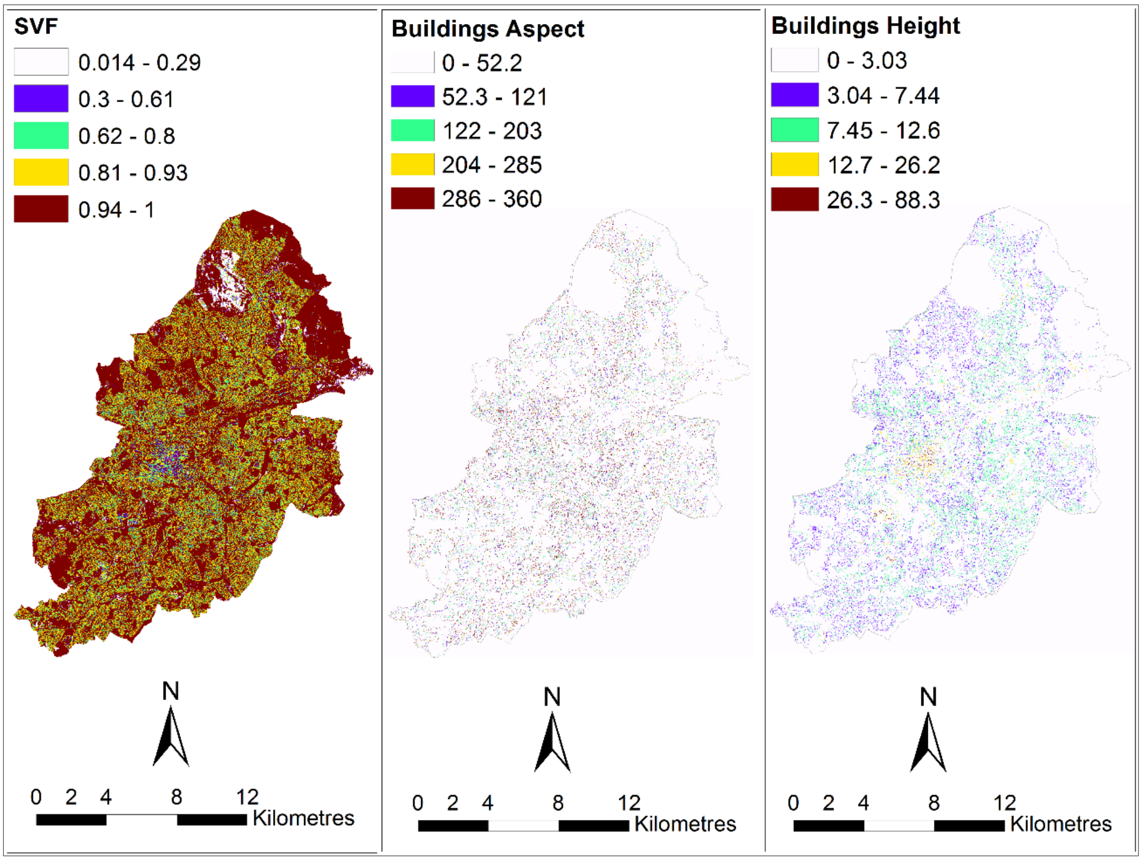

Figure 6.3: Birmingham's SVF (dimensionless), wall aspect (degrees) and height (metres). Derived from Birmingham's DSM using the pre-processor of UMEP.

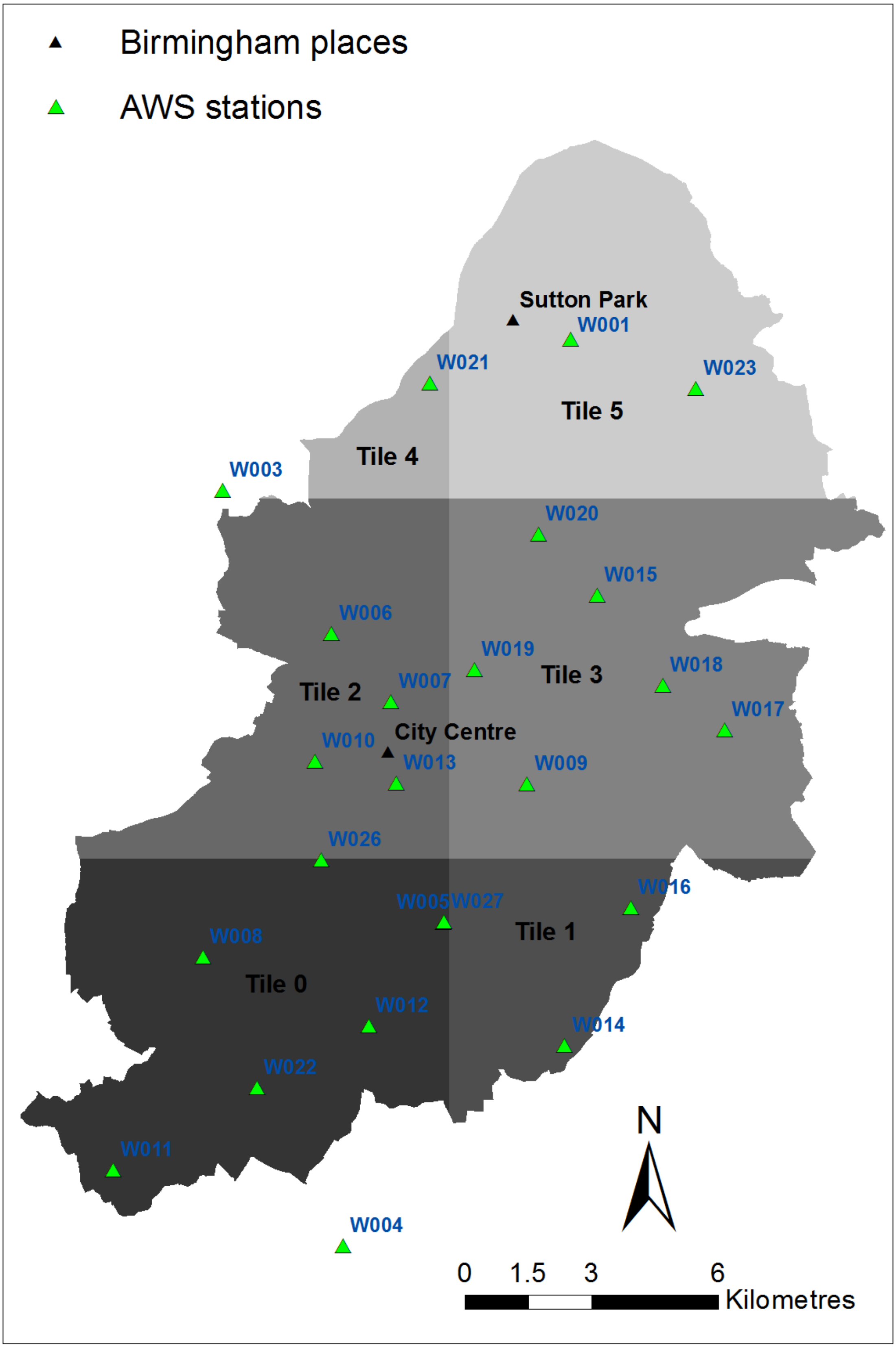

Figure 6.4: AWS stations to provide input meteorological data, and split tiles to divide Birmingham to six zones with some important places in the city.

6.3.2 SOLWEIG Processing

For the application of the SOLWEIG plugin, it is essential to have all the spatial grids with the same extent and pixel size, and each grid should not be larger than 4000000 pixels (Lindberg et al., 2016a). Hence, the study area was split into six tiles before running the model as shown in Figure 6.5. The split tiles were overlapped by 100 metres (20 pixels), to overcome the problem of edge effects when merging the outputs later. As a result, modelling one day required to run the plugin six times, which increased the processing time multiple folds. However, this limitation was employed to test the impact of spatially varying the temporal meteorological data, since the model is only able to include the temporal meteorological data, and it is not possible to spatially vary the meteorological data. The model was tested by using spatially averaged meteorological data, and then the meteorological data were varied for each tile. The inputs required by the SOLWEIG plugin are the spatial, meteorological, environmental, optional settings, human exposure data as well as the types of output maps.

The meteorological inputs adopted hourly increments for four days to represent the four seasons in Birmingham. The four days were chosen to be the same to those used earlier in Tables 5.4, 5.5, 5.6, and 5.7, and most of the averaged meteorological inputs used for SOLWEIG were presented in those tables. However, the tiled T_{mrt} was simulated using 24 meteorological input files to represent the six tiles for the four days as shown in Appendix E., Tables (E.1- E.6). The chosen output maps were T_{mrt}, K_{down} (downward shortwave radiation), K_{up} (upward shortwave radiation), L_{down} (downward longwave radiation), L_{up} (upward longwave radiation), and *shadow* patterns. Moreover, an optional output was used to calculate the daily average T_{mrt}. The T_{mrt} was calculated for a standing or walking person, and the input coefficients of K and L radiation absorption were 0.70 and 0.95 respectively (Lindberg et al., 2016a). The values of albedo for walls and ground were 0.2 and 0.15, and the emissivity for walls and ground were 0.9 and 0.95 respectively according to Oke (1988). In general, the default values of the parameters were applied as described by Lindberg et al. (2016a).

6.3.3 Post-processing

The output maps from the UMEP-SOLWEIG are geoTIFF images just like the input data. The flexibility of using common formats like geoTIFF, makes it easy to deal with the outputs by other software that support this format. Thus, the output data were uploaded to ArcMap, as it provides simple and powerful tools compared with QGIS. The time-consuming task was mosaicking the tiled images for all outputs (T_{mrt}, K_{up}, K_{down}, L_{up}, L_{down}, and *shadow*). And before that the images were masked to the extent of the Birmingham City boundaries. These processes were repeated for the averaged input meteorological datasets and tiled input meteorological datasets. Then, the day and night averages were calculated from the hourly outputs, which gives better presentation of the results. Besides, it is not possible to display all the hourly outputs for all the results. The RUHI is calculated by subtracting the pixel T_{mrt} from the minimum T_{mrt} for each output map per hour. Furthermore, the areas of high and low RUHI were investigated, and the spatiotemporal change of RUHI was identified. Also, the influencing parameters on the magnitude of T_{mrt} were clarified.

6.4. Results and discussion

The results and discussion are separated into three parts. The spatial change of RUHI is investigated to identify the locations of hot and cold spots. Then, the occurrence time of these hot and cold spots is determined. After that, the influencing parameters on the formation of RUHI in particular radiation fluxes are examined.

6.4.1 RUHI spatial change

The spatial change of RUHI was investigated by employing only temporarily varying meteorological data, and then using the spatiotemporal change of meteorological data. Indeed, the temporal and spatial change of RUHI are interconnected, so the spatial change cannot be investigated without varying the time as different times give various spatial variations. Figures 6.5, 6.6, 6.7 and 6.8 demonstrate the simulated RUHI using the same averaged meteorological data for all tiles. The average maximum magnitude of RUHI could reach up to 23 ºC during the daytime on the 18th of April 2014 as shown in Figure 6.5. Whereas, the all-day average maximum RUHI was about 15.5 ºC just over the night-time which recorded 11.4 ºC on average. It is important to notice that the word diurnal was not used here and the word average or all day was employed. This is because diurnal was used to describe the average daytime and night-time LST, as the MODIS data has a day and night visit. So, to discriminate the average of 24-hour simulation of the T_{mrt}, a different word was used in this chapter to describe the daily mean.

The spatial variability of daytime RUHI is higher than the night-time, due to the presence of the sunshine. The all-day averages seem to be high in open spaces, and peak in dense trees to decrease in built-up areas (Figure 6.5). This is because, the built-up areas provide shadow which relieves the RUHI intensity. The daytime RUHI peaks in the open spaces when the city works as Radiant Urban Cool Island (RUCI). Lau et al. (2015) examined the daytime heat stress in three European cities (Gothenburg, Frankfurt, & Porto) to represent the northern, central, and southern European climates. They concluded that maximum daytime T_{mrt} is found in open spaces in all three cities despite differences in their geographical locations. Dense urban buildings with their narrow street canyons could mitigate the heat stress in the summer without causing significant changes in the winter. The situation during the night-time is reversed, the city has RUHI higher than surrounding areas. Though, the Sutton Park' trees still have high RUHI always, that does not appear to be because of the land cover type. However, the geometry of the trees prevents the required ventilation to release the heat, as they have the lowest SVF among other urban features. Similarly, Lau et al. (2015) demonstrated that T_{mrt} is strongly influenced by urban geometry in the urban environment.

Moving from a spring day to a summer day, Figure 6.6 gives a few differences from Figure 6.5. The average maximum magnitude of RUHI was about 22.9 ºC during the daytime on the 6th of July 2013, whilst, the all-day average maximum RUHI was 16.2 ºC, and the night-time did not exceed 10 ºC on average. The spatial distribution of RUHI revealed that open spaces still have high RUHI during the daytime and all-day, but they do not have the highest values in these times. So, during the daytime the highest RUHI appears in the areas north-east of the City Centre where the main rails and streets transportation infrastructure run towards the city. This pattern can also be seen in the all-day average map in Figure 6.6, and the City Centre worked as RUCI in the daytime and RUHI in the night-time. Another major difference between the spring and summer days is the Sutton Park's trees did have the highest RUHI during the daytime on the 6th of July 2013. Figure 6.6 shows similar patterns to Figure 6.5, the only difference is the intensity of RUHI. The all-day, daytime and night-time averages of maximum RUHI were 13, 18.5 and 10.9 ºC respectively on the 5th of September 2013.

The spatial distribution of RUHI on the 1st of December 2013 gives different behaviour from previous days. Figure 6.8 gives an example of the winter RUHI, when the sun energy that reaches the ground is low which noticeably differs from the autumn example (Figure 6.7). The all-day, daytime and night-time averages of maximum RUHI were 9.29, 9.34, and 9.63 ºC respectively. The City Centre worked as a RUHI in the night-time, however, it did act as a RUCI during the daytime. The trees in the Sutton Park recorded the highest RUHI for the all-day, daytime and night-time averages. Similarly, high LST of the trees in the Sutton Park was identified using the night-time airborne thermal image of Birmingham. Indeed, the Sutton Park does not contain only trees, and there are areas of grass and soil. So, it can be considered a benchmark to identify the presence of RUHI in the City Centre. When land cover types other than trees have low RUHI, the RUHI peaks at the City Centre.

The LULC of Birmingham City was clarified earlier in the previous chapters, and the visual interpretation of the results in this section builds on the already introduced knowledge. The open spaces and suburban areas did not have the maximum RUHI in all times, and the intensity of RUHI did not give high spatial differences for most of the city parts for the winter day. The open spaces still have higher RUHI during the daytime compared with built-up areas; however, transportation routes and water bodies show higher RUHI (Figure 6.8). The open spaces receive higher amount of diffuse shortwave radiation from the sky (Lindberg et al., 2014), than the narrow canyons due to the variability of SVF for the different places. The anthropogenic heat released from vehicles might play a major role to elevate the RUHI of the transportation routes. With respect to water bodies, they have been recognised earlier as good heat stores, as they keep their temperature high compared to other land cover types especially in the winter. Lindberg et al. (2014) clarifies that the spatial patterns of T_{mrt} are altered, and its differences in magnitude are reduced if the cloudiness increases. Also, Chen et al. (2016) clarified that the intra-urban differences of the T_{mrt} are large due to a number of factors. Accordingly, the spatial change of RUHI varies in magnitude and distribution for the four seasons.

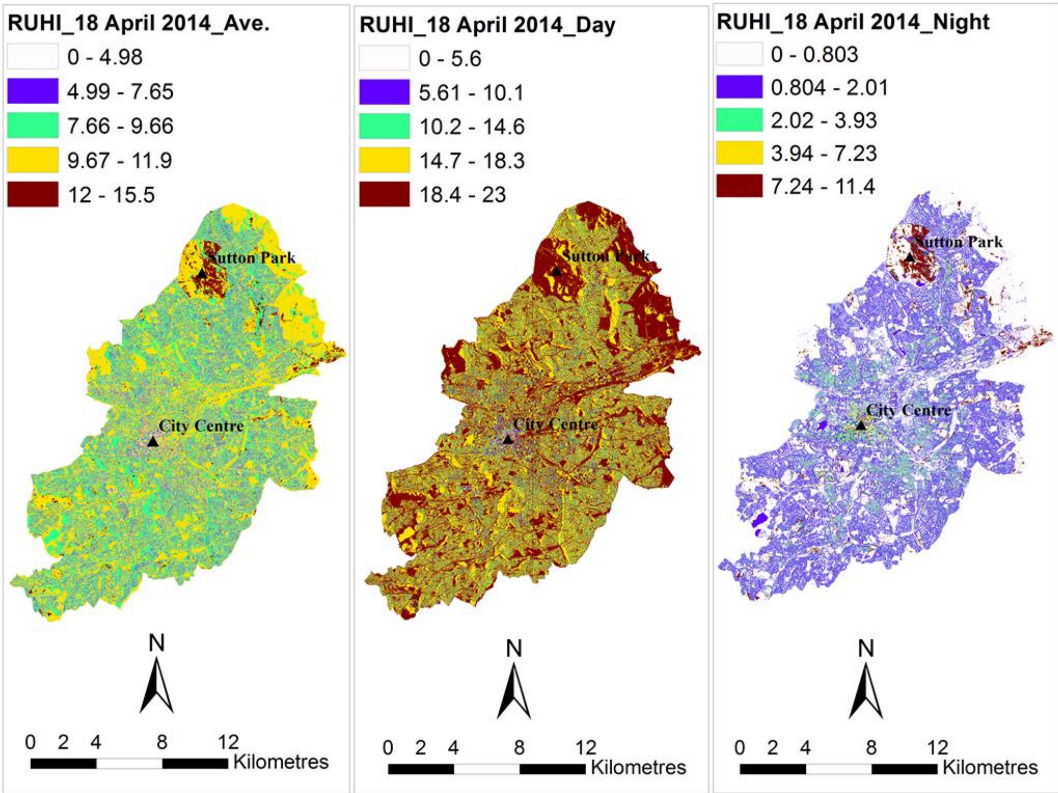

Figure 6.5: Spatial change of ave., day & night RUHI calculated from T_{mrt} of Birmingham on the 18 April 2014 (°C).

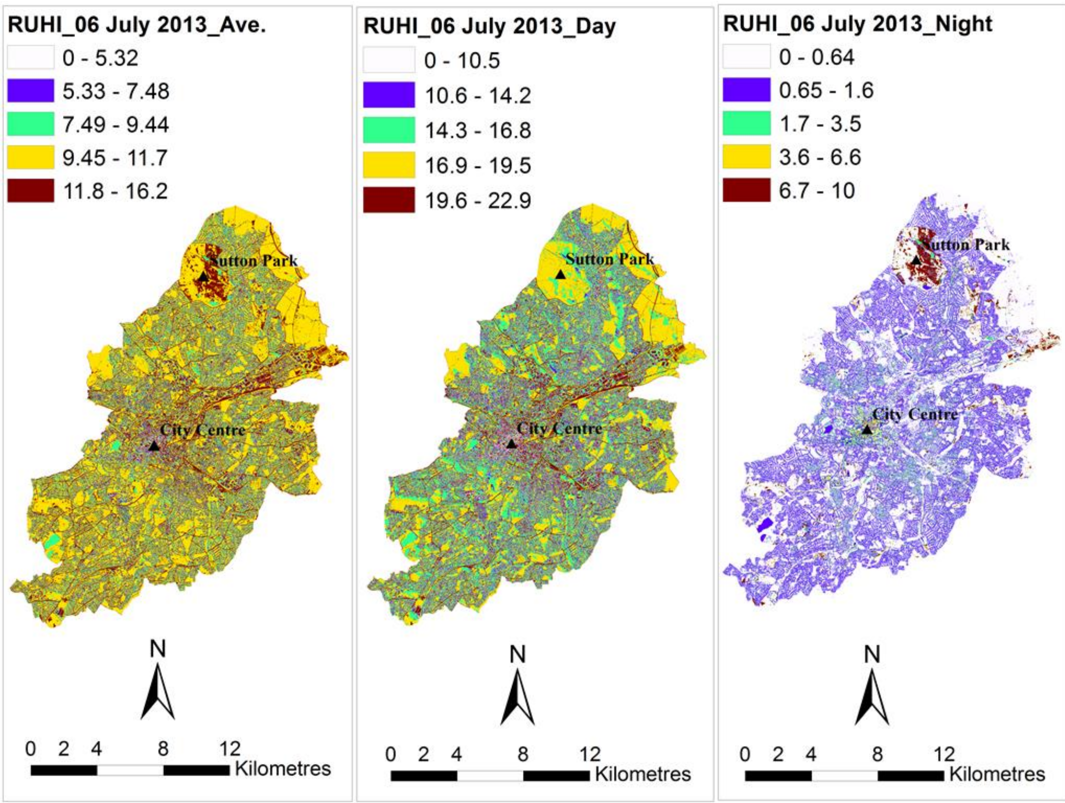

Figure 6.6: Spatial change of ave., day & night RUHI calculated from T_{mrt} of Birmingham on the 06 July 2013 (°C).

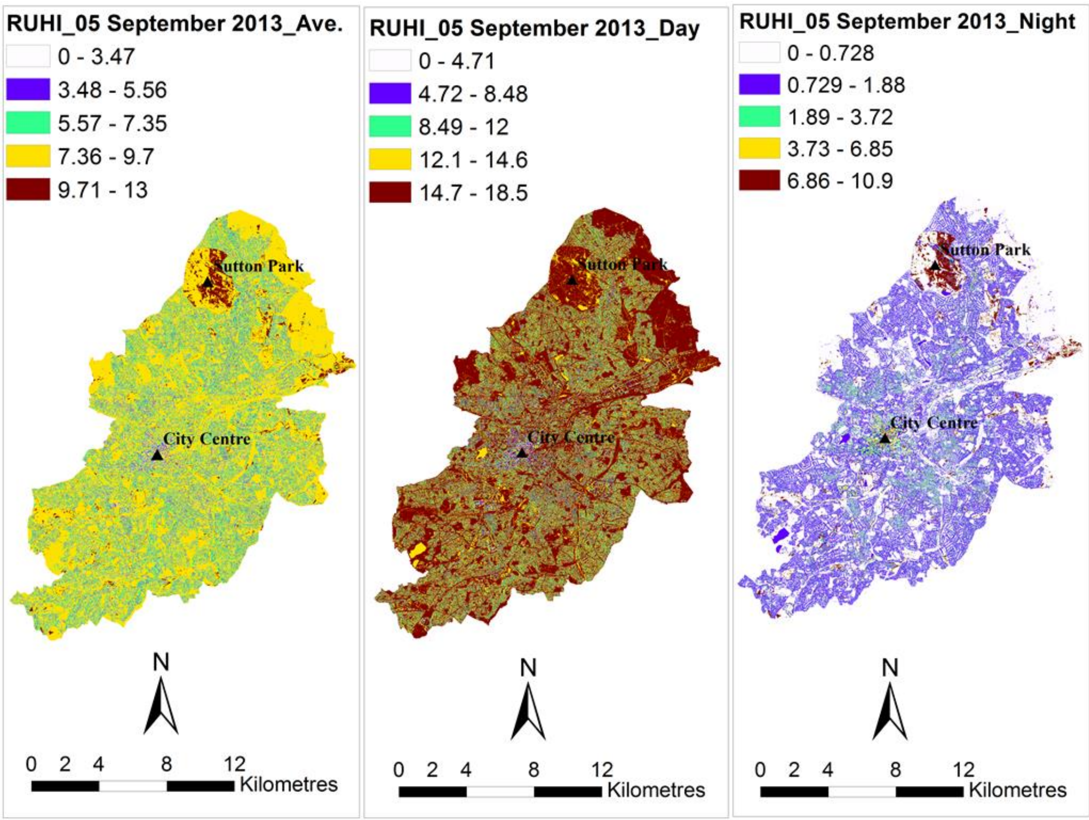

Figure 6.7: Spatial change of ave., day & night RUHI calculated from T_{mrt} of Birmingham on the 05 September 2013 (°C).

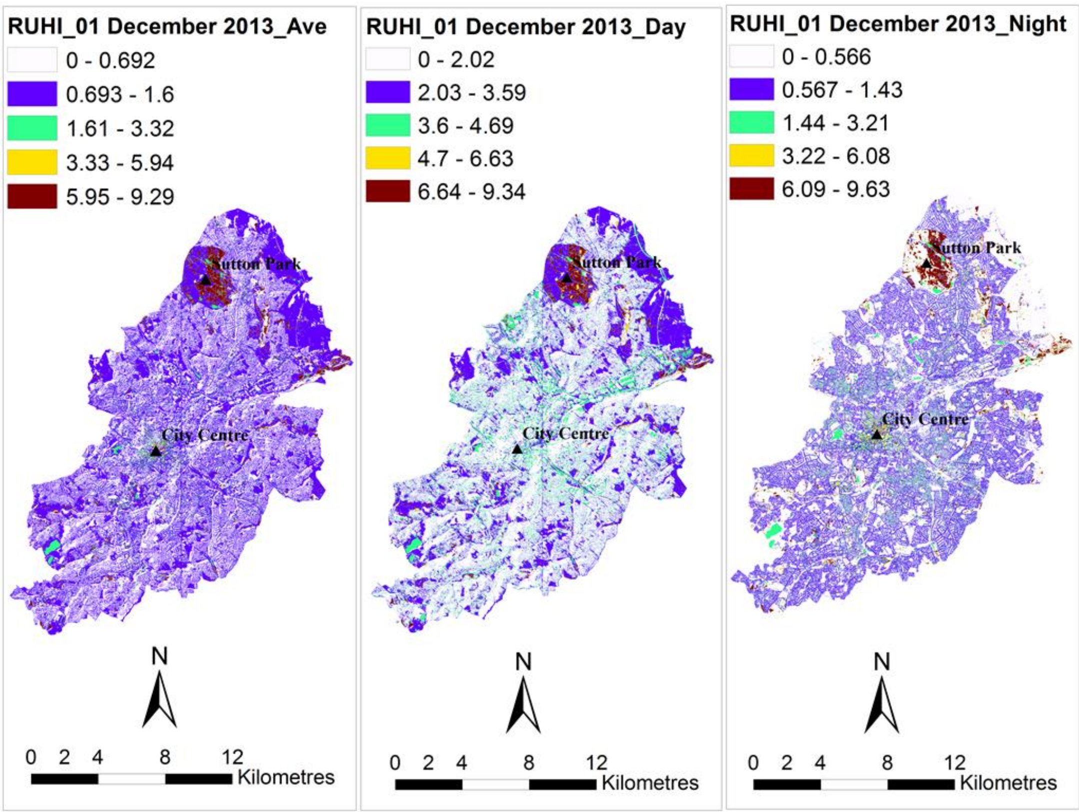

Figure 6.8: Spatial change of ave., day & night RUHI calculated from T_{mrt} of Birmingham on the 01 December 2013 (°C).

Next, the meteorological inputs were varied for each tile to test the influence of meteorological data spatial variability. The outputs demonstrated in Figures 6.9, 6.10, 6.11 and 6.12 show high spatial heterogeneity of RUHI for the tiles that did not appear before when using averaged meteorological inputs. For the magnitude of RUHI intensity, however, the winter and spring days did not show high differences between averaged and tiled meteorological data. Unlike, the summer and autumn days that gave slightly higher RUHI for the tiled meteorological inputs compared to averaged ones. Thus, on the 18th of April 2014 the all-day, daytime and night-time averages of maximum tiled RUHI were 16.4, 24.3, and 13.2 ºC respectively. And on the 1st of December 2013 the all-day, daytime and night-time averages of maximum tiled RUHI were 10.2, 10.5, and 10.7 ºC respectively. The RUHI intensity for these two days only differs by about 1 ºC increase for most maps when compared to the outputs of the averaged meteorological inputs.

On the other hand, on the 6th of July 2013 the all-day, daytime and night-time averages of maximum tiled RUHI were 19, 25.1, and 14.6 ºC respectively. Moreover, the all-day, daytime and night-time averages of maximum tiled RUHI on the 5th of September 2013 were 15.4, 21.2, and 14.4 ºC respectively. Which indicates (2-4) ºC rise in RUHI intensity of the tiled meteorological inputs over the averaged values of the meteorological data. So, it can be concluded that the spatial variability of meteorological inputs induces the formation of higher RUHI. Though, the spatial patterns of RUHI for specific feature in the city such as the City Centre and Sutton Park's trees are still similar when using tiled meteorological inputs to the averaged ones. Nevertheless, the sharp transition in magnitudes of RUHI among the tiles prevent the formation of smooth colour balance for the entire map due to values variability. Consequently, the averaged meteorological inputs are only used for further analysis of the results in the incoming sections. The limitation of the current version of UMEP (0.3.0) model to use spatially variable meteorological inputs was a barrier, as only temporal meteorological datasets are allowed (Lindberg et al., 2016a). The temporal investigation of RUHI is built on the spatial change findings. So, the focus will be on locations such as the City Centre and Suttons Park, with other places that show specific patterns.

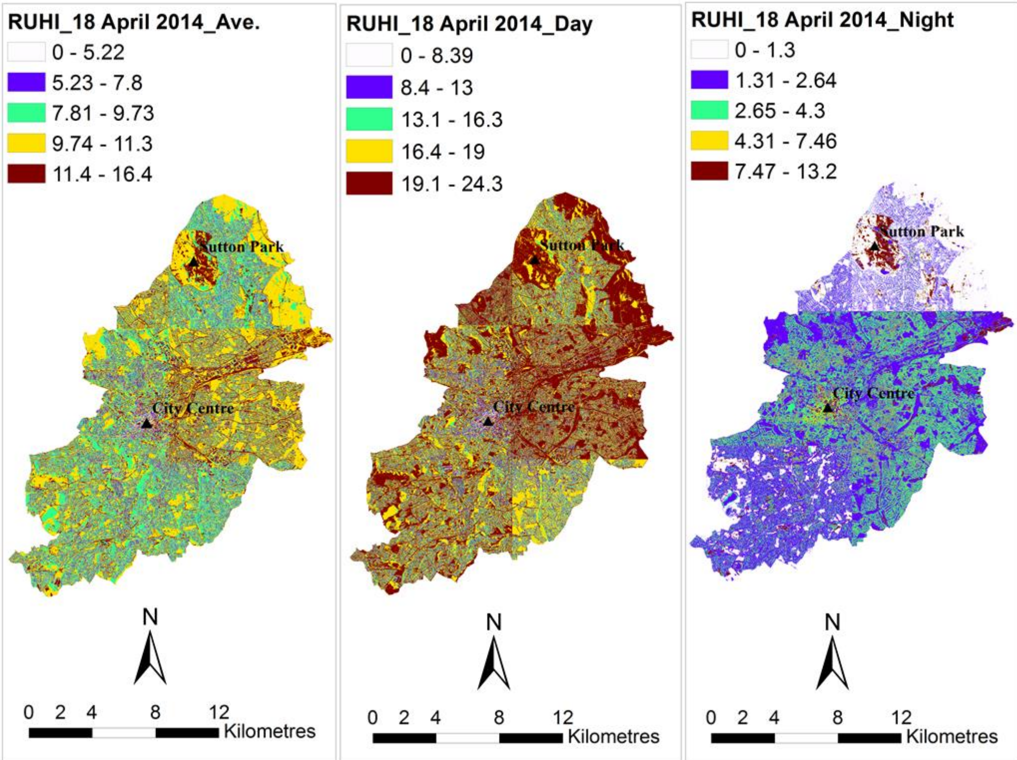

Figure 6.9: Spatial change of tiled ave., day & night RUHI calculated from T_{mrt} of Birmingham on the 18 April 2014 (°C).

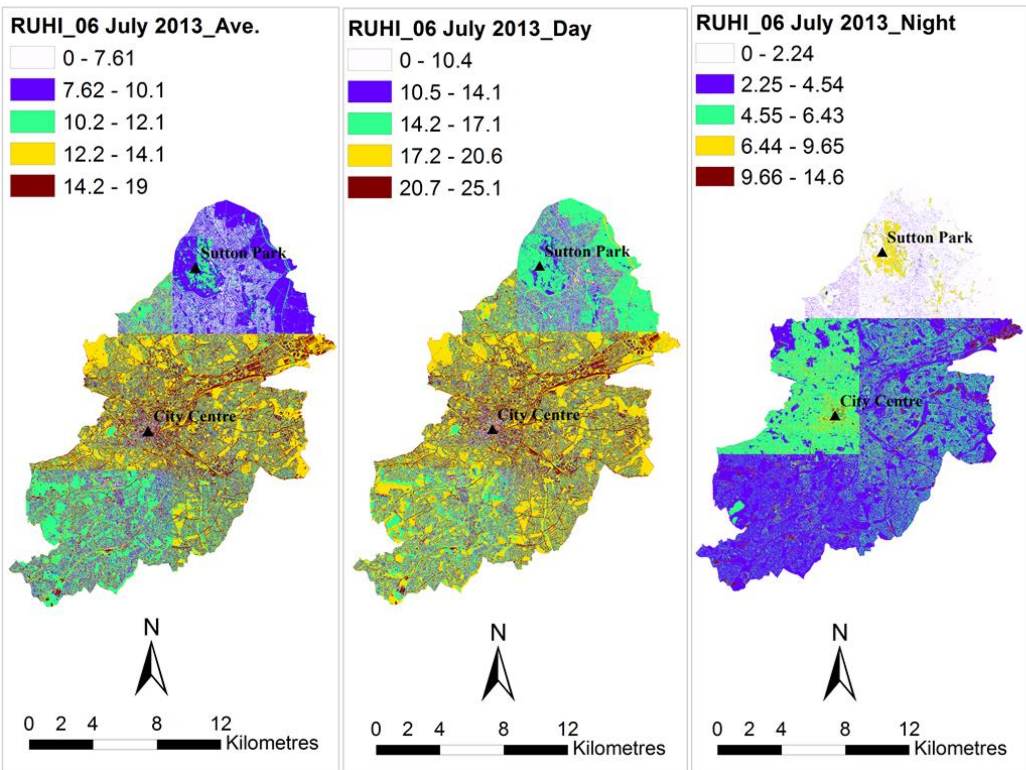

Figure 6.10: Spatial change of tiled ave., day & night RUHI calculated from T_{mrt} of Birmingham on the 06 July 2013 (°C).

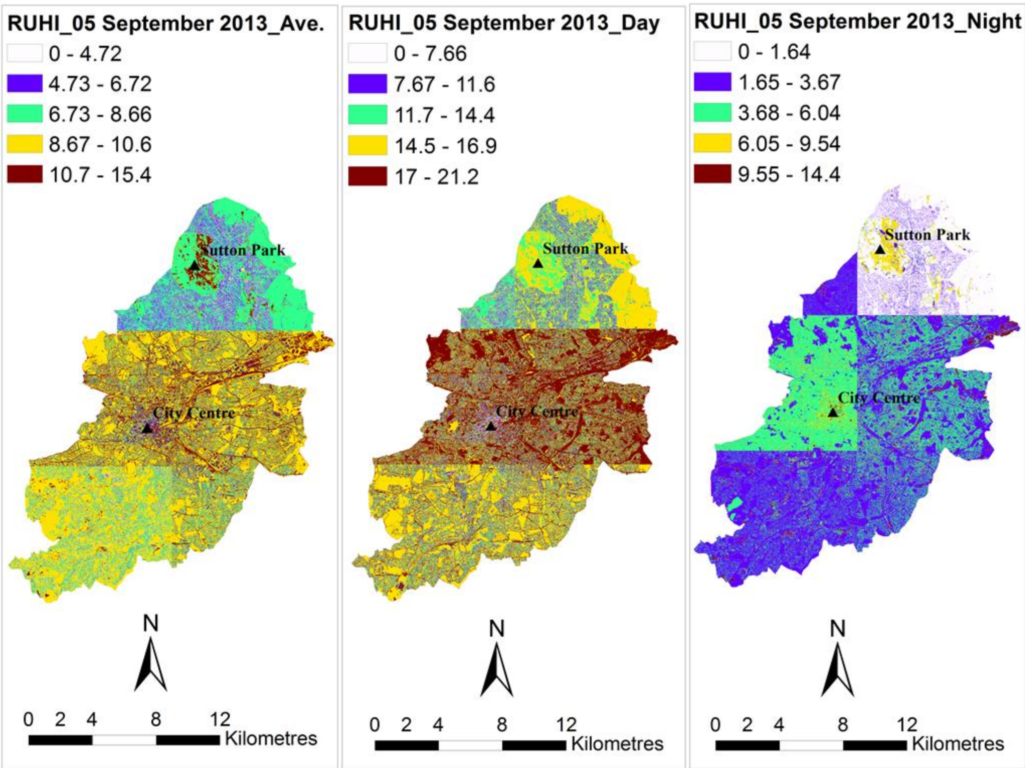

Figure 6.11: Spatial change of tiled ave., day & night RUHI calculated from T_{mrt} of Birmingham on the 05 September 2013 (°C).

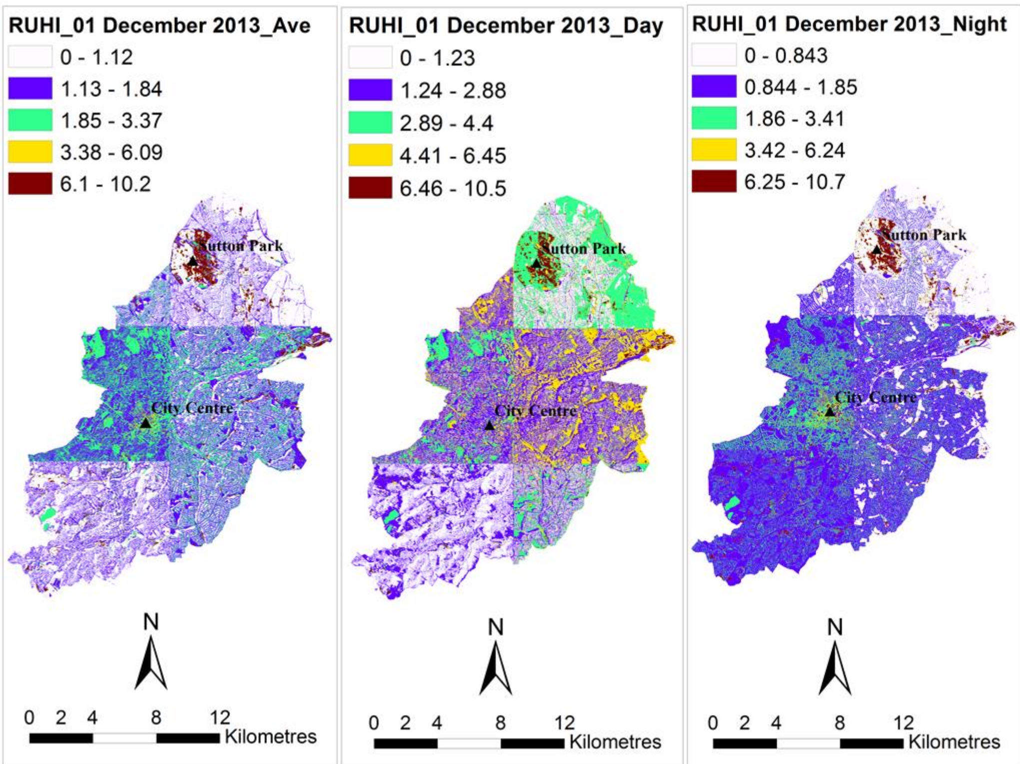

Figure 6.12: Spatial change of tiled ave., day & night RUHI calculated from T_{mrt} of Birmingham on the 01 December 2013 (°C).

6.4.2 RUHI temporal change

The temporal averages of T_{mrt}, T_a, and RUHI are investigated in Figure 6.13. The values were averaged for the entire Birmingham area on an hourly basis. The T_{mrt} magnitudes significantly increased for the four days during the daytime, when the downward shortwave radiation increases. Also, the T_a relatively increased during the daytime for the four days that represent the four seasons. However, the RUHI does not show the same behaviour for the four days, as the values here were calculated for the entire city. So, the intensity of RUHI might not be concentrated in the City Centre, and further analysis is needed to identify the RUHI peaks places.

On the 18th of April 2014, the T_{mrt} peaked at 11 a.m. by over 42 ºC, and decreased to about -6 ºC in the early morning at 5 a.m. The peak of T_a did not coincide with the peak of T_{mrt}, and both did not coincide with the RUHI peak. The RUHI intensity which represent the spatial differences of T_{mrt}, recorded higher values during the night-time than the daytime. The RUHI peaked at 6 a.m. by around 18 ºC, and the lowest was 3.8 ºC at 5 p.m. The temporal change of T_{mrt}, T_a, and RUHI on the 6th of July 2013 resembles the patterns on the 18th of April 2014. However, the main difference is the magnitudes of T_{mrt}, T_a, and RUHI between the two days. On the 6th of July 2013, the highest T_{mrt} was 55.2 ºC at 11 a.m., and the lowest was 4.93 ºC at 4 a.m. Lau et al. (2015) have set thresholds for three European cities as indicators of the moderate and severe heat stress. The severe threshold is 59.4 ºC, and the moderate value is 55.5 ºC. So, the highest T_{mrt} on the 6th of July was close to the condition of moderate heat stress. Furthermore, the highest RUHI intensity was 20.08 ºC at 5 a.m., and the lowest was 3.93 ºC at 6 p.m.

A new temporal pattern of T_{mrt} and RUHI can be seen on the 5th of September in Figure 6.13. The trend of the T_{mrt} looks like the trend of RUHI, and the only difference between them is the magnitudes. The maximum T_{mrt} and RUHI were 50.37 ºC and 34.28 ºC respectively at 10 a.m. The minimum T_{mrt} was 2.47 ºC at 5 a.m., and the minimum RUHI was 6.54 ºC at 5 p.m. The T_a showed similar temporal behaviours for the last three days. The T_a recorded higher values than the T_{mrt} during the night-time, while, the T_{mrt} values were well higher than the T_a values during the daytime.

Nevertheless, the T_a temporal change on the 1st of December 2013 showed different behaviour. The T_a values were almost higher than the T_{mrt} for the night-time and daytime, because of the low sun energy radiation reaching ground during the winter. Moreover, unlike the other days the maximum RUHI is higher than the T_{mrt} on the 1st of December 2013. The maximum and minimum T_{mrt} values were 10.26 ºC and -1.75 ºC at 12 p.m. and 7 p.m. respectively. While, the maximum and minimum RUHI values were 30.09 ºC and 5.95 ºC at 9 a.m. and 12 p.m. respectively. Accordingly, the temporal change of T_{mrt}, T_a, and RUHI demonstrated a notable distinction between daytime and night-time, and the four days revealed seasonal variations. However, the preceding discussion employed the averaged values of the indicators of the entire city, which does not reflect the behaviour of specific places.

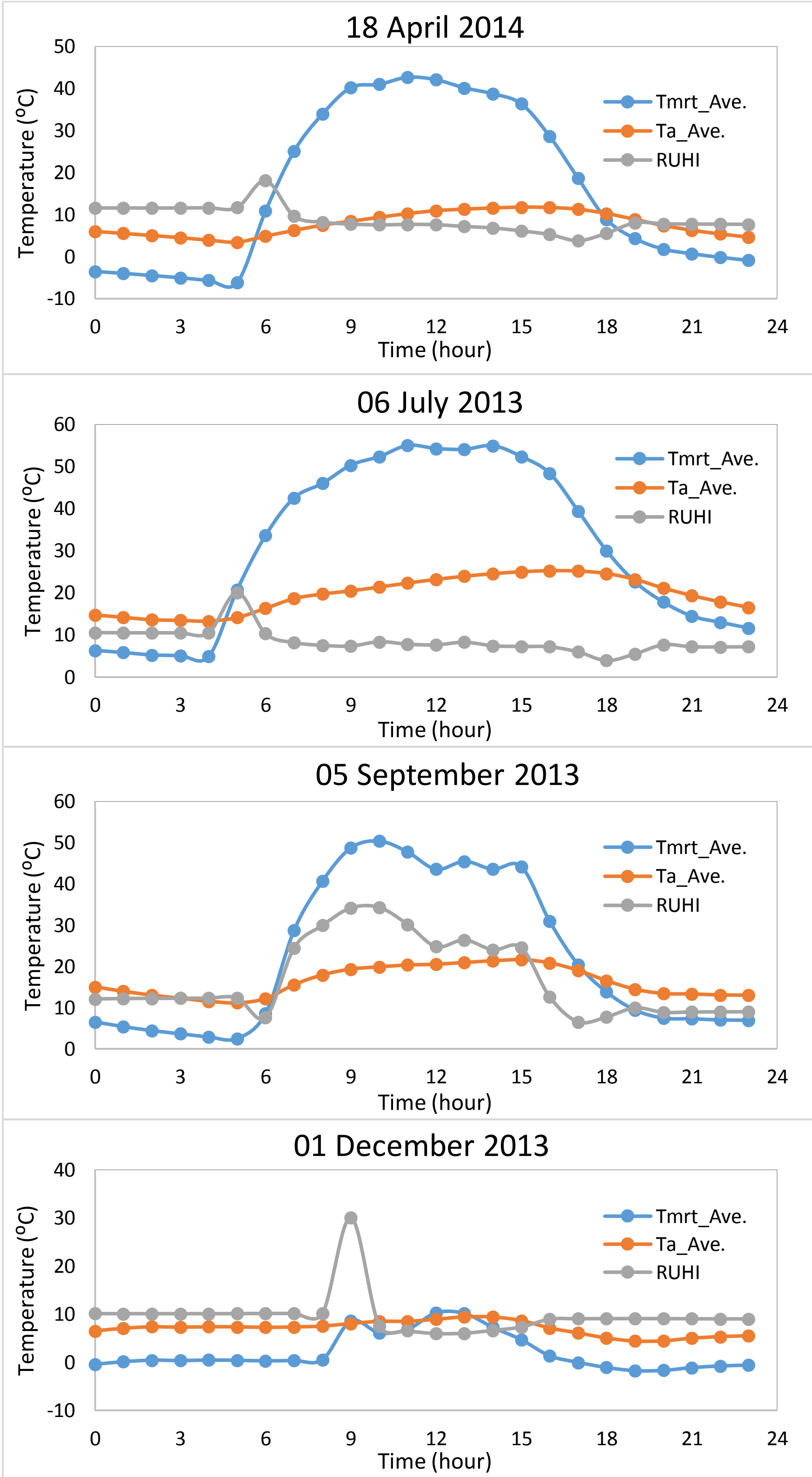

Figure 6.13: Seasonal averages of T_{mrt}, T_a, and RUHI of Birmingham City on hourly basis.

The temporal change of T_{mrt} and RUHI was further investigated for the City Centre and Sutton Park, since, these places are the most important features in terms of the T_{mrt} temporal change. Figure 6.14 compares the temporal patterns between the City Centre and Sutton Park. For the Sutton Park, pixels other than dense trees were chosen to represent the status of rural areas for two reasons. The first reason is that the dense trees showed very high values of T_{mrt}, this might be due to the lack of ventilation or overestimation. This supports the finding of Lindberg and Grimmond (2011a), when they assessed the influence of vegetation on shadow patterns and T_{mrt}. They found a small overestimation of the T_{mrt} values at locations shadowed by vegetation. For the same reason Lai et al. (2017) suggested larger SVF for cooling open spaces if direct sunlight is blocked by the trees morphology. The second reason is the analysis of the spatial variation of RUHI, CUHI and SUHI showed that the Sutton Park can be a typical location to identify the presence of UHI.

The intensity of RUHI in Figure 6.14 was characterised into two major events. If the T_{mrt} values in the City Centre were higher than the Sutton Park, the phenomenon here called RUHI. However, if the T_{mrt} values in the City Centre were lower than the Sutton Park, the city works as Cool Island and the phenomenon called RUCI with negative values. On the 18th of April 2014, the T_{mrt} values dramatically increased during the daytime for both City Centre and Sutton Park. However, during the night-time the values of T_{mrt} in the City Centre are higher than in the Sutton Park. In the daytime the situation is reversed, as the values of T_{mrt} in the City Centre are by far lower than their values in the Sutton Park. The T_{mrt} peaked in the Sutton Park at 11 a.m. by 43.35 ºC. Whereas, it peaked in the City Centre at 3 p.m. by 33.01 ºC. So, the T_{mrt} peaks at different times for the different places in Birmingham. The RUHI temporal patterns show night-time RUHI and daytime RUCI. Furthermore, the intensity of RUHI peaked at 5 a.m. by approximate 5 ºC. Conversely, the intensity of RUCI peaked at 9 a.m. by about -30.98 ºC. There is a difference between the T_{mrt} and T_a in terms of the magnitudes in outdoor conditions. Walikewitz et al. (2015) clarifies that T_{mrt} can be more than 30 K above T_a, and shows a clear spatial pattern.

On the 6th of July 2013, the maximum T_{mrt} in the City Centre was 51.68 ºC at 2 p.m., where, the maximum in the Sutton Park was 53.77 ºC at 11 p.m. The maximum RUHI was 3.92 at 12 a.m., but, RUCI was at its maximum by -25.62 ºC at 10 a.m. On the 5th of September 2013, the temporal patterns and intensities of the T_{mrt}, RUHI, and RUCI did not significantly differ from those on the 6th of July 2013. Nonetheless, the temporal trends of the T_{mrt} did show significant variation between the City Centre and Sutton Park during the day and night-time on the 1st of December 2013. With a slight increase of the T_{mrt} values during the daytime compared to the night-time. The T_{mrt} peaked at the City Centre at 1 p.m. by 8.18 ºC, while, it peaked in the Sutton Park at 9 a.m. by 20.30 ºC. The RUHI peaked at 6 a.m. by 2.88 ºC, and the RUCI peaked at 9 a.m. by -16.48 ºC. Only one hour separates the peak of RUHI and RUCI, because, this hour was the sunrise time on the on the 1st of December 2013. Which tells how much the sun energy is important in the urban energy balance.

In general, the temporal patterns of the four days demonstrate significantly higher T_{mrt} in the daytime compared to the night-time except for the winter day. Lindberg et al. (2014) found large T_{mrt} differences among seasons and between the day and night-time. Furthermore, the City Centre works as RUHI during the night-time, and RUCI during the daytime. Thus, built up areas can reduce the heat stress during the daytime through providing shadows. This agrees with Lau et al. (2015), as they suggested that dense urban structure can decrease the heat stress during the daytime through reducing the T_{mrt} in the summer. In opposition, the Sutton Park works as RUCI during the night-time, and RUHI during the daytime. The RUCI intensities are much higher than the RUHI as shown in Figure 6.14. The cold-related deaths were reported in the literature, which is expected to decrease due to milder winters (Astrom et al., 2013). However, the risk of heatwaves on the populations that adopted to long periods of cold weather might be greater, since they have not adapted to long hot periods (Astrom et al., 2013).

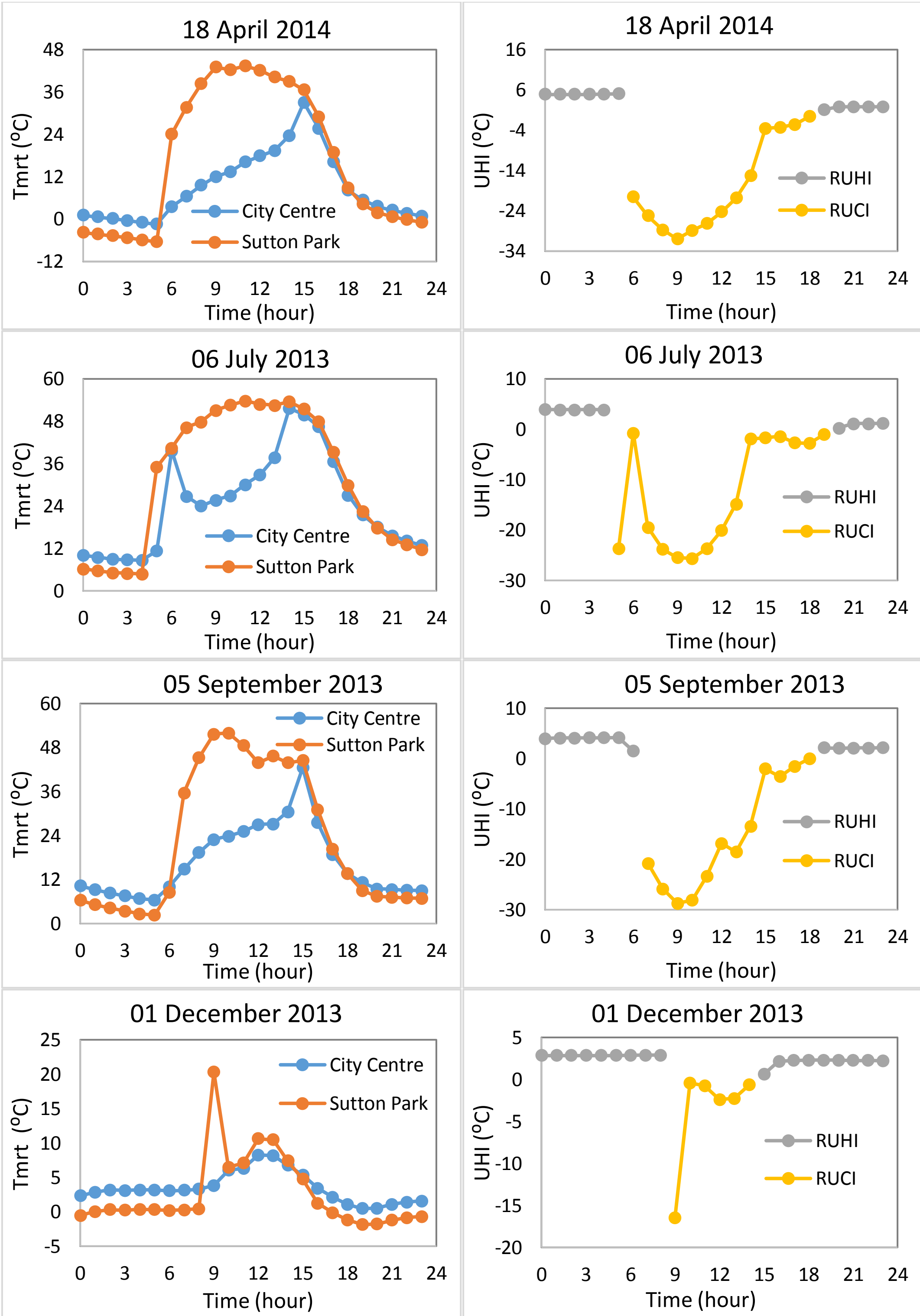

Figure 6.14: Seasonal T_{mrt} (left), RUHI and RUCI (right) of Birmingham's City Centre and Sutton Park on hourly basis.

6.4.3 Radiation fluxes, RUHI, and RUCI

The radiation fluxes have great impact on the T_{mrt}, since the T_{mrt} includes the calculation of the shortwave and longwave radiation fluxes from the three dimensional surroundings of human (east, west, north, south, upward, and downward) (Thorsson et al., 2014). However, the calculation or measurement of radiation fluxes over a large extent is a challenging task. Therefore, another approach was investigated to model the energy balance on a large scale. This approach is called the Surface Energy Balance Algorithm for Land (SEBAL), that uses satellite based data (Shunlin et al., 2013). Both SOLWEIG and SEBAL calculate the outgoing shortwave and longwave radiation based on Stefan-Boltzmann law. Also, both approaches combine remote sensing images and routine meteorological data to derive the net all wavelength radiation. Nevertheless, SEBAL models the L_{down} with a very course resolution, as it relies on the air temperature stations. Furthermore, SEBAL is often applied over flat surfaces, and when applied over mountainous areas adjustments based on a DEM need to be made (Bala et al., 2013). A promotion to the SOLWEIG model, it accounts the impacts of sky view factor and shadow patterns by employing a DSM of the study site (Lindberg and Thorsson, 2009). Hence, SOLWEIG model was employed to calculate the shortwave and longwave radiation fluxes as well as shadow patterns, as it overcomes several limitations that SEBAL surfers from. This section is meant to investigate the effects of radiation fluxes as influencing parameters on the spatial variability of the maximum RUHI and RUCI.

6.4.3.1 Radiation fluxes and RUHI

The RUHI was identified when it peaked in the City Centre, which took place during the night-time. Figures 6.15, 6.16, 6.17 and 6.18 show the RUHI, L_{up}, L_{down}, K_{down}, K_{up}, and *shadow*, that represent the simulation of SOWLEIG at the time of maximum RUHI for the four seasons. Since the maximum RUHI occurs during the night-time where there is no sun energy, the K_{down}, K_{up}, and *shadow* have zero values. Therefore, the maps of K_{down}, K_{up}, and *shadow* do not show any variation in Figures 6.15, 6.16, 6.17 and 6.18. Which means that they do not have any impact on the formation of RUHI during the night-time. Hence, both longwave radiations Lup and L_{down} are dominant during the night-time to influence the RUHI. On the 18th of April 2014 at 5 a.m., the Lup peaked in the built-up areas to 325 W/m^2, and it did not show significant variation between the City Centre and other built-up areas. While, the L_{down} maximum was 324 W/m^2 with spatial variation like the RUHI (Figure 6.15). Which means the L_{down} is the major contributor to the RUHI during the night-time to cause the high T_{mrt} in the City Centre.

On the 6th of July 2013 at 12 a.m., the Lup peaked at the City Centre by 382 W/m^2, and the L_{down} recorded its maximum in the Sutton Park's trees by 382 W/m^2. Though the spatial variation of RUHI looks like the L_{down}, the Lup seems to have higher impact on the formation of RUHI in the City Centre (Figure 6.16). This reflects the influence of seasonal variation on the RUHI. When the RUHI was mainly influenced by the L_{down} in the spring, the Lup had larger impact on the RUHI in the summer. Lindberg et al. (2008) clarifies that the L_{down} is modelled by using input information of air temperature and relative humidity, while, the ground surface's temperature and properties are dominant in the calculation of Lup based on the Stefan-Boltzmann law. From that the summer *Lup* played a major role in the RUHI formation compared to the spring day. And for both days the L_{down} contributed to the RUHI, with more noticeable impact on the spring day.

Moving to an autumn day on the 5th of September 2013 at 5 a.m., the behaviour of Lup and L_{down} was almost like the summer day. The only minor difference is the maximum intensity of the Lup and L_{down} values. The maximum value for both Lup and L_{down} was 363 W/m^2 (Figure 6.17). The situation of the radiation fluxes in the winter day on the 1st of December 2013 at 6 a.m. as shown in Figure 6.18 did not differ from the spring day. The intensity of the fluxes was the only difference between the winter and spring days. The maximum values of Lup and L_{down} were 344 and 345 W/m^2 respectively as shown in Figure 6.18. Accordingly, the influencing parameters on the variation of RUHI showed seasonal difference in terms of the distribution and intensity. The K_{down}, K_{up} and *shadow* did not have any impact on the RUHI. However, the Lup and L_{down} were the major contributors to the RUHI. The Lup has higher impact on the RUHI during the hot days in the summer and autumn, while, the L_{down} has higher effect during the winter and spring. In other words, the ground surface's properties and temperature are the major players in the formation of RUHI in the summer and autumn, nevertheless, in the winter and spring the sky's temperature and properties played a major role in the formation of RUHI.

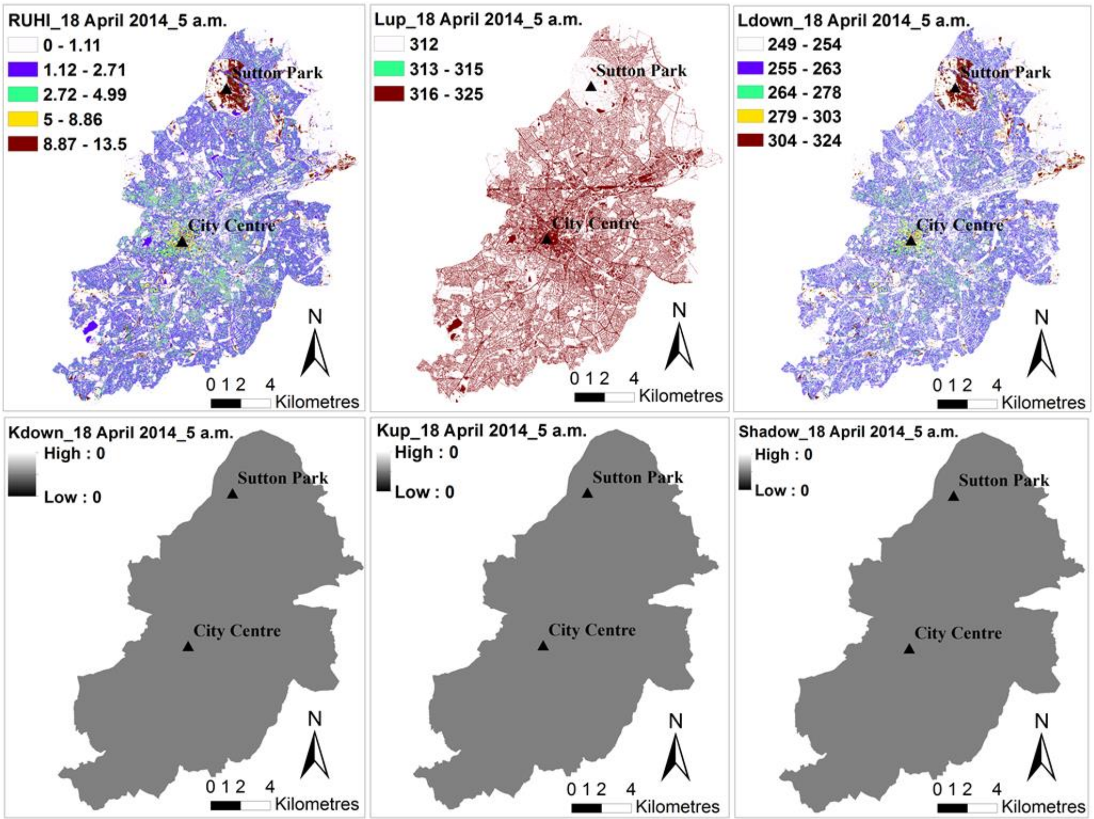

Figure 6.15: RUHI (°C), L_{up} (W/m^2), L_{down} (W/m^2), K_{down} (W/m^2), K_{up} (W/m^2), and *shadow* of Birmingham on the 18th April 2014 at 5 a.m. There is no *K* component and *shadow* because the times stated were prior sunrise.

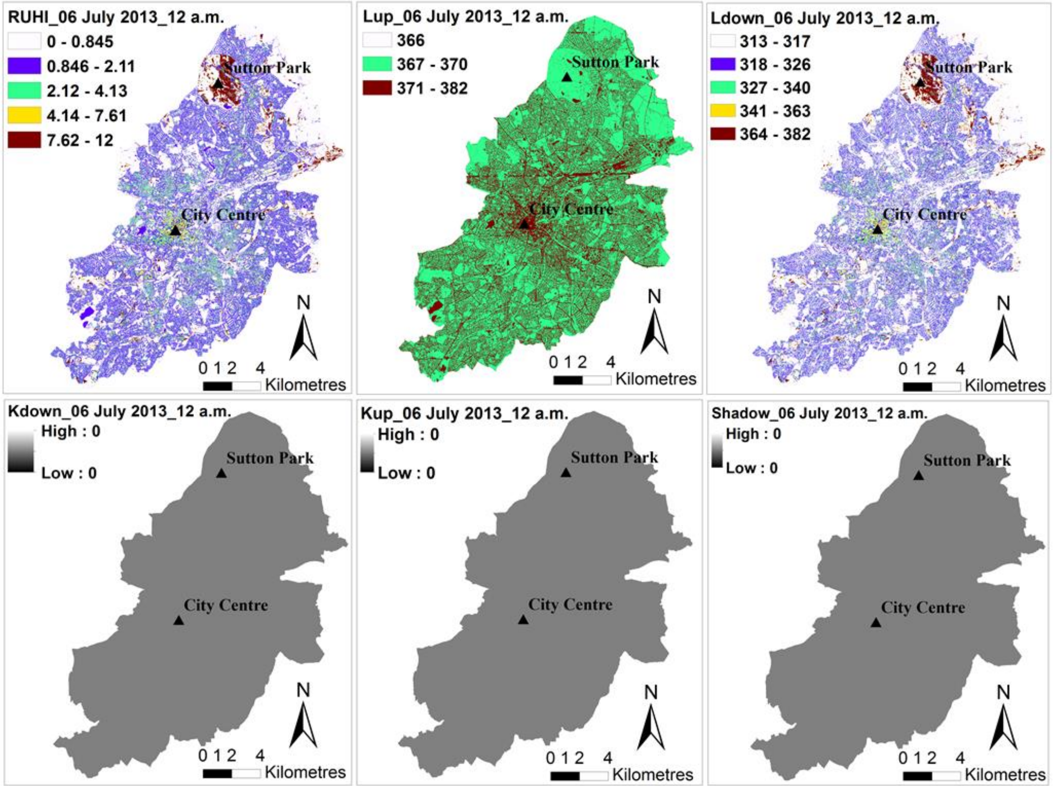

Figure 6.16: RUHI (°C), L_{up} (W/m^2), L_{down} (W/m^2), K_{down} (W/m^2), K_{up} (W/m^2), and *shadow* of Birmingham on the 6th July 2013 at 12 a.m. There is no *K* component and *shadow* because the times stated were prior sunrise.

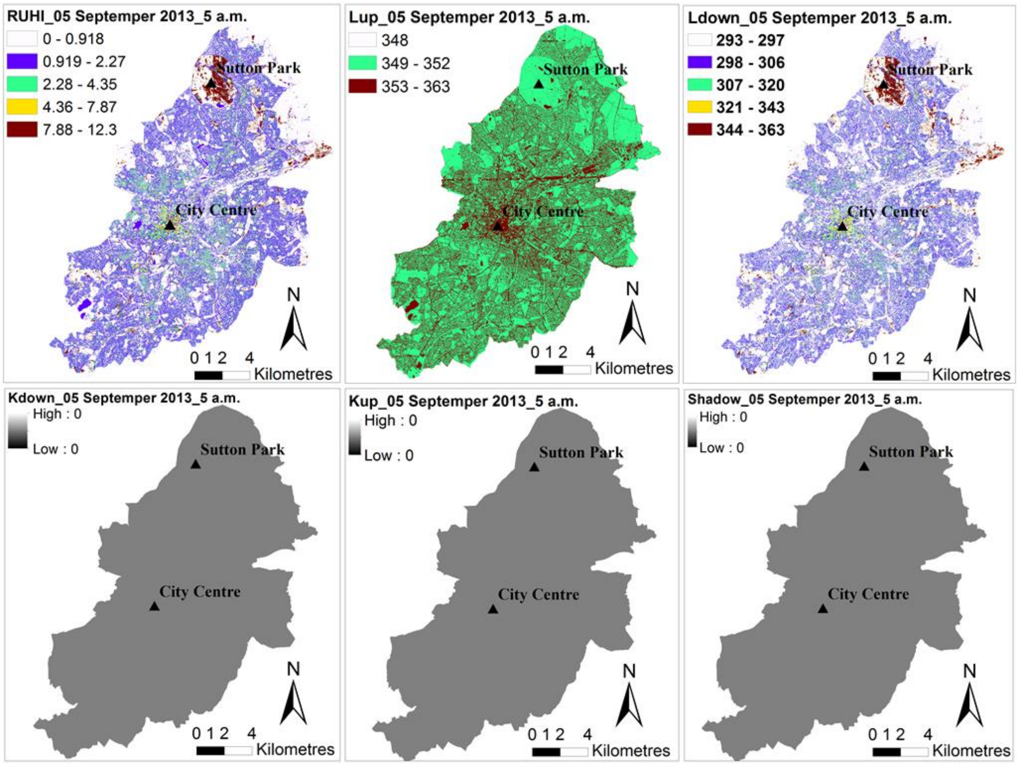

Figure 6.17: RUHI (°C), L_{up} (W/m^2), L_{down} (W/m^2), K_{down} (W/m^2), K_{up} (W/m^2), and *shadow* of Birmingham on the 5th September 2013 at 5 a.m. There is no *K* component and *shadow* because the times stated were prior sunrise.

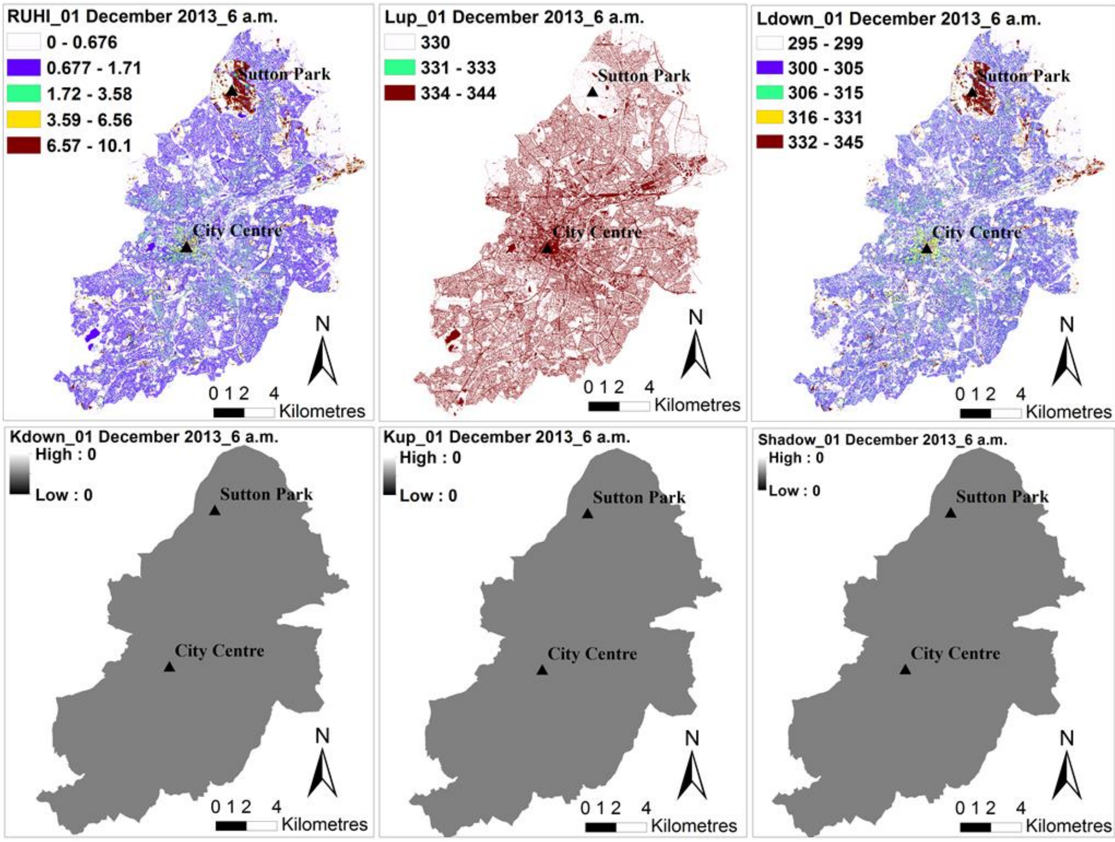

Figure 6.18: RUHI (°C), L_{up} (W/m^2), L_{down} (W/m^2), K_{down} (W/m^2), K_{up} (W/m^2), and *shadow* of Birmingham on the 1st December 2013 at 6 a.m. There is no *K* component and *shadow* because the times stated were prior sunrise.

6.4.3.2 Radiation fluxes and RUCI

The City Centre works as a Cool Island in the daytime, when the buildings provide shadow to the street canyons, which significantly reduces the intensity of T_{mrt}, and in turns maximises the differences between the roof's tops and street's ground as shown in Figure 6.19. The roofs in the City Centre are directly exposed to the sun energy just like the open spaces. The RUCI was calculated by subtracting the pixel value from the minimum value over the entire city. Even though the RUCI was calculated by subtracting the minimum value across the city, this does not make much difference because the edges of the city were assumed to have similar temperature to the surroundings. Thus, the zero pixels means that these pixels work as Cool Islands towards others. Jänicke et al. (2016) demonstrates that there is a differentiation in T_{mrt} between sunlit and shaded areas during the day. They added that the inner-city areas established an urban cool island during the day when analysing the T_{mrt} for the city of Berlin, Germany.

The seasonal changes of RUCI are represented in Figures 6.20, 6.21, 6.22 and 6.23, when all the radiation fluxes exist during the daytime. Figure 6.20 shows the RUCI, radiation fluxes and shadow on the 18th of April 2014 at 9 a.m. The maximum values of L_{up}, L_{down}, K_{down}, and K_{up} were 380, 408, 568, and 149 W/m^2 respectively. The shadow is concentrated in the City Centre with a value of 1, and zero values means no shadow exists. The L_{up} and L_{down} are low in the open spaces, and relatively high close the built-up areas, while, the K_{down} is low in the canyons of the City Centre and within the trees. Lindberg et al. (2008) explains that the K_{down} is the summation of direct, diffuse and global radiation, while, the K_{up} is the K_{down} times the albedo. The direct radiation is low in the city canyons where the buildings prevent the penetration of radiation. This is the major cause of RUCI, when the shadow relives the T_{mrt} considerably.

Next, the maximum values of L_{up}, L_{down}, K_{down}, and K_{up} were 522, 522, 738, and 194 W/m^2 respectively on the 6th of July 2013 at 10 a.m. The spatial variation of radiation fluxes and shadow patterns in Figure 6.21 resembles those in Figure 6.20. So, the only difference between the spring and summer days is the intensity of radiation fluxes. On the 5th of September 2013 at 9 a.m. the maximum values of L_{up}, L_{down}, K_{down}, and K_{up} were 431, 463, 542, and 142 W/m^2 respectively. When more features other than street canyons worked as Cool Islands to give slightly different spatial patterns of RUCI from the spring and summer days (see Figures 6.19 and 6.22). Nevertheless, the typical RUCI can be seen in the winter on the 1st of December 2013, when almost all the city features worked as Cool islands as shown in Figures 6.19 and 6.23. The maximum values of L_{up}, L_{down}, K_{down}, and K_{up} were 347, 346, 46.1, and 11.6 W/m^2 respectively (Figure 6.23).

There are two reasons behind having different spatial patterns of the RUCI in the winter compared to other seasons. The first one, the K_{down} values for the spring, summer and autumn are higher other radiation fluxes, while the K_{down} values in the winter are lower than the L_{up} and L_{down} due to the insufficient sun energy reaching the ground because of the clouds and sun angle. Lindberg et al. (2015b) found that the overall K_{down} is higher during summer, when comparing a winter and a summer month. The second reason is that the *shadow* is concentrated in the City Centre for the spring, summer and autumn. In the winter; however, the *shadow* is spread across the entire city except for the open spaces, because of the inclined sun angle with the ground surface. Therefore, Lau et al. (2015) suggested a more diverse urban thermal environment in dense urban settings, to compensate for reduced solar access in the winter. The seasonal magnitudes of the T_{mrt} increase when the shortwave and longwave radiations increase. This agrees with Lai et al. (2017) who concluded that the increase of either shortwave or longwave fluxes by10 W/m^2 leads to 1.6 Kelvin increase of T_{mrt} across different open spaces. Furthermore, a study by Marino et al. (2017) predicted that the direct component of solar radiation is strongly responsible for the rise of T_{mrt} during the daytime as well as the diffuse and reflected components. In general, the Kdown and shadow patterns primarily derived the spatial and temporal variation of RUCI.

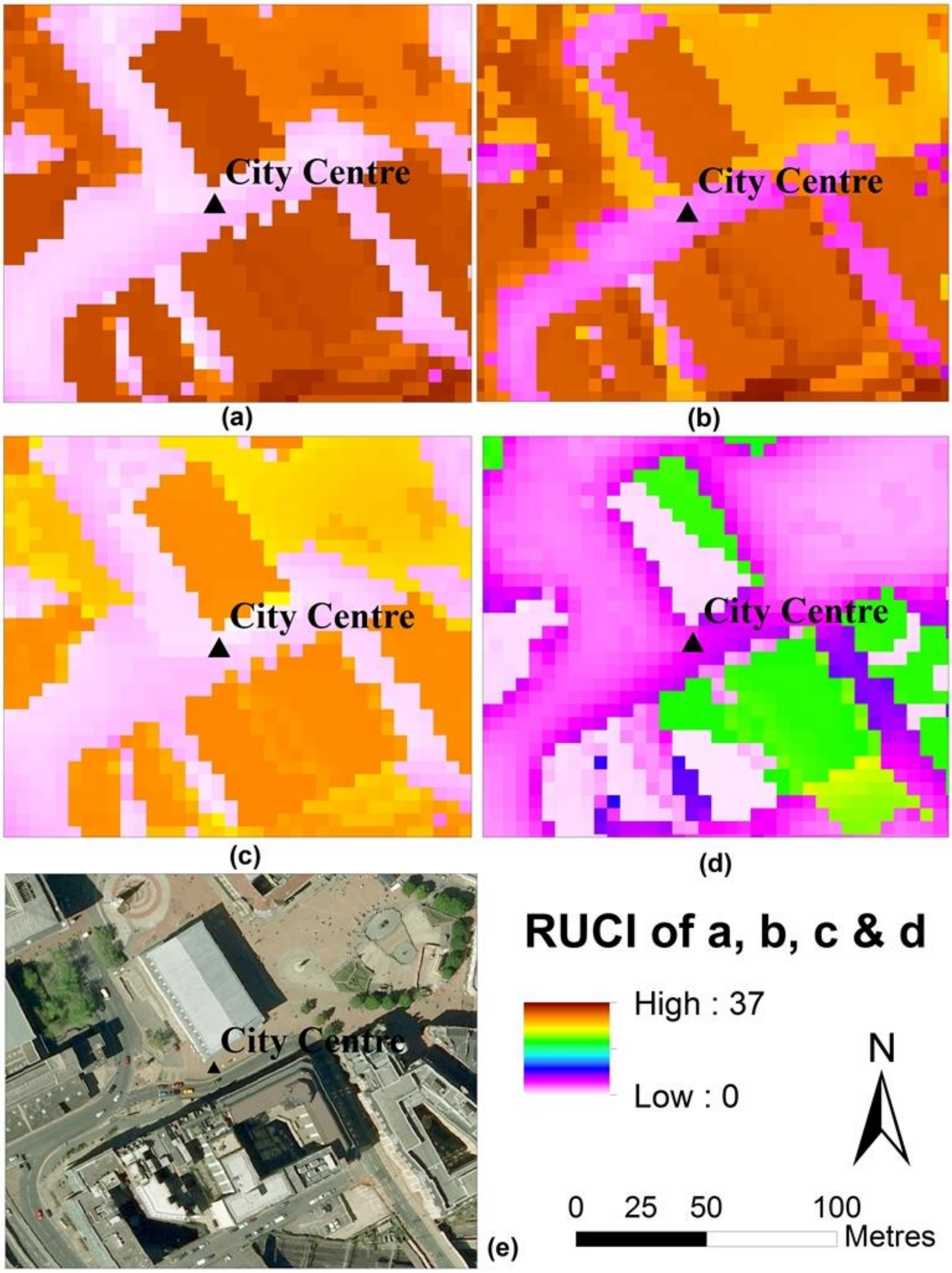

Figure 6.19: Seasonal RUCI (°C) at the City Centre of Birmingham (a) on the 18th of April 2014 at 9 a.m., (b) on the 6th of July 2013 at 10 a.m., (c) on the 5th of September 2013 at 9 a.m., (d) on the 1st of December 2013 at 9 a.m., & (e) aerial photograph of City.

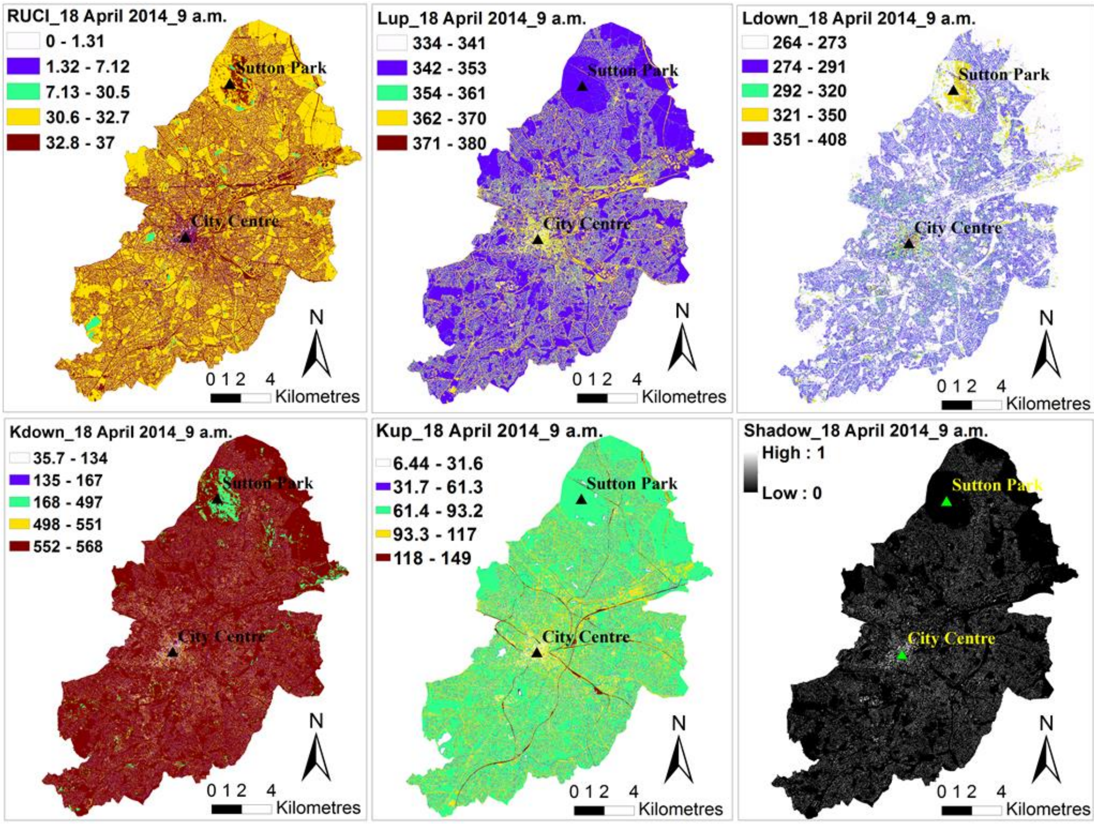

Figure 6.20: RUCI (°C), L_{up} (W/m²), L_{down} (W/m²), K_{down} (W/m²), K_{up} (W/m²), and *shadow* of Birmingham on the 18th April 2014 at 9 a.m.

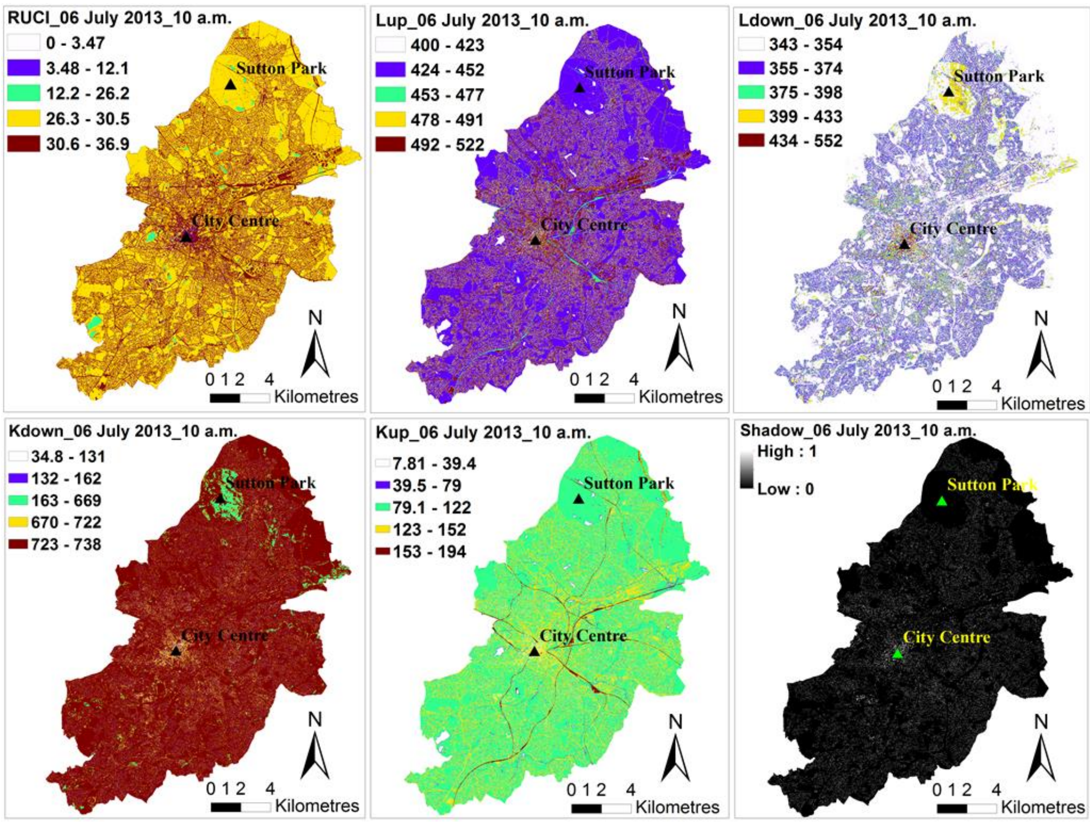

Figure 6.21: RUCI (°C), L_{up} (W/m²), L_{down} (W/m²), K_{down} (W/m²), K_{up} (W/m²), and *shadow* of Birmingham on the 6th July 2013 at 10 a.m.

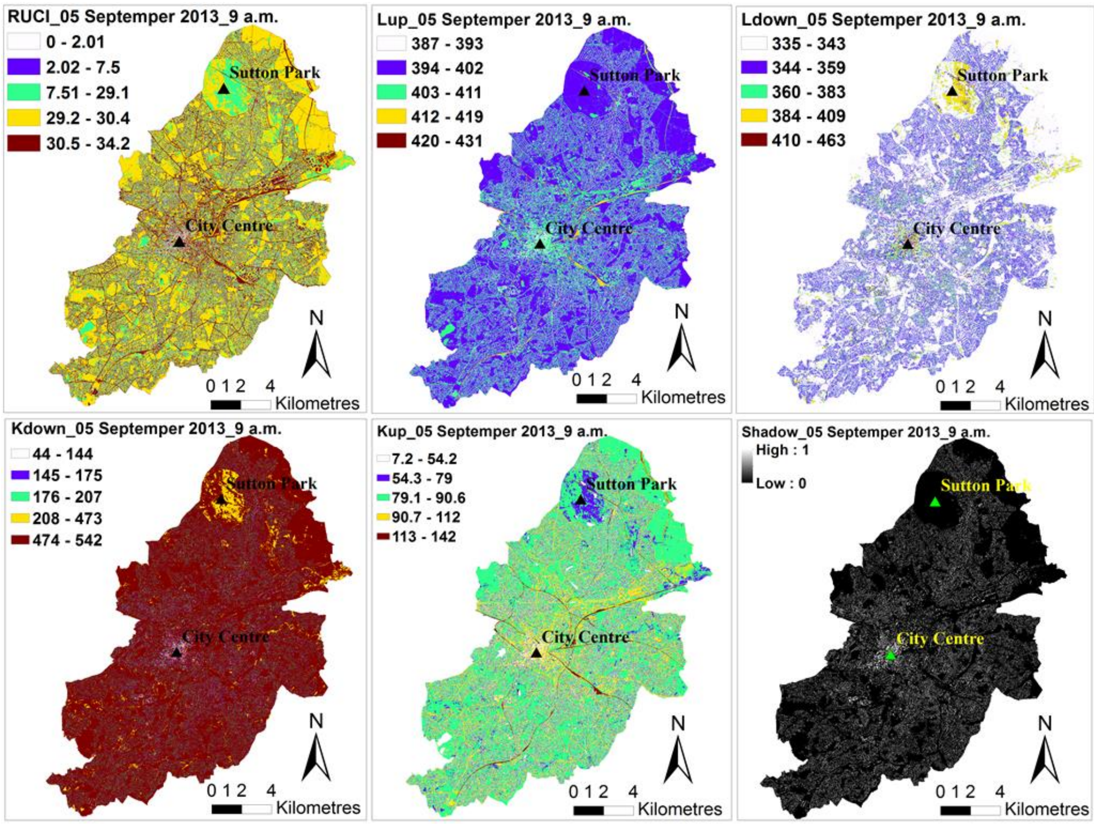

Figure 6.22: RUCI (°C), L_{up} (W/m²), L_{down} (W/m²), K_{down} (W/m²), K_{up} (W/m²), and *shadow* of Birmingham on the 5th September 2013 at 9 a.m.

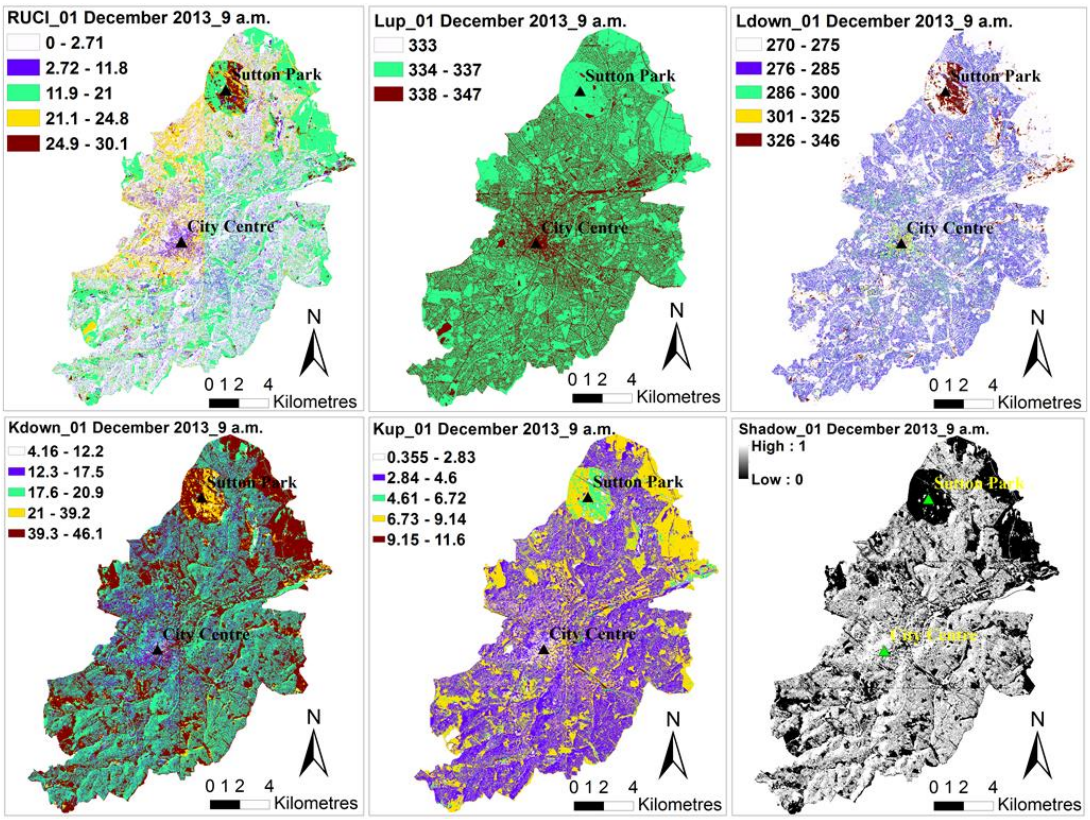

Figure 6.23: RUCI (°C), L_{up} (W/m²), L_{down} (W/m²), K_{down} (W/m²), K_{up} (W/m²), and *shadow* of Birmingham on the 1st December 2013 at 9 a.m.

6.5 Discussion

The use of T_{mrt} to measure the UHI in this study is an innovative approach as the common use of T_{mrt} is mainly for outdoor human thermal comfort. This approach has enabled the author to compare the use of T_{mrt}, T_a and LST as predictors of the UHI presence. However, a comparison of the relevance of the findings in this study compared to the previously published research about the outdoor microclimate that adopted the T_{mrt} is needed to validate the research outcomes. Chen et al. (2016) studied the thermal radiant environment using the SOLWEIG model in Shanghai under heat waves, and found that the heat stress is quite severe in daytime with T_{mrt} commonly well above 60 ºC. Furthermore, they concluded that the spatial differences of T_{mrt} are largely influenced by building density and height, street orientation and vegetation. Similarly, in this study a spatial and temporal change of T_{mrt} was found with high magnitudes in hot weather. For example, the average T_{mrt} reached 55 ºC on the 6th of July 2013 when using averaged meteorological data.

Lau et al. (2016) simulated the T_{mrt} using the SOLWEIG model in Hong Kong, and the results showed that urban geometry plays an important role in intra-urban differences in the summer daytime. Likewise, this study revealed that open areas are generally warmer than surrounding narrow street canyons in the daytime of the four seasons. Lindberg et al. (2016b) found that the shadow patterns of buildings and vegetation govern the spatial pattern of T_{mrt} during warm and clear weather in Gothenburg, Sweden. The open locations were found to have the highest average daytime T_{mrt} due to the high frequency of sunlit occasions. This agrees with this study finding that the shortwave radiation and shadow patterns govern the spatial change of daytime T_{mrt}. The Land cover types also influenced the magnitude of the T_{mrt} where the grass for example had the lowest T_{mrt} in hot daytimes. In the same way, the vegetation was effective at reducing the heat stress in London within dense urban environments in the summer (Lindberg and Grimmond, 2011b).

There are differences among the RUHI, SUHI and CUHI in terms of their spatiotemporal change and the contributing parameters of Birmingham. The City Centre worked as a RUCI in the daytime, while, the night-time induced the development of RUHI. The K_{down}, K_{up} and *shadow* did not have any impact on the RUHI during the night-time, however, the L_{up} and L_{down} were the major contributors to the RUHI. On the other hand, the densely built-up areas and the business districts recorded the largest LST at times of high anthropogenic activities. The land cover indices negatively correlated with LST, and could explain up to 70 % of the LST variation for the significant models. Whereas, the high intensity CUHI happened during the clear and calm weather. The CUHI occurred in the suburban areas as well as the urban areas due to the presence of impervious surfaces and anthropogenic activities. The regression models could explain up to 95% of the air temperature variations when laid under the components of LULC, geometrical factors, and synoptic weather factors. In summary, the findings of this research are supported by the previously published researches, and the employed integrated approach of using three indicators to model the UHI has shown the spatiotemporal patterns of each approach and quantified their various influencing parameters.

6.6 Conclusions

This chapter used a new indictor of the presence of UHI. T_{mrt} includes the calculation of the longwave and shortwave radiation fluxes in the three-dimensional surroundings of human (east, west, north, south, upward, and downward). The modelled T_{mrt} was used to investigate the presence of a new type of UHI which differs from SUHI and CUHI. The term RUHI was introduced for the first time to measure the difference between the pixel T_{mrt} and minimum T_{mrt} within the city of Birmingham. The spatiotemporal change of RUHI was explored to compare it with the SUHI and CUHI. Furthermore, the shortwave and longwave upward and downwards radiations were modelled as the influencing parameters on the RUHI formation. The SOLWEIG plugin in the UMEP was employed to model the T_{mrt}, L_{up}, L_{down}, K_{down}, and K_{up}, and *shadow* as an open source climate service tool accessed through QGIS.

The pre-processors in UMEP were used to prepare the spatial and meteorological inputs such as SVF, walls height and aspects, as well as meteorological files. However, other spatial data were created using ArcMap such as DEM, ground and building DSM, vegetation DSM, and the land cover. Due to the limitation of the UMEP, the spatial grids did not exceed 4000000 pixels per tile. Thus, the city of Birmingham was split into six tiles before running the model. The split tiles were overlapped by 100 metres (20 pixels), to overcome the problem of edge effects when merging the outputs later. The meteorological inputs applied two times when modelling the spatial change of RUHI, to identify the impact of varying the meteorological inputs. Four days were chosen to represent the four seasons in Birmingham, and the same days were used to identify the CUHI.

The averaged meteorological inputs showed the presence of daytime RUCI in the City Centre, while, the night-time induced the development of RUHI. The spatial change of RUHI varied in magnitude and distribution for the four seasons. The open spaces revealed relatively high daytime RUHI, and low night-time RUHI except for the winter. The maximum averaged RUHI reached 16.2 ºC on the 6th of July 2013, and it was at its minimum on the 1st of December 2013 by 9.29 ºC. The spatial variability of the meteorological inputs induced the formation of higher RUHI. Although, the spatial patterns of RUHI for specific feature in the city such as the City Centre and Sutton Park' trees still similar when using tiled meteorological inputs compared to the averaged ones. Nonetheless, the sharp transition in magnitudes of RUHI among the tiles prevented the formation of smooth colour balance for the entire map due to values variability. Consequently, only the averaged meteorological inputs were used for further analysis of the results.

The temporal change of T_{mrt}, T_a, and RUHI demonstrated a notable distinction between daytime and night-time, and the four days revealed seasonal variations. It demonstrated significantly higher T_{mrt} in the daytime compared to the night-time except for the winter day. The City Centre worked as RUHI during the night-time, and RUCI during the daytime just opposite to the Sutton Park. The RUCI intensities (up to – 30 ºC) were much higher than the RUHI (+5 ºC) in the City Centre compared to the Sutton Park. The K_{down}, K_{up} and *shadow* did not have any impact on the RUHI during the night-time. However, the Lup and Ldown were the major contributors to the RUHI. The Lup had higher impact on the RUHI during the hot days in the summer and autumn, while, the L_{down} had higher effect during the winter and spring. Furthermore, the K_{down} and *shadow* patterns primarily derived the spatial and temporal variation of RUCI during the daytime. In general, the presence of RUHI and RUCI became evident, and the need for a new UHI indicator was crucial. Future work should allow the spatial variability of meteorological data and employ lager number of days to investigate the temporal variability of RUHI and RUCI.

Chapter 7: Research Findings, Contributions and Limitations

7.1 Introduction

Three major approaches were employed, and three terabytes of data were used to fulfil the aims of this research. For the SUHI, three study areas were undertaken Baghdad, London and Birmingham, however, Birmingham was the only case study of the CUHI and RUHI. Therefore, a comparison among SUHI, CUHI and RUHI is only possible for Birmingham City. Accordingly, the three types of UHI were investigated for the City of Birmingham. The term UHI referred to the three types of UHI (SUHI, CUHI, and RUHI) that were carried out by this research. The only type of UHI missing from this study that is reported in the literature is the BUHI. Since the BUHI studies the air layer above the average building's height, the CUHI represented the AUHI as it is closer to where people live. The SUHI was studied for the period (2000-2015), and the CUHI was investigated from June 2012 to June 2014. The RUHI was simulated for four days to represent the four seasons of Birmingham City. The day and night average SUHI was called diurnal, however, the averages of hourly RUHI were named all-day averages just to differentiate them from the diurnal. This chapter provides answers to the research's questions, highlights the research's contributions, and admits the research's limitations.

7.2 Research findings: fulfilment of research objectives

In this study, four research questions were raised, and subsequently four objectives were formed to answer these questions. The research objectives are undertaken in the same order they originally formed, as they are linked to each other and should be discussed in that order.

Objective 1: Investigate the spatial change of UHI using air, surface and mean radiant temperatures.

The UHI refers to the SUHI, CUHI, and RUHI, and to investigate the change of UHI, the outcomes from the three types of UHI need to be incorporated. First, The SUHI showed different behaviour for the three cities (Baghdad, London & Birmingham), as these cities gave different spatial SUHI change, in particular, Baghdad and London. The various SUHI spatial distributions are attributed to the specific LULC features of each city, the climatic and geographical condition, as well as population density. For Baghdad, the built-up areas recorded relatively higher LST at night-time, and during the daytime they had lower LST to act as a Cool Island using Landsat and ASTER data. The high spatial resolution of Landsat and ASTER images has made the high temperature of water bodies visible during the cold nights, which is probably due to its high thermal capacity. The Industrial areas and highly populated attached urban configurations were recognised as daytime SUHI high intensity places, unlike the night-time SUHI, where all the urban areas exhibited higher temperature compared to the city boundary.

Moving to London, the high daytime SUHI appeared in the heart of the city where the built-up areas are dominant using Landsat and ASTER data. The night-time SUHI also peaked in the city to decrease towards the surrounding areas, except for water areas on cold nights. Similarly, the City of London had the highest daytime SUHI compared to other urban areas using MODIS images. At night-time, the water bodies and adjacent areas had the peak SUHI. The high intensity of SUHI over water areas was evident for the three cities during cold nights. Thus, the term WUHI was introduced for the first time to describe this phenomenon as a unique fining of this study.

Birmingham daytime SUHI showed similar patterns to London, it concentrated in the urban fabric as well as industrial and commercial units using Landsat and ASTER images. However, the night-time high spatial resolution airborne thermal image could identify the trees to have the second highest temperature after water bodies. This pattern did not appear in London and Baghdad using the moderate and course spatial resolution satellite data. Birmingham daytime SUHI intensity peaked at the City Centre using MODIS data, and the lowest intensity could be seen in the Sutton Park. Furthermore, the night-time SUHI maximised at the City Centre to extend to the adjacent suburban's areas. Using MODIS data from 2003 to 2015, the diurnal averages of SUHI were 9.41, 11.29, and 7.63 ºC for Baghdad, London, and Birmingham respectively. Although, the higher diurnal, daytime and night-time LST of Baghdad compared to London and Birmingham, the London SUHI intensities were higher than those of Baghdad.

The CUHI, on the other hand, was found to be concentrated in the City Centre of Birmingham when its intensity was close to the mean values. However, the extreme intensities were seen to stretch to the suburban areas due to the weather parameters; in particular, the wind. The coldest spots clearly appeared in the Sutton Park which is the largest park in Birmingham that has vegetation and trees. The CUHI peaked at the City Centre when the wind speed is lower than 2 m/s (light air), and its direction above the city is heading towards the north. The daily CUHI concentrated in and around the City Centre during the night and early morning, to move clockwise to the Sutton Park and return to the City Centre after the sunset. The maximum CUHI intensity in Birmingham during the period of the study (June 2012-June 2014) was 13.53 °C. The wind speed and direction had important impact on the spatial distribution of the hot spots, as well as the extent of the CUHI. The CUHI occurred in the suburban areas as well as the urban areas due to the presence of impervious surfaces and anthropogenic activities. The extreme CUHI events (UHI > 10 °C) took place in the suburban areas far from the City Centre during the time of out of working hours. The occurring time of the UHI over 10 °C events were between 4 p.m. in day and 6 am in the next day, and the locations are almost suburban areas. However, the typical CUHI was found to have an intensity close to its mean magnitude pulse the standard deviation.

Next, the simulation of T_{mrt} using averaged meteorological inputs showed the presence of daytime RUCI in the City Centre, while, the night-time induced the development of RUHI. The spatial change of RUHI varied in magnitude and distribution for the four seasons. The open spaces revealed relatively high daytime RUHI, and low night-time RUHI except for the winter. The maximum averaged RUHI reached 16.2 ºC on the 6th of July 2013, and it was at its minimum on the 1st of December 2013 by 9.29 ºC. The spatial variability of daytime RUHI is higher than the night-time, this is due to the presence of the sun energy in the daytime. The all-day averages RUHI seemed to be high in open spaces, and peaked in dense trees to decrease in built-up areas.

To sum up, the SUHI occurred at the City Centre of London and Birmingham during the daytime and night-time. However, Baghdad core was a SUCI during the day, to be a heat island in the night. The daily cycle of CUHI in Birmingham concentrated at the City Centre during the night-time, to stretch to the suburb and move to the Sutton Park clockwise during the daytime, and return to the City Centre after the sunset. The RUCI appeared in Birmingham City during the daytime, and both the CUHI and RUHI peaked in the night-time at the City Centre.

Objective 2: Investigate the temporal change of UHI using air, surface and mean radiant temperatures.

The temporal change of UHI is also discussed based on the type of UHI. For Baghdad during the period (2003-2015) the averages of daytime SUHI fluctuated around 11.56 ºC with 2.8 SD, which is higher than the night-time SUHI as it was about 7.26 ºC with 1.38 SD. The areas of daytime SUHI in Baghdad were found to be in high population density places where the urban form configurations are mainly attached buildings when using high temporal resolution images (MODIS data). Although the trend of the average daytime SUHI went down, the magnitude of the daytime SUHI remained high compared to the night-time. The monthly analysis of LST showed different degrees of LST increases over the study period, and spring had the more noticeable rise. However, for some months the LST and NLST did not have the same trend direction, and in a few cases, they had the opposite behaviour. The average SUHI intensity fluctuated from about 8.05 ºC for December to around 10.51 ºC for May.

For London during the period (2003-2015) the average diurnal SUHI did not change that much. The average of daytime SUHI was 13.52 °C with 5.90 SD, and the average of night-time SUHI was 9.07 °C with 3.01 SD. The spring and summer showed a slight decrease in LST, whereas, the autumn and winter reflected a bit of increase. The monthly average SUHI intensity fluctuated from about 9.29 ºC with 3.49 SD for December to around 13.99 ºC with 6.19 SD for July. The NLST for some months gave opposite trends to the LST, especially for December and March. The overall temporal change of LST and SUHI did not show significant change; unlike Baghdad, which experienced an increase in LST and decrease in SUHI averages.

Birmingham during the period (2003-2015); on the other hand, had an average daytime SUHI around 10.14 °C with 5.14 SD, and the average of night-time SUHI was 5.13 °C with 2.41 SD. The summer showed a slight decrease in LST, whereas, the autumn and spring reflected a bit of increase to moderate the winter temporal LST decrease. The NLST for some months gave opposite trends to the LST, especially, for September and March. The monthly temporal change of SUHI appeared to fluctuate for the different months, thus, the weak increase (July – December) moderated by the weak decrease of (January, March, April & June). All in all, the temporal change of average LST and SUHI for Birmingham did not show significant change over the study period just like London; however, they both gave high spatial variability.

The hourly statistical analysis of the CUHI for 2 years of measurements demonstrated that around 56% of total 17520 hours gave an air temperature variation more than 1.5 °C in Birmingham. The highest CUHI intensity was in September by 13.5 °C, and the lowest intensity

5 °C was in January. However, the monthly highest average CUHI 3.9 °C was monitored in July, whereas, the lowest average was in January by 2.3 °C. Besides, the longest hours of CUHI occurrence were in June by 1323 hours, and the shortest 471 hours of occurrence were in February. It was found that the CUHI occurs in all seasons, day and night based on the climate condition. However, the high intensity CUHI happened during the clear and calm weather.

The temporal change of T_{mrt}, T_a, and RUHI demonstrated an important distinction between the daytime and night-time, and the four days revealed seasonal variations. It demonstrated significantly higher T_{mrt} in the daytime compared to the night-time except for the winter day. The City Centre worked as RUHI during the night-time, and it was a RUCI during the daytime just opposite to the Sutton Park. The RUCI intensities (up to – 30 ºC) were much higher than the RUHI (+5 ºC) in the City Centre compared to the Sutton Park. The SUHI, CUHI and RUHI showed temporal variability between the day and night, and demonstrated monthly and seasonal variation over the different study periods.

Objective 3: Identify the relationship between the dependant variables (temperature layers) and independent variables (influencing parameters) by the statistical or visual analysis.

Various influencing parameters contributed to the different types of UHI. The land cover types and anthropogenic heat were the main contributors to the SUHI. Fourteen controllable and uncontrollable predictors controlled the CUHI development. On the other hand, the radiation fluxes and shadow patterns directed the RUHI formation.

The densely populated attached houses, and their adjacent industrial and commercial areas motivated higher daytime SUHI compared to other urban areas in Baghdad. Interestingly, some of the urbanised areas (mainly low density residential areas) acted as SUCI, and other built-up areas (mainly high density residential areas, commercial and industrial units) acted as SUHI at the same daytime. This leads to the distinction between the development of SUHI due to the land use, and the formation of the SUCI because of the land cover. The land cover has a direct impact on the net radiations, while, the land use affects the anthropogenic heat. Accordingly, each of the major two inputs to the surface energy equation might lead to a different microclimate behaviour. Although, there are only 9,000 residents living within the Square Mile of the City of London, which is one of the world's main financial districts (City of London Corporation, 2007). However, it experienced day and night SUHI, because over 300,000 people work in the City and almost 30,000 go there to study every day (City of London Corporation, 2007). Furthermore, the high daytime and night-time SUHI intensity in Birmingham presented in the densely populated areas, which is used for residential, industrial, and commercial purposes. Overall, the anthropogenic heat released by the people, transportation or industrial and commercial activities was found responsible for the development of SUHI for the three cities.

The quantification of the influence of the land cover indices on the SUHI demonstrated negative correlation between these indices and LST for the three cities, with different degrees based on the nature of the index. Some of the indices such as NDVI, MSAVI, NDMI and NBR2 showed very significant negative correlation with LST. The land cover indices could explain up to

70% of the LST variation for the significant models. For Baghdad, low SUHI intensity was associated with dense vegetation and high moisture during the day. For example, NDMI had a noticeable negative correlation with LST. In London, green spaces and water bodies were significant parameters to reduce the high LST. NDVI and MSAVI played a major role to relieve the LST with up to 0.81 R^2 for NDVI on the 19 of June 2000, for instance. The LST of Birmingham could be dramatically reduced by enhancing the vegetation and moisture of the surface cover, which showed a similar behaviour to London. The NDVI could explain 77% of the LST variation on the 10th June 2006, and the MSAVI formed about 0.62 R^2 of the LST model on the 16th of April 2003, for examples.

For Birmingham, the air temperature was reduced by up to 2 °C due to the shadow of buildings. This led to lower temperature in the City Centre canyons which has relatively lower values of SVF and VS. The regression models could explain up to 95% of the air temperature variations, and the contributing components were LULC, geometrical factors, and synoptic weather factors. Though the uncontrollable parameters dominated the significant models, some controllable ones were constantly participating in forming the highly significant models. Fourteen predictors could explain up to 0.91, 0.71, 0.84 and 0.95% of the Ta in the spring, summer, autumn and winter respectively. Moreover, the weather averages gave an indication about the climatic condition for each hourly regression model. This highlighted the importance of the hourly synoptic weather to model the CUHI, though the controllable parameters played a significant role to make up the significant models.

On the other hand, the influencing parameters were visualised for Birmingham using T_{mrt}. The K_{down}, K_{up} and *shadow* did not have any impact on the RUHI during the night-time. However, the L_{up} and L_{down} were the major contributors to the RUHI during the night-time. The L_{up} had higher impact on the RUHI during the hot days in the summer and autumn, while, the L_{down} had higher effect during the winter and spring. Furthermore, the K_{down} and *shadow* patterns primarily derived the spatial and temporal variation of the RUCI during the daytime.

In summary, the land cover types and anthropogenic activities are the biggest influencing parameters on the SUHI formation. The uncontrollable parameters (such as synoptic weather variables) have higher impact on the CUHI than the controllable parameters. However, the shadow reduces the daytime CUHI and RUHI. The shortwave radiations control the daytime RUCI, and the longwave radiations govern the night-time RUHI.

Accordingly, the mitigation measures to minimise the UHI effects should focus on the significant influencing parameters. For instance, vertical expansion is advised in London and Birmingham to keep the green surfaces, and to minimise the UHI effect, more vegetation should be planted. The greenery does not have to be on the ground as green roofs and walls can reduce the heat stress and improve the air quality in the city without exploiting more lands. For Baghdad, horizontal expansion will cover the hot soil and change that to cooler built-up or vegetated areas. Moreover, increasing the shadow from trees and high buildings, while, allowing the wind flow to penetrate the closed spaces would minimise the UHI. Furthermore, using cool materials for the walls and roofs and pavements would reduce the UHI significantly when applied with the previous mitigation strategies.

Objective 4: Use the best available free remotely sensed, GIS and ground based data to enhance the spatial and temporal resolution of UHI visual and statistical models.

The use of LST provided high spatial resolution representation of the UHI, which gives per pixel measurements of SUHI. The different urban features were captured and their thermal behaviour was evaluated. However, the surface temperature measures the radiant heat from the ground surface, and it only provides bird’s eye vision, so roofs and pavements are not captured. Nevertheless, the vertical objects such as walls are not involved in the sensing, and the inclined surfaces are seen as horizontal planes. The temporal revisit of LST by RS is limited to the satellite overpass, which provides in the best cases a day image and a night image. Therefore, temporal gaps are present using only RS techniques, and the problem of clouds makes a lot of scenes not useful, in particular, in the wet environments where clear weather is not common. These challenges have induced the researchers to use the air temperature, since the air temperature is ground measured and not affected by the sky condition.

The ground measurements are usually cheaper than the RS for a point source reference, and ground measurement can have much higher temporal resolution than the RS. The spatial coverage of ground measurements adopted in this study is lower than the RS. Nevertheless, the HiTemp project could provide per minute air temperature readings, which were averaged to hourly basis. The HiTemp project consists of AWS and ASM sensors, and the ASM sensors have approximately 3 km average spacing. When it is compared to the MODIS 1 km thermal images, it can be found that RS provided at least 3 times better spatial coverage than the ground measurement technique in this study. However, Landsat TM and ETM+ provide 60 m TIR image spatial resolution, and ASTER gives 90 m as well as Landsat 8 originally produces 120 m resampled to 30 m.

In regard to the temporal coverage of RS and HiTemp, MODIS provided about two daily visits for MODIS and HiTemp measurements were rescaled to hourly readings. Hence, the daily coverage of HiTemp is simply twelve times the thermal images. Even if the spatial coverage of the ground measurements were significantly increased, and the temporal coverage of the thermal images doubled in case of using both of MODIS/Aqua and MODIS/Terra, the type of information provided by air and surface temperature differs, as each indicator conveys the characteristics of its medium. The air temperature gives information about the air layer 3 m above the ground for HiTemp, and the surface temperature indicates how much longwave radiation in the region of TIR is released from the different features on the ground. Consequently, air and surface temperature thermal behaviour integrate each other and they do not substitute each other.

The SUHI showed much higher spatial variability than the CUHI. The Landsat and ASTER data were found to be indispensable to study the spatial variability of SUHI. However, using the MODIS data provided better temporal coverage, even though, mixed pixels of different land cover types were present in MODIS pixel more than when using Landsat or ASTER images. The common technique that was used to process both of the RS and ground measurement is GIS. The ground measurements were converted to temperature maps by the interpolation tools, and the RS images were converted to classified maps by RS and GIS means. The ground and RS measuring techniques required a modelling approach to fill the gap in each of them. This why SOLWEIG was adopted as a microclimate model to include a large number of influencing parameters on the formation of different types of UHI.

The simulated T_{mrt} combines the influencing parameters on the development of both of the SUHI and CUHI. Furthermore, it compensates the two-dimensional demonstration of the UHI by using only RS and ground measurements, by a 3D model that could show the impact of vertical objects such as trees. As the presence of RUHI and RUCI has become evident, so the need for a new UHI indicator was obvious. UMEP as a climate service tool to host the SOWLEIG and other applications that use the QGIS have facilitated the viewing, editing and analysis capabilities. From that the spatial and temporal representation of UHI have been enhanced dramatically, and better data were fed to the statistical packages (such as Excel, SPSS, and MATLAB). Accordingly, the integration of different measuring and modelling techniques is the key solution to improve the representation of the visual and statistical UHI models.

7.3 Research contributions

The outcomes of this research might be beneficial to different aspects of life for the experts and public. The contributions of this study were drawn from the gaps in knowledge. Initially, increasing the people’s awareness of the serious threats due to the elevating global temperature and the increasing intra-urban differences was one of the contributions. The findings showed that there are high spatial differences in air and surface temperatures within the same city. People might need to do preparations when travelling inside their cities such as extra or less clothes. The common practice of people is using the weather applications when travelling to different cities to take actions or when leaving homes under unstable conditions. However, these applications mainly provide the averages for a city and do not show the spatial variations of the weather variables for different places within the same city. Thus, higher spatial resolution of climatic parameters should be provided to people, as they affect their health and comfort. People’s health and comfort influence their productivity and participation in the society.

The spatial variability of the temperature means different energy consumption. So, higher outdoor temperature needs more indoor cooling loads to moderate the atmosphere, and low outdoor temperature induces more heating inside homes. This leads to variability in the energy bills which directly impact the economic budgets of individuals. Based on that places can be classified according to their environment to economically affordable or unaffordable. Furthermore, the construction practices and materials of buildings should vary to adapt with the environment. From that the term environmentally friendly buildings comes, which again a building either costs more or less to construct. Consequently, climatic maps and zones are becoming important sources of information for urban planners and engineers. The urban areas are experiencing irreversible expansion and accumulation of people masses. Therefore, engineering practices should be adopted to deal with the different needs of urban sprawl.

One of the most significant contributions of this research is employing three approaches to model the UHI with unprecedented spatial and temporal resolution. Moreover, a large number of influencing parameters on the formation of UHI were investigated some of them were not studied by previous researches. The SUHI chapter gave a comparison among three cities in terms of their SUHI spatiotemporal change and the contributing parameters in particular the land use/cover. Specific patterns of SUHI and SUCI were identified in this study that were unknown previously. For example, the daytime SUCI appeared in Baghdad's low-density population areas, while, at the same time highly populated areas showed SUHI behaviour. Besides, the WUHI was distinguished over the water areas in cold nights. Thermal images and land cover indices were acquired for about 15 years for the three cities which was not done in a single study.

The representation of the CUHI was improved significantly by employing hourly measurements of over 100 sensors for two years that covered the entire city of Birmingham. Fourteen controllable and uncontrollable parameters were investigated to model the CUHI with R^2 of up to 95%, and this percentage has not been reached by any other study. The T_{mrt} was introduced as a new predictor to model the RUHI which advances the traditional 2D UHI representation to 3D UHI for the first time in the literature. The RUHI and RUCI were identified just similar to the traditional surface and canopy UHI behaviour. Also, the impact of shortwave and longwave radiations on the RUHI was highlighted on hourly basis which was not done before.

Furthermore, this is the only study that compares among three types of UHI with their influencing parameters for the scale of a city using remote sensing, GIS and ground measurements data. Also, this research employed the intra-urban differences of temperatures to measure the UHI by assuming that the boundary of a city represents the rural areas. This will enable the researchers to find solutions of the UHI problems from the city itself without the need to use the rural areas as a reference to measure the UHI. So, the size of the study area will be limited to the city boundary which will reduce the size of the data of the thermal images in particular. In this case larger cities can be studied with lower computing capabilities, and storage as the satellite and airborne data require huge storage space.

Another contribution of this research is highlighting the complexity of the UHI phenomenon. This phenomenon does not only describe the temperature difference between two places. Nonetheless, it tells about the thermal behaviour, environmental patterns, level of development, geographical location and biophysical characteristics between the two places. This is why only one predictor was not enough to identify such a large number of variables. On the other hand, due to the large amount of data used with their different formats and nature, the methods employed in this study provide pathways to deal with huge spatial and temporal information. Moreover, the study makes use the different approaches of measuring and modelling techniques which might be used to study other topics that share similar characteristics with UHI. The critical gap in the UHI studies used to be employing a certain approach which adopts a limited amount of data. That was highlighted by using unprecedented number of approaches and a large amount of data. Subsequently, the findings were novel in this field of the discipline.

7.4 Research limitations

The representation of the real world with its variation and complexity is not possible. However, the study areas were chosen based on the data availability to give examples of different climates with a novel spatiotemporal resolution, and the results can be applicable for similar places. Moreover, the influencing parameters on the UHI formation are very broad and this study tried to investigate the important factors based on the data availability, and some parameters will be suggested for future studies. Nevertheless, the large number of included influencing parameters in this study has not been adopted before by other studies.

Another limitation is that the available technology does not provide data for the full classification of urban material due to the limited spectral and spatial resolution of the satellite data; however, this might be possible in the future using data from the Sentinel program and other projects. The land cover indices were acquired for only daytime Landsat HLPs to model the SUHI influencing parameters, as the Landsat mainly provides daytime images. The land cover indices were assumed as a major contributor to SUHI, and they could explain 70 % of the LST variation; however, the 30 % remaining might incorporate other influencing parameters. Besides, the spectral indices did not represent all the land cover types for the three study areas, and other spectral indices should be included such as Normalised Difference Built-up index (NDBI).

Furthermore, free of charge data and applications were pursued due to the limited fund for the study, but it did not affect the novelty. The HiTemp data were acquired for only two years, and the project is still ongoing. The two years might not be enough to represent the historical record of the temperature and other climatic variables. Thus, longer temporal coverage of HiTemp data would help for a better understanding of the CUHI temporal change. Moreover, only four days were simulated to model the T_{mrt} to represent the four seasons in Birmingham. These days might not give the full seasonal changes of the RUHI, and more days should be modelled by future work. Furthermore, the spatial variability of the meteorological data was not included in the SOLWEIG model, and further development is needed by the producers. The SUHI was investigated for three cities, however, the CUHI and RUHI were studied for only Birmingham. So, the results of CUHI and RUHI are applicable for only Birmingham and similar places in terms of environment, climate, demography and level of development. So, more cities should be included in the investigation of the different types of UHI. Finally, the time was a limitation that minimised the research objectives to be achievable within the study timeline.

Chapter 8: Conclusions and Recommendations

8.1. Conclusions

The significant findings of this research are briefly summarised as below:

- ❖ The City Centre of Baghdad works as SUHI during the night-time, and SUCI in the daytime, except for some industrial areas and attached urban configurations that showed high SUHI intensity in the daytime.
- ❖ The City Centre of London and Birmingham work as SUHI in the day and night-time, and water has high LST in the cold nights.
- ❖ The diurnal averages of SUHI (2003-2015) were 9.41, 11.29, and 7.63 ºC for Baghdad, London, and Birmingham respectively.
- ❖ The correlation between SUHI and LST is negative for the three cities, and Baghdad's SUHI showed a bit of decrease between (2003- 2015) opposite to London and Birmingham.
- ❖ Land cover indices could explain up to 70% of the LST variations, and population as well as other anthropogenic activities contributed to the SUHI for the three cities.
- ❖ Birmingham experienced the difference in air temperature above 1.5 ºC for 56% of the total hours from June 2012 to June 2014, and the CUHI reached up to 13.53 ºC.
- ❖ The CUHI appeared daytime and night-time in Birmingham urban and suburban areas throughout the different seasons, and peaked during the calm and clear nights.
- ❖ Fourteen controllable and uncontrollable predictors could explain up to 95% of the air temperature variations, grouped into LULC, geometrical factors, and synoptic weather parameters.
- ❖ The T_{mrt} was introduced as an UHI indicator besides the air and surface temperatures.
- ❖ The simulation of T_{mrt} showed the presence of daytime RUCI in the City Centre of Birmingham, while, the night-time induced the development of RUHI.
- ❖ The shortwave radiations control the daytime RUCI, and the longwave radiations govern the night-time RUHI.
- ❖ The air and surface temperature thermal behaviour integrate each other, and they do not substitute each other, so the need for a new UHI indictor was crucial.
- ❖ The integration of different measuring and modelling techniques is the key solution to improve the representation of visual and statistical UHI models.

8.2. Recommendations and future work

The UHI is a complicated phenomenon as it is connected to local, regional and global thermal and biophysical characteristics. Since, the UHI showed high spatial and temporal variability, generalising the findings from a specific place to other places might give biased conclusions. Similarly, using the characteristics of a certain type of UHI (SUHI for instance) to model another UHI's type (CUHI for example) would lead to inadequate findings. For the SUHI, the use of different RS data is recommended to substitute the lack of temporal coverage especially for places that suffer from the presence of clouds all year round. For such places ground measurements are needed to fill the gaps of absent satellite images, nevertheless, thermal RS and air ground measurement would show different behaviours.

The 1 km spatial resolution of MODIS data could help to identify some ground features, however, there were a lot of ground features smaller than 1 km not identified. Accordingly, it can be considered that the 1 km pixel size as the minimum spatial resolution required to study the SUHI. The ideal pixel size to identify all the important urban features is 1 m. The one metre spatial resolution can capture the thermal behaviour not only for features but compound materials might be investigated. The night-time airborne thermal image of Birmingham could show unprecedented SUHI patterns, in particular the high LST of the trees in the Sutton Park. That urges the crucial need for high spatial resolution thermal images to study the SUHI. Alternatively, the 3D SOLWEIG microclimate model can highlight the distinctive thermal behaviour of the trees in the Sutton Park.

The spatiotemporal change of CUHI was investigated for only two years, and longer time scale is needed to identify the anomalies or events that were not picked up in this study. Since the HiTemp project is still ongoing and more data can be obtained. Moreover, the CUHI should be investigated for other places that have similar dense meteorological stations to be compared with Birmingham. The use of T_{mrt} opens the door for the researchers to investigate the potential of other indicators to identify and quantify the UHI. However, the new indicator should build on the current use of air and surface temperatures, as they represent the traditional definition of UHI. For the validation of the RUHI and RUCI presence longer time scale simulation is required. Furthermore, the spatial variability of the meteorological data should be included in the SOWLEIG model. Also, the input coefficients of shortwave and longwave radiation absorption as well as the emissivity and albedo should vary spatially and temporarily when running the SOWLEIG model.

The use of a certain type of UHI depends on the objectives of the study and the availability of the data. Therefore, the SUHI is recommended to study phenomena related to land surface characteristics, and when the LST is a critical parameter. While, the climate of the canopy layer can be investigated by modelling the CUHI when two dimensional or a bird vision scale is sufficient. However, the RUHI is needed when the aim is to study the outdoor thermal comfort in three dimensional settings. Furthermore, the availability of the data is a crucial point to decide which type of UHI to be undertaken. The ideal representation of the CUHI requires a dense meteorological network of the study area, whereas, the thermal maps provides a better spatial representation of the UHI when only pairs of stations is available. On the other hand, the RUHI requires a high spatial resolution DSM and detailed land cover information.

Future studies should adopt finer spatial resolution of multi day and night thermal images, coincide with high spatial resolution of visible to shortwave images. The later should be classified to have detailed LULC maps that provide information about the nature of ground surface materials. Furthermore, geometrical and demographical information should be incorporated to derive the influencing parameters as well as land cover indices. Furthermore, the effects of total anthropogenic heat fluxes on the UHI formation should be identified. The population density was used in this study as a component of the total anthropogenic heat fluxes; however, other heat sources such as transportation and industry were not included. The inputs to the energy balance equation are the net radiation fluxes plus the anthropogenic fluxes. The net radiation fluxes were modelled using the SOWLEIG model, nevertheless, a robust modelling or measuring technique for the total anthropogenic fluxes is still under development by the researchers.

References

AGARWAL, R., SHARMA, U. & TAXAK, A. 2014. Remote sensing Based Assessment of Urban Heat Island Phenomenon in Nagpur Metropolitan Area. *International Journal of Information & Computation Technology,* 4**,** 1069-1074.

AGENCY, E. P. 2013. *Heat Island Impacts* [Online]. Washington: US Environmental Protection Agency. Available: http://www.epa.gov/heatisland/impacts/index.htm [Accessed 10 June 2014 2014].

AKBARI, H. 2005. *Energy Saving Potentials and Air Quality Benefits of Urban HeatIslandMitigation*.

AKBARI, H. & KOLOKOTSA, D. 2016. Three decades of urban heat islands and mitigation technologies research. *Energy and Buildings,* 133**,** 834-842.

AKBARI, H. & MUSCIO, A. 2015. Cooling Heat Islands. *Urban Climate,* 14, Part 2**,** 139-140.

AKBARI, H., ROSE, L. S. & TAHA, H. 1999. Characterizing the Fabric of the Urban Environment: A Case Study of Sacramento, California. *Other Information: PBD: 1 Dec 1999.*

AL-LAMI, A. M. 2014. Study of Urban Heat Island Phenomena for Baghdad City using Landsat-7 ETM+ Data.

AL-MUSAED, A., ALMSSAD, A & KHALIL, Z 2007. Heat island effects upon the human life on the city of Basra. *Conference on Building Low Energy Cooling and Advanced Ventilation Technologies in the 21st Century.* Crete Island, Greece.

ALCOFORADO, M. & ANDRADE, H. 2008. Global Warming and the Urban Heat Island. *In:* MARZLUFF, J., SHULENBERGER, E., ENDLICHER, W., ALBERTI, M., BRADLEY, G., RYAN, C., SIMON, U. & ZUMBRUNNEN, C. (eds.) *Urban Ecology.* Springer US.

ALDRIDGE, H., BORN, T. B., TINSON, A. & MACINNES, T. 2015. *London's Poverty Profile 2015*, Trust for London/New Policy Institute.

ALI-TOUDERT, F., DJENANE, M., BENSALEM, R. & MAYER, H. 2005. Outdoor thermal comfort in the old desert city of Beni-Isguen, Algeria. *Climate Research,* 28**,** 243-256.

ALI, J. M., MARSH, S. H. & SMITH, M. J. 2016. Modelling the spatiotemporal change of canopy urban heat islands. *Building and Environment,* 107**,** 64-78.

ALI, J. M., MARSH, S. H. & SMITH, M. J. 2017. A comparison between London and Baghdad surface urban heat islands and possible engineering mitigation solutions. *Sustainable Cities and Society,* 29**,** 159-168.

ALOBAYDI, D., BAKARMAN, M. A. & OBEIDAT, B. 2016. The Impact of Urban Form Configuration on the Urban Heat Island: The Case Study of Baghdad, Iraq. *Procedia Engineering,* 145**,** 820-827.

AMERICAN FORESTS. 2002. *Citygreen 5.0 User Manual* [Online]. Washington DC: American Forests. Available: http://www.planta.cn/forum/files_planta/citygreen_brochure_156.pdf [Accessed 15/2/2016 2016].

AMINIPOURI, M. & KNUDBY, A. Spatio-temporal analysis of surface urban heat island (SUHI) using MODIS land surface temperature (LST) for summer 2003–2012, A case study of the Netherlands. 2014 IEEE Geoscience and Remote Sensing Symposium, 2014. IEEE, 3192-3193.

AMIRI, R., WENG, Q., ALIMOHAMMADI, A. & ALAVIPANAH, S. K. 2009. Spatial–temporal dynamics of land surface temperature in relation to fractional vegetation cover and land use/cover in the Tabriz urban area, Iran. *Remote Sensing of Environment,* 113**,** 2606-2617.

ARCGIS RESOURCE CENTER. 2011. *Hillshade* [Online]. Esri. Available: www.help.arcgis.com/en/arcgisdesktop/10.0/help [Accessed 20/8/2015 2015].

ARNFIELD, A. J. 1990. Canyon geometry, the urban fabric and nocturnal cooling: a simulation approach. *Physical Geography,* 11**,** 220-239.
ARNFIELD, A. J. 2003. Two decades of urban climate research: a review of turbulence, exchanges of energy and water, and the urban heat island. *International journal of climatology,* 23**,** 1-26.
ARUP 2016. Seasonal health and resilience for ageing urban populations and environments. online: ARUP
ASTROM, D. O., FORSBERG, B., EBI, K. L. & ROCKLOV, J. 2013. Attributing mortality from extreme temperatures to climate change in Stockholm, Sweden. *Nature Clim. Change,* 3**,** 1050-1054.
ATKINSON, B. W. 1982. The urban climate, By H. E. Landsberg. International Geophysics Series, Vol. 28. Academic Press, New York. 1981, Pp. 275. $29.50 £19.60. *Quarterly Journal of the Royal Meteorological Society,* 108**,** 733-734.
AWADH, S. M. & AHMAD, L. M. 2010. CLIMATIC PREDICTION OF THE TERRESTRIAL AND COASTAL AREAS, IRAQ CASE STUDY. *Iraqi Desert Studies,* 2**,** 1994-7801
AXINTE, A. 2015. HLC Final Project Report. *In:* COUNCIL, D. D. O. B. C. (ed.). Birmingham, UK: Birmingham City Council.
AZEVEDO, J. A., CHAPMAN, L. & MULLER, C. L. 2016a. Quantifying the daytime and night-time urban heat island in Birmingham, UK: A comparison of satellite derived land surface temperature and high resolution air temperature observations. *Remote Sensing,* 8**,** 153.
AZEVEDO, J. A., CHAPMAN, L. & MULLER, C. L. 2016b. Urban heat and residential electricity consumption: A preliminary study. *Applied Geography,* 70**,** 59-67.
BALA, A., SINGH, R. K. & GAYATHRI, V. 2013. Review on different surface energy balance algorithms for estimation of evapotranspiration through remote sensing. *IJETAE,* 3**,** 582-588.
BALLING, R. B., SW 1988. High-resolution surface-temperature patterns in a complex urban terrain. *Photographic Engineering Remote Sensing,* 54**,** 1289– 1293.
BANSAL, G. 2015. *What is the difference between coefficient of determination, and coefficient of correlation?* [Online]. Green Bay, Wisconsin: University of Wisconsin. Available: http://blog.uwgb.edu/bansalg/statistics-data-analytics/linear-regression/what-is-the-difference-between-coefficient-of-determination-and-coefficient-of-correlation/ [Accessed 31-10-2016 2016].
BASARA, J. B., ILLSTON, B. G., FIEBRICH, C. A., BROWDER, P. D., MORGAN, C. R., MCCOMBS, A., BOSTIC, J. P., MCPHERSON, R. A., SCHROEDER, A. J. & CRAWFORD, K. C. 2011. The Oklahoma city micronet. *Meteorological applications,* 18**,** 252-261.
BASSETT, R., CAI, X., CHAPMAN, L., HEAVISIDE, C., THORNES, J. E., MULLER, C. L., YOUNG, D. T. & WARREN, E. L. 2016. Observations of urban heat island advection from a high-density monitoring network. *Quarterly Journal of the Royal Meteorological Society*.
BÖHNER, J. & ANTONIĆ, O. 2009. Chapter 8 Land-Surface Parameters Specific to Topo-Climatology. *In:* TOMISLAV, H. & HANNES, I. R. (eds.) *Developments in Soil Science.* Elsevier.
BRADLEY, A. V., CHAPMAN, L. & THORNES, J. E. 2001. Modelling of road surface temperature from a geographical parameter database. Part 2: Numerical. *Meteorological Applications,* 8**,** 421-436.
BRAZEL, A. J., SELOVER, N. J., VOSE, R. J. & HEISLER, G. J. 2000. The tale of two climates -- Baltimore and Phoenix urban LTER sites. *Climate Research,* 15**,** 123-135.
BRIMICOMBE, A. 2010. *GIS, environmental modelling and engineering / Allan Brimicombe*, CRC Press.
BRINKHOFF, T. 2016. *City Population* [Online]. City Population Available: http://www.citypopulation.de/Iraq.html [Accessed 03-10-2016 2016].
BRITTER, R. E. & HANNA, S. R. 2003. Flow and dispersion in urban areas. *Annual Review of Fluid Mechanics,* 35**,** 469-496.

BRUSE, M. 2006. *ENVI-met 3 – a three dimensional microclimate model* [Online]. Geomatik: Ruhr Universit¨at Bochum, Geographischer Institut. Available: http://www.envi-met.com [Accessed 7/10/2016 2016].
BUCL. 2014a. *HiTemp Project* [Online]. University of Birmingham Available:http://www.birmingham.ac.uk/schools/gees/centres/bucl/hitemp/index.aspx [Accessed 20 Augest 2014 2014].
BUCL. 2014b. *Metadata* [Online]. CEDA. Available: http://data.ceda.ac.uk/badc/hitemp/metadata/ [Accessed 4-3-2015 2015].
BURKE, J. 2015. India heatwave death toll rises as awareness campaigns launch. *Guardian*.
BUSATO, F., LAZZARIN, R. M. & NORO, M. 2014. Three years of study of the Urban Heat Island in Padua: Experimental results. *Sustainable Cities and Society,* 10**,** 251-258.
CAI, G. & DU, M. Relationship between thermal inertia and urban heat sink in Beijing derived from Satellite images. 2009 Joint Urban Remote Sensing Event, 2009. IEEE, 1-5.
CAO, X., ONISHI, A., CHEN, J. & IMURA, H. 2010. Quantifying the cool island intensity of urban parks using ASTER and IKONOS data. *Landscape and Urban Planning,* 96**,** 224-231.
CARLSON, T. N. & RIPLEY, D. A. 1997. On the relation between NDVI, fractional vegetation cover, and leaf area index. *Remote sensing of Environment,* 62**,** 241-252.
CERMAK, J. E., DAVENPORT, A. G., PLATE, E. J. & VIEGAS, D. X. Wind climate in cities. 1995. Kluwer Academic Publishers.
CHANDLER, T. J. 1965. *The climate of London*, Hutchinson.
CHANG, B., WANG, H.-Y., PENG, T.-Y. & HSU, Y.-S. 2010. Development and Evaluation of a City-Wide Wireless Weather Sensor Network. *Educational Technology & Society,* 13**,** 270-280.
CHAPMAN, L., MULLER, C. L., YOUNG, D. T., WARREN, E. L., GRIMMOND, C., CAI, X.-M. & FERRANTI, E. J. 2015a. The Birmingham urban climate laboratory: An open meteorological test bed and challenges of the smart city. *Bulletin of the American Meteorological Society,* 96**,** 1545-1560.
CHAPMAN, L., MULLER, C. L., YOUNG, D. T., WARREN, E. L., GRIMMOND, C., CAI, X.-M. & FERRANTI, E. J. 2015b. The Birmingham Urban Climate Laboratory: An open meteorological testbed and challenges of the smart city. *Bulletin of the American Meteorological Society*.
CHEN, L., YU, B., YANG, F. & MAYER, H. 2016. Intra-urban differences of mean radiant temperature in different urban settings in Shanghai and implications for heat stress under heat waves: A GIS-based approach. *Energy and Buildings,* 130**,** 829-842.
CHEOS 2016. China High-resolution Earth Observation System (CHEOS) *In:* ADMINISTRATION, C. N. S. (ed.). China: CNSA (China National Space Administration).
CHEUNG, K. W. 2011. An urban heat island study for building and urban design.
CHOW, W. T., BRENNAN, D. & BRAZEL, A. J. 2012. Urban heat island research in Phoenix, Arizona: Theoretical contributions and policy applications. *Bulletin of the American Meteorological Society,* 93**,** 517-530.
CHRYSOULAKIS, N., DE CASTRO, E. A. & MOORS, E. J. 2014. *Understanding urban metabolism: A tool for urban planning*, Routledge.
CHRYSOULAKIS, N. & GRIMMOND, C. S. B. 2016. Understanding and reducing the anthropogenic heat emission. *Urban Climate Mitigation Techniques***,** 27.
CHUVIECO, E. & HUETE, A. 2010. *Fundamentals of satellite remote sensing / Emilio Chuvieco and Alfredo Huete*, CRC.
CITY OF LONDON CORPORATION 2007. City of London resident population analysis. *In:* SERVICE, T. D. O. C. C. S. S. S. (ed.). London: City of London Corporation
CITY POPULATION. 2013. *Governorates & Regions* [Online]. City Population Available: http://www.citypopulation.de/ [Accessed July 2014].

CLIMATE-DATA. 2016. *CLIMATE: LONDON* [Online]. online: CLIMATE-DATA.ORG. Available: http://en.climate-data.org/location/1/ [Accessed 13-10-2016 2016].
CLIMATE DATA. 2016. *CLIMATE: Birmingham* [Online]. online: CLIMATE-DATA.ORG. Available: http://en.climate-data.org/location/47/ [Accessed 23-10-2016 2016].
COUNCIL, B. C. 2003. *Wards and constituencies* [Online]. Birmingham, UK: Birmingham City Council
Available:https://www.birmingham.gov.uk/info/20057/about_birmingham/665/wards_and_constituencies [Accessed 25-10-2016 2016].
COUNCIL, B. C. 2011. *Census 2011 Key Statistics Quick Ward Profile* [Online]. Birmingham, UK: Birmingham City Council
Available:https://www.birmingham.gov.uk/downloads/file/81/census_2011_key_statistics_quick_ward_profile [Accessed 26-10-2016 2016].
COUNCIL, B. C. 2016. *Sutton Park* [Online]. Birmingham, UK: Birmingham City CouncilAvailable:https://www.birmingham.gov.uk/info/20089/parks/405/sutton_park [Accessed 26-10-2016 2016].
DABBERDT, W., KOISTINEN, J., POUTIAINEN, J., SALTIKOFF, E. & TURTIAINEN, H. 2005. Research: the helsinki mesoscale testbed: an invitation to use a new 3-D observation network. *Bulletin of the American Meteorological Society,* 86**,** 906-907.
DALLAL, G. E. 2000. *P Values* [Online]. Gerard E. Dallal. Available: http://www.jerrydallal.com/lhsp/pval.htm [Accessed 15/1/2016 2016].
DASH, P., GÖTTSCHE, F.-M., OLESEN, F.-S. & FISCHER, H. 2001. Retrieval of land surface temperature and emissivity from satellite data: Physics, theoretical limitations and current methods. *Journal of the Indian Society of Remote Sensing,* 29**,** 23-30.
DAVID WEISBURD, C. B. 2007. *Statistics in Criminal Justice,* USA, Springer US.
DAVIES, L., BELL, J., BONE, J., HEAD, M., HILL, L., HOWARD, C., HOBBS, S., JONES, D., POWER, S. & ROSE, N. 2011. Open Air Laboratories (OPAL): A community-driven research programme. *Environmental Pollution,* 159**,** 2203-2210.
DENG, C. & WU, C. 2013. Examining the impacts of urban biophysical compositions on surface urban heat island: A spectral unmixing and thermal mixing approach. *Remote Sensing of Environment,* 131**,** 262-274.
DEWAN, A. M. & YAMAGUCHI, Y. 2009. Using remote sensing and GIS to detect and monitor land use and land cover change in Dhaka Metropolitan of Bangladesh during 1960–2005. *Environmental monitoring and assessment,* 150**,** 237-249.
DOICK, K. J., PEACE, A. & HUTCHINGS, T. R. 2014. The role of one large greenspace in mitigating London's nocturnal urban heat island. *Sci Total Environ,* 493**,** 662-71.
DOUSSET, B. & GOURMELON, F. 2003. Satellite multi-sensor data analysis of urban surface temperatures and landcover. *ISPRS Journal of Photogrammetry and Remote Sensing,* 58**,** 43-54.
DRAPER, N. R. S., H 1998. *Applied regression analysis* New York, Wiley.
DRUSCH, M., DEL BELLO, U., CARLIER, S., COLIN, O., FERNANDEZ, V., GASCON, F., HOERSCH, B., ISOLA, C., LABERINTI, P., MARTIMORT, P., MEYGRET, A., SPOTO, F., SY, O., MARCHESE, F. & BARGELLINI, P. 2012. Sentinel-2: ESA's Optical High-Resolution Mission for GMES Operational Services. *Remote Sensing of Environment,* 120**,** 25-36.
DU, H., WANG, D., WANG, Y., ZHAO, X., QIN, F., JIANG, H. & CAI, Y. 2016a. Influences of land cover types, meteorological conditions, anthropogenic heat and urban area on surface urban heat island in the Yangtze River Delta Urban Agglomeration. *Science of The Total Environment,* 571**,** 461-470.
DU, S., XIONG, Z., WANG, Y.-C. & GUO, L. 2016b. Quantifying the multilevel effects of landscape composition and configuration on land surface temperature. *Remote Sensing of Environment,* 178**,** 84-92.

DURAN, C. 2015. Drought and vegetation analysis in Tarsus River Basin (Southern Turkey) using GIS and Remote Sensing data. *Journal of Human Sciences,* 12**,** 1853-1866.
EDINA. 2015. *Digimap: Data download, OS Terrian 5 DTM* [Online]. Available: www.digimap.edina.ac.uk/datadownlaod/osdownlaod [Accessed 15/5/2015 2015].
EDINA. 2016. *Digimap: Data download, Boundary and location data* [Online]. University of Edinburgh. Available: www.digimap.edina.ac.uk/datadownlaod/osdownlaod [Accessed 25/10/2016 2016].
EEA. 2010. *Urban Atlas* [Online]. Denmark European Environment Agency. Available: http://www.eea.europa.eu/data-and-maps/data/urban-atlas [Accessed 1/5/2015 2015].
EEA. 2014. *Urban Atlas* [Online]. Denmark: European Environment Agency. Available: www.eea.europa.eu/data-and-maps/data/
[Accessed 18 Sep. 2015 2015].
ELIASSON, I. & SVENSSON, M. 2003. Spatial air temperature variations and urban land use-a statistical approach. *Meteorological Applications,* 10**,** 135-149.
ENVIRONMENTAL PROTECTION AGENCY. 2008. *Reducing Urban Heat Islands: Compendium of Strategies* [Online]. : EPA. Available: http://www.epa.gov/heatisland/resources/pdf/BasicsCompendium.pdf [Accessed 1 June 2014 2014].
EOPORTAL. 2016. *GF-1 (Gaofen-1) High-resolution Imaging Satellite / CHEOS series of China* [Online]. world of Earth Observation resources. Available: https://directory.eoportal.org/web/eoportal/satellite-missions/g/gaofen-1 [Accessed 14-4-2016 2016].
EPTING, J., VERBYLA, D. & SORBEL, B. 2005. Evaluation of remotely sensed indices for assessing burn severity in interior Alaska using Landsat TM and ETM+. *Remote Sensing of Environment,* 96**,** 328-339.
ERELL, E., PEARLMUTTER, D. & WILLIAMSON, T. J. 2011. *Urban Microclimate: Designing the Spaces Between Buildings*, Earthscan.
ERELL, E. & WILLIAMSON, T. 2007. Intra-urban differences in canopy layer air temperature at a mid-latitude city. *International Journal of Climatology,* 27**,** 1243-1255.
ESA. 2016. *Sentinel-2* [Online]. ESA. Available: http://www.esa.int/Our_Activities/Observing_the_Earth/Copernicus/Sentinel-2/Facts_and_figures [Accessed 8 June 2016 2016].
ESOC. 2016. *89 Neighborhoods in Baghdad* [Online]. Princeton University: The Empirical Studies of Conflict Project (ESOC). Available: https://esoc.princeton.edu/files/89-neighborhoods-baghdad [Accessed 27-09-2016 2016].
ESRI. 2015. *Basemaps* [Online]. online. Available: http://www.esri.com/data/basemaps [Accessed 20/10/2015 2015].
FARINA, A. 2012. Exploring the relationship between land surface temperature and vegetation abundance for urban heat island mitigation in Seville, Spain. *LUMA-GIS Thesis*.
FENNER, D., MEIER, F., SCHERER, D. & POLZE, A. 2001. Spatial and temporal air temperature variability in Berlin. *Germany, during the years,* 2010**,** 308-331.
FOODY, G. M. 2002. Status of land cover classification accuracy assessment. *Remote sensing of environment,* 80**,** 185-201.
FOODY, G. M. 2004. Thematic map comparison. *Photogrammetric Engineering & Remote Sensing,* 70**,** 627-633.
FREY, C. M., RIGO, G. & PARLOW, E. 2005. Investigation of the daily Urban Cooling Island (UCI) in two coastal cities in an arid environment: Dubai and Abu Dhabi (UAE). *City,* 81**,** 2.06.
FREY, C. M., RIGO, G., PARLOW, E. & MARÇAL, A. The cooling effect of cities in a hot and dry environment. Global Developments in Environmental Earth

Observation from Space. Proceedings 25th Symposium of the European-Association of Remote Sensing Laboratories (EARSeL) Pages, 2006. 169-174.

GAL, T., LINDBERG, F. & UNGER, J. 2009. Computing continuous sky view factors using 3D urban raster and vector databases: comparison and application to urban climate. *Theoretical and applied climatology,* 95**,** 111-123.

GÁL, T. M., SKARBIT, N. & UNGER, J. 2016. Urban heat island patterns and their dynamics based on an urban climate measurement network. *Hungarian Geographical Bulletin*.

GALLO, K., MCNAB, A., KARL, T., BROWN, J., HOOD, J. & TARPLEY, J. 1993. The use of NOAA AVHRR data for assessment of the urban heat island effect. *Journal of Applied Meteorology,* 32**,** 899-908.

GARTLAND, L. 2008. *Heat Islands: understanding and mitigating heat in urban areas,* UK & USA, Earthscan.

GARTLAND, L., KONOPACKI, S. J. & AKBARI, H. 1996. Modeling the effects of reflective roofing. Lawrence Berkeley National Lab., CA (United States).

GEDZELMAN, S., AUSTIN, S., CERMAK, R., STEFANO, N., PARTRIDGE, S., QUESENBERRY, S. & ROBINSON, D. 2003. Mesoscale aspects of the urban heat island around New York City. *Theoretical and Applied Climatology,* 75**,** 29-42.

GEOMATICS. 2014. *LIDAR* [Online]. UK: Environment Agency. Available: https://www.geomatics-group.co.uk/GeoCMS/Products/LIDAR.aspx 2014].

GIBSON, P. 2013. *Introductory remote sensing principles and concepts*, Routledge.

GILLESPIE, A., ROKUGAWA, S., MATSUNAGA, T., COTHERN, J. S., HOOK, S. & KAHLE, A. B. 1998. A temperature and emissivity separation algorithm for Advanced Spaceborne Thermal Emission and Reflection Radiometer (ASTER) images. *IEEE transactions on geoscience and remote sensing,* 36**,** 1113-1126.

GIVONI, B. 1998. *Climate considerations in building and urban design*, John Wiley & Sons.

GORSEVSKI, V., TAHA, H, QUATTROCHI, D, LUVALL, J 1998. Air Pollution Prevention Through Urban Heat Island Mitigation: An Update on the Urban Heat Island Pilot Project. *ACEEE Summer Study on Energy Efficiency in Buildings Proceedings,* 9.

GREATER LONDON AUTHORITY 2006. London's Urban Heat Island:A Summary for Decision Makers. London, UK.

GREATER LONDON.AUTHORITY. 2016. *London Borough Profiles* [Online]. Mayor of London. Available: https://data.london.gov.uk/dataset/london-borough-profiles [Accessed 18-10-2016 2016].

GRIMMOND, C. S. B., WARD, H. C. & KOTTHAUS, S. 2015. How is urbanization altering local and regional climate? *In:* SETO, K. C., SOLECKI, W. D. & GRIFFITH, C. A. (eds.) *The Routledge Handbook of Urbanization and Global Environmental Change.* Routledge.

GRIMMOND, S. 2007. Urbanization and global environmental change: local effects of urban warming. *The Geographical Journal,* 173**,** 83-88.

GUAN, K. K. 2011. Surface and ambient air temperatures associated with different ground material: A case study at the University of California, Berkeley.

HADJIMITSIS, D. G., RETALIS, A., MICHAELIDES, S., TYMVIOS, F., PARONIS, D., THEMISTOCLEOUS, K. & AGAPIOU, A. 2013. *Satellite and Ground Measurements for Studying the Urban Heat Island Effect in Cyprus*.

HEIDEN, U., HELDENS, W., ROESSNER, S., SEGL, K., ESCH, T. & MUELLER, A. 2012. Urban structure type characterization using hyperspectral remote sensing and height information. *Landscape and Urban Planning,* 105**,** 361-375.

HINKEL, K. M. & NELSON, F. E. 2007. Anthropogenic heat island at Barrow, Alaska, during winter: 2001–2005. *Journal of Geophysical Research: Atmospheres,* 112.

HJORT, J., SUOMI, J. & KÄYHKÖ, J. 2011. Spatial prediction of urban–rural temperatures using statistical methods. *Theoretical and applied climatology,* 106**,** 139-152.

HO, H. C., KNUDBY, A., SIROVYAK, P., XU, Y., HODUL, M. & HENDERSON, S. B. 2014. Mapping maximum urban air temperature on hot summer days. *Remote Sensing of Environment,* 154**,** 38-45.

HONJO, T., YAMATO, H., MIKAMI, T. & GRIMMOND, C. 2015. Network optimization for enhanced resilience of urban heat island measurements. *Sustainable Cities and Society,* 19**,** 319-330.

HÖPPE, P. 1999. The physiological equivalent temperature – a universal index for the biometeorological assessment of the thermal environment. *International Journal of Biometeorology,* 43**,** 71-75.

HOWARD, L. 2007. THE CLIMATE OF LONDON.

HU, L. & BRUNSELL, N. A. 2013. The impact of temporal aggregation of land surface temperature data for surface urban heat island (SUHI) monitoring. *Remote Sensing of Environment,* 134**,** 162-174.

HUGHES, L. 2000. Biological consequences of global warming: is the signal already apparent? *Trends in Ecology & Evolution,* 15**,** 56-61.

HUNG, T. K. & WO, O. C. 2012. Development of a Community Weather Information Network (Co-WIN) in Hong Kong. *Weather,* 67**,** 48-50.

IAMARINO, M., BEEVERS, S. & GRIMMOND, C. 2012. High-resolution (space, time) anthropogenic heat emissions: London 1970–2025. *International Journal of Climatology,* 32**,** 1754-1767.

IDRE. 2016. *Regression with SPSS* [Online]. University of California Los Angeles: Institute for Digital Research and Education Home. Available: http://www.ats.ucla.edu/stat/spss/webbooks/reg/chapter2/spssreg2.htm [Accessed 12-10-2016 2016].

IVAJNŠIČ, D., KALIGARIČ, M. & ŽIBERNA, I. 2014. Geographically weighted regression of the urban heat island of a small city. *Applied Geography,* 53**,** 341-353.

JAMES, W. 2002. Green Roads: Research into permeable pavers, investigation of infiltration capacity, pavement leachate, and runoff temperature. *Stormwater, The Journal for Surface Water Quality Professional***,** 49-50.

JÄNICKE, B., MEIER, F., LINDBERG, F., SCHUBERT, S. & SCHERER, D. 2016. Towards city-wide, building-resolving analysis of mean radiant temperature. *Urban Climate,* 15**,** 83-98.

JANKOVIĆ, V. 2013. A historical review of urban climatology and the atmospheres of the industrialized world. *Wiley Interdisciplinary Reviews: Climate Change,* 4**,** 539-553.

JASSIM, S. Z. & GOFF, J. C. 2006. *Geology of Iraq*, DOLIN, sro, distributed by Geological Society of London.

JIM, C. 2015. Assessing climate-adaptation effect of extensive tropical green roofs in cities. *Landscape and Urban Planning,* 138**,** 54-70.

JIN, L., WHITEHEAD, P. G., FUTTER, M. N. & LU, Z. 2012. Modelling the impacts of climate change on flow and nitrate in the River Thames: assessing potential adaptation strategies. *Hydrology Research,* 43**,** 902-916.

JIN, M. & LIANG, S. 2006. An improved land surface emissivity parameter for land surface models using global remote sensing observations. *Journal of Climate,* 19**,** 2867-2881.

JOHNSON, D. 1985a. Urban modification of diurnal temperature cycles in Birmingham, UK. *Journal of climatology,* 5**,** 221-225.

JOHNSON, D. B. 1985b. Urban modification of diurnal temperature cycles in birmingham, U.K. *Journal of Climatology,* 5**,** 221-225.

JUSUF, S. K., WONG, N. H., HAGEN, E., ANGGORO, R. & HONG, Y. 2007. The influence of land use on the urban heat island in Singapore. *Habitat International,* 31**,** 232-242.

KATO, S. & YAMAGUCHI, Y. 2005. Analysis of urban heat-island effect using ASTER and ETM+ Data: Separation of anthropogenic heat discharge and natural heat radiation from sensible heat flux. *Remote Sensing of Environment,* 99**,** 44-54.

KHAN, S. & SIMPSON, R. 2001. Effect Of A Heat Island On The Meteorology Of A Complex Urban Airshed. *Boundary-Layer Meteorology,* 100**,** 487-506.
KRÜGER, E., MINELLA, F. & MATZARAKIS, A. 2014. Comparison of different methods of estimating the mean radiant temperature in outdoor thermal comfort studies. *International journal of biometeorology,* 58**,** 1727-1737.
KUENZER, C. & DECH, S. 2013. Thermal infrared remote sensing. *Sensors, Methods, Applications, Remote Sensing and Digital Image Processing,* 17.
KUMI-BAOTENG, B., STEMN, E. & AGYAPONG, A. 2015. Effect of Urban Growth on Urban Thermal Environment: A Case Study of Sekondi-Takoradi Metropolis of Ghana. *Journal of Environment and Earth Science,* 5**,** 32-41.
LAI, A., MAING, M. & NG, E. 2017. Observational studies of mean radiant temperature across different outdoor spaces under shaded conditions in densely built environment. *Building and Environment,* 114**,** 397-409.
LAU, K. K.-L., LINDBERG, F., RAYNER, D. & THORSSON, S. 2015. The effect of urban geometry on mean radiant temperature under future climate change: a study of three European cities. *International journal of biometeorology,* 59**,** 799-814.
LAU, K. K.-L., REN, C., HO, J. & NG, E. 2016. Numerical modelling of mean radiant temperature in high-density sub-tropical urban environment. *Energy and Buildings,* 114**,** 80-86.
LAWRENCE, M. G. 2005. The relationship between relative humidity and the dewpoint temperature in moist air: A simple conversion and applications. *Bulletin of the American Meteorological Society,* 86**,** 225-233.
LEE, D. O. 1992. Urban warming?—an analysis of recent trends in London's heat island. *Weather,* 47**,** 50-56.
LEE, S.-H. & BAIK, J.-J. 2010. Statistical and dynamical characteristics of the urban heat island intensity in Seoul. *Theoretical and Applied Climatology,* 100**,** 227-237.
LELOVICS, E., UNGER, J., SAVIĆ, S., GÁL, T. M., MILOSEVIC, D., GULYÁS, Á., MARKOVIC, V., ARSENOVIC, D. & GÁL, C. 2016. Intra-urban temperature observations in two Central European cities: a summer study. *IDŐJÁRÁS/QUARTERLY JOURNAL OF THE HUNGARIAN METEOROLOGICAL SERVICE*.
LENZHOLZER, S. 2015. *Weather in the city : how design shapes the urban climate / Sanda Lenzholzer ; translation Jean Tee*, nai010.
LI, H., JIANG, J., CHEN, B., LI, Y., XU, Y. & SHEN, W. 2016. Pattern of NDVI-based vegetation greening along an altitudinal gradient in the eastern Himalayas and its response to global warming. *Environmental Monitoring and Assessment,* 188**,** 186.
LI, R. & ROTH, M. Spatial variation of the canopy-level urban heat island in Singapore. Proceedings of the Seventh International Conference on Urban Climate, Yokohama, Japan, 2007.
LI, Z.-L., BECKER, F., STOLL, M. P. & WAN, Z. 1999. Evaluation of Six Methods for Extracting Relative Emissivity Spectra from Thermal Infrared Images. *Remote Sensing of Environment,* 69**,** 197-214.
LI, Z.-L., TANG, B.-H., WU, H., REN, H., YAN, G., WAN, Z., TRIGO, I. F. & SOBRINO, J. A. 2013. Satellite-derived land surface temperature: Current status and perspectives. *Remote Sensing of Environment,* 131**,** 14-37.
LIANG, S., LI, X. & WANG, J. 2012. Acknowledgments. *Advanced Remote Sensing.* Boston: Academic Press.
LINDBERG, F. & GRIMMOND, C. 2010. Continuous sky view factor maps from high resolution urban digital elevation models. *Climate Research,* 42**,** 177-183.
LINDBERG, F. & GRIMMOND, C. 2011a. The influence of vegetation and building morphology on shadow patterns and mean radiant temperatures in urban areas: model development and evaluation. *Theoretical and applied climatology,* 105**,** 311-323.

LINDBERG, F. & GRIMMOND, C. S. B. 2011b. Nature of vegetation and building morphology characteristics across a city: Influence on shadow patterns and mean radiant temperatures in London. *Urban Ecosystems,* 14**,** 617-634.
LINDBERG, F., GRIMMOND, C. S. B. & MARTILLI, A. 2015a. Sunlit fractions on urban facets – Impact of spatial resolution and approach. *Urban Climate,* 12**,** 65-84.
LINDBERG, F., GRIMMOND, S., CAPEL-TIMMS, I., CHANG, Y., GABEY, A., HUANG, B., JARVI, L., KENT, C., KOKKONEN, T., KRAVE, N., OLOFSON, F., ONOMURA, S., SUN, T., TAN, J., WARD, H., XUE, L. & BERGE, K. 2016a. *Urban Multi-scale Environmental Predictor (UMEP) Manual* [Online]. University of Reading UK, University of Gothenburg Sweden, SIMS China. Available: http://urban-climate.net/umep/UMEP_Manual [Accessed 20/12/2016 2016].
LINDBERG, F., HOLMER, B. & THORSSON, S. 2008. SOLWEIG 1.0 – Modelling spatial variations of 3D radiant fluxes and mean radiant temperature in complex urban settings. *International Journal of Biometeorology,* 52**,** 697-713.
LINDBERG, F., HOLMER, B., THORSSON, S. & RAYNER, D. 2014. Characteristics of the mean radiant temperature in high latitude cities—implications for sensitive climate planning applications. *International Journal of Biometeorology,* 58**,** 613-627.
LINDBERG, F., JONSSON, P., HONJO, T. & WÄSTBERG, D. 2015b. Solar energy on building envelopes – 3D modelling in a 2D environment. *Solar Energy,* 115**,** 369-378.
LINDBERG, F. & THORSSON, S. SOLWEIG-The new model for calculating the mean radiant temperature. The Seventh International Conference on Urban Climate, 2009.
LINDBERG, F., THORSSON, S., RAYNER, D. & LAU, K. 2016b. The impact of urban planning strategies on heat stress in a climate-change perspective. *Sustainable Cities and Society,* 25**,** 1-12.
LO, C. & QUATTROCHI, D. A. 2003. Land-Use and Land-Cover Change, Urban Heat Island Phenomenon, and Health Implications. *Photogrammetric Engineering & Remote Sensing,* 69**,** 1053-1063.
LPDAAC. 2014a. *NASA and USGS partnership* [Online]. U.S. Department of the Interior, U.S. Geological Survey. Available: https://lpdaac.usgs.gov/ [Accessed 14-4-2016 2016].
LPDAAC. 2014b. *On Demand Surface Emissivity* [Online]. Sioux Falls, South Dakota: U.S. Department of the Interior. Available: https://lpdaac.usgs.gov/dataset_discovery/aster/aster_products_table/ast_05 [Accessed 7-4-2016 2016].
LPDAAS. 2014a. *MRTWeb* [Online]. U.S. Department of the Interior, LAND PROCESSES DISTRIBUTED ACTIVE ARCHIVE CENTER. Available: https://lpdaac.usgs.gov/data_access/mrtweb [Accessed 5-4-2016.
LPDAAS. 2014b. *On Demand Surface Kinetic Temperature* [Online]. U.S. Department of the Interior, LAND PROCESSES DISTRIBUTED ACTIVE ARCHIVE CENTER. Available:https://lpdaac.usgs.gov/dataset_discovery/aster/aster_products_table/ast_08 [Accessed 6-4-2016 2016].
MAGLI, S., LODI, C., LOMBROSO, L., MUSCIO, A. & TEGGI, S. 2015. Analysis of the urban heat island effects on building energy consumption. *International Journal of Energy and Environmental Engineering,* 6**,** 91-99.
MANLEY, G. 1958. On the frequency of snowfall in metropolitan England. *Quarterly Journal of the Royal Meteorological Society,* 84**,** 70-72.
MARINO, C., NUCARA, A., PIETRAFESA, M. & POLIMENI, E. 2017. The effect of the short wave radiation and its reflected components on the mean radiant temperature: modelling and preliminary experimental results. *Journal of Building Engineering,* 9**,** 42-51.
MARTIN, P., BAUDOUIN, Y. & GACHON, P. 2015. An alternative method to characterize the surface urban heat island. *International journal of biometeorology,* 59**,** 849-861.

MARTOS, A., PACHECO-TORRES, R., ORDÓÑEZ, J. & JADRAQUE-GAGO, E. 2016. Towards successful environmental performance of sustainable cities: Intervening sectors. A review. *Renewable and Sustainable Energy Reviews,* 57**,** 479-495.
MASEK, J. G., VERMOTE, E. F., SALEOUS, N. E., WOLFE, R., HALL, F. G., HUEMMRICH, K. F., GAO, F., KUTLER, J. & LIM, T.-K. 2006. A Landsat surface reflectance dataset for North America, 1990-2000. *Geoscience and Remote Sensing Letters, IEEE,* 3**,** 68-72.
MATERIA, S., BORRELLI, A., BELLUCCI, A., ALESSANDRI, A., DI PIETRO, P., ATHANASIADIS, P., NAVARRA, A. & GUALDI, S. 2014. Impact of atmosphere and land surface initial conditions on seasonal forecasts of global surface temperature. *Journal of Climate,* 27**,** 9253-9271.
MATZARAKIS, A., RUTZ, F. & MAYER, H. Estimation and calculation of the mean radiant temperature within urban structures. Biometeorology and Urban Climatology at the Turn of the Millenium (ed. by RJ de Dear, JD Kalma, TR Oke and A. Auliciems): Selected Papers from the Conference ICB-ICUC, 2000. 273-278.
MELVIN, P., BRIAN, P., HASHEM, A. & SHENG-CHIEH, C. 2000. The effect of pavements' temperatures on air temperatures in large cities. Berkeley, CA.
MET OFFICE. 2013. *High and low pressure* [Online]. UK: MetOffice. Available:http://www.metoffice.gov.uk/learning/learn-about-the weather/how-weather-works/highs-and-lows/pressure [Accessed 9/1/2017 2017].
MET OFFICE. 2015. *July 2013 heat wave* [Online]. UK: Met Office Available: www.metoffice.gov.uk/learning/learn-about-the-weather/weather-phenomena/case-studies/heat-wave-july2013 [Accessed 29/7/2015 2015].
MET OFFICE. 2016. *Beaufort wind force scale* [Online]. UK: Met Office. Available: http://www.metoffice.gov.uk/guide/weather/marine/beaufort-scale [Accessed 25-5-2016 2016].
METOFFICE. 2017. *2016: one of the warmest two years on record* [Online]. UK: Met Office. Available: http://www.metoffice.gov.uk/news/releases/2017/2016-record-breaking-year-for-global-temperature [Accessed 22/1/2017 2017].
MIDAS. 2015. *MIDAS* [Online]. UK: CEDA. Available: www.catalogue.eda.ac.uk/uuid/220a65615218d5c9cc9e4785a3234bd0 [Accessed 26/6/2015 2015].
MILLS, G. 2014. Urban climatology: History, status and prospects. *Urban Climate,* 10**,** 479-489.
MIRZAEI, P. A. 2015. Recent challenges in modeling of urban heat island. *Sustainable Cities and Society,* 19**,** 200-206.
MIRZAEI, P. A. & HAGHIGHAT, F. 2010. Approaches to study Urban Heat Island – Abilities and limitations. *Building and Environment,* 45**,** 2192-2201.
MOHAMAD, I. B. & USMAN, D. 2013. Standardization and its effects on k-means clustering algorithm. *Research Journal of Applied Sciences, Engineering and Technology,* 6**,** 3299-3303.
MONTÁVEZ, J. P., RODRÍGUEZ, A. & JIMÉNEZ, J. I. 2000. A study of the Urban Heat Island of Granada. *International Journal of Climatology,* 20**,** 899-911.
MONTEITH, J. 1981. Evaporation and surface temperature. *Quarterly Journal of the Royal Meteorological Society,* 107**,** 1-27.
MORICE, C. P., KENNEDY, J. J., RAYNER, N. A. & JONES, P. D. 2012. Quantifying uncertainties in global and regional temperature change using an ensemble of observational estimates: The HadCRUT4 data set. *Journal of Geophysical Research: Atmospheres,* 117.
MORINI, E., TOUCHAEI, A. G., CASTELLANI, B., ROSSI, F. & COTANA, F. 2016. The Impact of Albedo Increase to Mitigate the Urban Heat Island in Terni (Italy) Using the WRF Model. *Sustainability,* 8**,** 999.

MORRIS, C. J. G. & SIMMONDS, I. 2000. Associations between varying magnitudes of the urban heat island and the synoptic climatology in Melbourne, Australia. *International Journal of Climatology,* 20**,** 1931-1954.
MULLER, C. L., CHAPMAN, L., GRIMMOND, C., YOUNG, D. T. & CAI, X. 2013. Sensors and the city: a review of urban meteorological networks. *International Journal of Climatology,* 33**,** 1585-1600.
MURTY, R. N., MAINLAND, G., ROSE, I., CHOWDHURY, A. R., GOSAIN, A., BERS, J. & WELSH, M. Citysense: An urban-scale wireless sensor network and testbed. Technologies for Homeland Security, 2008 IEEE Conference on, 2008. IEEE, 583-588.
NASA. 2004. *LATEST FEATURED IMAGE FROM ASTER* [Online]. USA: California Institue of Technology. Available: http://asterweb.jpl.nasa.gov/index.asp [Accessed July 2014].
NASA. 2010. *MODIS* [Online]. USA: NASA. Available: http://modis.gsfc.nasa.gov/ [Accessed July 2014].
NASA. 2017. *NASA, NOAA Data Show 2016 Warmest Year on Record Globally* [Online]. NASA. Available: https://www.nasa.gov/press-release/nasa-noaa-data-show-2016-warmest-year-on-record-globally [Accessed 22/01/2017 2017].
NG, E. & REN, C. 2015. *The Urban Climatic Map: A Methodology for Sustainable Urban Planning*, Routledge.
NIKOLOPOULOU, M., BAKER, N. & STEEMERS, K. 2001. Thermal comfort in outdoor urban spaces: understanding the human parameter. *Solar energy,* 70**,** 227-235.
OFFICE FOR NATIONAL STATISICS. 2015. *Anuual Mid-year Population Estimates, 2014* [Online]. UK. [Accessed 12-08-2015 2015].
OKE, T. R. 1981. Canyon geometry and the nocturnal urban heat island: Comparison of scale model and field observations. *Journal of Climatology,* 1**,** 237-254.
OKE, T. R. 1988. Boundary layer climates (Second edition). By T. R. Oke. Methuen. 1987. Pp. 435 + xvi. £39.95 hardback; £14.95 paperback. *Quarterly Journal of the Royal Meteorological Society,* 114**,** 1568-1568.
OKE, T. R., SPRONKEN-SMITH, R. A., JÁUREGUI, E. & GRIMMOND, C. S. B. 1999. The energy balance of central Mexico City during the dry season. *Atmospheric Environment,* 33**,** 3919-3930.
ONS. 2016. *Greater London and the London Boroughs* [Online]. UK: The Office for National Statistics Available: http://webarchive.nationalarchives.gov.uk/20160105160709/http://www.ons.gov.uk/ons/site-information/information/terms-and-conditions/index.html [Accessed 13-10-2016 2016].
ORDNANCE SURVEY. 2014. *Research At Ordnance Survey* [Online]. UK: Ordnance Survey Available: www.ordnancesurvey.co.uk/eduaction-research/research/index.html [Accessed 23 Feb. 2014 2014].
ORDNANCE SURVEY. 2015. *Topography [FileGeoDatabase geospatial data]* [Online]. UK: EDINA Digimap Ordnance Survey Service. Available: http://digimap.edina.ac.uk.
ORLOV, M. L. 1996. Multiple Linear Regression Analysis Using Microsoft Excel.
OS 2015. Research Data Agreement. *In:* LIMITED, O. S. (ed.). SOUTHAMPTON, UK: UK Ordnance Survey.
OSWALD, E. M., ROOD, R. B., ZHANG, K., GRONLUND, C. J., O'NEILL, M. S., WHITE-NEWSOME, J. L., BRINES, S. J. & BROWN, D. G. 2012. An Investigation into the Spatial Variability of Near-Surface Air Temperatures in the Detroit, Michigan, Metropolitan Region*. *Journal of Applied Meteorology and Climatology,* 51**,** 1290-1304.
OWEN, S. M., MACKENZIE, A. R., BUNCE, R. G. H., STEWART, H. E., DONOVAN, R. G., STARK, G. & HEWITT, C. N. 2006. Urban land classification and its uncertainties using principal component and cluster analyses: A case study for the UK West Midlands. *Landscape and Urban Planning,* 78**,** 311-321.

PARK, K.-H. & SUH, M.-S. Assessment of surface urban heat island over East Asia using the land surface temperature data retrieved from COMS data. EGU General Assembly Conference Abstracts, 2013. 4577.

PENG, S., PIAO, S., CIAIS, P., FRIEDLINGSTEIN, P., OTTLE, C., BRÉON, F.-M., NAN, H., ZHOU, L. & MYNENI, R. B. 2011. Surface Urban Heat Island Across 419 Global Big Cities. *Environmental Science & Technology,* 46**,** 696-703.

PETRALLI, M., MASSETTI, L. & ORLANDINI, S. 2011. Five years of thermal intra-urban monitoring in Florence (Italy) and application of climatological indices. *Theoretical and applied climatology,* 104**,** 349-356.

PIRINGER, M., GRIMMOND, C. S. B., JOFFRE, S. M., MESTAYER, P., MIDDLETON, D. R., ROTACH, M. W., BAKLANOV, A., DE RIDDER, K., FERREIRA, J., GUILLOTEAU, E., KARPPINEN, A., MARTILLI, A., MASSON, V. & TOMBROU, M. 2002. Investigating the Surface Energy Balance in Urban Areas – Recent Advances and Future Needs. *Water, Air and Soil Pollution: Focus,* 2**,** 1-16.

RABEE, A. M. 2014. Estimating the health risks associated with air pollution in Baghdad City, Iraq. *Environmental Monitoring and Assessment,* 187**,** 1-12.

RADHI, H., FIKRY, F. & SHARPLES, S. 2013. Impacts of urbanisation on the thermal behaviour of new built up environments: A scoping study of the urban heat island in Bahrain. *Landscape and Urban Planning,* 113**,** 47-61.

RAKIB, Z. B. 2013. Extreme Temperature Climatology and Evaluation of Heat Index in Bangladesh During 1981-2010. *PRESIDENCY,* 2**,** 84-95.

RASUL, A., BALZTER, H. & SMITH, C. 2015. Spatial variation of the daytime Surface Urban Cool Island during the dry season in Erbil, Iraqi Kurdistan, from Landsat 8. *Urban Climate,* 14, Part 2**,** 176-186.

RASUL, A., BALZTER, H. & SMITH, C. 2016. Diurnal and Seasonal Variation of Surface Urban Cool and Heat Islands in the Semi-Arid City of Erbil, Iraq. *Climate,* 4**,** 42.

RASUL, A., BALZTER, H., SMITH, C., REMEDIOS, J., ADAMU, B., SOBRINO, J. A., SRIVANIT, M. & WENG, Q. 2017. A Review on Remote Sensing of Urban Heat and Cool Islands. *Land,* 6**,** 38.

RASUL, A. O. 2016. *Remote Sensing of Surface Urban Cool and Heat Island Dynamics in Erbil, Iraq, between 1992 and 2013.* Department of Geography.

RIPLEY, E., ARCHIBOLD, O. & BRETELL, D. 1996. Temporal and spatial temperature patterns in Saskatoon. *Weather,* 51**,** 398-405.

RIZWAN, A. M., DENNIS, L. Y. & CHUNHO, L. 2008. A review on the generation, determination and mitigation of Urban Heat Island. *Journal of Environmental Sciences,* 20**,** 120-128.

ROGAN, J., ZIEMER, M., MARTIN, D., RATICK, S., CUBA, N. & DELAUER, V. 2013. The impact of tree cover loss on land surface temperature: A case study of central Massachusetts using Landsat Thematic Mapper thermal data. *Applied Geography,* 45**,** 49-57.

ROSSI, F., ANDERINI, E., CASTELLANI, B., NICOLINI, A. & MORINI, E. 2015a. Integrated improvement of occupants' comfort in urban areas during outdoor events. *Building and Environment,* 93**,** 285-292.

ROSSI, F., MORINI, E., CASTELLANI, B., NICOLINI, A., BONAMENTE, E., ANDERINI, E. & COTANA, F. Beneficial effects of retroreflective materials in urban canyons: results from seasonal monitoring campaign. Journal of Physics: Conference Series, 2015b. IOP Publishing, 012012.

ROTH, M. 2012. Urban Heat Islands. *Handbook of Environmental Fluid Dynamics, Volume Two.* CRC Press.

ROTH, M., OKE, T. & EMERY, W. 1989. Satellite-derived urban heat islands from three coastal cities and the utilization of such data in urban climatology. *International Journal of Remote Sensing,* 10**,** 1699-1720.

RPF. 2016. *Visit the parks* [Online]. UK: Royal Parks Foundation. Available: http://www.supporttheroyalparks.org/visit_the_parks?gclid=Cj0KEQjw4fy_BRCX7b6rq_WZgI0BEiQAl78nd7atVZR1iNi3h7xoYbBDDZIusshpBgbOorPQNwx7QWQaAglH8P8HAQ [Accessed 13-10-2016 2016].

RUDAW. 2015. *Rudaw*.
RYU, Y.-H. & BAIK, J.-J. 2012. Quantitative Analysis of Factors Contributing to Urban Heat Island Intensity. *Journal of Applied Meteorology and Climatology,* 51**,** 842-854.
SÁ, J. P. M. D. 2007. *Applied Statistics Using SPSS, STATISTICA, MATLAB and R,* New York Springer Berlin Heidelberg.
SAILOR, D. J. & DIETSCH, N. 2007. The urban heat island mitigation impact screening tool (MIST). *Environmental Modelling & Software,* 22**,** 1529-1541.
SALEH, S. A. 2011a. Air quality over Baghdad City using earth observation and Landsat thermal data. *Journal of Asian Scientific Research,* 1**,** 291.
SALEH, S. A. 2011b. Remote Sensing and GIS Techniques for Urban Growth Monitoring of Basarah City. *International Journal of Remote Sensing and Earth Sciences (IJReSES),* 7.
SALEH, S. A. H. 2010. <IMPACT OF URBAN EXPANSION ON SURFACE TEMPERATURE IN Baghdad.pdf>. *Journal of Al-Nahrain University,* 13**,** 48-59.
SANTAMOURIS, M. 2013. *Energy and climate in the urban built environment*, Routledge.
SCARANO, M. & SOBRINO, J. A. 2015. On the relationship between the sky view factor and the land surface temperature derived by Landsat-8 images in Bari, Italy. *International Journal of Remote Sensing,* 36**,** 4820-4835.
SCHWARZ, N., LAUTENBACH, S. & SEPPELT, R. 2011. Exploring indicators for quantifying surface urban heat islands of European cities with MODIS land surface temperatures. *Remote Sensing of Environment,* 115**,** 3175-3186.
SCHWARZ, N., SCHLINK, U., FRANCK, U. & GROßMANN, K. 2012. Relationship of land surface and air temperatures and its implications for quantifying urban heat island indicators—An application for the city of Leipzig (Germany). *Ecological Indicators,* 18**,** 693-704.
SCOTT, J. R. S., E.G. MCPHERSON 2004. Effects of Tree Cover on Parking Lot Microclimate and Vehicle Emissions. *Journal of Arboriculture,* 25
ŠEĆEROV, I., SAVIĆ, S., MILOŠEVIĆ, D., MARKOVIĆ, V. & BAJŠANSKI, I. 2015. Development of an automated urban climate monitoring system in Novi Sad (Serbia). *Geographica Pannonica,* 19**,** 174-183.
SENATE, U. S. U.S. Senate Environment and Public Works Committee Minority Staff Report (Inhofe). United Nations Climate Change Conference 2009 Poznan, Poland.
SHAHMOHAMADI, P., CHE-ANI, A., MAULUD, K., TAWIL, N. & ABDULLAH, N. 2011. The Impact of Anthropogenic Heat on Formation of Urban Heat Island and Energy Consumption Balance. *Urban Studies Research,* 2011.
SHALABY, A. S. 2012. URBAN HEAT ISLAND AND CITIES DESIGN: A Conceptual Framework of Mitigation Tools in Hot-arid Regions.
SHANGMING, D., WANRONG, X., BO, D., HUIXI, X. & JIAYI, H. Comparison and analysis of research methods for urban heat island effect based on Landsat TM6. 2010 Second IITA International Conference on Geoscience and Remote Sensing, 28-31 Aug. 2010 2010. 161-164.
SHEN, G., IBRAHIM, A. N., WANG, Z., MA, C. & GONG, J. 2015. Spatial–temporal land-use/land-cover dynamics and their impacts on surface temperature in Chongming Island of Shanghai, China. *International Journal of Remote Sensing,* 36**,** 4037-4053.
SHIGETA, Y., OHASHI, Y. & TSUKAMOTO, O. Urban cool island in daytime—analysis by using thermal image and air temperature measurements. The Seventh International Conference on Urban Climate, 2009.
SHISHEGAR, N. 2014. The impact of green areas on mitigating urban heat island effect: a review. *Int J Environ Sustain,* 9**,** 119-30.
SHUNLIN, L., XIAOTONG, Z., TAO, H., JIE, C. & DONGDONG, W. 2013. Remote Sensing of the Land Surface Radiation Budget. *Remote Sensing of Energy Fluxes and Soil Moisture Content.* CRC Press.

SISMANIDIS, P., KERAMITSOGLOU, I. & KIRANOUDIS, C. T. A satellite-based system for continuous monitoring of Surface Urban Heat Islands. *Urban Climate*.

SMOLIAK, B. V., SNYDER, P. K., TWINE, T. E., MYKLEBY, P. M. & HERTEL, W. F. 2015. Dense Network Observations of the Twin Cities Canopy-Layer Urban Heat Island*. *Journal of Applied Meteorology and Climatology,* 54**,** 1899-1917.

SOBRINO, J. A., JIMÉNEZ-MUÑOZ, J. C. & PAOLINI, L. 2004. Land surface temperature retrieval from LANDSAT TM 5. *Remote Sensing of Environment,* 90**,** 434-440.

SOBRINO, J. A., JIMÉNEZ-MUÑOZ, J. C., SÒRIA, G., ROMAGUERA, M., GUANTER, L., MORENO, J., PLAZA, A. & MARTÍNEZ, P. 2008. Land surface emissivity retrieval from different VNIR and TIR sensors. *IEEE Transactions on Geoscience and Remote Sensing,* 46**,** 316-327.

SOBRINO, J. A., OLTRA-CARRIÓ, R., SÒRIA, G., JIMÉNEZ-MUÑOZ, J. C., FRANCH, B., HIDALGO, V., MATTAR, C., JULIEN, Y., CUENCA, J. & ROMAGUERA, M. 2013. Evaluation of the surface urban heat island effect in the city of Madrid by thermal remote sensing. *International journal of remote sensing,* 34**,** 3177-3192.

SOLWEIG-TEAM. 2015. *SOLWEIG: A climate design tool* [Online]. Sweden: Department of Earth Sciences Available: http://gvc.gu.se/digitalAssets/1536/1536051_solweig_manual.pdf [Accessed 20/7/2015 2016].

SOUZA, L. C. L., RODRIGUES, D. S. & MENDES, J. F. 2003. Sky view factors estimation using a 3d-gis extension. *Eighth International IBPSA Conference* Eindhoven, Netherlands Building Simulation.

SRIVANIT, M. & HOKAO, K. 2012. Thermal Infrared Remote Sensing for Urban Climate and Environmental Studies: An Application for the City of Bangkok, Thailand.

STEADMAN, R. G. 1971. Indices of Windchill of Clothed Persons. *Journal of Applied Meteorology,* 10**,** 674-683.

STEADMAN, R. G. 1979. The Assessment of Sultriness. Part I: A Temperature-Humidity Index Based on Human Physiology and Clothing Science. *Journal of Applied Meteorology,* 18**,** 861-873.

STEIN, P. 2001. *Global Warming: A Threat to Our Future*, The Rosen Publishing Group.

STEINECKE, K. 1999. Urban climatological studies in the Reykjavık subarctic environment, Iceland. *Atmospheric environment,* 33**,** 4157-4162.

STEWART, I. 2007. Landscape representation and the urban-rural dichotomy in empirical urban heat island literature, 1950–2006. *Acta Climatologica et Chorologica,* 40**,** 111-121.

STEWART, I. & OKE, T. Newly developed "thermal climate zones" for defining and measuring urban heat island magnitude in the canopy layer. Eighth Symposium on Urban Environment, Phoenix, AZ, 2009.

STREUTKER, D. R. 2002. A remote sensing study of the urban heat island of Houston, Texas. *International Journal of Remote Sensing,* 23**,** 2595-2608.

SUNG, C. Y. 2013. Mitigating surface urban heat island by a tree protection policy: A case study of The Woodland, Texas, USA. *Urban Forestry & Urban Greening,* 12**,** 474-480.

TAN, J., YANG, L., GRIMMOND, C., SHI, J., GU, W., CHANG, Y., HU, P., SUN, J., AO, X. & HAN, Z. 2015. Urban integrated meteorological observations: practice and experience in Shanghai, China. *Bulletin of the American Meteorological Society,* 96**,** 85-102.

THE COMPLETE UNIVERSITY GUIDE. 2016. *Top Reasons to Attend University in Birmingham*
[Online]. UK: Birmingham Tourism Centre and Ticket Shop Available: http://www.thecompleteuniversityguide.co.uk/cities/birmingham/ [Accessed 20-10-2016 2016].

THORSSON, S., LINDBERG, F., ELIASSON, I. & HOLMER, B. 2007. Different methods for estimating the mean radiant temperature in an outdoor urban setting. *International Journal of Climatology,* 27**,** 1983-1993.
THORSSON, S., ROCKLÖV, J., KONARSKA, J., LINDBERG, F., HOLMER, B., DOUSSET, B. & RAYNER, D. 2014. Mean radiant temperature–A predictor of heat related mortality. *Urban Climate,* 10**,** 332-345.
TIME AND DATE. 2013. *Sun in Birmingham* [Online]. website. Available: www.timeanddate.com/sun/uk/birmingham?mont=9&year=2013 [Accessed 12/8/2015 2015].
TODHUNTER, P. E. 1996. Environmental indices for the Twin Cities Metropolitan Area (Minnesota, USA) urban heat island - 1989. *Climate Research,* 06**,** 59-69.
TOMLINSON, C., PRIETO-LOPEZ, T., BASSETT, R., CHAPMAN, L., CAI, X. M., THORNES, J. & BAKER, C. 2013. Showcasing urban heat island work in Birmingham–measuring, monitoring, modelling and more. *Weather,* 68**,** 44-49.
TOMLINSON, C. J., CHAPMAN, L., THORNES, J. E. & BAKER, C. J. 2012. Derivation of Birmingham's summer surface urban heat island from MODIS satellite images. *International Journal of Climatology,* 32**,** 214-224.
TRAN, H., UCHIHAMA, D., OCHI, S. & YASUOKA, Y. 2006. Assessment with satellite data of the urban heat island effects in Asian mega cities. *International Journal of Applied Earth Observation and Geoinformation,* 8**,** 34-48.
TYSON, P. D., GARSTANG, M., EMMITT, G. D. & STUDIES, U. O. T. W. D. O. G. A. E. 1973. *The structure of heat islands*, University of the Witwatersrand, Dept. of Geography and Environmental Studies.
UK ENVIRONEMNT AGENCY 2014. TABI Thermal Airborne Imagery *In:* GEOMATICS, N. O. (ed.). Bath, UK: ENVIRONMENT AGENCY
UK ENVIRONMENT AGENCY 2014. Special Licence – Non-Commercial *In:* TEAM, A. D. (ed.). Bath, UK: Geomatics, National Operations.
UN. 2015. *Framework Convention on Climate Change: Mitigation* [Online]. Paris: United Nations
Available: http://unfccc.int/focus/mitigation/items/7169.php [Accessed 7/2/2016.
UNWIN, D. J. 1980. THE SYNOPTIC CLIMATOLOGY OF BIRMINGHAM'S URBAN HEAT ISLAND, 1965–74. *Weather,* 35**,** 43-50.
USDA FOREST SERVICE. 2007. *i-Tree Software, Tools for assessing and managing community forests* [Online]. Washington DC: US Department of Agriculture (USDA) Forest Service. Available: https://www.itreetools.org/ [Accessed 16/2/2016 2016].
USGS. 2013. *Landsat Project Description* [Online]. USA: U.S. Department of the Interior. Available: http://landsat.usgs.gov/about_project_descriptions.php [Accessed 1June 2014].
USGS 2016a. EARTH RESOURCES OBSERVATION AND SCIENCE (EROS) CENTER SCIENCE PROCESSING ARCHITECTURE (ESPA) ON DEMAND INTERFACE. Department of the Interior.
USGS 2016b. LANDSAT 4-7 CLIMATE DATA RECORD (CDR) SURFACE REFLECTANCE. Department of the Interior.
USGS. 2016c. *Landsat Higher Level Science Data Products*
[Online]. U.S. Department of the Interior Available: http://landsat.usgs.gov/CDR_ECV.php [Accessed 20-1-2016 2016].
USGS 2016d. LANDSAT SURFACE REFLECTANCE-DERIVED SPECTRAL INDICES Department of the Interior.
USGS. 2016e. *Water properties: Temperature* [Online]. U.S.: U.S. Department of the Interior. Available: http://water.usgs.gov/edu/temperature.html [Accessed 15-10-2016 2016].
USGS. 2017a. *LANDSAT 4-7 SURFACE REFLECTANCE (LEDAPS) PRODUCT* [Online]. USA: USGS. Available: https://landsat.usgs.gov/sites/default/files/documents/ledaps_product_guide.pdf [Accessed 1/5/2017 2017].

USGS. 2017b. *LANDSAT 8 SURFACE REFLECTANCE CODE (LASRC) PRODUCT* [Online]. USA: USGS. Available: https://landsat.usgs.gov/sites/default/files/documents/lasrc_product_guide.pdf [Accessed 2/5//2017 2017].
VANDERBEI, R. J. 2008. *Linear programming : foundations and extensions,* New York, Springer.
VERMOTE, E., JUSTICE, C., CLAVERIE, M. & FRANCH, B. 2016. Preliminary analysis of the performance of the Landsat 8/OLI land surface reflectance product. *Remote Sensing of Environment,* 185**,** 46-56.
VIRK, G., MYLONA, A., MAVROGIANNI, A. & DAVIES, M. 2015. Using the new CIBSE design summer years to assess overheating in London: Effect of the urban heat island on design. *Building Services Engineering Research and Technology,* 36**,** 115-128.
VOOGT, J. A. 2004. Urban heat islands: hotter cities.
WALIKEWITZ, N., JÄNICKE, B., LANGNER, M., MEIER, F. & ENDLICHER, W. 2015. The difference between the mean radiant temperature and the air temperature within indoor environments: A case study during summer conditions. *Building and Environment,* 84**,** 151-161.
WANG, J., ZHAN, Q. & GUO, H. 2015. The Morphology, Dynamics and Potential Hotspots of Land Surface Temperature at a Local Scale in Urban Areas. *Remote Sensing,* 8**,** 18.
WANG, Z.-H., BOU-ZEID, E. & SMITH, J. 2011. A Spatially-Analytical Scheme for Surface Temperatures and Conductive Heat Fluxes in Urban Canopy Models. *Boundary-Layer Meteorology,* 138**,** 171-193.
WATKINS, R., PALMER, J., KOLOKOTRONI, M. & LITTLEFAIR, P. 2002. The balance of the annual heating and cooling demand within the London urban heat island. *Building Services Engineering Research and Technology,* 23**,** 207-213.
WEATHER UNDERGROUND. 2016. *Weather History for KQTZ* [Online]. The Weather Company, LLC. Available: https://www.wunderground.com/history/airport/KQTZ/2015/11/18/DailyHistory.html?req_city=&req_state=&req_statename=&reqdb.zip=&reqdb.magic=&reqdb.wmo= [Accessed 24/09/2016 2016].
WEBB, B. 2016. The use of urban climatology in local climate change strategies: a comparative perspective. *International Planning Studies***,** 1-17.
WENG, Q. 2012. Remote sensing of impervious surfaces in the urban areas: Requirements, methods, and trends. *Remote Sensing of Environment,* 117**,** 34-49.
WENG, Q. & FU, P. 2014. Modeling annual parameters of clear-sky land surface temperature variations and evaluating the impact of cloud cover using time series of Landsat TIR data. *Remote Sensing of Environment,* 140**,** 267-278.
WHO 2008. Integrated weather, climate, hydrology and related environment services for sustainable cities. Switzerland: World Meteorological Organization.
WONG, P. P.-Y., LAI, P.-C., LOW, C.-T., CHEN, S. & HART, M. 2016. The impact of environmental and human factors on urban heat and microclimate variability. *Building and Environment,* 95**,** 199-208.
WU, C.-D., LUNG, S.-C. C. & JAN, J.-F. 2013. Development of a 3-D urbanization index using digital terrain models for surface urban heat island effects. *ISPRS Journal of Photogrammetry and Remote Sensing,* 81**,** 1-11.
XU, Z. & COORS, V. 2012. Combining system dynamics model, GIS and 3D visualization in sustainability assessment of urban residential development. *Building and Environment,* 47**,** 272-287.
YAMATO, H., TAKAHASHI, H. & MIKAMI, T. New urban heat island monitoring system in Tokyo metropolis. Proceeding of the 7th International Conference on Urban Climate, June, 2009.
YAN, H., FAN, S., GUO, C., HU, J. & DONG, L. 2014. Quantifying the impact of land cover composition on intra-Urban air temperature variations at a mid-latitude city. *Plos one,* 9**,** e102124.

YANG, P., REN, G. & LIU, W. 2013. Spatial and temporal characteristics of Beijing urban heat island intensity. *Journal of Applied Meteorology and Climatology,* 52**,** 1803-1816.
YANG, X. 2011. *Urban remote sensing : monitoring, synthesis and modeling in the urban environment / [editor] Xiaojun Yang*, Wiley-Blackwell.
YOW, D. M. & CARBONE, G. J. 2006. The urban heat island and local temperature variations in Orlando, Florida. *southeastern geographer,* 46**,** 297-321.
YU JOE, H., HASHEM, A. & HAIDER, T. 1990. The wind-shielding and shading effects of trees on residential heating and cooling requirements. *Proceedings of the ASHRAE Winter Conference.*
YUAN, F. & BAUER, M. E. 2007. Comparison of impervious surface area and normalized difference vegetation index as indicators of surface urban heat island effects in Landsat imagery. *Remote Sensing of Environment,* 106**,** 375-386.
ZHANG, F. 2015. *The impacts of temperature and the urban heat island on mortality in the West Midlands and greater London.* University of Birmingham.
ZHANG, H., QI, Z.-F., YE, X.-Y., CAI, Y.-B., MA, W.-C. & CHEN, M.-N. 2013. Analysis of land use/land cover change, population shift, and their effects on spatiotemporal patterns of urban heat islands in metropolitan Shanghai, China. *Applied Geography,* 44**,** 121-133.
ZHANG, P., IMHOFF, M. L., WOLFE, R. E. & BOUNOUA, L. 2010. Characterizing urban heat islands of global settlements using MODIS and nighttime lights products. *Canadian Journal of Remote Sensing,* 36**,** 185-196.
ZHANG, X. & LIANG, R.-F. 2012. Studies of the Thermal Radiation Characteristics of Urban Typical Surface Features. *Spectroscopy and Spectral Analysis,* 32**,** 92-95.
ZHANG, Y., LI, Z. & LI, J. 2014. Comparisons of emissivity observations from satellites and the ground at the CRCS Dunhuang Gobi site. *Journal of Geophysical Research: Atmospheres,* 119.
ZHAO, S., ZHOU, D. & LIU, S. 2016. Data concurrency is required for estimating urban heat island intensity. *Environmental Pollution,* 208, Part A**,** 118-124.
ZHOU, D., ZHANG, L., HAO, L., SUN, G., LIU, Y. & ZHU, C. 2015. Spatiotemporal trends of urban heat island effect along the urban development intensity gradient in China. *Sci Total Environ,* 544**,** 617-626.

Appendices

Appendix A. Landsat and ASTER images of Baghdad, London, and Birmingham

Table A. 1: Baghdad's Landsat and ASTER raw data used to derive the LST and land cover indices.

Satellite/Sensor	Date	Time (GMT)	Cloud Cover %	Path/ Row	Image Quality	Spatial Resolution Multispectral/ Thermal
Landsat 5/ TM	08/09/2000	07:11	0	168/37	7	30 m/120 m
Landsat 5/ TM	01/10/2000	07:18	0	169/37	9	30 m/120 m
Landsat 7/ ETM+	02/10/2000	07:24	0	168/37	9	30 m/60 m
Landsat 7/ ETM+	25/10/2000	07:30	0.74	169/37	9	30 m/60 m
Landsat 7/ ETM+	02/04/2003	07:22	0		9	30 m/60 m
Landsat 5/ TM	14/07/2006	07:33	0	169/37	7	30 m/60 m
Landsat 7/ ETM+	08/03/2003	07:28	0	169/37	9	30 m/60 m
Landsat 5/ TM	14/06/2006	07:33	0	169/37	7	30 m/120 m
Landsat 8/ OLI & TIRS	20/05/2015	07:38	0.01	169/37	9	30 m/100 m
Landsat 7/ ETM+	21/05/2015	07:33	0	168/37	9	30 m/60 m
Landsat 7/ ETM+	08/07/2001	07:28	0	169/37	9	30 m/60 m
Landsat 7/ ETM+	22/04/2002	07:28	1.1	169/37	9	30 m/60 m
Landsat 7/ ETM+	15/10/2002	07:27	0	169/37	9	30 m/60 m
Landsat 7/ ETM+	22/03/2014	07:36	0	169/37	9	30 m/60 m
Landsat 7/ ETM+	20/11/2015	07:40	0.8	169/37	9	30 m/60 m
Landsat 7/ ETM+	13/11/2015	07:34	0	168/37	9	30 m/60 m
Landsat 7/ ETM+	06/04/2002	07:28	9.9	169/37	9	30 m/60 m
Terra/ASTER/TIR	30/09/2005	07:50	0	168/37	-	15,30 m/90 m
Terra/ASTER/TIR	25/09/2003	07:50	0	168/37	-	15,30 m/90 m
Terra/ASTER/TIR	20/4/2002	19:12	1	34/207	-	15,30 m/90 m
Terra/ASTER/TIR	13/10/2002	19:11	1	34/207	-	15,30 m/90 m
Terra/ASTER/TIR	30/9/2003	19:10	1	34/207	-	15,30 m/90 m
Terra/ASTER/TIR	03/12/2003	19:11	1	34/207	-	15,30 m/90 m
Terra/ASTER/TIR	05/10/2005	19:09	7	34/207	-	15,30 m/90 m
Terra/ASTER/TIR	18/11/2015	19:11	0	34/207	-	15,30 m/90 m

Table A. 2: London's Landsat and ASTER raw data used to derive the LST and land cover indices.

Satellite/Sensor	Date	Time (GMT)	Cloud Cover %	Path/ Row	Quality	Spatial Resolution Multispectral/ Thermal
Landsat 7/ ETM+	07/04/2000	10:51	2	202/24	9	30 m/60 m
Landsat 7/ ETM+	19/06/2000	10:44	0	201/24	9	30 m/60 m
Landsat 7/ ETM+	12/05/2001	10:48	0	202/24	9	30 m/60 m
Landsat 7/ ETM+	28/03/2002	10:47	0	202/24	9	30 m/60 m
Landsat 7/ ETM+	16/04/2003	10:47	0	202/24	9	30 m/60 m
Landsat 5/ TM	24/09/2003	10.30	0	201/24	9	30 m/120 m
Landsat 5/ TM	28/08/2005	10:40	10	201/24	9	30 m/120 m
Landsat 7/ ETM+	10/05/2006	10:48	2	202/24	9	30 m/60 m
Landsat 5/ TM	12/06/2006	10:45	10	201/24	9	30 m/120 m
Landsat 5/ TM	11/05/2006	10:44	4	201/24	9	30 m/120 m
Landsat 7/ ETM+	02/11/2006	10:48	1	202/24	9	30 m/60 m
Landsat 7/ ETM+	20/09/2008	10:47	1.77	202/24	9	30 m/60 m
Landsat 7/ ETM+	29/09/2011	10:52	0	202/24	9	30 m/60 m
Landsat 5/ TM	30/09/2011	10:40	0	201/24	9	30 m/120 m
Landsat 7/ ETM+	11/11/2012	10:48	0	201/24	9	30 m/60 m
Landsat 7/ ETM+	18/11/2012	10:54	1	202/24	9	30 m/60 m
Landsat 7/ ETM+	20/04/2013	10:48	0	201/24	9	30 m/60 m
Landsat 8/ OLI & TIRS	08/07/2013	11:00	2	202/24	9	30 m/100 m
Landsat 8/ OLI & TIRS	17/07/2013	10:54	11	201/24	9	30 m/100 m
Landsat 8/ OLI & TIRS	01/02/2014	10:59	11	202/24	9	30 m/100 m
Landsat 8/ OLI & TIRS	04/07/2014	10:52	10	201/24	9	30 m/100 m
Landsat 8/ OLI & TIRS	09/04/2015	10:58	4	202/24	9	30 m/100 m
Landsat 8/ OLI & TIRS	27/05/2015	10:57	14	202/24	9	30 m/100 m
Landsat 8/ OLI & TIRS	02/10/2015	10:58	7	202/24	9	30 m/100 m
Terra/ASTER/TIR	23/07/2004	11:15	1	201/24	-	15,30 m/90 m
Terra/ASTER/TIR	26/05/2012	11:15	1	201/24	-	15,30 m/90 m
Terra/ASTER/TIR	12/07/2006	21:43	1	59/220	-	15,30 m/90 m
Terra/ASTER/TIR	19/10/2007	21:44	2	59/220	-	15,30 m/90 m
Terra/ASTER/TIR	12/09/2011	21:43	1	59/220	-	15,30 m/90 m
Terra/ASTER/TIR	09/10/2015	21:44	0	59/220	-	15,30 m/90 m

Table A. 3: Birmingham's Landsat and ASTER raw data used to derive the LST and land cover indices.

Satellite/Sensor	Date	Time (GMT)	Cloud Cover %	Path/ Row	Quality	Spatial Resolution Multispectral/ Thermal
Landsat 7/ ETM+	07/04/2000	10:51	2	202/24(23)	9	30 m/60 m
Landsat 7/ ETM+	12/05/2001	10:48	0	202/24(23)	9	30 m/60 m
Landsat 7/ ETM+	28/03/2002	10:47	0	202/24	9	30 m/60 m
Landsat 7/ ETM+	04/04/2002	10:53	5	203/23	9	30 m/60 m
Landsat 7/ ETM+	11/09/2002	10:52	0	203/24	9	30 m/60 m
Landsat 7/ ETM+	22/03/2003	10:53	0	203/23	9	30 m/60 m
Landsat 7/ ETM+	16/04/2003	10:47	0	202/24(23)	9	30 m/60 m
Landsat 5/ TM	13/07/2003	10:35	0	202/24(23)	9	30 m/120 m
Landsat 7/ ETM+	19/11/2004	10:53	5	203/23	9	30 m/60 m
Landsat 7/ ETM+	10/05/2006	10:48	0	202/24(23)	9	30 m/60 m
Landsat 5/ TM	10/06/2006	10:57	6	203/23	9	30 m/120 m
Landsat 7/ ETM+	20/07/2006	10:53	4	203/23	9	30 m/60 m
Landsat 5/ TM	21/07/2006	10:51	13	202/24(23)	9	30 m/120 m
Landsat 5/ TM	28/07/2006	10:57	9	203/23	9	30 m/120 m
Landsat 7/ ETM+	02/11/2006	10:48	6	202/24(23)	9	30 m/60 m
Landsat 7/ ETM+	18/11/2006	10:48	2	202/24(23)	9	30 m/60 m
Landsat 7/ ETM+	20/09/2008	10:47	12	202/24	9	30 m/60 m
Landsat 7/ ETM+	22/06/2010	10:50	11	202/23	9	30 m/60 m
Landsat 5/ TM	20/10/2010	10:48	2	202/24(23)	9	30 m/120 m
Landsat 5/ TM	30/04/2011	10:48	0	202/24(23)	9	30 m/120 m
Landsat 5/ TM	28/09/2011	10:52	0	203/23	9	30 m/120 m
Landsat 7/ ETM+	29/09/2011	10:52	0	202/24(23)	9	30 m/60 m
Landsat 7/ ETM+	18/11/2012	10:54	1	202/24(23)	9	30 m/60 m
Landsat 8/ OLI & TIRS	18/11/2013	10:59	8	202/24(23)	9	30 m/100 m
Landsat 8/ OLI & TIRS	19/01/2015	10:58	12	202/24	9	30 m/100 m
Landsat 8/ OLI & TIRS	09/04/2015	10:58	2	202/24(23)	9	30 m/100 m
Landsat 8/ OLI & TIRS	08/07/2013	11:00	14	202/24(23)	9	30 m/100 m
Terra/ASTER/TIR	01/06/2009	11:28	0	203/24	-	15,30 m/90 m
Terra/ASTER/TIR	27/09/2011	11:27	0	203/24	-	15,30 m/90 m

Appendix B. Conversion of BT to LST

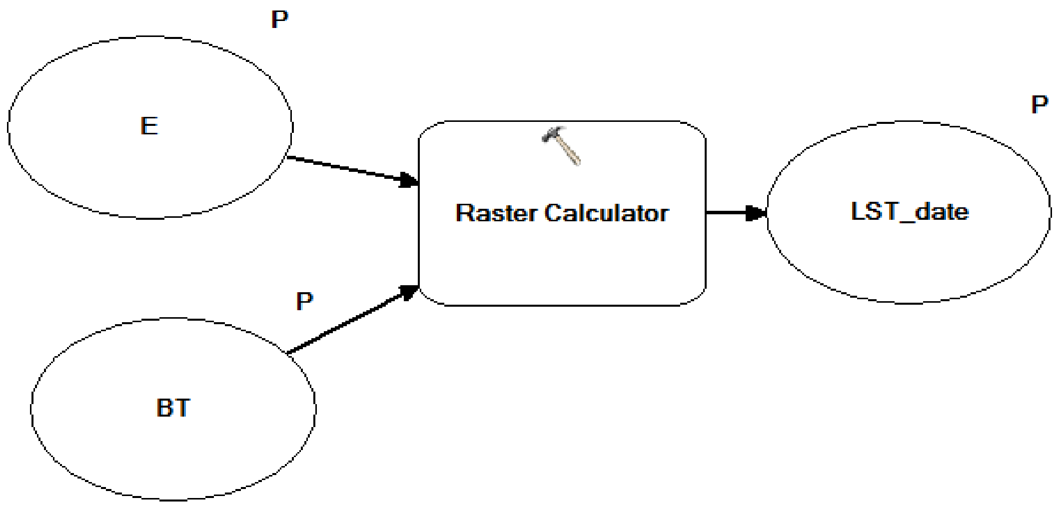

Figure B. 1: ArcGIS model builder flowchart to derive the land surface temperature (LST) from the brightness temperature (BT).

Appendix C. Masking and rescaling of Satellite images

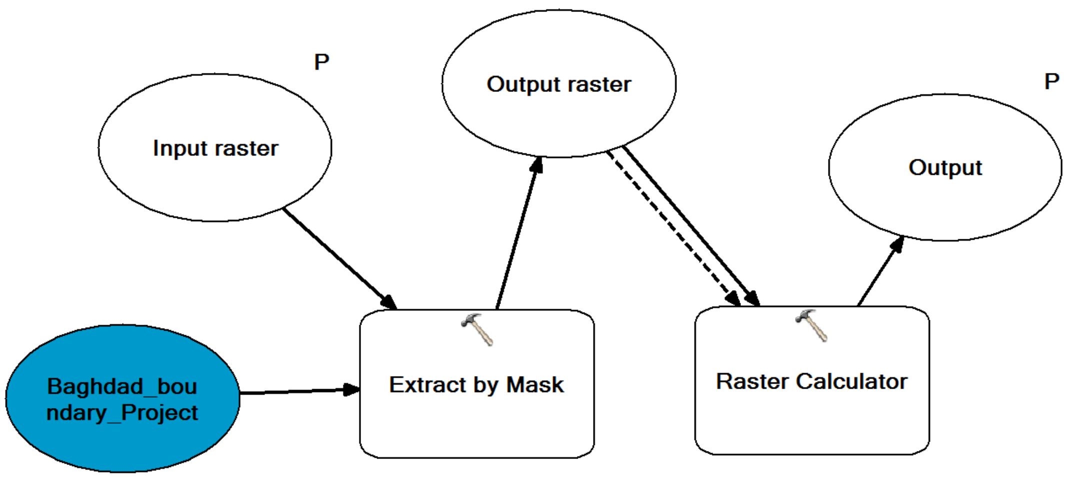

Figure C. 1: ArcGIS model builder flowchart to mask and rescale the satellite images

Appendix D. MATLAB code to extract HiTemp data

```
%Main function frame
clear all;
close all;
clear
clc
%Loop to read all input files for the study peorid
path_asm = 'F:\HiTEMP\raw data\ASM_Data_csv\';
path_wxt = 'F:\HiTEMP\raw data\WXT_Data_csv\';
for week =1:1
time_periods_filename =['time_periodsall.csv'];
fid = fopen(time_periods_filename);
tline = fgets(fid);
i=1;
while ischar(tline)
    %disp(tline)
    if ( tline(1) ~= '#' )
        [a,b,c,d,e,f,g]=strread(tline,'%s %s %s %s %s %s
%s','delimiter',',','emptyvalue',NaN);
        if(i == 1)
            time_periods =
struct('year',a,'month',b,'day_of_month',c,'hour',d,'min',e,'sec',f,'data_length',g);
        else
            time_periods = [time_periods ;
struct('year',a,'month',b,'day_of_month',c,'hour',d,'min',e,'sec',f,'data_length',g)];
        end
        i=i+1;
    end
    tline = fgets(fid);
end
fclose(fid);
mkdir('Output');
current_time = clock;
i = 1;
%Connection to the secondary function (run_test_day)
while (i <= size(time_periods,1))
    current =  time_periods(i,:);
    results_tmp =
run_test_day(str2num(current.year),str2num(current.month),str2num(current.day_of_month),str2
num(current.hour),str2num(current.min),str2num(current.sec),str2num(current.data_length),pat
h_asm, path_wxt  ) ;
        results_tmp = [];
    i = i + 1;
end
fclose ('all');
end


%Secondary function (run_test_day)
function [results ] = run_test_day(
year,month,day_of_month,hour,min,sec,data_length,path_asm, path_wxt )
```

```
results =[];
pwd;
%Open files
fid_output_names = fopen([ num2str(year) '_' num2str(month) '_'  num2str(day_of_month) '_'
num2str(hour) '_' num2str(min) '.txt'  ], 'w');
fprintf(fid_output_names,[ 'station' ',' 'latitude' ',' 'longitude' ',' 'elevation' ','
'air_temp' '\n' ]);
i = 1;
loop = 0;
[ndata, text, alldata] = xlsread('ASM_Location_Elevation.xlsx',
'BUCL_WIRELESS_TEMPERATURE_SENSO');
[ndata_w, text_w, alldata_w] = xlsread('WXT_Location_Elevation_Metadata.xlsx',
'BUCLmetadata');
station_name_without_S = strrep(alldata(2:end,2), 'S', '');
no_station = size(station_name_without_S);
%Loop to read all the stations
while( i <= no_station(1,1))
    station_number = cell2mat(station_name_without_S(i,1));
    station_file_path = [path_asm 'S' num2str(station_number) '\' num2str(year) '\S'
num2str(station_number) '_MinRes_QAQC01_Data_' num2str(year) '-' num2str(month,'%02d') '-'
num2str(day_of_month,'%02d') '.csv' ];
%Get ASM (Aginova Sentinel Micro stations) values using another function
    [ results_point ] = get_asm_values( year,month,day_of_month,hour,min ,station_file_path
);
    if isnumeric(results_point)
    loop = loop+1;
        lat = alldata{i+1,4};
        long = alldata{i+1,5};
        h = alldata{i+1,6};
        %fprintf(fid_output_names,[ 'S' num2str(i,'%03d') '\t' num2str(lat) '\t'
num2str(long) '\t' num2str(h) num2str(results_point) '\n' ]);
        results(loop).station = ['S' num2str(station_number,'%03d')];
        results(loop).lat = lat;
        results(loop).long = long;
        results(loop).h = h;
        results(loop).temp = results_point;
    else
    end
    i = i + 1;
end
i=1;
%for WXT
station_name_without_W = strrep(alldata_w(2:end,2), 'W', '');
no_station_W = size(station_name_without_W);
while( i <= no_station_W(1,1))
%Convert files format to CSV
    station_number_W = cell2mat(station_name_without_W(i,1));
    station_file_path_W = [path_wxt 'W' num2str(station_number_W) '\' num2str(year)
'\MinRes_QAQC02_Data\W' num2str(station_number_W) '_MinRes_QAQC02_Data_' num2str(year) '-'
num2str(month,'%02d') '-' num2str(day_of_month,'%02d') '.csv' ];
```

```
    flag_W_path = [path_wxt 'W' num2str(station_number_W) '\' num2str(year)
'\MinRes_QAQC02_NumericFlags\W' num2str(station_number_W) '_MinRes_QAQC02_NumericFlags_'
num2str(year) '-' num2str(month,'%02d') '-' num2str(day_of_month,'%02d') '.csv' ];
%Get WXT (Automatic Weather Stations ) values using another function
    [ results_point ] = get_wxt_values( year,month,day_of_month,hour,min
,station_file_path_W,flag_W_path );
    if (results_point ~= 1000)
    loop = loop+1;
        lat = alldata_w{i+1,9};
        long = alldata_w{i+1,10};
        h = alldata_w{i+1,11};
%Output files preparation
        results(loop).station = ['W' num2str(station_number_W,'%03d')];
        results(loop).lat = lat;
        results(loop).long = long;
        results(loop).h = h;
        results(loop).temp = results_point;
    else
    end
    i = i + 1 ;
end
%Output print
for printing = 1:loop
          fprintf(fid_output_names,[ results(printing).station ',']);
          fprintf(fid_output_names,[ num2str(results(printing).lat) ',']);
          fprintf(fid_output_names,[ num2str(results(printing).long)  ',']);
          fprintf(fid_output_names,[ num2str(results(printing).h) ',']);
          fprintf(fid_output_names,[ num2str(results(printing).temp)  '\n']);
end
%Move outputs to another path
fclose(fid_output_names);
fid_output_names_before_moving = [num2str(year) '_' num2str(month) '_'
num2str(day_of_month) '_' num2str(hour) '_' num2str(min) '.txt'];
moving_file_name_path = ['Output\' num2str(year) '_' num2str(month) '_'
num2str(day_of_month) '_' num2str(hour) '_' num2str(min) '.txt' ];
system(['move ' fid_output_names_before_moving ' ' moving_file_name_path  ]);


end



%Get WXT (Automatic Weather Stations) values function
  function [ out_value ] = get_wxt_values( year,month,day_of_month,hour,min
,station_file_path, flag_W_path )
fid = fopen(station_file_path);
fid_flag = fopen(flag_W_path);
if fid <0
   % if fid_flag < 0
    out_value = 1000;
    %end
```

```
else
i=1;
tline = fgets(fid);
tline_flag = fgets(fid_flag);
j = 1;
available = 2;
bad = 1;
tline = fgets(fid);
tline_flag = fgets(fid_flag);
tline = fgets(fid);
tline_flag = fgets(fid_flag);
tline = fgets(fid);
tline_flag = fgets(fid_flag);
%Define the columns of the files
while (ischar(tline))&& (available ==2) && ischar(tline_flag)
    [year_file,month_file,day_file,hour_file,min_file,value_file,
r1,r2,r3,r4,r5,r6,r7,r8,r9,r10,r11,r12] = strread(tline,'%f %f %f %f %f %f %f %f %f %f %f %f
%f %f %f %f %f %f','delimiter',',','emptyvalue',NaN);
[year_file_w,month_file_w,day_file_w,hour_file_w,min_file_w,TAIR,TDEW,RELH,PRES,PMSL,SRAD,RT
OT,RRAT,WSPD,WDIR,WMAX,HAIL,flag] = strread(tline_flag,'%f %f %f %f %f %f %f %f %f %f %f %f
%f %f %f %f %f %f','delimiter',',','emptyvalue',NaN);
%Clean the data based on the quality
         if(hour_file == hour)
             if(min_file == min)
                 available = 1;
                 if (flag == 9) || (flag == 2)
                     %the value is bad
                     bad = 1;
                 else
                     %the value is trusted
                     bad = 0;
                     value = value_file;
                 end
             end
         end
      tline = fgets(fid);
      tline_flag = fgets(fid_flag);
      clear year_file month_file day_file hour_file min_file value_file year_file_w
month_file_w day_file_w hour_file_w min_file_w value_file_ flag
end
if (bad == 0);
out_value = value;
else
    out_value = 1000;
end
fclose(fid);
end
end
```

```
%ASM (Aginova Sentinel Micro stations) values function
function [ out_value ] = get_asm_values( year,month,day_of_month,hour,min ,station_file_path
)
fid=fopen(station_file_path);
if fid <0
    out_value = 'bad';
else
i=1;
tline = fgets(fid);
j = 1;
available = 2;
bad = 1;
tline = fgets(fid);
     tline = fgets(fid);
     tline = fgets(fid);
%Define the columns of the files
while (ischar(tline))&& (available ==2)
         [year_file,month_file,day_file,hour_file,min_file,value_file, flag] =
strread(tline,'%f %f %f %f %f %f %f','delimiter',',','emptyvalue',NaN);
%Clean the data based on the quality
         if(hour_file == hour)
             if(min_file == min)
                 available = 1;
                 if (flag == 9) || (flag == 2)
                     %the value is bad
                     bad = 1;
                 else
                     %the value is trusted
                     bad = 0;
                     value = value_file;
                 end

             end
         end
      tline = fgets(fid);
      clear year_file month_file day_file hour_file min_file value_file flag
end
if (bad == 0);
out_value = value;
else
    out_value = 'bad';
end
fclose(fid);
end

end
```

Appendix E. Meteorological inputs of the six tiles

Table E. 1: Tile 0 meteorological inputs to model the T_{mrt} for the four days using UMEP plugin in QGIS.

01/12/2013							05/09/2013						
HOUR	**TAIR**	**RELH**	**PRES**	**SRAD**	**WSPD**	**WDIR**	**HOUR**	**TAIR**	**RELH**	**PRES**	**SRAD**	**WSPD**	**WDIR**
0	5.88	81.56	101.20	0.00	0.79	254.85	**0**	15.41	72.66	99.55	0.00	0.48	167.66
1	6.30	81.10	101.18	0.00	0.99	261.73	**1**	14.25	76.77	99.50	0.00	0.54	175.90
2	6.99	80.05	101.19	0.00	1.23	287.99	**2**	13.05	82.20	99.44	0.00	0.43	174.63
3	7.38	78.08	101.19	0.00	1.34	288.56	**3**	12.45	85.45	99.38	0.00	0.32	182.86
4	7.39	77.89	101.18	0.00	1.37	298.41	**4**	11.41	88.47	99.34	0.00	0.30	216.84
5	7.37	77.35	101.18	0.00	1.54	298.47	**5**	10.74	91.46	99.33	7.78	0.30	218.32
6	7.27	76.21	101.19	0.00	1.45	290.50	**6**	12.46	87.73	99.34	80.49	0.57	231.54
7	7.31	76.09	101.24	0.48	1.43	297.38	**7**	16.28	73.85	99.36	189.39	0.82	247.65
8	7.48	75.10	101.31	12.29	0.94	281.92	**8**	17.80	67.66	99.36	401.77	1.42	287.51
9	7.98	74.16	101.36	36.66	0.55	268.90	**9**	19.03	63.30	99.35	574.42	1.60	279.81
10	8.39	74.04	101.40	41.78	0.77	289.32	**10**	19.95	60.18	99.30	677.28	1.34	252.01
11	8.49	77.43	101.39	51.35	1.15	292.77	**11**	20.36	58.59	99.27	685.79	1.38	277.10
12	8.66	77.45	101.37	56.39	1.12	281.96	**12**	20.65	57.12	99.25	561.78	1.53	280.69
13	9.14	76.20	101.37	84.24	0.85	257.89	**13**	20.87	53.50	99.22	622.75	1.79	287.92
14	9.21	74.64	101.37	36.92	0.62	199.13	**14**	21.28	45.81	99.17	493.14	1.57	286.74
15	8.79	75.76	101.40	15.01	0.43	196.30	**15**	21.41	45.50	99.14	385.81	1.80	278.98
16	7.13	81.38	101.42	0.90	0.29	171.80	**16**	20.49	49.52	99.13	176.25	1.49	295.75
17	5.74	87.13	101.47	0.00	0.23	197.95	**17**	19.07	57.10	99.12	72.84	1.78	300.83
18	4.78	89.67	101.52	0.00	0.21	230.88	**18**	16.50	69.98	99.15	9.59	2.06	310.63
19	4.47	91.16	101.57	0.00	0.27	141.29	**19**	14.29	77.07	99.20	0.04	1.99	318.74
20	4.13	91.91	101.59	0.00	0.31	173.70	**20**	13.40	76.77	99.19	0.00	2.08	310.60
21	4.75	92.39	101.61	0.00	0.44	117.61	**21**	13.11	74.87	99.18	0.00	1.91	318.66
22	5.25	91.65	101.64	0.00	0.31	205.45	**22**	12.95	73.27	99.16	0.00	1.73	307.53
23	5.45	91.21	101.66	0.00	0.27	191.71	**23**	12.94	72.98	99.13	0.00	1.66	302.38
06/07/2013							18/04/2014						
HOUR	**TAIR**	**RELH**	**PRES**	**SRAD**	**WSPD**	**WDIR**	**HOUR**	**TAIR**	**RELH**	**PRES**	**SRAD**	**WSPD**	**WDIR**
0	15.36	78.55	100.84	0.00	0.52	143.44	**0**	5.90	82.21	99.92	0.00	1.78	307.88
1	15.13	82.77	100.82	0.00	0.90	141.94	**1**	5.41	82.05	99.94	0.00	1.39	295.16
2	14.77	84.87	100.82	0.00	0.92	135.82	**2**	5.00	83.23	99.96	0.00	1.34	294.04
3	14.45	84.65	100.82	0.86	0.78	141.75	**3**	4.51	85.21	99.97	0.00	1.25	293.89
4	14.15	84.82	100.84	21.75	0.73	146.22	**4**	4.00	85.09	99.99	0.40	0.86	294.29
5	15.15	80.72	100.86	100.12	0.78	141.20	**5**	3.55	85.44	100.03	24.10	0.48	223.79
6	16.56	75.04	100.87	214.40	1.00	133.82	**6**	5.01	77.77	100.08	109.96	0.91	192.59
7	18.45	65.54	100.88	401.54	1.01	152.20	**7**	6.20	65.06	100.13	246.95	1.46	73.67
8	19.55	62.06	100.89	609.90	1.07	158.54	**8**	7.02	56.25	100.17	379.17	1.56	64.82
9	19.97	61.19	100.89	635.70	1.38	141.69	**9**	7.84	52.41	100.19	494.34	1.68	114.41
10	20.71	58.68	100.88	720.30	1.35	140.89	**10**	8.72	50.41	100.18	575.48	1.55	161.44
11	21.94	53.79	100.87	800.72	1.38	151.30	**11**	9.73	46.24	100.17	662.88	1.92	192.33
12	22.62	51.57	100.84	835.04	1.54	145.73	**12**	10.57	40.20	100.17	716.63	1.91	157.75
13	23.38	48.40	100.81	844.45	1.26	146.69	**13**	11.04	38.38	100.14	702.77	1.77	125.40
14	24.06	45.14	100.79	755.19	1.16	155.33	**14**	11.30	38.44	100.12	618.82	1.77	117.47
15	24.60	42.69	100.78	643.58	0.98	176.17	**15**	11.55	38.70	100.09	507.26	1.65	111.20
16	24.62	41.66	100.78	514.84	0.94	180.81	**16**	11.34	40.30	100.05	355.88	1.72	83.06
17	24.46	41.75	100.78	280.25	0.85	195.43	**17**	10.93	42.51	100.04	191.98	1.72	69.10
18	23.72	43.85	100.81	107.23	0.70	203.80	**18**	10.08	46.52	100.04	42.44	1.55	72.96
19	22.76	47.82	100.84	43.60	0.45	205.74	**19**	8.99	50.37	100.06	1.98	1.02	88.49
20	20.70	54.61	100.89	5.34	0.25	220.66	**20**	7.67	56.59	100.09	0.00	0.74	119.20
21	19.33	69.19	100.96	0.06	0.99	279.39	**21**	6.54	63.86	100.08	0.00	0.63	141.93
22	17.75	76.04	101.01	0.00	1.18	280.66	**22**	5.65	68.99	100.07	0.00	0.74	151.97
23	16.63	77.48	101.04	0.00	1.11	284.22	**23**	4.63	74.39	100.07	0.00	0.58	152.79

Table E. 2: Tile 1 meteorological inputs to model the T_{mrt} for the four days using UMEP plugin in QGIS.

01/12/2013							05/09/2013						
HOUR	**TAIR**	**RELH**	**PRES**	**SRAD**	**WSPD**	**WDIR**	**HOUR**	**TAIR**	**RELH**	**PRES**	**SRAD**	**WSPD**	**WDIR**
0	6.24	80.93	101.43	0.00	1.00	249.89	**0**	15.52	71.86	99.85	0.00	0.30	173.57
1	6.81	80.03	101.41	0.00	1.22	259.06	**1**	14.28	75.87	99.80	0.00	0.24	172.84
2	7.43	78.60	101.42	0.00	1.57	295.55	**2**	13.31	79.25	99.74	0.00	0.23	186.89
3	7.64	77.24	101.42	0.00	1.26	284.36	**3**	12.47	82.41	99.68	0.00	0.30	197.90
4	7.65	77.33	101.41	0.00	1.30	293.75	**4**	11.97	83.81	99.64	0.00	0.31	198.84
5	7.58	76.82	101.41	0.00	1.37	290.28	**5**	11.57	84.96	99.63	8.08	0.35	219.27
6	7.42	75.92	101.41	0.00	1.69	300.94	**6**	12.86	80.64	99.63	70.35	0.53	228.95
7	7.46	75.92	101.48	0.84	1.09	286.51	**7**	16.02	72.84	99.65	221.57	0.56	214.34
8	7.70	75.10	101.55	15.05	0.78	262.10	**8**	18.95	62.77	99.65	397.46	1.09	264.76
9	8.10	74.02	101.59	48.54	0.75	273.57	**9**	20.13	58.70	99.64	561.16	1.06	229.78
10	8.71	73.13	101.62	62.86	1.05	294.90	**10**	21.17	54.58	99.59	707.69	1.15	208.47
11	8.74	76.60	101.61	68.85	1.09	287.81	**11**	21.64	54.49	99.56	656.94	1.22	213.49
12	8.81	77.79	101.60	91.26	0.90	248.89	**12**	21.81	54.00	99.53	545.66	1.26	177.22
13	9.34	74.54	101.60	82.58	1.14	90.49	**13**	21.80	52.51	99.51	577.75	1.27	212.72
14	9.46	72.70	101.60	56.50	1.03	45.25	**14**	21.75	46.69	99.47	369.13	1.17	236.67
15	8.94	73.06	101.63	20.09	0.80	45.51	**15**	22.20	42.41	99.43	482.42	1.26	178.52
16	7.26	80.52	101.66	1.67	0.35	94.18	**16**	21.43	46.06	99.42	171.69	1.21	228.47
17	5.75	86.59	101.70	0.00	0.26	133.18	**17**	19.92	53.80	99.41	71.16	1.46	154.11
18	5.04	89.41	101.76	0.00	0.30	123.62	**18**	17.68	64.92	99.44	12.45	1.30	240.26
19	4.79	90.75	101.81	0.00	0.42	85.27	**19**	15.17	73.31	99.49	0.06	1.48	278.77
20	5.15	90.01	101.83	0.00	0.61	86.46	**20**	14.14	74.32	99.49	0.00	1.29	252.23
21	5.63	88.91	101.85	0.00	0.77	75.62	**21**	13.81	72.56	99.48	0.00	1.27	264.01
22	5.79	88.08	101.87	0.00	0.43	109.41	**22**	13.50	71.66	99.45	0.00	1.15	264.50
23	5.79	88.54	101.90	0.00	0.24	192.65	**23**	13.48	70.57	99.42	0.00	1.14	255.94
06/07/2013							18/04/204						
HOUR	**TAIR**	**RELH**	**PRES**	**SRAD**	**WSPD**	**WDIR**	**HOUR**	**TAIR**	**RELH**	**PRES**	**SRAD**	**WSPD**	**WDIR**
0	15.87	76.45	101.19	0.00	0.67	204.80	**0**	6.51	76.17	100.31	0.00	1.31	283.32
1	15.02	81.85	101.18	0.00	0.87	201.51	**1**	6.11	79.15	100.32	0.00	1.30	295.34
2	14.71	84.35	101.17	0.00	0.86	198.01	**2**	5.62	80.97	100.35	0.00	0.95	271.80
3	14.39	85.10	101.18	1.04	0.77	192.41	**3**	5.07	82.52	100.36	0.00	0.87	233.25
4	13.83	87.13	101.19	20.25	0.81	195.69	**4**	4.62	81.78	100.37	0.44	0.73	167.63
5	14.30	84.12	101.22	106.68	0.87	197.16	**5**	4.69	78.60	100.42	27.12	0.80	56.00
6	16.21	74.84	101.22	245.12	1.04	201.28	**6**	5.67	73.16	100.47	116.33	1.51	44.56
7	18.10	66.77	101.23	455.67	1.32	208.50	**7**	6.51	64.09	100.52	291.35	2.74	45.03
8	19.08	64.99	101.24	574.55	1.82	208.94	**8**	7.37	57.30	100.56	464.33	2.62	51.33
9	20.14	61.49	101.24	736.98	1.52	205.73	**9**	8.27	52.55	100.58	565.17	2.53	52.22
10	21.76	52.66	101.23	868.83	1.48	203.83	**10**	9.38	48.28	100.58	615.31	2.14	57.32
11	22.28	51.70	101.22	819.65	1.57	202.51	**11**	10.28	42.12	100.57	697.73	2.27	82.56
12	23.20	49.30	101.19	772.67	1.33	207.16	**12**	10.87	38.90	100.56	620.32	2.15	67.70
13	23.97	46.76	101.15	870.90	1.36	196.41	**13**	11.31	38.84	100.54	606.79	1.95	72.70
14	24.60	44.36	101.14	770.69	1.24	178.17	**14**	11.75	38.85	100.52	558.83	1.89	83.14
15	25.15	41.91	101.12	646.10	1.16	194.24	**15**	11.77	39.83	100.49	418.05	1.75	64.76
16	25.34	40.81	101.12	533.53	1.12	222.06	**16**	11.55	40.47	100.45	243.04	1.93	68.53
17	25.11	38.70	101.13	301.69	1.17	212.53	**17**	11.15	43.05	100.44	108.69	2.01	63.20
18	24.55	40.14	101.15	173.52	1.24	219.55	**18**	10.51	45.31	100.44	34.01	1.70	68.43
19	23.70	44.70	101.18	49.12	0.77	224.01	**19**	9.52	49.55	100.46	1.96	1.11	88.04
20	22.09	51.25	101.23	5.50	0.37	219.12	**20**	8.26	56.42	100.48	0.00	0.61	122.00
21	20.53	60.48	101.29	0.00	0.63	271.52	**21**	7.38	61.42	100.47	0.00	0.79	108.92
22	19.09	71.27	101.34	0.00	0.99	304.24	**22**	6.33	67.31	100.47	0.00	0.94	103.33
23	17.51	74.38	101.38	0.00	1.12	309.12	**23**	5.37	72.09	100.47	0.00	0.66	109.61

Table E. 3: Tile 2 meteorological inputs to model the T_{mrt} for the four days using UMEP plugin in QGIS.

01/12/2013							05/09/2013						
HOUR	TAIR	RELH	PRES	SRAD	WSPD	WDIR	HOUR	TAIR	RELH	PRES	SRAD	WSPD	WDIR
0	6.56	80.13	101.42	0.00	1.45	251.39	0	17.26	67.11	99.84	0.00	0.89	190.70
1	7.21	79.29	101.40	0.00	1.68	275.60	1	16.39	68.75	99.79	0.00	0.81	188.54
2	7.53	78.21	101.40	0.00	2.01	287.32	2	15.42	72.10	99.74	0.00	0.71	198.96
3	7.51	78.06	101.40	0.00	1.96	278.58	3	14.30	77.37	99.67	0.00	0.50	200.08
4	7.51	77.95	101.40	0.02	1.90	266.90	4	13.13	83.04	99.63	0.00	0.59	199.65
5	7.54	76.64	101.40	0.03	2.11	289.12	5	13.24	83.59	99.62	8.04	0.64	168.38
6	7.53	75.35	101.41	0.02	2.13	285.09	6	14.01	81.97	99.63	79.46	0.49	172.47
7	7.54	75.35	101.47	0.96	1.70	272.23	7	17.16	69.98	99.65	243.50	0.91	257.49
8	7.63	75.01	101.53	15.56	1.28	256.18	8	18.26	65.39	99.66	414.87	1.27	278.29
9	8.15	73.59	101.58	45.96	0.97	276.77	9	19.42	61.68	99.65	595.90	1.45	278.72
10	8.51	74.23	101.62	52.67	1.32	280.06	10	19.64	61.97	99.61	604.70	1.52	271.88
11	8.52	78.35	101.61	55.13	1.35	266.19	11	20.06	60.49	99.58	631.72	1.44	243.20
12	8.86	77.55	101.60	112.84	1.25	260.46	12	20.20	58.88	99.56	541.72	1.46	262.01
13	9.51	74.38	101.59	116.64	1.16	190.32	13	20.81	52.02	99.53	603.25	1.50	264.99
14	9.48	72.59	101.59	49.43	1.11	131.05	14	21.40	47.22	99.48	558.40	1.52	263.54
15	9.03	74.46	101.63	23.01	0.95	119.29	15	21.61	46.20	99.45	455.63	1.62	254.22
16	7.73	79.65	101.65	1.59	0.83	98.62	16	20.84	48.98	99.43	261.75	1.63	249.98
17	6.94	82.76	101.70	0.00	0.88	145.36	17	19.06	58.02	99.43	86.48	1.69	228.58
18	6.10	85.36	101.75	0.00	0.82	174.23	18	16.30	70.94	99.46	12.13	1.99	285.85
19	5.43	87.95	101.80	0.00	0.92	139.87	19	14.41	75.43	99.50	0.07	2.06	298.47
20	5.49	89.00	101.82	0.00	0.87	96.30	20	13.66	75.05	99.50	0.00	1.90	285.34
21	5.86	88.02	101.85	0.00	0.89	97.23	21	13.35	73.92	99.48	0.00	1.80	283.54
22	5.89	87.90	101.87	0.00	0.70	141.02	22	13.12	73.20	99.46	0.00	1.69	290.65
23	5.86	88.47	101.89	0.00	0.77	170.74	23	13.13	72.59	99.43	0.00	1.49	273.62
06/07/2013							18/04/2014						
HOUR	TAIR	RELH	PRES	SRAD	WSPD	WDIR	HOUR	TAIR	RELH	PRES	SRAD	WSPD	WDIR
0	17.82	66.73	101.38	0.00	0.86	159.42	0	6.33	79.39	100.31	0.00	1.89	281.73
1	16.86	73.25	101.36	0.00	1.58	196.23	1	5.87	80.51	100.32	0.00	1.83	289.88
2	16.14	77.90	101.35	0.00	1.44	174.68	2	5.33	82.13	100.36	0.00	1.50	260.71
3	15.73	78.72	101.36	1.01	1.50	164.45	3	4.66	84.61	100.37	0.00	1.32	259.98
4	15.48	78.40	101.37	18.49	1.23	160.28	4	4.36	84.07	100.38	0.44	1.41	208.23
5	15.78	77.07	101.40	89.76	1.07	182.69	5	4.15	83.02	100.42	18.41	1.22	100.66
6	17.35	69.35	101.41	261.98	1.28	185.81	6	4.95	79.22	100.48	88.02	1.64	90.71
7	18.75	62.70	101.41	434.38	1.54	199.39	7	6.57	65.04	100.53	279.30	2.29	68.74
8	19.79	58.62	101.43	583.38	1.63	209.46	8	7.61	54.70	100.56	444.70	2.32	73.15
9	20.68	55.86	101.42	653.93	1.64	189.89	9	8.51	50.95	100.59	551.23	2.29	78.16
10	21.33	54.26	101.42	756.66	1.59	195.11	10	9.35	48.68	100.58	555.35	2.06	119.37
11	22.40	49.65	101.41	791.93	1.71	192.20	11	10.25	44.54	100.57	660.50	2.17	92.34
12	23.53	47.10	101.37	866.43	1.61	182.33	12	11.02	38.73	100.57	710.09	1.85	94.01
13	24.26	44.89	101.34	886.02	1.56	190.25	13	11.49	37.90	100.55	647.70	1.74	105.00
14	24.87	41.53	101.32	776.81	1.45	202.33	14	11.84	38.08	100.52	561.49	1.60	103.02
15	25.21	39.28	101.31	661.96	1.43	204.47	15	11.95	38.68	100.49	440.13	1.44	95.70
16	25.36	39.36	101.30	537.80	1.42	202.49	16	11.80	39.87	100.45	320.65	1.46	79.45
17	25.53	38.11	101.31	370.56	1.19	240.63	17	11.38	41.94	100.44	165.84	1.72	71.44
18	25.26	38.11	101.34	200.19	1.19	229.03	18	10.55	45.52	100.43	42.66	1.84	86.52
19	24.29	41.09	101.36	64.52	1.15	250.58	19	9.66	48.14	100.46	1.97	1.62	97.84
20	22.77	48.81	101.43	5.69	0.87	277.18	20	8.73	53.12	100.48	0.00	1.34	102.20
21	20.06	68.29	101.49	0.00	1.33	286.65	21	7.80	58.67	100.47	0.00	1.24	120.65
22	18.07	72.92	101.55	0.00	1.15	273.18	22	6.88	64.28	100.47	0.00	1.36	113.57
23	16.89	75.26	101.58	0.00	1.34	271.82	23	5.95	69.09	100.47	0.00	1.35	111.48

Table E. 4: Tile 3 meteorological inputs to model the T_{mrt} for the four days using UMEP plugin in QGIS.

01/12/2013							05/09/2013						
HOUR	**TAIR**	**RELH**	**PRES**	**SRAD**	**WSPD**	**WDIR**	**HOUR**	**TAIR**	**RELH**	**PRES**	**SRAD**	**WSPD**	**WDIR**
0	6.68	81.32	101.72	0.00	1.37	274.82	**0**	16.25	69.94	100.12	0.00	0.57	154.70
1	7.38	78.72	101.70	0.00	1.96	293.41	**1**	15.07	72.96	100.07	0.00	0.57	176.26
2	7.66	77.63	101.71	0.00	2.28	304.35	**2**	14.02	76.24	100.02	0.00	0.41	194.05
3	7.42	78.17	101.71	0.00	1.73	301.80	**3**	13.15	79.51	99.96	0.00	0.34	195.02
4	7.44	78.51	101.70	0.00	2.08	308.64	**4**	12.61	81.31	99.91	0.00	0.38	203.59
5	7.44	77.60	101.70	0.00	2.39	306.01	**5**	12.29	82.72	99.90	11.01	0.45	219.43
6	7.29	76.54	101.71	0.00	2.24	305.69	**6**	13.67	78.88	99.91	106.30	0.41	223.07
7	7.41	76.24	101.77	0.99	1.58	307.58	**7**	16.91	69.77	99.93	269.30	0.79	229.78
8	7.55	76.49	101.84	16.22	1.19	295.49	**8**	18.68	63.74	99.93	411.63	1.52	285.36
9	8.11	75.06	101.88	48.91	1.06	281.97	**9**	19.68	60.80	99.91	557.09	1.51	287.77
10	8.55	74.91	101.92	66.87	1.64	303.71	**10**	20.45	58.76	99.87	726.71	1.66	266.95
11	8.58	78.50	101.91	57.33	1.57	303.61	**11**	20.85	57.65	99.84	679.49	1.50	277.78
12	9.09	78.09	101.90	134.19	1.46	282.73	**12**	20.86	57.38	99.82	554.23	1.73	261.19
13	9.42	74.11	101.89	84.17	1.29	243.17	**13**	21.24	52.85	99.79	628.80	1.91	303.30
14	9.51	72.34	101.90	49.49	1.09	152.29	**14**	21.45	46.54	99.74	430.29	1.75	298.00
15	8.83	74.96	101.93	21.14	0.68	127.79	**15**	21.92	44.56	99.71	489.30	1.86	287.29
16	7.30	79.96	101.96	1.60	0.45	123.65	**16**	21.19	47.18	99.69	215.04	1.79	290.05
17	6.43	84.08	102.00	0.01	0.35	143.69	**17**	19.51	56.85	99.69	82.17	2.10	306.78
18	5.52	86.88	102.06	0.00	0.34	147.26	**18**	17.24	67.32	99.72	13.92	2.21	301.39
19	4.82	89.57	102.11	0.00	0.43	159.17	**19**	14.93	73.84	99.77	0.03	2.30	311.92
20	5.07	89.94	102.13	0.00	0.59	105.43	**20**	14.00	74.26	99.77	0.00	2.17	310.05
21	5.44	89.45	102.16	0.00	0.56	104.49	**21**	13.70	73.38	99.76	0.00	1.95	311.30
22	5.60	88.86	102.18	0.00	0.42	202.23	**22**	13.42	72.76	99.74	0.00	1.75	307.61
23	5.65	89.10	102.20	0.00	0.29	223.34	**23**	13.37	71.70	99.70	0.00	1.72	301.68
06/07/2013							**18/04/2014**						
HOUR	**TAIR**	**RELH**	**PRES**	**SRAD**	**WSPD**	**WDIR**	**HOUR**	**TAIR**	**RELH**	**PRES**	**SRAD**	**WSPD**	**WDIR**
0	16.75	71.50	101.37	0.00	0.57	156.61	**0**	6.34	75.52	100.64	0.01	1.94	300.04
1	15.85	77.22	101.35	0.00	0.58	175.45	**1**	5.86	79.44	100.65	0.01	1.80	302.25
2	14.89	82.68	101.35	0.00	0.55	168.13	**2**	5.34	81.67	100.69	0.01	1.35	294.58
3	14.49	84.01	101.36	0.90	0.60	170.51	**3**	4.84	83.08	100.70	0.01	1.19	292.09
4	14.37	84.02	101.37	21.55	0.62	168.09	**4**	4.49	82.30	100.72	0.44	1.01	285.68
5	15.12	80.93	101.40	112.39	0.77	167.87	**5**	4.34	80.88	100.76	26.77	0.78	231.74
6	17.20	71.31	101.40	287.88	0.94	164.24	**6**	5.59	74.80	100.82	149.92	1.07	185.57
7	19.09	62.84	101.41	460.88	1.02	184.47	**7**	6.85	63.64	100.87	317.25	1.92	88.41
8	20.17	58.77	101.42	597.19	1.23	186.37	**8**	7.62	56.74	100.90	468.05	2.16	93.15
9	20.84	56.84	101.41	700.22	1.33	170.85	**9**	8.57	51.50	100.92	591.86	1.93	102.26
10	21.60	54.08	101.40	735.45	1.24	197.23	**10**	9.56	47.42	100.91	650.68	1.91	125.27
11	22.66	48.78	101.40	888.80	1.43	169.46	**11**	10.42	41.67	100.91	725.97	2.10	134.58
12	23.44	47.72	101.36	873.89	1.47	186.79	**12**	11.00	38.93	100.90	731.00	2.06	113.65
13	24.18	45.64	101.33	846.35	1.24	180.49	**13**	11.48	38.98	100.88	672.85	1.66	99.77
14	24.72	43.31	101.31	768.79	1.21	169.61	**14**	11.85	39.19	100.86	596.16	1.63	118.70
15	25.21	40.44	101.29	640.66	1.19	194.32	**15**	11.92	39.79	100.83	484.10	1.65	83.04
16	25.65	38.71	101.28	525.00	1.05	237.96	**16**	11.87	40.63	100.79	304.87	1.60	94.76
17	25.51	38.79	101.29	302.21	1.04	231.16	**17**	11.43	42.99	100.77	153.25	1.55	84.55
18	25.16	39.01	101.32	144.08	0.88	252.45	**18**	10.63	45.70	100.77	46.36	1.40	84.59
19	24.19	43.21	101.34	53.33	0.95	251.11	**19**	9.55	49.79	100.79	2.10	1.05	98.83
20	22.86	47.49	101.41	5.96	0.96	273.17	**20**	8.49	55.20	100.82	0.01	0.90	112.99
21	20.64	65.82	101.47	0.01	1.77	298.23	**21**	7.53	60.57	100.81	0.01	0.84	112.36
22	18.38	72.45	101.53	0.00	1.70	295.68	**22**	6.59	66.42	100.81	0.01	1.04	113.74
23	17.02	75.49	101.56	0.00	1.44	296.43	**23**	5.58	71.47	100.81	0.01	0.81	101.06

Table E. 5: Tile 4 meteorological inputs to model the T_{mrt} for the four days using UMEP plugin in QGIS.

01/12/2013							05/09/2013						
HOUR	TAIR	RELH	PRES	SRAD	WSPD	WDIR	HOUR	TAIR	RELH	PRES	SRAD	WSPD	WDIR
0	6.81	81.87	101.41	0.00	1.63	284.22	0	14.18	82.32	99.83	0.00	0.45	194.07
1	7.37	79.11	101.39	0.00	2.29	308.13	1	13.26	82.89	99.78	0.00	0.53	182.07
2	7.42	79.31	101.39	0.00	2.49	313.93	2	12.41	83.93	99.73	0.00	0.38	181.76
3	7.12	80.41	101.39	0.00	2.13	321.82	3	11.90	84.88	99.67	0.00	0.46	221.57
4	7.28	80.09	101.39	0.00	2.18	321.81	4	11.52	85.15	99.62	0.00	0.49	187.26
5	7.36	78.73	101.39	0.00	2.47	316.53	5	10.99	86.81	99.62	5.06	0.48	217.70
6	7.37	76.94	101.39	0.00	2.61	316.59	6	11.48	86.82	99.62	26.84	0.82	241.82
7	7.41	76.98	101.46	0.97	2.07	319.53	7	14.29	83.85	99.64	218.48	1.21	266.03
8	7.55	76.85	101.52	15.54	1.35	312.32	8	17.23	73.04	99.65	373.63	1.48	314.09
9	8.05	75.87	101.57	48.54	1.25	306.43	9	18.66	66.60	99.64	458.06	1.85	302.58
10	8.32	77.50	101.61	56.32	1.77	315.08	10	18.50	69.00	99.61	382.64	1.69	310.77
11	8.37	80.98	101.60	50.74	1.72	314.74	11	19.07	66.13	99.58	452.62	1.52	308.74
12	8.98	78.69	101.59	127.36	1.59	318.27	12	19.28	63.10	99.56	473.55	1.45	324.11
13	9.46	75.13	101.59	115.40	1.41	297.91	13	20.17	55.80	99.53	552.63	1.50	316.23
14	9.48	73.76	101.59	52.36	1.09	239.71	14	21.00	50.48	99.48	562.91	1.97	324.23
15	8.89	76.03	101.62	22.32	0.63	103.69	15	21.11	50.00	99.45	442.81	1.97	324.03
16	7.45	80.74	101.65	1.53	0.46	104.23	16	20.43	52.26	99.43	253.63	2.13	331.49
17	6.31	84.68	101.69	0.00	0.37	148.76	17	18.34	62.03	99.43	89.35	2.41	332.73
18	4.73	88.44	101.75	0.00	0.40	201.61	18	15.49	74.75	99.45	13.68	2.55	329.21
19	3.54	90.73	101.79	0.00	0.54	170.69	19	13.93	77.80	99.50	0.09	2.40	324.62
20	3.48	91.19	101.82	0.00	0.66	139.49	20	12.15	85.71	99.65	0.00	1.11	260.78
21	3.95	91.46	101.84	0.00	0.53	135.80	21	12.98	76.68	99.48	0.00	1.92	326.40
22	4.57	91.47	101.87	0.00	0.37	173.56	22	12.80	75.70	99.46	0.00	1.91	326.82
23	5.08	91.28	101.89	0.00	0.27	157.98	23	12.76	75.72	99.42	0.00	1.76	326.79
06/07/2013							18/04/2014						
HOUR	TAIR	RELH	PRES	SRAD	WSPD	WDIR	HOUR	TAIR	RELH	PRES	SRAD	WSPD	WDIR
0	11.26	92.82	101.63	0.00	0.32	183.19	0	5.81	80.47	100.30	0.00	1.91	321.43
1	10.73	93.32	101.62	0.00	0.37	168.72	1	5.36	82.71	100.31	0.00	1.98	331.68
2	10.72	93.79	101.61	0.00	0.41	181.02	2	4.70	84.86	100.34	0.00	1.76	330.74
3	11.42	94.38	101.62	0.93	0.62	192.62	3	4.28	85.73	100.36	0.00	1.30	292.91
4	11.66	94.17	101.63	18.51	1.01	212.07	4	3.34	86.44	100.38	0.45	0.70	268.17
5	13.07	94.52	101.66	117.22	0.32	221.97	5	2.47	87.14	100.41	23.86	0.57	246.32
6	16.09	84.77	101.66	256.72	0.98	190.78	6	4.31	83.96	100.47	135.97	0.88	202.98
7	18.95	66.27	101.67	428.72	1.37	182.03	7	6.52	67.67	100.52	311.60	1.52	65.94
8	19.73	61.44	101.68	566.34	2.07	217.79	8	7.55	58.34	100.55	467.64	1.73	73.91
9	20.46	59.83	101.68	644.93	1.73	194.01	9	8.52	53.59	100.58	601.58	1.74	76.49
10	21.42	56.05	101.67	765.77	1.69	192.28	10	9.41	50.24	100.57	658.13	2.06	162.86
11	22.48	52.13	101.66	839.67	1.77	185.81	11	10.20	46.88	100.56	663.42	1.88	156.32
12	23.26	50.35	101.63	801.39	1.76	184.04	12	11.11	41.53	100.56	740.90	1.74	138.13
13	23.98	46.29	101.59	800.58	1.73	191.17	13	11.32	40.17	100.54	720.41	1.84	158.50
14	24.65	43.78	101.57	702.84	1.38	209.34	14	11.70	40.46	100.51	613.60	1.72	101.65
15	24.95	41.82	101.56	603.23	1.21	226.91	15	12.00	40.53	100.48	521.69	1.48	127.72
16	25.31	39.68	101.55	486.63	1.02	220.15	16	12.03	41.67	100.44	348.37	1.34	83.74
17	25.21	39.90	101.56	331.43	0.95	193.59	17	11.52	43.85	100.43	205.00	1.27	95.53
18	25.00	43.20	101.59	184.64	0.73	253.22	18	10.34	48.17	100.42	56.16	1.11	92.42
19	22.96	47.35	101.62	51.40	0.62	266.78	19	8.48	55.40	100.45	2.23	0.76	112.51
20	20.84	60.49	101.68	5.74	1.34	302.53	20	6.66	64.09	100.47	0.00	0.70	158.94
21	19.01	71.80	101.76	0.02	2.05	334.89	21	5.38	70.53	100.46	0.00	0.75	155.30
22	17.26	75.34	101.81	0.00	1.87	329.62	22	4.42	76.39	100.46	0.00	0.75	166.00
23	16.06	78.15	101.85	0.00	0.99	290.77	23	4.22	78.71	100.46	0.00	0.60	149.93

Table E. 6: Tile 5 meteorological inputs to model the T_{mrt} for the four days using UMEP plugin in QGIS.

01/12/2013							05/09/2013						
HOUR	TAIR	RELH	PRES	SRAD	WSPD	WDIR	HOUR	TAIR	RELH	PRES	SRAD	WSPD	WDIR
0	6.91	83.06	101.62	0.00	1.24	292.37	0	11.46	92.77	100.06	0.00	0.31	218.43
1	7.30	78.91	101.60	0.00	1.47	294.62	1	10.46	92.98	100.02	0.00	0.28	250.84
2	7.16	79.95	101.61	0.00	1.01	270.83	2	9.91	93.18	99.96	0.00	0.38	330.98
3	6.65	81.56	101.61	0.00	0.76	253.12	3	9.35	93.14	99.90	0.00	0.31	269.54
4	6.98	81.27	101.61	0.00	0.90	274.48	4	8.57	93.25	99.86	0.02	0.25	258.56
5	6.82	81.65	101.60	0.00	1.09	287.32	5	8.05	93.32	99.85	6.47	0.29	285.87
6	6.65	81.19	101.61	0.01	1.23	298.80	6	8.70	93.60	99.85	41.85	0.21	174.30
7	6.92	80.27	101.68	1.07	0.98	286.52	7	12.63	93.75	99.88	241.68	0.28	157.18
8	7.16	80.02	101.74	16.36	0.69	267.58	8	16.69	83.23	99.88	384.95	0.64	205.07
9	7.92	78.05	101.79	48.12	0.62	247.31	9	19.04	68.83	99.87	516.44	1.16	235.26
10	8.50	77.57	101.83	64.52	0.98	299.71	10	19.62	67.85	99.84	506.39	0.83	230.00
11	8.41	81.07	101.82	46.34	0.94	280.25	11	20.02	66.23	99.80	444.56	0.91	244.38
12	9.16	78.36	101.81	118.88	0.98	250.11	12	20.32	62.92	99.78	508.95	0.95	233.79
13	9.76	74.16	101.81	95.60	0.88	177.40	13	20.79	56.98	99.75	533.87	1.00	260.98
14	9.23	76.15	101.81	39.56	0.42	182.60	14	21.21	53.76	99.71	506.00	1.04	247.37
15	7.50	82.59	101.85	22.10	0.41	225.36	15	21.47	51.71	99.67	461.64	1.07	252.90
16	5.85	87.83	101.87	1.33	0.41	237.30	16	20.75	54.97	99.66	301.73	0.96	267.97
17	5.35	88.82	101.92	0.00	0.31	243.98	17	18.32	65.05	99.66	89.29	0.94	271.89
18	4.07	91.27	101.98	0.00	0.41	299.09	18	15.95	74.80	99.67	14.24	1.10	270.53
19	3.34	91.90	102.02	0.00	0.57	188.06	19	14.01	79.64	99.72	0.08	1.06	288.37
20	3.40	92.50	102.05	0.00	0.49	180.56	20	13.16	79.76	99.72	0.00	0.97	236.05
21	4.33	91.99	102.07	0.00	0.45	201.98	21	12.87	79.29	99.70	0.00	0.90	270.51
22	4.87	91.87	102.09	0.00	0.38	258.49	22	12.58	78.84	99.68	0.00	0.90	233.49
23	5.16	91.80	102.11	0.00	0.29	243.07	23	12.38	79.09	99.65	0.00	0.60	184.24
06/07/2013							18/04/2014						
HOUR	TAIR	RELH	PRES	SRAD	WSPD	WDIR	HOUR	TAIR	RELH	PRES	SRAD	WSPD	WDIR
0	11.50	93.00	101.50	0.00	0.33	267.78	0	5.58	79.22	1005.07	0.00	1.14	297.05
1	11.50	93.00	101.50	0.00	0.33	267.78	1	5.15	82.46	1005.18	0.00	1.15	318.05
2	10.51	93.59	101.48	0.00	0.24	308.05	2	4.76	84.98	1005.58	0.00	0.83	266.78
3	10.27	93.73	101.49	0.84	0.25	241.27	3	4.27	85.62	1005.72	0.00	0.70	287.70
4	10.29	93.90	101.50	15.25	0.27	233.55	4	3.44	86.24	1005.92	0.45	0.43	227.72
5	11.36	94.14	101.53	43.44	0.27	220.83	5	2.81	87.19	1006.32	23.08	0.43	219.04
6	14.56	92.01	101.53	217.88	0.48	92.86	6	4.58	82.28	1006.85	126.08	0.98	124.53
7	18.50	69.02	101.54	398.49	0.83	182.16	7	5.02	67.47	1007.46	317.36	1.74	128.39
8	20.03	60.05	101.54	505.42	1.17	204.83	8	7.72	59.54	1007.84	470.77	1.87	101.22
9	20.85	57.79	101.54	611.37	1.16	177.61	9	8.70	54.00	1008.01	600.50	2.02	99.00
10	21.46	55.53	101.53	581.34	1.17	168.99	10	9.84	49.23	1007.86	616.49	1.43	152.94
11	22.21	51.84	101.53	729.59	1.33	166.43	11	10.60	43.29	1007.85	737.85	1.94	123.42
12	23.16	48.51	101.49	783.61	1.29	208.82	12	11.08	41.69	1007.83	749.47	1.72	112.80
13	23.85	47.74	101.45	732.18	1.24	192.12	13	11.22	42.57	1007.62	600.19	1.45	146.28
14	24.47	45.38	101.44	678.86	1.10	213.23	14	11.23	43.36	1007.36	449.92	1.55	126.62
15	24.99	43.22	101.42	549.95	0.94	191.44	15	11.52	43.95	1007.07	452.29	1.57	122.02
16	25.39	41.53	101.41	437.84	0.73	224.15	16	11.47	43.83	1006.69	327.85	1.41	128.01
17	25.34	43.92	101.42	330.83	0.61	187.24	17	11.15	46.03	1006.55	191.74	1.21	132.98
18	23.90	50.50	101.45	147.48	0.66	164.59	18	9.81	51.24	1006.46	28.87	0.85	115.37
19	21.38	63.62	101.48	41.38	0.57	254.88	19	7.62	60.55	1006.69	2.01	0.42	179.87
20	17.61	79.36	101.53	5.31	0.53	308.01	20	5.52	69.63	1006.94	0.00	0.43	284.08
21	16.66	85.06	101.60	0.00	0.37	159.63	21	4.18	75.86	1006.88	0.00	0.37	261.94
22	16.72	82.10	101.65	0.00	0.59	164.53	22	3.47	80.90	1006.89	0.00	0.55	173.92
23	15.32	85.79	101.69	0.00	0.29	100.64	23	2.89	84.26	1006.93	0.00	0.46	187.16